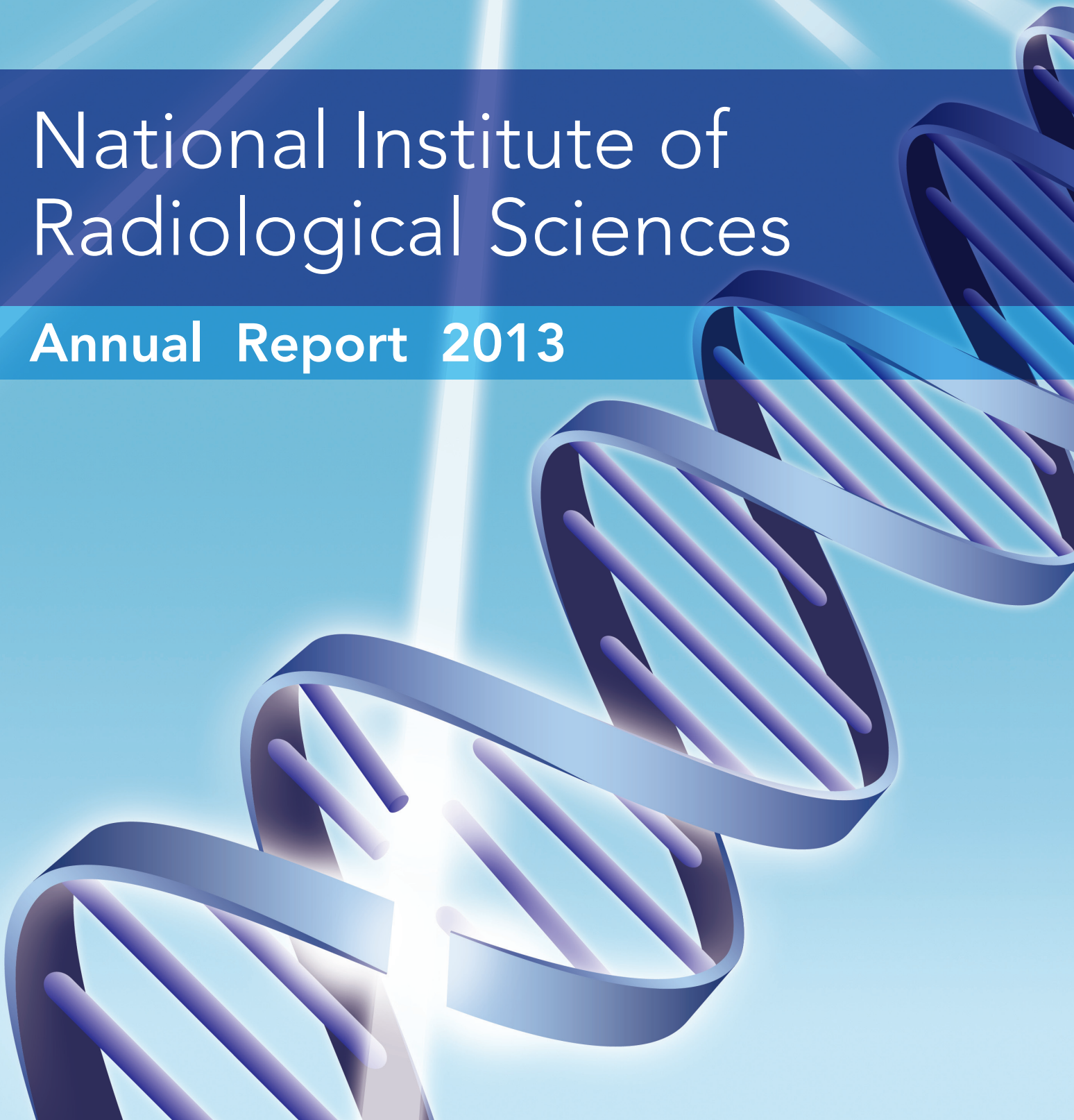


National Institute of Radiological Sciences

Annual Report 2013



**Annual Report 2013
(April 2013-March 2014)**

NATIONAL INSTITUTE OF
RADIOLOGICAL SCIENCES

Date of Publication August 2014
Editing and Publication Research Information Science
Dept. of Information Technology
Research, Development and Support Center
National Institute of Radiological Sciences
Anagawa 4-9-1, Inage-ku, Chiba, 263-8555 Japan
Tel : +81-43-206-3485
Fax : +81-43-290-1112
E-mail: kagakujohoka@nirs.go.jp

Homepage:<http://www.nirs.go.jp>

Full Text: <http://www.nirs.go.jp/ENG/publications/index.shtml>

Copyright ©2014 National Institute of Radiological Sciences All Rights Reserved

Printed in Japan

ISSN 0439-5956

NIRS-52

Editorial Note

This document presents the research and development results of NIRS for the fiscal year of 2013 (April 2013 - March 2014). When the 3rd mid-term plan of NIRS was begun in fiscal year 2011, we felt it was a good opportunity to revise the contents and format of the annual report. For the Annual Report 2013, we decided to follow this editing policy and we made a full-fledged revision of the contents. Our main revision was to publish summarized results on each research theme as “Highlights”. Then, “Topics” sections were prepared that selected five results and outcomes with a technical research and development component. Finally, as an appendix we include the “List of original papers” for readers who are looking for more details.

This report is available as an electronic edition on the NIRS web site (<http://www.nirs.go.jp/ENG/publications/index.shtml>). The Editorial staff hopes that our readers will find it to be a handy resource describing what NIRS researchers have been doing. Finally, we thank the various persons who worked on the production and English proofreading.

Editorial Staff

Reiko ISHII

Ryouji MIMIDUKA

Masanori OKAMOTO

Takeo SHIMOMURA

Katsumi UZAWA

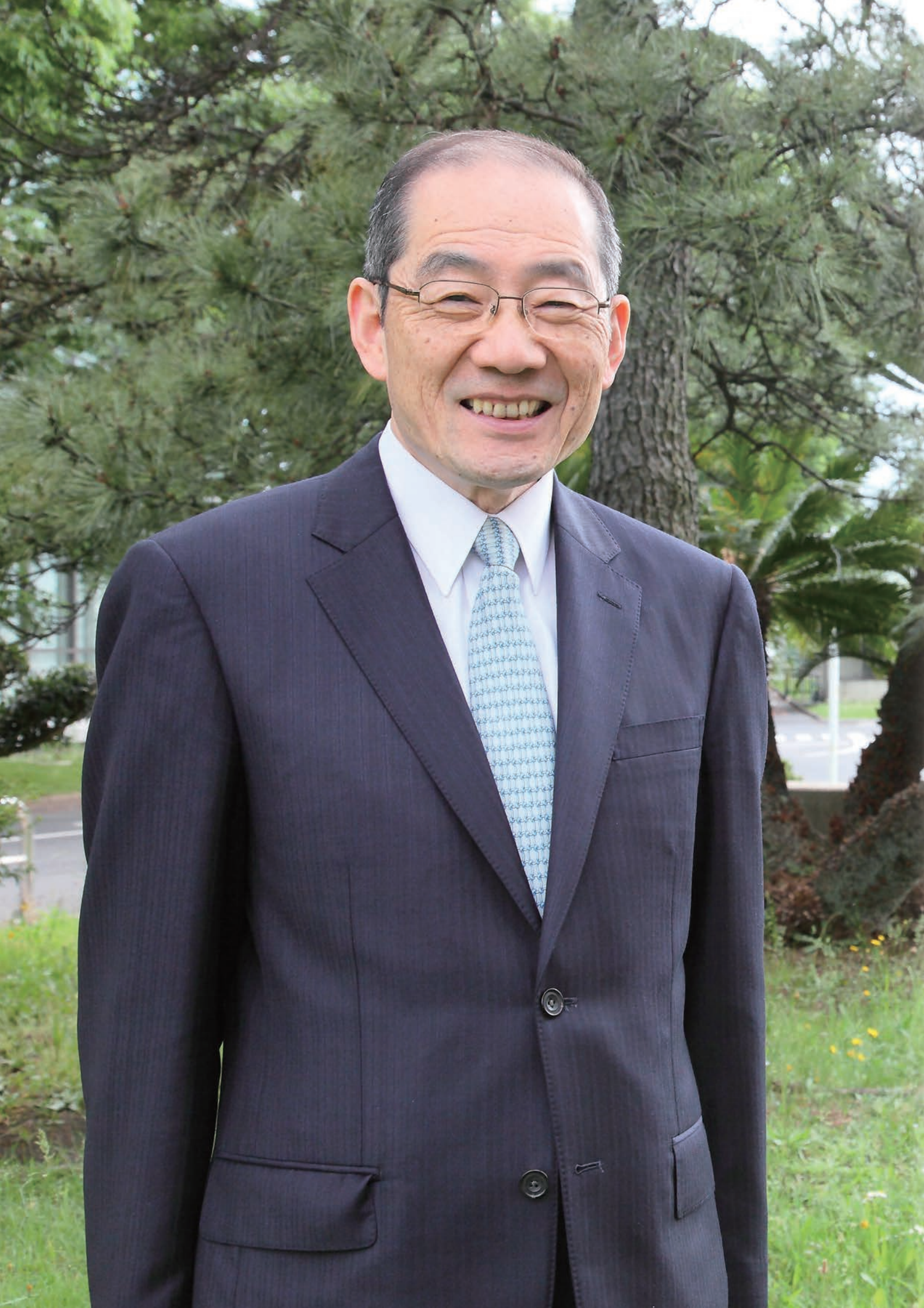
Satomi WATANABE

Contents

Preface	8
■ Outline of Research Activities	10
■ Research on Cancer Therapy with Carbon Beams	12
<Department of Accelerator and Medical Physics>	
<i>Highlights</i>	
Measurement of neutron ambient dose equivalent in the HIMAC new treatment room	14
¹⁰ / ¹¹ C molecule production/separation system for ¹⁰ / ¹¹ C ion acceleration	16
<Research on the Standardization and Clarification of Charged Particle Therapy>	
<i>Highlight</i>	
Carbon-ion radiotherapy for locally advanced uterine cervical cancer	18
<Research and Development on Medical Physics and Biology>	
<i>Highlights</i>	
Modeling of normal tissue response in C-ion RT	20
Measurement of RBE and OER of clinical carbon beams: An in vivo study	22
<Basic Research on the Estimation of Effectiveness of Radiotherapy for Individual Cancer Patients>	
<i>Highlights</i>	
New aspects of FGF radioprotectors	24
Irradiation responsive miRNA “miR-574-3p” delays cell growth by suppressing cell cycle-related gene “enhancer of rudimentary homolog (ERH)”	26
<Research and Development for the International Promotion of Carbon Ion Radiotherapy>	
<i>Highlights</i>	
Enhanced lethal effect via bystander effect using carbon-ion microbeams simulating the 3D fast spot scanning system	28
The Research Project with Heavy Ions at NIRS-HIMAC	30
■ Molecular Imaging Research for Functional Diagnosis	32
<Development and Production of PET Probes for Molecular Imaging>	
<i>Highlights</i>	
Imaging of activity of the ATP-binding cassette transporter ABCC1 in the lungs	34
Development of radiolabeling technique for cyclic RGD peptide by using carbon-11 formaldehyde	36
<Research and Development of Advanced Bioimaging and Quantitative Analysis System>	
<i>Highlights</i>	
Multimodal functional imaging of nigral dopaminergic neurons with PET and MRI	38
Development of the X'tal cube PET detector: the use of scintillator plates	40
<Research on Pathophysiological Diagnosis of Cancer and Other Diseases with Molecular Imaging>	
<i>Highlights</i>	
Development of positron emission tomography probe for imaging CD147 expression in tumors	42
Fatty acid synthase is a key target in multiple essential tumor functions: [1- ¹¹ C]acetate PET to predict the targeted therapy outcome	44
<Molecular Imaging Research on Neuropsychiatric Disorders>	
<i>Highlights</i>	
In-vivo visualization of tau pathology in living mouse model and patients with Alzheimer's disease and related neurodegenerative tauopathies	46
Antidepressants and norepinephrine transporter in the brain: Clinical positron emission tomography studies using (S, S)-[¹⁸ F]FMeNER-D ₂	48

■ Research on Radiation Protection	50
<Biospheric Assessment for Waste Disposal>	
<i>Highlights</i>	
Root uptake of radiocesium by a vegetable growing on various potting mixes.....	54
Ecological half-lives of radiocesium in some marine biota caught offshore of Fukushima Prefecture.....	56
<Experimental Studies on the Radiation Protection of Children>	
<i>Highlights</i>	
Cancer prevention by adult-onset calorie restriction after infant exposure to ionizing radiation in B6C3F1 male mice	58
Effect of age at exposure on hematopoietic stem and progenitor survival	60
<Mechanistic Studies on the Reduction of Risks Relating to Radiation>	
<i>Highlights</i>	
Generation of breast cancer stem cells by steroid hormones in irradiated human mammary cell lines.....	62
Most hydrogen peroxide-induced histone H2AX phosphorylation is mediated by ATR and is not dependent on DNA double-strand breaks.....	64
<Bridging the Gap between Scientific Knowledge and Society: Regulatory Sciences Research>	
<i>Highlights</i>	
Radiation monitoring at the summit of Mt. Fuji for the study of high-altitude radiation environment	66
Methodological extensions of meta-analysis with excess relative risk estimates	68
■ Research on Radiation Emergency Medicine	70
<Research on Treatment and Diagnosis for Traumatic Radiation Damage>	
<i>Highlights</i>	
Radiation increases the cellular uptake of exosomes through CD29/CD81 complex formation	72
Preparation of agarose beads containing Prussian blue and magnetite for internal decorporation of radiocesium.....	74
<Research on the Development of Dosimetric Technology>	
<i>Highlights</i>	
Accuracy investigation of whole body counters operated in Fukushima Prefecture	76
Biodosimetry of restoration workers for Fukushima Daiichi Nuclear Power Station accident.....	78
■ Development of Fundamental Technologies in Radiological Science	80
<Research Toward the Development of Fundamental Technologies that Support the Use of Radiation>	
<i>Highlights</i>	
Verification of shielding method with water-filled materials for space radiation protection.....	82
Development of a novel method for prediction of mouse embryo viability	84
A genome-wide analysis of point mutations in embryonic stem cells and induced pluripotent stem cells	86
■ Fukushima Project Headquarters	88
<Project for Environmental Dynamics and Radiation Effects>	
<i>Highlights</i>	
Effects of chronic γ -irradiation on the Tohoku hynobiid salamander, <i>Hynobius lichenatus</i>	90
Radionuclides in the marine environment off the coast of Fukushima Prefecture after the TEPCO Fukushima Daiichi Nuclear Power Station accident.....	92
<Radiation Effect Accumulation and Prevention Project>	
<i>Highlight</i>	
Effects of gamma-rays on hair follicle regeneration in mice.....	94

■ Research on Evaluation of Medical Exposure	96
<i>Highlights</i>	
Evaluation of extra-pelvic organ doses in radiotherapy of uterine cervical cancer	98
Pediatric CT dose study at a tertiary children's hospital	100
■ International Open Laboratory at NIRS (Second Term)	102
<i>Highlights</i>	
Radiation Response Model Research Unit	104
Oxygen enhancement ratio (OER) and LET to heavy ion beams at different pO ₂ concentrations.....	106
■ Topics	108
Research on the standardization and clarification of charged particle therapy	108
Total-body low dose irradiation induces early transcriptional alteration without late Alzheimer's disease-like pathogenesis and memory impairment in mice	110
Telephone consultations on radiation exposure	
- Tabulated results from the year following the TEPCO Fukushima Daiichi Nuclear Power Station accident -	112
Imaging of radioactive contaminants with a characteristic X-ray camera	114
Designation as WHO Collaborating Centre.....	116
■ Organization Chart, Board Members, International Collaboration, Budget, Personnel	118
■ Appendix: List of Original Papers	126



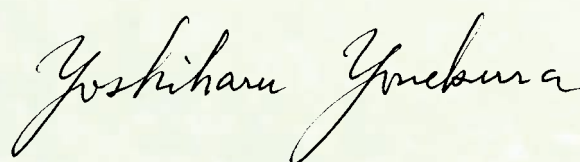
Preface

The National Institute of Radiological Sciences (NIRS) is Japan's leading medical research institution dedicated to comprehensive research on radiation and human health. NIRS has carried out various scientific activities related to radiological sciences over the half-century since its foundation in 1957. This annual report summarizes our accomplishments and research outcomes in fiscal year 2013 (April 2013—March 2014).

NIRS continues its scientific research and development, according to the third mid-term plan (2011—2016), to promote medical applications of radiological sciences and to protect people from radiation injury. The work for restoration after the severe nuclear power plant accident in 2011 keeps NIRS staff busy. Training experts and professionals in radiological procedures and radiation protection is an important mission of NIRS in responding to the requests of society. Studies on the health effects of low dose radiation are the most important topics. NIRS has worked as an IAEA Collaborating Centre (IAEA-CC) since 2006. We completed the second term of IAEA-CC activities (2010—2013) in three scientific fields, including biological effects of low dose radiation, molecular imaging and carbon ion radiotherapy. This work has now been extended to the third term for another four years until 2017.

The efforts to integrate various scientific fields, from basic physics, chemistry, biology, engineering, and computer science to clinical medicine, have brought fruitful outcomes in a wide range of radiological sciences. The most successful outcome of these efforts is represented by realization of carbon ion radiotherapy. Clinical studies with more than 8000 patients during the past 20 years have clearly demonstrated the outstanding capability of this treatment for patients having locally advanced cancer. A new scanning system with pencil beam irradiation has further improved the treatment by providing a better dose distribution and shorter treatment period. Now, these results are being transferred to clinical practice in newly established facilities throughout Japan. Remarkable progress has been made in molecular imaging research which also requires the joint efforts of multi-disciplinary experts. A new molecular imaging probe developed for detection of abnormal 'tau' protein in the brain of patients with cognitive disorders has attracted the world-wide attention of scientists and neurologists working in brain science.

Cancer, cognitive disorders and health effects of radiation exposure are the major health concerns of society nowadays. NIRS continues its efforts to deal with these problems, and to establish a solid base promoting comprehensive scientific research in a wide range of radiological sciences, as 'Visible NIRS', 'NIRS in the World' and 'NIRS in History'.



Yoshiharu Yonekura, M.D., Ph.D.

President



Outline of Research Activities

Makoto Akashi, M.D., Ph. D.
Executive Director for Research

Since re-organization as an independent administrative institution in April 2001, researchers at the National Institute of Radiological Sciences (NIRS) have been performing studies according to mid-term plans that have been revised every 5 years. The first mid-term plan was started in April 2001; the second, in April 2006; and the third, in April 2011. NIRS has five fields of research activities: heavy charged particle therapy, molecular imaging, radiation protection, radiation emergency medicine, and radiation technology.

The third mid-term plan has been carried out by four research centers and one fundamental technology center. In May 2012, the program for recovery from the Fukushima Daiichi Nuclear Power Plant (NPP) accident was started as a new center. In March 2013, a new department was also established; the Radiation Emergency Medical Assistant Team (REMAT) now plays an important part in medical response to accidents including the after effects of the Fukushima NPP accident. In this report, the research activities at NIRS during the third year of the third mid-term plan (April 2013 to March 2014) are presented.

The Great East Japan Earthquake triggered tsunami with over 10 meter-high waves that damaged facilities of the Fukushima Daiichi NPP of Tokyo Electric Power Company (TEPCO) and led to the nuclear accident. Since NIRS is designated as the national core center for radiation emergency medicine, many NIRS researchers continue to be involved in response activities to the accident, though almost 3 years have passed. Besides these activities many others are also being carried out and 356 original papers were published in FY 2013, in both interna-

tional and domestic journals of high reputation. Furthermore, more than 60 proceedings were published for international and domestic scientific meetings, and 460 oral presentations and 55 patent applications were made. Collaborative studies and exchanges of researchers were also actively carried out: 134 collaborative studies were done, 345 researchers worked as visiting staff, and 134 students were accepted as trainees.

The Research Center for Charged Particle Therapy, as a leading research organization in this field, has been conducting clinical, biological and physics research studies using heavy ions generated from the heavy ion medical accelerator in Chiba (HIMAC). In FY 2013, 888 patients were treated. In FY 2013, the clinical trial team treated 7 tumor types of cancers: prostate, lung, head and neck, bone and soft tissue, liver, pancreas and post-operative pelvic recurrence of rectal cancer. Highlights of research progress are shown in detail in other sections.

The Molecular Imaging Research Center, consisting of four groups, has long experience with medical imaging technologies including positron emission tomography (PET), single photon emission tomography (SPECT), and magnetic resonance imaging (MRI). The Center conducts basic science and technology studies for molecular imaging and also application studies for diagnosis and pathophysiology of oncology and psychiatry. Current projects include the development of molecular probes and radiopharmaceutical production techniques and the investigation of measurement techniques for PET and MRI, in addition to preclinical and clinical applications in oncology and psychiatric and neurological diseases. One of the

most important topics in 2013 was determining the structure of new tau ligand PBB3 and labeling it with C-11.

The Research Center for Radiation Protection has been providing a scientific basis for establishing regulations with global standards for radiation protection, security and safety, focusing on effects of low-dose radiation derived from human activities and from natural environmental radiation. For this purpose, the results of basic radiobiological research have been provided to promote understanding of radiation effects and to encourage enactment of more reasonable regulations for the safe and secure use of radiation in our daily life. On March 5-7, 2014, the 6th International Systems Radiation Biology Workshop was held as a Research Center Symposium, jointly with DoReMi (Low Dose Research towards Multidisciplinary Integration, supported by the EC).

NIRS has been designated as the national center for radiation emergency medicine in Japan, providing direct or consultative services to local governments and hospitals in the event of a radiation incident. Since REMAT has been established, the Research Center for Radiation Emergency Medicine is now responsible for basic research studies; the Center is focusing its efforts on three projects: developing and modifying the most appropriate methodologies for evaluating radiation exposure, exploring and supplying effective drugs to reduce the radiotoxicity and metallic toxicity of internal actinide contamination, and applying mesenchymal stem cells (MSCs) as regenerative medicine to treat radiation exposure injuries.

Services provided by REMAT include providing exposed victims (patients) with the most advanced radiation emergency medicine treatments possible and making dose assessments. REMAT especially is playing an important role in medical response to the Fukushima NPP accident. REMAT also carries out activities to maintain and strengthen the emergency preparedness system and has worked to establish three nation-wide network councils for medicine, bio-dosimetry with chromosome analysis, and physical dosimetry. REMAT has also introduced several courses at NIRS on radiation emergency medical preparedness for medical professionals of the Asian region. In September 2013, NIRS was designated as a collaborating Center of the World Health Organization (WHO); the terms of reference are: strengthening preparedness to radiation emergencies and REMPAN activities; providing medical and technical assistance to WHO in response to radiation emergencies; carrying out biodosimetry and BioDoseNet (cytogenetics and internal contamination monitoring); analyzing radiation protection for indoor radon exposure; and promoting radioprotection in the field of medical exposure to ionizing radiation, with the focus on risks assessment and risk management.

Together, the Research Center for Radiation Protection and REMAT also acted as a national hub in collaboration with international organizations including the International Atomic Energy Agency (IAEA), International Commission on Radiological Protection (ICRP), and United Nations Scientific Committee on the Effects of Atomic Radiation (UNSCEAR).

The Fundamental Technology Center, which was established to support various studies performed in NIRS using advanced fundamental technologies, has been carrying out maintenance and quality control of institute accelerators including the single particle irradiation system to cell (SPICE), the particle induced X-ray emission (PIXE) analysis and tandem accelerator (PASTA), and the neutron exposure accelerator system for biological effects experiments (NASBEE), as well as radiation measurement apparatuses for cosmic rays. Efforts have also been extended to establish and support experimental animal laboratories for internal and external researchers.

In May 2012, the program for recovery from the Fukushima Daiichi NPP accident was started. This program includes four research projects and a system of cooperation. Research projects are the study for long-term and environmental effects of radiation, the health effect survey for emergency workers at the NPP, and the study of environmental dynamics of radionuclides and radiation in the ecosystems in Fukushima Prefecture. The system of cooperation is for collaboration with researchers at the Fukushima Medical University (FMU).

The second-term of the International Open Laboratory (IOL) began in April 2011 and was concluded in March 2014. Four units were approved, including the Particle Therapy Molecular Target Unit, the Particle Beam Quality Unit, the Space Radiation Research Unit, and the Radiation Response Model Unit. During the three years of operation, the IOL conducted top level research by collaborating with distinguished scientists from leading research institutes world-wide and promoted further internationalization at NIRS by actively supporting research collaborations with foreign scientists.

Some other research programs have also been continued or were newly started with the support of funding agencies including the Ministry of Education, Culture, Sports, Science and Technology (MEXT), the Ministry of Economy, Trade and Industry (METI), the Ministry of the Environment, and the Nuclear Regulation Authority (NRA).

In this report readers will be able to learn about the substantial research that was performed in the 3rd year of the third mid-term plan. I would like to conclude with heartfelt thanks for the cooperation and advice generously provided to us by all parties concerned.

Research on Cancer Therapy with Carbon Beams — Development of Human-Friendly Cancer Therapy with Carbon Ion Beams —

Tadashi Kamada, M.D., Ph.D.

Director of Research Center for Charged Particle Therapy

E-mail: t_kamada@nirs.go.jp

The Research Center for Charged Particle Therapy (hereafter, referred to as the Center) was established in 1993 when NIRS completed construction of the HIMAC. Since then it has been carrying out clinical, biological and physics research using heavy ions generated from the HIMAC.

In 2011, when the Third Mid-Term of NIRS was initiated, the Center was reorganized to conduct research on heavy ion beams using carbon ions and to develop more patient-friendly next generation heavy ion treatment systems. These will eventually contribute to the improvement of cancer cures and quality of life. The Center is organized as: four research programs, the department of physics (Director: Koji Noda, and the hospital (Director: Yutaka Ando). Progress of research and practice in the fiscal year (FY) 2013 are summarized here for the following: 1) Research program for carbon ion therapy and diagnostic imaging (Program Leader: Hiroshi Tsuji); 2) Medical physics research program for development of a novel irradiation system for charged particle therapy (PL: Toshiyuki Shirai); 3) Advanced radiation biology research program (PL: Takashi Imai); 4) Research Program for the application of heavy ions in medical sciences (PL: Takeshi Murakami); and 5) Hospital.

Research program for carbon ion therapy and diagnostic imaging (PL: Hiroshi Tsuji)

This program consists of the clinical trial research team, applied PET research team, applied MRI research team, and clinical database research team. According to the long-term objectives, research on developing advanced clinical therapy using carbon ion beam was aggressively carried out in FY 2012 and FY 2013. The clinical trial team has successfully treated quite large numbers of patients each year by carbon ion radiotherapy (C-ion RT) and it has continued clinical trials for pancreas, esophagus, uterus, kidney, and breast cancers. A total of 888 patients were treated with C-ion RT in FY 2013; that is a new record for the HIMAC. It could be achieved mainly by the increase in capacity of scanning irradiation. Prostate, lung, head and neck, bone and soft tissue, liver tumors, post operative pelvic recurrence of rectal cancer and pancreatic cancer are the leading 7 tumor types in the trials. The outcomes of C-ion RT in tumors that were hard to cure with other



modalities revealed quite high probability of local control, a survival benefit, and acceptable morbidity. In addition, clinical trials for establishment of hypofractionated C-ion RT in common cancers, such as lung, liver, and prostate cancers have also been successfully achieved. Recently, four operating carbon therapy facilities in Japan, NIRS, HIBMC (Hyogo), GHMC (Gunma), and HIMAT (Saga) organized a cooperative study group to collaborate on standardizing carbon-ion therapy in various tumor entities. The database research team developed a database system that can store the integrated information of patients treated at all the institutions of this study group, in collaboration with the clinical trial research team. In addition, a conversion tool was developed which is suitable for the different types of medical information of the respective institutions. Some details of the research progress in FY 2013 are shown in the Highlight.

Medical physics research program for development of a novel irradiation system for charged particle therapy (PL: Toshiyuki Shirai)

This program consists of the beam delivery system research team, treatment planning system research team, radiation effect research team, experimental therapy research team, and image guided radiotherapy research team. In FY2013, the number of the patients at the new treatment facility increased to about 300 and we have developed efficient daily and patient-specific QA methods for a 3D scanning irradiation system and an imaging system. We have also prepared the scanning irradiation mode for a moving target, including establishment of a QA method, implementation of a field specific target volume using 4D-CT images into the treatment planning system, and implementation of a markerless fluoroscopic respiration gating system. Especially, a clinical trial of the 4D-CT imaging system and the fluoroscopic respiration gating

system have been successfully carried out. The detailed design of a superconducting rotating gantry was finished and the construction of the main body was started. Most of the superconducting magnets for the gantry were completed and they are now being evaluated regarding the magnetic field. The modeling of normal tissue responses in carbon-ion radiotherapy at HIMAC has made good progress and results are shown in the Highlight. We have examined the LET dependence of biological effects such as the RBE and the OER within the SOBP carbon-ion beams in vivo. These results are also presented in the Highlight.

Advanced radiation biology research program (PL: Takashi Imai)

This program consists of the cancer system biology team, cancer metastasis research team, and radio-redox-response research team. These teams use different approaches to address the following research aims of the program. Many favorable outcomes have been reported in clinical trials for carbon-ion radiotherapy of several types of malignant tumors. However, some biological issues still remain to be resolved for the improvement of long-term survival. We have focused on the following fundamental issues. 1) Some tumor cells are pathologically indistinguishable from others, despite sometimes showing radio-resistance. What makes these tumor cells radio-resistant? 2) What causes distant metastases after local treatment? Are the metastatic cells simply overlooked before starting radiotherapy? If the metastatic cells are affected by irradiation, what are the molecular mechanisms? What types of tumor cells are susceptible to metastasis? How can we detect and suppress distant metastases? 3) How do reactive oxygen species generated by irradiation affect cellular functions? Can radioprotective agents, such as anti-reactive oxygen species, protect normal tissue surrounding tumor cells? Through these studies, we have considered the effects of the genetic differences in the subjects or the experimental materials such as cell lines and mouse strains used on radio-sensitivity. Thus far, in the study of molecular mechanisms in the invasive cells after irradiation, we found that irradiation alters the invasive potential of particular pancreatic cancer cell lines via altering functioning protease expression and its activities, and it also affects mesenchymal and amoeboid mode transition. We also showed that fibroblast growth factor-12 plays an essential role in radioprotective effects on intestinal radiation damage. The detailed reports including this growth factor function and a newly identified radioresponsive miRNA are highlighted elsewhere in this chapter.

Research Program for the application of heavy ions in medical sciences (PL: Takeshi Murakami)

This program consists of the: (1) heavy ion radiotherapy promotion team; (2) HIMAC research collaboration team; (3) cellular and molecular biology research team; and (4) international radiotherapy joint research team. This program mainly carried out the following activities in FY2013.

(1) Promotion of carbon ion radiotherapy

A wide range of knowledge and know-how is necessary for promotion of carbon ion radiotherapy. Research and analyses were carried out on technical developments, treatment procedures, and the social environment as related to carbon ion radiotherapy. The findings were assembled as review reports. Procedures to transfer these results and know-how to new projects at NIRS and

other facilities such as in Saga and Kanagawa were also established.

(2) Promotion of collaborative research, internationally and domestically

Since 1994 the HIMAC has been made available to researchers worldwide in the field of ion-beam sciences other than carbon-beam radiotherapy. There are four experimental halls (Physics, Biology, Secondary beam and Medium-energy halls) as well as three treatment rooms at HIMAC. During the daytime from Tuesday through Friday, HIMAC is operated for patient treatments. At nights and weekends the four halls can be used for various experiments with ion beams. The latter framework is specified as "The Research Project with Heavy Ions at NIRS-HIMAC". The Research Project with Heavy Ions at NIRS-HIMAC is a centerpiece of collaborative research using heavy ions. Proposals exceeding 120 in number were accepted and carried out. The total beam time of more than 5,000 hours was supplied to those research studies. The research progress is highlighted elsewhere in this chapter.

The International Open Laboratory is our other framework for collaborative research. Two units of the IOL from its total of four are involved.

Hospital, Research Center for Charged Particle Therapy (Director: Yutaka Ando)

The Research Center Hospital for Charged Particle Therapy at NIRS is unique in its specialization in radiotherapy for cancer. There are 100 beds for inpatients, while 60 to 100 outpatients can be handled daily. The diagnostic radiology department has one CT-scanner with a 64-line detector, a 1.5 T MRI, a 3.0 T MRI, two PET/CTs, and one gamma camera. The oncology department has five fixed beam treatment rooms for carbon ion therapy (one vertical beam room, one horizontal beam room and three both beam rooms) and one linear accelerator for x-ray therapy. In March 2012, we implemented the Electronic Medical Record (EMR) system and developed a simple input method for each patient's findings, symptoms, tumor responses, and toxic reactions that should be estimated by the responsible physician during the clinical interview.

Department of physics (Director: Koji Noda)

At present, the department of physics at NIRS is one of the most active and leading departments of ion beam therapy related applied physics worldwide. Reliable operation of the HIMAC, a gigantic accelerator system and continuous development of novel techniques have been keeping us as the "center of excellence" in this field for many years. Highlights of the department's research progress are shown later.

Highlight

Measurement of neutron ambient dose equivalent in the HIMAC new treatment room

Shunsuke Yonai

E-mail: yonai@nirs.go.jp

INTRODUCTION

In ion beam radiotherapy (IBRT), secondary neutrons are inevitably produced because primary charged particles interact with beam line devices and the patient. The secondary neutrons lead to an undesired dose outside the target volume (out-of-field dose). The out-of-field dose in IBRT is considerably lower than the in-field dose; however, it should be considered for secondary cancer risk especially in younger patients who can be long-term survivors.

We have been continuing investigations of the out-of-field dose in carbon-ion radiotherapy (CIRT) with a passive beam delivery system. NIRS started CIRT with an active scanned delivery system at the new treatment research facility in May 2011. In theory, this system can reduce the production of secondary neutrons, because it does not require several beam line devices in which secondary neutrons can be produced. The purpose of this study was to experimentally demonstrate the reduction. Therefore, we measured neutron ambient dose equivalents at the patient position during CIRT with an active beam delivery system at the new facility. The measured results were compared to those with a passive carbon beam and an active proton beam.

MATERIALS AND METHODS

Experimental setup

Fig.1 shows a photograph of the experimental setup. A water

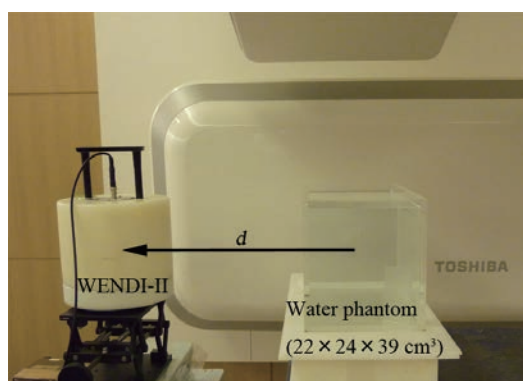


Fig.1 Photograph of the experimental setup.



phantom was placed to simulate the patient and the center of the phantom coincided with the I.C. The center of the neutron rem meter, WENDI-II was set at the I.C. height and on the I.C. line orthogonal to the beam axis. The measured positions, represented as the distance between the I.C. and the center of WENDI-II, d , were 50, 100, 150 and 200 cm.

Scanning beam method

In IBRT with an active beam delivery system, a pencil beam is scanned transversely by a pair of scanning magnets to cover the target volume. Three different techniques are used for achieving the depth-dose distribution in the target volume: range shifter scanning (RS), energy scanning (ES) and hybrid depth scanning (HS). At NIRS, the RS technique was used in the treatment for the first year; at present, only the HS technique is used [1]. Measurements for the RS and HS techniques were performed in this study.

Beam parameters

Table 1 shows the beam parameters used in this study. Case Nos. 1, 2, 4 and 5 were selected to follow those of our previous

Table 1 Beam parameters used in this study.

Case No.	Max. beam energy [MeV/u]	Irradiation volume [mm ³]
1	290	58×50×60
2	290	58×50×120
3	290	100×100×60
4	400	58×50×60
5	400	58×50×120
6	400	100×100×60
7	350	100×100×100

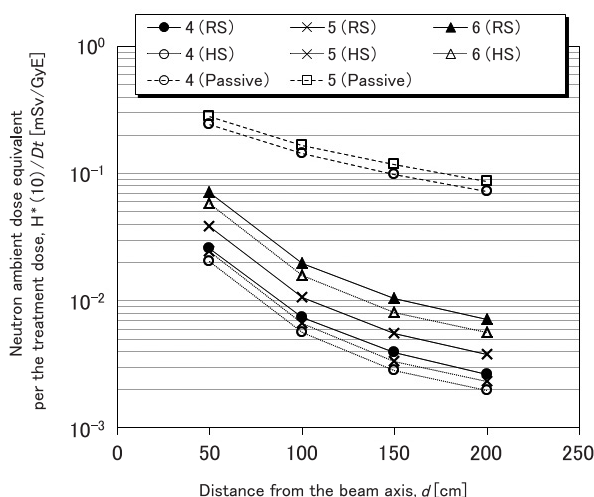


Fig.2 Measured $H^*(10)/D_t$ in CIRT along with passive beams [2]. The legends represent the beam parameter Case No. in Table 1 and the irradiation technique.

work [2] so that the doses of the active scanned and passive beams could be directly compared. Case Nos. 3 and 6 were selected to compare the doses when the irradiation volume was different. Case No.7 was selected to compare the doses with active carbon-ion and proton beams. The measured neutron ambient dose equivalents with the 177 MeV proton beam at the spot scanning beam line of the Paul Scherrer Institute (PSI) have been reported [3]. In the present study, the maximum target depth was set to 20.7 cm, which was the same as in [3].

RESULTS AND DISCUSSION

Neutron ambient dose equivalent at patient position

Fig.2 shows the measured neutron ambient dose equivalents per treatment dose, $H^*(10)/D_t$, for the beam parameters of Case Nos. 4-6 shown in Table 1, together with those with a passive beam [2]. When the irradiation target was the same, the measured $H^*(10)/D_t$ with the active beam was at most about 15% of that with the passive beam. This percentage became smaller at larger distances from the I.C. The values of $H^*(10)/D_t$ at $d=150$ and 200 cm with an active beam were as little as 2% of that with a passive beam. This tendency was expected to be due to the presence of two kinds of secondary neutrons: internal and external neutrons. Theoretically, the numbers of external neutrons, which are produced outside the patient by the interactions between charged particles and beam line devices, are greatly reduced by using an active beam compared to a passive beam, while the production of internal neutrons in the patient does not differ greatly between active and passive beams. Since internal neutrons are produced strongly in the forward direction due to the direct reaction process, their dose is higher at the positions closer to the irradiation target. Thus, the difference in $H^*(10)/D_t$ between active and passive beams was larger at larger distances from the I.C.

Fig.3 compares the measured neutron ambient dose equivalents in CIRT and proton radiotherapy with active scanned beams [3]. $H^*(10)/D_t$ for the carbon-ion active beam was comparable to that for the proton beam. This similarity in $H^*(10)/D_t$ was not observed for the passive beams: when using a passive beam, $H^*(10)/D_t$ in CIRT was more than 2 times lower than that in proton ra-

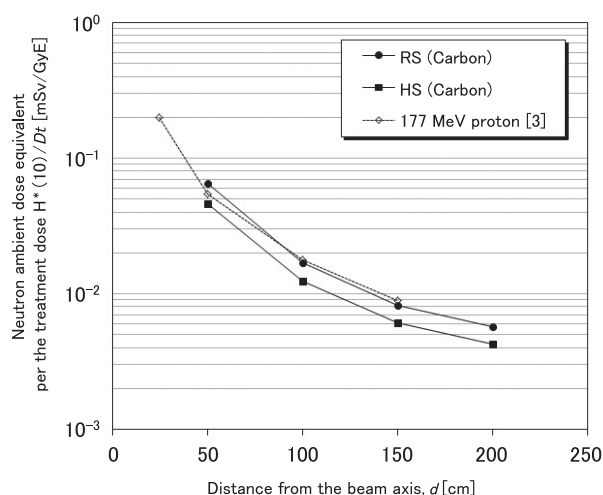


Fig.3 Comparison of $H^*(10)/D_t$ in carbon-ion and proton radiotherapies with active scanned beam [3]. Here, the number of protons for the irradiation dose of 1 Gy into a box target of $100 \times 100 \times 100 \text{ mm}^3$ was 8.61×10^{10} . Also, the RBE in proton radiotherapy was assumed to be 1.1.

diotherapy [2]. Neutron doses of passive beams basically vary with the facility, because external neutrons, which depend on the operational beam setting and the design of a beam delivery system, strongly contribute to the dose. By contrast, the facility dependency for active beams should be lower, because neutrons are mainly produced in the patient. Therefore, the facility dependency is one of the reasons for the difference in passive beams. Additionally, there was a difference in the detector response between WENDI-II and the conventional rem counter, LB6411, which was used in [3]. In principle, WENDI-II has a higher response than LB6411 in most energy ranges. In addition, LB6411 has quite low response in the energy range above 20 MeV, and consequently the results of the measurements with LB6411 might be underestimated. Further measurements with a dosimeter with a response in the high energy range such as WENDI-II are required to compare $H^*(10)$ between carbon-ion and proton beams.

CONCLUSION

The neutron ambient dose equivalents at the patient position in CIRT with an active scanned beam were measured in the NIRS treatment room. These results demonstrated that the use of an active scanned beam in CIRT as well as proton radiotherapy can greatly reduce the secondary neutron dose. It was found that the neutron dose per treatment dose for the carbon-ion active beam was comparable to that of the proton beam. In addition, the HS technique could improve the out-of-field dose as well as the beam quality. Currently, NIRS is trying to implement the ES technique into actual patient treatments. This implementation will lead to a further reduction in the out-of-field dose.

References

- [1] Inaniwa T, Furukawa T, Kanematsu N, *et al.*: Evaluation of hybrid depth scanning for carbon-ion radiotherapy, *Med Phys* 39, 2820-2825, 2012.
- [2] Yonai S, Matsufuji N, Kanai T, *et al.*: Measurement of neutron ambient dose equivalent in passive carbon-ion and proton radiotherapies, *Med Phys* 35, 4782-4792, 2008.
- [3] Schneider U, Agosteo S, Pedroni E, *et al.*: J. Secondary neutron dose during proton therapy using spot scanning, *Int J Radiat Oncol Biol Phys* 53, 244-251, 2002.

Highlight

$^{10/11}\text{C}$ molecule production/separation system for $^{10/11}\text{C}$ ion acceleration

Ken Katagiri

E-mail: tag410@nirs.go.jp

Introduction

Heavy-ion cancer therapy using the Heavy-Ion Medical Accelerator synchrotron in Chiba (HIMAC), Japan, has been administered to more than 8000 patients since 1994. A new treatment using a three-dimensional irradiation system with pencil-beam scanning was started in May 2011 to enhance the treatment quality through precise dose control [1,2]. Positron Emission Tomography (PET) imaging using $^{10/11}\text{C}$ beams has been expected to allow for further accurate control of the irradiation field during scanning irradiation. For that reason, $^{10/11}\text{C}$ beam production was carried out by using a projectile fragmentation process between incident ^{12}C beams and a Be target. However, it was found that the method had undesirable characteristics, such as wide momentum spread, large emittance, and low beam rate due to the low yield of the reaction. To overcome those disadvantages and realize the $^{10/11}\text{C}$ beam production, we have proposed a method whereby $^{10/11}\text{C}$ ions are produced from radioisotope gases by using an ion source and then subsequently accelerated for cancer treatment.

$^{10/11}\text{C}$ ion production system

Fig. 1 shows a conceptual diagram of the HIMAC and a $^{10/11}\text{C}$ ion production system. The $^{10/11}\text{C}$ ion production system is composed of an ion source, a $^{10/11}\text{C}$ Molecule Production/separation System (CMPS), and a small cyclotron. A boron compound target in the CMPS is irradiated by proton beams delivered by the cyclotron to

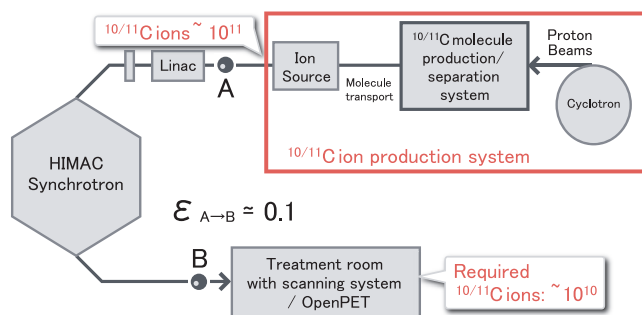
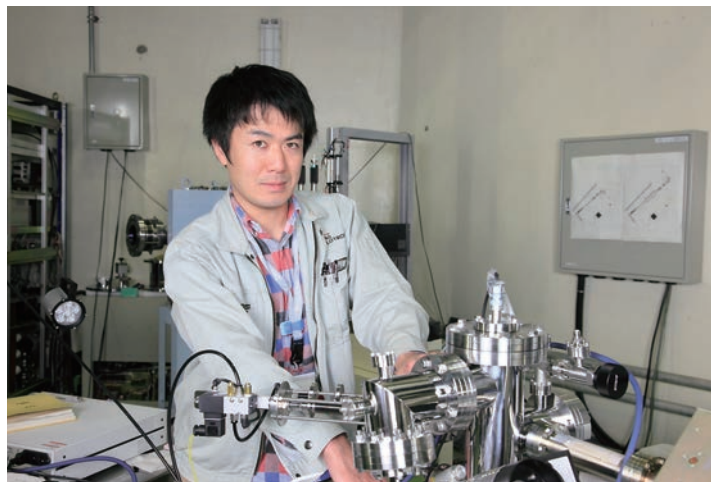


Fig. 1 Conceptual diagram of the HIMAC and $^{10/11}\text{C}$ ion production system.



produce $^{10/11}\text{C}$ molecules by means of the $^{10/11}\text{B}(p,n)^{10/11}\text{C}$ reaction. The CMPS separates the $^{10/11}\text{C}$ molecules from impurities and provides them to the downstream ion source. The ion source needs to produce 10^{11} $^{10/11}\text{C}$ ions to provide the necessary number of 10^{10} $^{10/11}\text{C}$ ions to the treatment room. If the ion source in the system has an ionization efficiency of the order of $\sim 1\%$, 10^{13} $^{10/11}\text{C}$ molecules have to be produced by the CMPS. It is also necessary for the CMPS to reduce the number of impurities to the same level as the number of $^{10/11}\text{C}$ molecules.

Development of the $^{10/11}\text{C}$ molecule production and separation system

We are developing the CMPS to achieve those requirements. In the CMPS, a cryogenic technique is employed to separate the $^{10/11}\text{C}$ molecules from other impurity molecules. Moreover, the target is irradiated in vacuum to reduce the impurities. Hence, the method requires that the target is a solid-state material.

As a first step in the development, we investigated the solid-state target suitable for proton irradiation use. We found that volatile $^{11}\text{CH}_4$ molecules could be directly produced and collected by using a sodium borohydride (NaBH_4) target and 30% of the total number of produced ^{11}C nuclides could be effectively collected due to their volatility. We also confirmed that the necessary number of $^{11}\text{CH}_4$ molecules could almost be achieved ($\approx 5 \times 10^{12}$) by the 20 min irradiation with 18 MeV, 18 μA proton beams. From these findings, NaBH_4 targets are expected to be applied in the new method for production and separation of $^{10/11}\text{C}$ molecules [3].

Based on those results, we started the design and development of the CMPS in 2013. Fig.2 shows a schematic diagram of the CMPS. $^{10/11}\text{CH}_4$ molecules produced by the proton irradiation move around in the vacuum chamber. The CMPS separates the CH_4 molecules from the impurities using the vapor pressure differ-

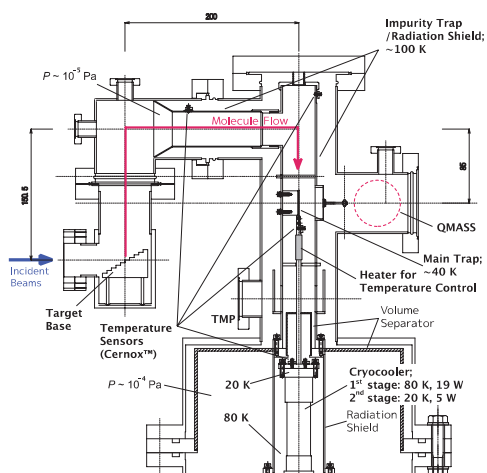


Fig. 2 Schematic diagram of $^{10/11}\text{C}$ molecule production/separation system.

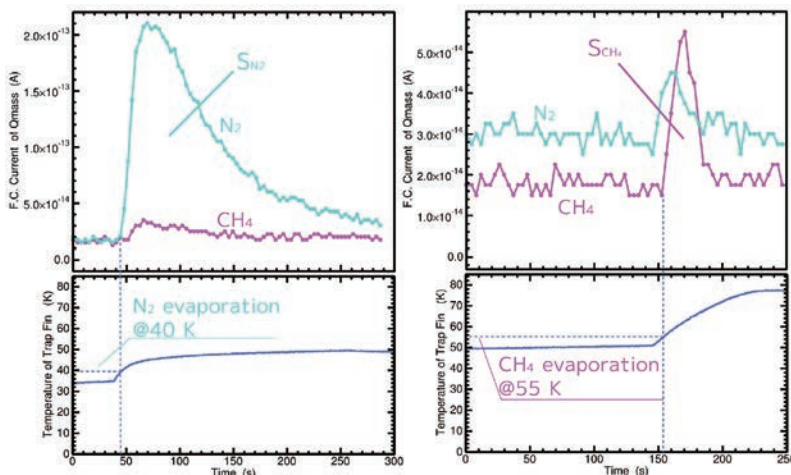


Fig. 4 Results of the separation experiments.

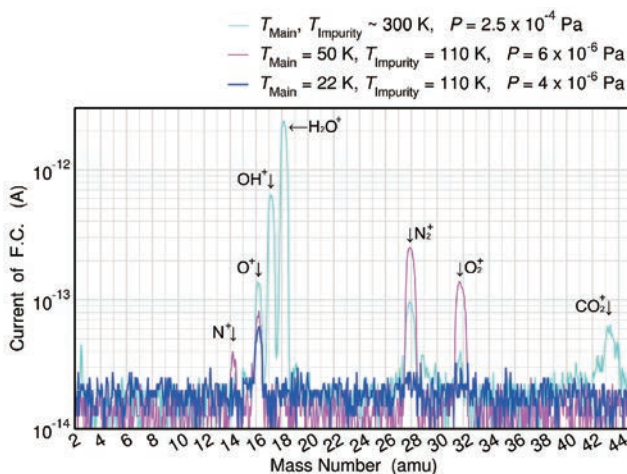


Fig. 3 Mass spectra measured by QMS.

ences among molecular species. The CMPS includes a main trap and an impurity trap, which are refrigerated by a cryocooler. The impurity trap reaches about 100 Kelvin and captures and condenses molecules that have relatively low vapor pressure, such as CO_2 and H_2O . On the other hand, the main trap can capture and condense molecules with high vapor pressure, such as N_2 and CH_4 , owing to its low temperature of about 20 Kelvin. By using a heater installed below the main trap, we can arbitrarily control the temperature of the main trap and selectively extract the CH_4 molecules. Existing molecules in the CMPS can be determined with a quadrupole mass spectrometer (QMS). Fig.3 shows the mass spectra for three different temperatures of the main and impurity traps. The most conspicuous spectrum peak of the room temperature chamber was H_2O^+ because H_2O molecules were released as outgas from the volume separator made of glass epoxy. With decreasing temperature, absolute pressure was decreased and most of the spectrum peaks became smaller. We confirmed that CO_2 and H_2O could be effectively removed by decreasing the temperature of the impurity trap.

We performed preliminary experiments using non-radioactive methane ($^{12}\text{CH}_4$) gas to investigate separation performance. Fig.4 shows the results of the separation experiment using nitrogen gas as the impurity. Temporal evolutions of analyzed ion current ob-

tained by QMS are plotted for CH_3^+ ($M=15$) ions and N_2^+ ions ($M=28$) in the upper graphs. The lower graphs show the temperature variation of the main trap. First, the trap temperature was increased from 35 Kelvin to 50 Kelvin. On reaching 40 Kelvin, evaporation of the N_2 molecules started and the N_2 signal could be detected. After sufficient evaporation, the trap temperature was increased again. On reaching 55 Kelvin, current signals of the methane ions could be detected. By estimating the area ratio of $\text{S}_{\text{N}_2}/\text{S}_{\text{CH}_4}$, we found twenty-fold impurities of nitrogen ions could be successfully separated from methane ions.

Strategy towards $^{10/11}\text{C}$ ion production

Based on these findings obtained so far, we started the development of the ion source in the spring of 2014. To achieve the ionization efficiency of $\sim 1\%$, we are planning to employ an electron impact ion source using filaments. The filament ion sources are commonly used for vacuum gages or mass spectrometry instruments. Principal features of the ion sources are small size and capability to operate in an ultra-high vacuum. Owing to this small size, the ion source can be installed in the CMPS. Consequently, we can avoid the reduction of molecular transport efficiency from the CMPS to the ion source. We can also reduce the amount of impurities by combining the CMPS and the ion source and decreasing the total volume of the $^{10/11}\text{C}$ ion production system. The filament ion source can effectively produce single charged methane ions (CH_3^+ , CH_2^+ , etc.) when the electron energy of the filament ion source is about 70 eV. Those single charged ions must be further ionized to provide them as C^{2+} ions to the downstream accelerator. We will consider using charge breeding techniques or a charge stripping method with electrostatic acceleration to achieve even further ionization.

References

- [1] Noda K, Furukawa T, et al.: New treatment facility for heavy-ion cancer therapy at HIMAC, *Nucl Instrum Meth Phys Res B* 266, 2182-2185, 2008.
- [2] Furukawa T, Inaniwa S, et al.: Performance of the NIRS fast scanning system for heavy-ion radiotherapy, *Med Phys* 37, 5672-5682, 2010.
- [3] Katagiri K, Nagatsu K, et al.: ^{11}C molecule production using a NaBH_4 target for ^{11}C ion acceleration, *Rev Sci Instrum* 85, 02C305-1-3, 2014.

Highlight

Carbon-ion radiotherapy for locally advanced uterine cervical cancer

Masaru Wakatsuki

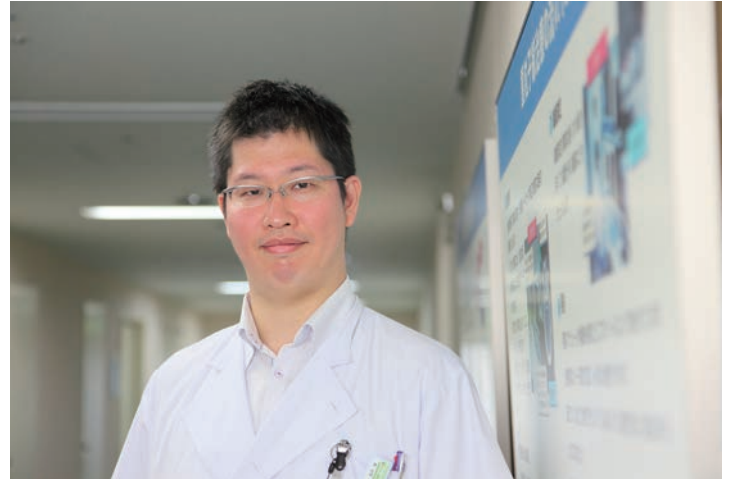
E-mail: waka@nirs.gp.jp

Introduction

Although the mortality rates of uterine cervical cancer have steadily decreased during the past 30 years with the introduction of Papanicolaou smear screening, uterine cervical cancer still remains the third most common cancer affecting women worldwide. Notably, the incidence and mortality rates of squamous cell carcinoma are declining. On the other hand, the incidence rates of adenocarcinoma and adenosquamous cell carcinoma have been increasing in many countries despite being relatively uncommon histologic subtypes of cervical cancer.

In the treatment for locally advanced carcinoma of the uterine cervix, cisplatin-based concurrent chemoradiation therapy (CCRT), including intracavitary brachytherapy (ICBT), has become the standard therapy according to the results of several randomized phase III clinical trials. However, the majority of patients participating in those studies had squamous cell histology; adenocarcinomas represented only approximately 10% of the patients enrolled, and adenocarcinoma of the uterine cervix is more radio-resistant than squamous cell carcinoma. Thus, CCRT for adenocarcinoma of the uterine cervix is still unsatisfactory and the treatment of locally advanced adenocarcinoma is in need of even more aggressive therapy.

To evaluate the toxicity and efficacy of C-ion RT for locally advanced adenocarcinoma of the uterine cervix or corpus, we conducted a phase I/II trial (Protocol 9704) between April 1998 and



January 2010 (Fig.1). This highlight describes the clinical outcomes of adenocarcinoma of the uterine cervix in this trial, excluding cases of the uterine corpus.

Results and Discussion

Between April 1998 and February 2010, 55 patients with locally advanced adenocarcinoma of the uterine cervix (Protocol 9704) were treated with carbon-ion radiotherapy (CIRT) (Fig.2) [1]. The numbers of patients with stage IIB, IIIB, and IVA disease were 20, 33, and 2, respectively. All patients with stage IVA had bladder invasion but no rectal invasion. Tumor size was 3.0-11.8 cm in maximum diameter (median 5.5 cm), and that of stage IIIB and IVA cases was 3.5-9.2 cm (median 5.8 cm). Histologically, 45 of 55 patients had adenocarcinoma and 13 patients had adenosquamous cell carcinoma. Twenty-four of the 55 patients had pelvic lymph node metastases. Seven of 55 patients received 62.4-64.8 GyE, 10 patients had 68.0 GyE, 21 patients had 71.2 GyE and 17 patients had 74.4 GyE. Overall treatment time (OTT) ranged from 32 to 40 days, with a median of 35 days. Median follow-up duration was 38 months (range, 7 to 141 months).

The 5-year local control rate, local control rate including salvage surgery, and overall survival rate in all stage cases were 54.5%, 68.2% and 38.1%, respectively (Fig.3). In stage IIIB and IVA cases, the three rates were 57.9%, 69.2% and 42.4%, respectively. Several studies have reported treatment outcomes of adenocarcinoma of the uterine cervix treated with RT or CCRT (Table 1). Niibe et al [2]. reported a 5-year local control rate of 36% for stage IIIB by RT alone or CCRT. Grigsby et al. [3] reported 33% for stage III adenocarcinoma of the uterine cervix by RT alone. Huang et al. [4] reported 58% for stage III and 48% for stage IB-IIA bulky (> 4 cm) by RT alone or CCRT. In the present study, the 5-year overall local control rate for stage IIIB or IVA was 57.9%

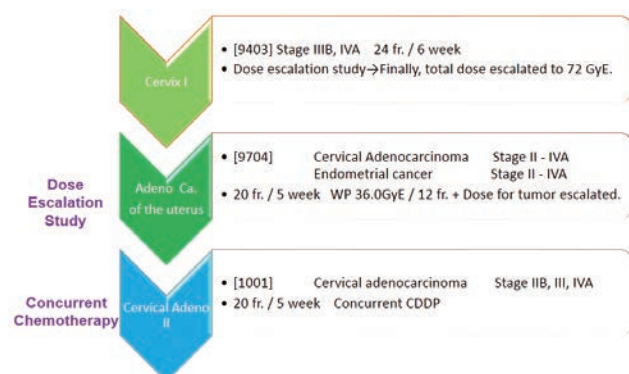


Fig.1 History of Protocol for Uterine Adenocarcinoma

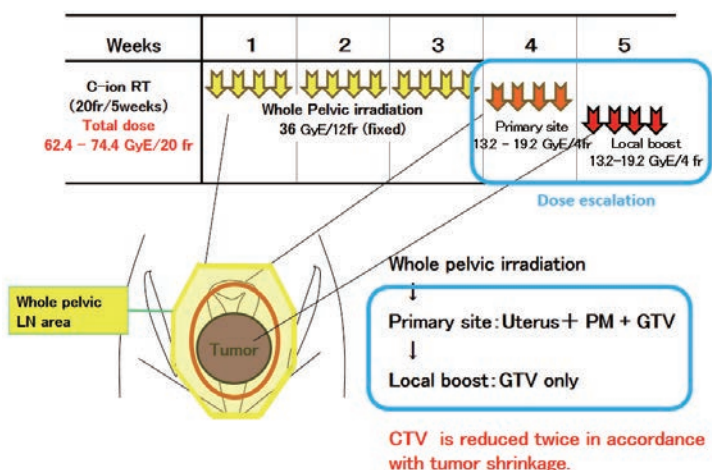


Fig.2 Treatment schedule of C-ion RT

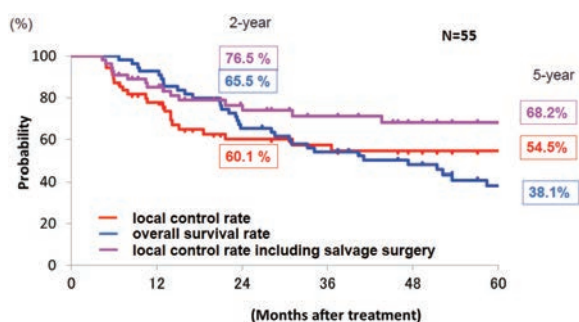


Fig.3 Local control rate, local control rate including salvage surgery, and overall survival rate in all cases

even though the median tumor size of our cases was 5.8 cm (3.5-9.2 cm). Although the number of patients in this study was small, the local control rate was relatively better than those of the conventional RT or CCRT studies.

On the other hand, the overall survival rate was less than satisfactory in this study (2-year: 65.5%, 5-year: 38.1%), even though the local control rate for bulky tumors was relatively favorable. Several researchers [4,5] showed that locally advanced adenocarcinoma of the uterine cervix had poor prognosis, with 5-year survival rates being only 25-29%. It was suggested that the reasons were poor local control and greater distant metastases. Huang et al. [4] reported a 5-year distant metastasis rate of 46% for stage III patients after RT alone or CCRT, and Eifel et al. [5] reported that 45% of patients with stage IIB or III showed distant metastases after RT. In the present study, 2-year and 5-year cumulative distant metastasis rates were 49.4% and 64.8%, respectively. These rates were higher than those in the other studies because our patients did not receive concurrent chemotherapy, tumor size was larger than in the other studies, and the overall survival rate was also higher. Thus, to improve the distant metastasis and local control rates, the use of chemotherapy in combination with CIRT should receive further consideration.

All of the observed acute and late toxicities are listed in Table 2. Although 24 patients developed acute GI and 12 patients had genitourinary (GU) toxicity (grade 1-2), all patients completed the scheduled therapy except one who was finally excluded from this study because of ischemic enteritis and bowel perforation during CIRT (64.8GyE for 18 fractions). This patient underwent surgery,

Table 1

Author (year)	Stage	No.	Treatment	(2y) 5y OS (%)	(2y) 5y LC (%)
Grigsby PW (1988)	III	12	RT	25	33
Eifel PJ (1990)	III	61	RT	(35) 26	46
Niibe Y (2010)	IIIB	61	RT / CRT	22	36
Huang Y-T (2011)	III	28	RT / CRT	29	58
NIRS (Current study)	All case	55	C-ion RT	(66) 38	(60) 55
	IIIB-IVA	38		(54) 42	(69) 58

Table 2 Acute and late toxicities

	N	Acute (CTCAE ver 3.0)					
		G0	G1	G2	G3	G4	G5
GI tract	55	32	20	3	0	0	0
GU tract	55	51	11	0	0	0	0
Skin	55	30	8	0	0	0	0

	N	Late (RTOG / EORTC)				
		G0	G1	G2	G3	G4
GI tract	55	43	10	2	0	1
GU tract	55	45	5	5	0	0
Skin	55	57	1	0	0	0

GI: gastrointestinal. GU: genitourinary

and the site of the ischemic enteritis and bowel perforation was proven to be outside of the irradiation area. No patient developed grade 3 or higher acute toxicity in the GI tract or GU tract. Late GI or GU toxicity was found in as many as 16 patients (27.6%) but the toxicity was grade 1 or 2 (except one case). One patient developed a grade 4 rectal complication, which was surgically salvaged. This case had uncontrolled severe diabetes mellitus (DM).

Conclusion

The number of patients in this study was small (55) and it was a dose escalation study, but the local control rate, although still unsatisfactory, was relatively better than in conventional studies. In addition, distant metastases also frequently occurred, so the overall survival rate was less than satisfactory. On the basis of these results, we are now conducting a new clinical trial of CIRT with concurrent chemotherapy for locally advanced adenocarcinoma of the uterine cervix.

References

- [1] Wakatsuki M, Kato S, Ohno T, et al.: Clinical outcomes of carbon ion radiotherapy for locally advanced adenocarcinoma of the uterine cervix in phase 1/2 clinical trial (protocol 9704), *Cancer* 2014, doi:10.1002/cncr.28621.
- [2] Niibe Y, Kenjo M, Onishi H, et al.: High-dose-rate intracavitary brachytherapy combined with external beam radiotherapy for stage IIIB adenocarcinoma of the uterine cervix in Japan: a multi-institutional study of Japanese Society of Therapeutic Radiology and Oncology 2006-2007 (study of JASTRO 2006-2007). *J J Clin Oncol* 40, 795-799, 2010.
- [3] Grigsby PW, Perez CA, Kuske RR, et al.: Adenocarcinoma of the uterine cervix: lack of evidence for a poor prognosis, *Radiotherapy and Oncology* 12, 289-296, 1988.
- [4] Huang YT, Wang CC, Tsai CS, et al.: Long-term outcome and prognostic factors for adenocarcinoma/adenosquamous carcinoma of cervix after definitive radiotherapy, *Inte J Radiat Oncol, Biol Phys* 80, 429-436, 2011.
- [5] Eifel PJ, Morris M, Oswald MJ, Wharton JT, Delclos L. Adenocarcinoma of the uterine cervix. Prognosis and patterns of failure in 367 cases, *Cancer* 65, 2507-2514, 1990.

Highlight

Modeling of normal tissue response in C-ion RT

**Naruhiko Matsufuji, Mai Fukahori,
Hiroaki Matsubara**

E-mail: matufuji@nirs.go.jp

Dose to be prescribed in radiation therapy are in principle designed in order to achieve a uniform anti-tumor effect throughout the target region. At HIMAC, HSG, an experimental cell line originating from human salivary gland tumor, has been used as a reference in the design. It should be noted, however, that the dose actually delivered to the tumor is sometimes limited if surrounding normal tissues develops any unacceptable side effect even if further irradiation is desired from the viewpoint of the tumor control. This suggests that precise understanding of the normal tissue response is the key for optimized radiation therapy. The modeling of normal tissue response is, however, far more complex in comparison to that of tumor control, mainly due to the vast variation in biological end point referred to as the "side effect", as well as variation in dose and radiation quality given in each case. In this respect, our Radiation Effect Research Team has been tackling the modeling of various normal tissue responses mainly in C-ion RT at HIMAC. The achievements in this context in 2013 are described in this highlight.

Skin

The degree of the skin reaction has been evaluated by introducing the diagnostic score which is evaluated by a medical doctor into discrete grades. We are trying to establish a quantitative and objective evaluation of the skin reaction.

Within a treatment protocol, the skin reaction is expected to be numerically expressed as a function of red inflammation. Red inflammation of skin is due to expansion of capillaries and increment of blood flow because of the biological repair reaction. Therefore, hemoglobin which is the color element of blood is considered to essentially relate to the degree of the red inflammation of skin. Two kinds of non-invasive techniques to measure hemoglobin have been developed. One is color element decomposition on an image using independent component analysis (ICA) [1] which is a multivariate statistics method. For this, skin color in a digital image is decomposed into hemoglobin, melanin, and others as relative values. The other technique uses a commercially available laser flow meter. The laser flow meter measures the reflected intensity of the laser on the skin and the modulated wavelength due to the Doppler effect. The laser flow meter detects he-



moglobin flow as an absolute value. We have combined these techniques for quantitative evaluation of the skin reaction.

Fig.1 shows an example of the skin color decomposition of a picture which was taken using a compact digital camera 1 month after C-ion RT had been carried out at HIMAC on a lung cancer. The red inflammation due to the two shots is only seen in panel (B)

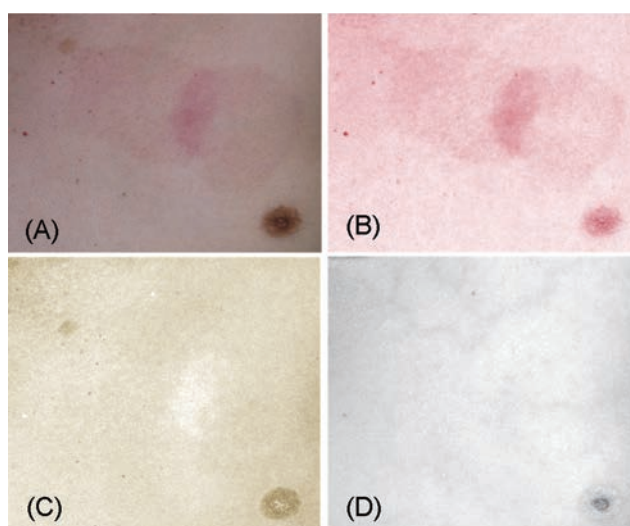


Fig.1 An example of the skin color decomposition on a picture which was taken using a compact digital camera 1 month after C-ion RT had been carried out at HIMAC on a lung cancer. The red inflammation due to the two shots is only seen in panel (B) of the hemoglobin image. Freckles and a mole are seen in panel (C) of the melanin image. The track of a vein is seen in panel (D) as another color because its blue color cannot be expressed by a combination of the color vectors of hemoglobin and melanin.

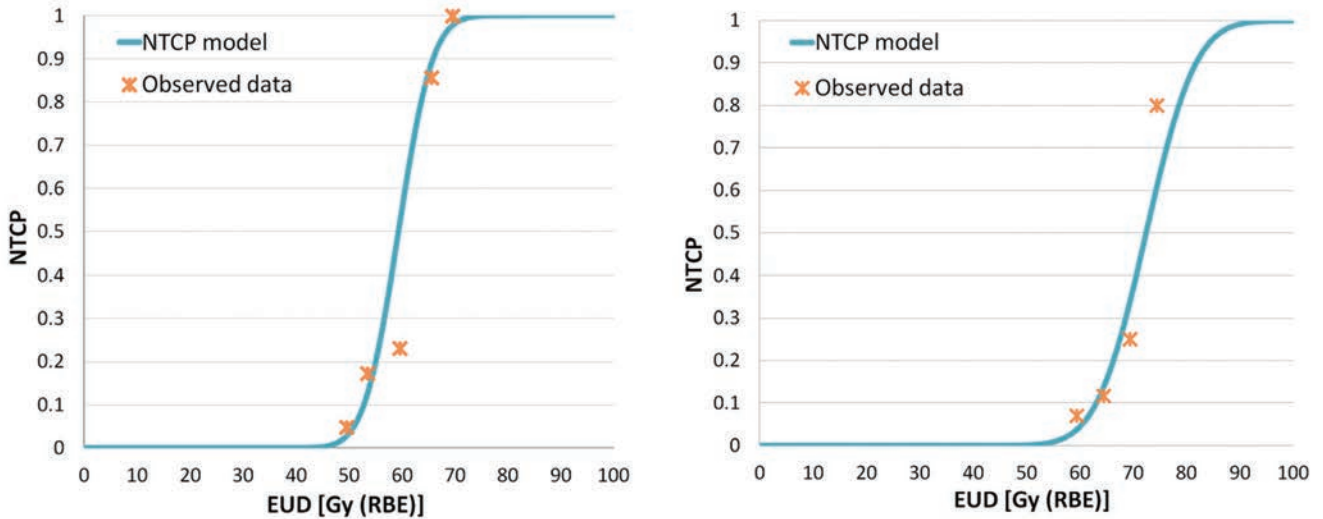


Fig.2 Derived NTCP curves of rectum (left) and urethra (right).

of the hemoglobin image. Freckles and a mole are seen in panel (C) of the melanin image. The track of a vein is seen in panel (D) as another color because its blue color cannot be expressed by a combination of the color vectors of hemoglobin and melanin. The fig. clearly shows that the skin color decomposition was successfully realized.

The basic study for quantitative evaluation of the skin reaction has been finished. Once a relationship between dose and increment of hemoglobin flow is known, a virtual skin image after irradiation is available by artificially controlling the pixel value in the hemoglobin image. We expect this will help doctors and their patients to decide and understand the appropriate treatment plan.

Rectum and Urethra

Radiation injury of the rectum is the major concern in RT for prostate cancer because it often threatens a patient's QOL. The aim of this study was to make use of the normal tissue complication probability (NTCP) model to understand rectal and urethral late complications after C-ion RT and clarify the characteristics of the C-ion RT.

Rectal and urethral dose-volume histograms (DVHs) were analyzed for 166 patients treated between June 1995 and July 2007. These patients received 54 -72 Gy (RBE) in dose escalation trials [2]. The end point for the analysis was Grade 1 or worse late complications for the rectum, and Grade 2 or worse complication probabilities for the urethra. Of the 166 patients, 29 patients experienced Grade 1 or worse late complications for the rectum and 24 experienced Grade 2 or worse late complications for the urethra after therapy-ion RT.

The Lyman-Kutcher-Burman (LKB) NTCP model was applied to the DVHs expressed as a function of the equivalent uniform dose (EUD).

$$NTCP(D, V) = \frac{1}{\sqrt{2\pi}} \int_{-\infty}^t \exp(-t^2/2) dt$$

$$t(D, V) = (EUD - TD_{50}(1)) / mTD_{50}(1)$$

$$EUD = \left(\sum_i v_i D_i^{\frac{1}{n}} \right)^n$$

Here n describes the volume dependence, m is the slope

Table 1 Estimated NTCP parameters with 95% CI

	n	m	$TD_{50}(1)$ [Gy (RBE)]
Rectum (C-ion)	0,058 (0,048-0,069)	0,086 (0,074-0,12)	59.3 (58.1-61.0)
Rectum (photon)	0,23 (0,14-0,42)	0,19 (0,15-0,25)	81.9 (76.8-91.2)
Urethra (C-ion)	0,0015 (0-0,75)	0,10 (0,083-0,13)	72.4 (70.3-74.4)

steepness of the complication probability versus dose curve and $TD_{50}(1)$ is the dose which can lead to a 50% complication probability when delivered to the whole organ. Maximum likelihood analysis was used to determine the values of the parameters (n , m and $TD_{50}(1)$).

Fig.2 presents the predicted NTCP curve obtained with the best estimated parameters for the LKB model as a function of EUD for rectum and urethra. Asterisk marks show the observed complication rates. Table 1 summarizes estimated parameter values with 95% CI with those for the conventional RT [3]. The volume effect parameter, n , for the rectum and urethra had values of 0.058 and 0.0015, respectively. These low values suggest that these seem to act as a serial-like organ and it is important not to exceed the tolerance dose at any point for C-ion RT. Furthermore, it is suggested that the urethra, even irradiated to only a somewhat high dose occurs a late complication easily because n value is close to zero.

The new NTCP parameter values are useful to compare the plans for therapy-ion RT.

References

- [1] Tsumura N, Ojima K, Shiraishi M, *et al.*: Image-based skin color and texture analysis/synthesis by extracting hemoglobin and melanin information in the skin, *ACM Trans Graphics* 22, 770-779, 2003.
- [2] Ishikawa H, Tsuji H, Kamada T, *et al.*: Carbon-ion radiation therapy for prostate cancer, *Int J Urol* 19, 296-305, 2012.
- [3] Rancati T, Fiorio C, Gagliardi G, *et al.*: Fitting late rectal bleeding data using different NTCP models: results from an Italian multi-centric study (AI-ROPROS0101), *Radio Oncol* 73, 21-32, 2004.

Highlight

Measurement of RBE and OER of clinical carbon beams: An in vivo study

Ryoichi Hirayama, Yoshiya Furusawa

E-mail: hirayama@nirs.go.jp

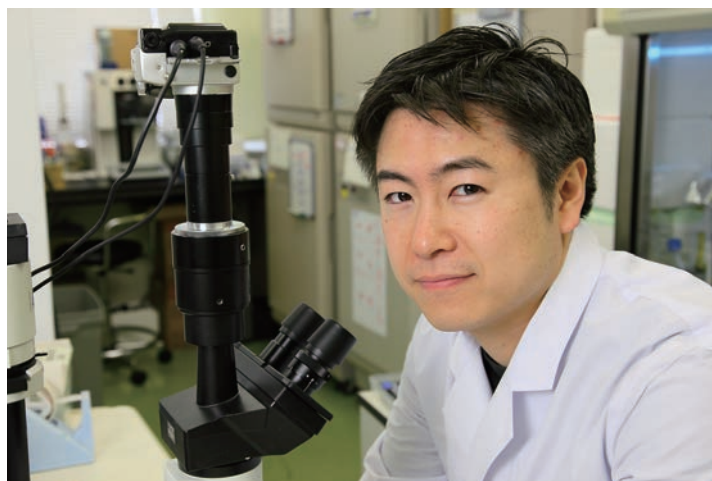
Introduction

It is known that accelerated carbon ions form a Bragg peak at a given depth, depending on the particle energy. Carbon ion beams are biologically heterogeneous along the beam path, due to the change of radiation quality, such as LET (linear energy transfer). This heterogeneity is most prominent in the spread-out Bragg peak (SOBP). At present, SOBP carbon ion beams are used for patient treatments at HIMAC. SOBP beams contain high LET components, and the LET increases within the SOBP beam path. High LET radiation has two indicators for therapeutic effects: relative biological effectiveness (RBE) and oxygen enhancement ratio (OER). When the therapeutic effects of charged particles are compared with those of photon radiation, the charged particles have the advantages of a large RBE and a small OER [1]. Clinical studies show that the large RBE and the small OER of charged particles are responsible for enhanced biological effects and improvement in hypoxia-induced radioresistance.

Several studies have shown that RBE values increase with increasing LET within the SOBP of carbon ion beams. These biological data have been used to design ridge filters that provide a uniform distribution of biological effectiveness within the SOBP beams. However, little is known about the LET dependence of OER within the SOBP beams. In this highlight we examine the LET dependence of biological effects such as the RBE and the OER within the SOBP carbon ion beams using clamped and non-clamped squamous cell carcinoma (SCCVII) tumors (in vivo). It is well known that solid tumors contain hypoxic cells. These hypoxic cells show resistance to low LET radiations and hence non-clamped SCCVII tumors may show the radioresistance from some hypoxic cells in the tumor. Thus we prepared single-cell suspension samples to determine the radiation response of aerobic cells directly (single-cell suspension) (Fig. 1).

Results

Fig. 2 shows the dose-response curve of SCCVII cell survival after irradiation by X-rays and carbon ion beams in three different oxygen states. The plating efficiencies of hypoxic tumor, normoxic tumor and aerobic cells were 0.45 ± 0.04 , 0.44 ± 0.05 and 0.58 ± 0.06 , respectively. These plating efficiencies were not affected



by different oxygen conditions ($P > 0.1$, by Kruskal-Wallis test). All survival curves were fitted by the LQ equation. Carbon ion beams with an LET at $80 \text{ keV}/\mu\text{m}$ showed the highest radiosensitivities under each tumor cell condition.

We observed that all survival curves had shoulders, whereas the curves for X-rays and carbon ion beams with an LET of $46 \text{ keV}/\mu\text{m}$ showed a curvature for high doses, indicating a more radioresistant subgroup of cells. The RBE values of carbon ions in three different oxygen conditions (hypoxic, normoxic and aerobic) increased with increasing the LET. The maximum RBE values were 2.16 ± 0.13 under hypoxic, 1.76 ± 0.13 under normoxic and 1.66 ± 0.04 under aerobic conditions at distal position ($80 \text{ keV}/\mu\text{m}$) within the SOBP carbon ion beams.

As expected, the RBE values under the hypoxic condition were

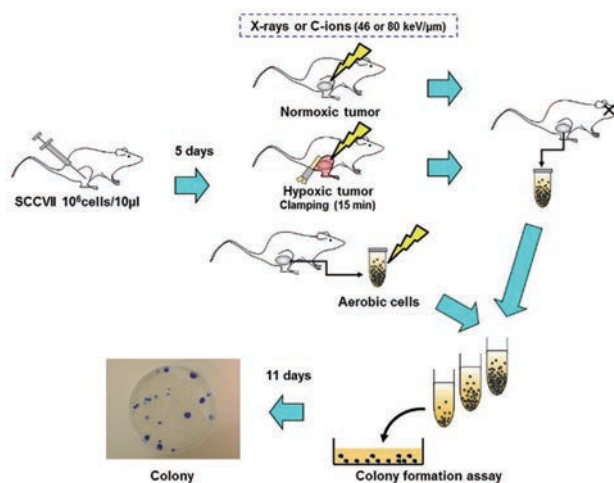


Fig.1 Experimental flow chart [2].

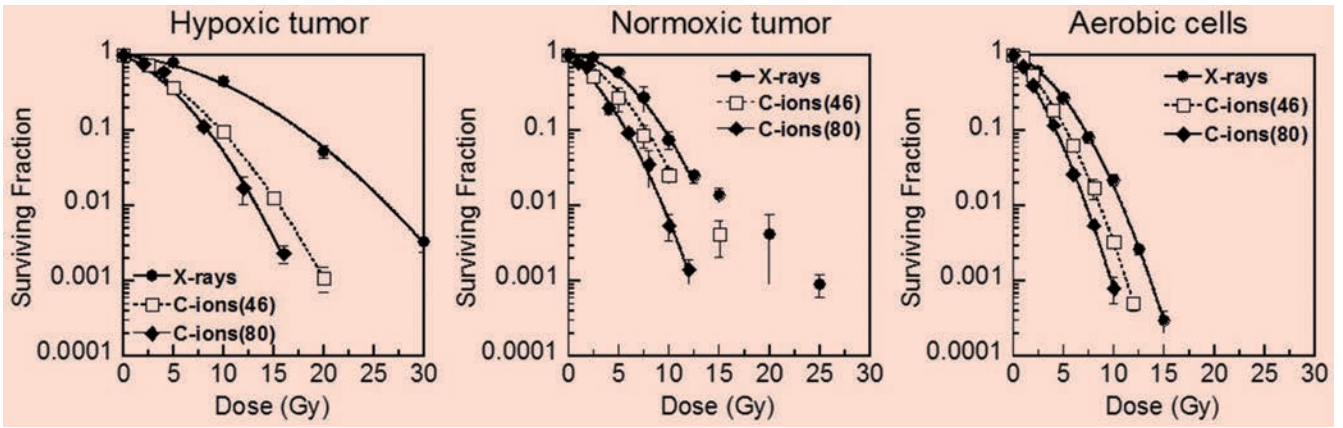


Fig.2 The surviving fractions of SCCVII tumor cells irradiated with 200 kV X-rays (●) or carbon-ion beams (46 keV/μm (□) and 80 keV/μm (◆)). The symbols and bars are the mean and standard error calculated from three or more independent experiments (6-12 mice at each point). The plots were fitted by the linear-quadratic (LQ) equation, $SF = \exp(-\alpha \cdot D - \beta \cdot D^2)$, with the exception of 15, 20 and 25 Gy in normoxic tumor condition [2].

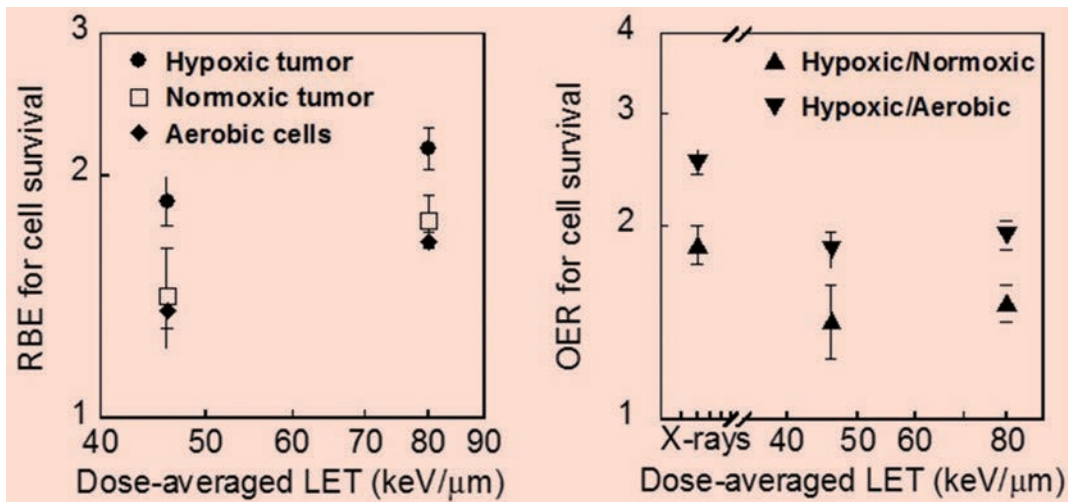


Fig.3 The distribution of RBE at the 10% survival level (●, hypoxic tumor; □, normoxic tumor; ◆, aerobic cells) and OER at the 10% survival level (▲, hypoxic/normoxic; ▼, hypoxic/aerobic) as a function of the dose-averaged LET within SOBP carbon ion beams. The RBE values are relative to 200 kV X-rays ($D_{10,X\text{-rays}}/D_{10,\text{carbon-ions}}$). The OER values were calculated as, $(D_{10,\text{hypoxic}})/(D_{10,\text{normoxic or aerobic}})$. The symbols and bars represent the mean and standard error [2].

larger than that under the normoxic and aerobic conditions in the SOBP beams (Fig. 3). The OER values were also calculated by D 10 values, and the OER values to normoxic tumor ($OER_{n/n}$) were smaller than those to aerobic cells ($OER_{n/a}$) (Fig. 3). The X-ray OER values (1.87 ± 0.13 for the ratio of hypoxic tumor to normoxic tumor and 2.52 ± 0.11 for the ratio of hypoxic tumor to aerobic cells) were larger than those of carbon ions. However the $OER_{n/n}$ values (1.43 ± 0.19 and 1.52 ± 0.10) and the $OER_{n/a}$ values (1.84 ± 0.12 and 1.94 ± 0.10) showed no significant change ($P > 0.3$, by t-test) at 46 keV/μm (proximal position) and 80 keV/μm (distal positions) within the SOBP beams, respectively.

In summary, in this study we found that the RBE values for cell survival increased with increasing LET and that the OER values had little change with increasing LET within the SOBP carbon ion beams.

References

[1] Hirayama R, Furusawa Y, Fukawa T, *et al.*: Repair kinetics of DNA-DSB induced by X-rays or carbon ions under oxic and hypoxic conditions, *J Radiat Res* 46, 325-332, 2005.
 [2] Hirayama R, Uzawa A, Takase N, *et al.*: Evaluation of SCCVII tumor cell survival in clamped and non-clamped solid tumors exposed to carbon-ion beams in comparison to X-rays, *Mutat Res* 756, 146-151, 2013.

New aspects of FGF radioprotectors

Fumiaki Nakayama

E-mail: f_naka@nirs.go.jp

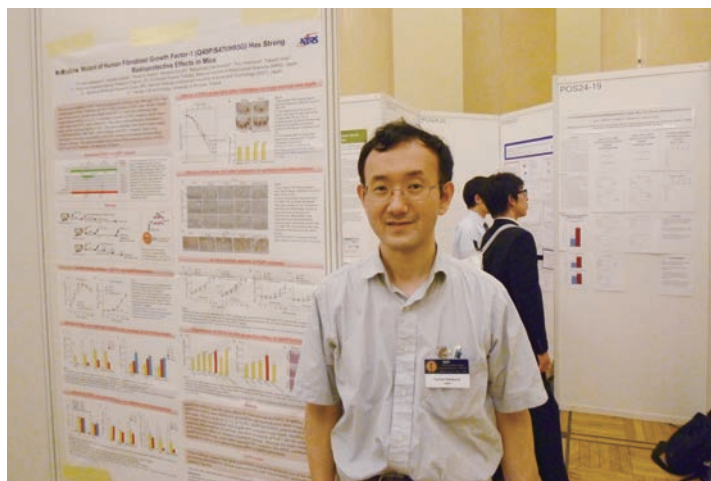
FGFs as radioprotectors

The gastrointestinal tract is so radiosensitive that abdominal radiotherapy of tumors always involves the risk of adverse reactions. Several fibroblast growth factors (FGFs) have been shown to inhibit radiation-induced tissue damage and are expected to have potential for clinical use as radioprotectors. The fibroblast growth factor receptor (FGFR) family is composed of four receptor tyrosine kinases (RTKs) designated as FGFR1, FGFR2, FGFR3, and FGFR4. Alternative splicing of FGFRs is critical for FGF-FGFR specificity. In particular, FGF receptor 2 IIIb (FGFR2b), the so called keratinocyte growth factor receptor (KGFR), may play an important role in intestinal tissue repair because it is expressed only in epithelial cells. FGF1 is able to not only activate all of the known tyrosine kinase FGFR subtypes, but also bind to FGFR2b with high affinity. In addition, the profiles of FGFR expression in intestinal damage by radiation seem to be favorable for the FGF1 signaling pathway. Therefore, the wide spectrum of FGF1 activity makes it an ideal FGF for the treatment of radiation injuries.

A stronger FGF1 radioprotector

The structural instability of wild-type FGF1, however, limits its potential for practical use. FGF1 has poor thermal stability and a relatively short half-life *in vivo*. Therefore, a number of FGF1 mutants have been created in order to increase its stability. Among such FGF1 mutants, Q40P, S47I, and H93G were identified as strongly stabilizing substitutions. Moreover, the combinations of each single mutation were able to enhance thermal stability more than single mutations. In particular, Q40P/S47I/H93G exhibited the highest thermal stability, the longest half-life and the lowest proteolytic susceptibility among the FGF1 mutants. Q40P/S47I/H93G could also activate all subtypes of FGF receptors *in vitro* much more strongly than the wild-type FGF1. Interestingly, not only pre-irradiation treatment with Q40P/S47I/H93G, but also post-irradiation treatment with Q40P/S47I/H93G was effective in promoting intestinal regeneration after radiation damage. Moreover, Q40P/S47I/H93G prolonged mouse survival after total body irradiation because of the repair of intestinal damage (Fig. 1) [1].

Accordingly, we obtained the interesting result that the structural stability of FGF1 could contribute to the enhancement of pro-



TECTIVE effects against radiation-induced intestinal damage. Therefore, Q40P/S47I/H93G is pharmacologically one of the most promising candidates for clinical applications for radiation-induced intestinal damage.

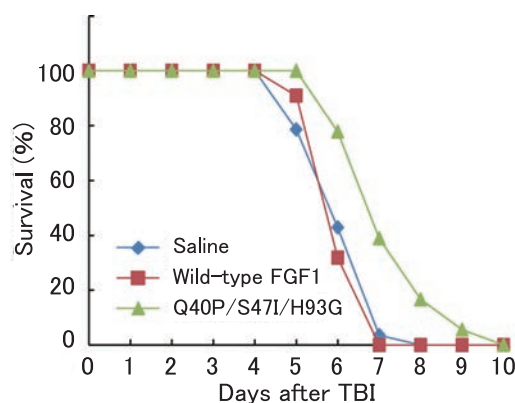


Fig.1 Prolongation of mouse survival after total body irradiation by stable FGF1 mutant.

FGFR-independent radioprotector

Unfortunately, deregulation of FGFR signaling was shown to be associated with the pathogenesis of several malignant tumors, such as bladder, endometrial, and gastric cancers; therefore, FGF radioprotectors might protect tumor cells. FGF12 was classified as an intracrine FGF because it does not activate any FGFRs and there is no evidence of it being secreted from cells, so that FGF12 has no risk to stimulate FGFRs of tumor cells. Surprisingly, a strong radioprotective effect of FGF12 given 24 h after irradiation was observed in the intestine in the crypt assay, the results of

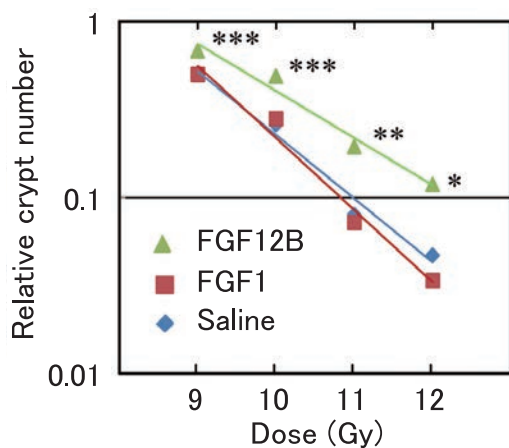


Fig.2 Protective effects of externally administered FGF12 against radiation-induced intestinal damage.

which were caused by not only apoptosis but also cell proliferation and differentiation in the intestine (Fig. 2) [2].

New mechanism of FGF radioprotectors

Generally, FGFs can function through the activation of surface FGFRs, while receptor-bound FGF1 can be endocytosed to reach the nucleus via the presence of a NLS, leading to DNA synthesis and cell proliferation. Its translocation depends on binding with FGFR1 and FGFR4 and requires phosphatidylinositol 3-kinase (PI 3K) activity and Hsp90. Moreover, FGF1 can interact with intracellular proteins such as FIBP, p34, casein kinase 2 (CK2), and mortalin, suggesting that endocytosed FGF1 plays multiple roles inside cells. We demonstrated for the first time that exogenous FGF12 could be internalized into cells very efficiently to play a role in physiological events. This process depends on two novel cell-penetrating peptide (CPP) domains of FGF12 (CPP-M and CPP-C). CPP-C, composed of approximately 10 amino acids, was identified as a specific domain of the FGF11 subfamily (FGF11-FGF14) in the C-terminal region, whereas CPP-M was shown to be a common domain in the internal region of the FGF family. Furthermore, CPP-C could deliver FGFs into cells independently of FGFR, so that an FGF1/CPP-C chimeric protein (FGF1/CPP-C) could be internalized into cells more efficiently than wild-type FGF1 (Fig. 3) [3].

A CPP-C deletion mutant that decreased cellular internalization of FGF12 also reduced radiation-induced apoptosis. In contrast, we found that FGF12 possessed two domains, amino acid residues 80-109 and 140-169 of FGF12B, which showed very potent protective effects against radiation-induced intestinal damage. Interestingly, these regions included the CPP-M and CPP-C domains, respectively, although CPP-C by itself did not show an anti-apoptotic effect. Moreover, internalized FGF12 suppressed the activation of p38 α after irradiation, resulting in reduced radiation-induced apoptosis. Consequently, our findings reveal that FGF12 can protect the intestine against radiation-induced injury through its internalization, independently of FGFRs, suggesting that cellular uptake of FGF12 is an alternative FGF signaling pathway potentially useful for cancer radiotherapy (Fig. 4) [2].

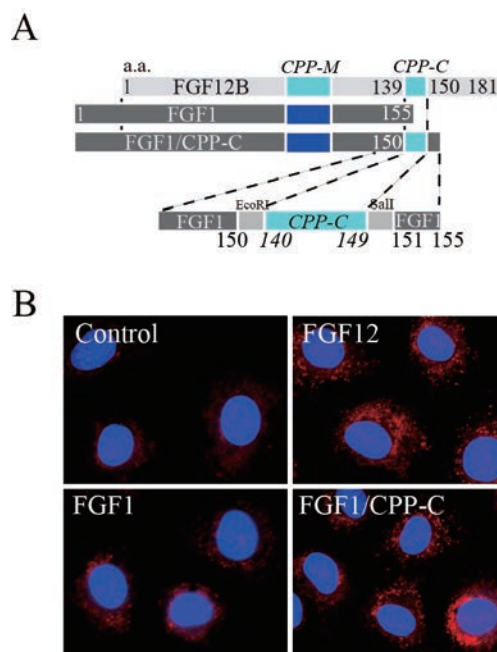


Fig.3 CPP sequence of FGF12 involved in cellular internalization.

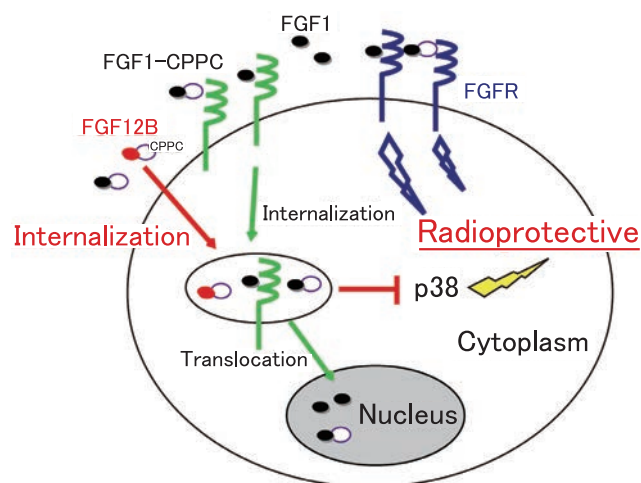


Fig.4 Radioprotective effects of internalized FGF12.

References

- [1] Nakayama F, Umeda S, Yasuda T, et al.: Structural stability of human fibroblast growth factor-1 is essential for protective effects against radiation-induced intestinal damage, *Int J Radiat Oncol Biol Phys* 85, 477-483, 2013.
- [2] Nakayama F, Umeda S, Yasuda T, et al.: Cellular internalization of fibroblast growth factor-12 exerts radioprotective effects on intestinal radiation damage independently of FGFR signaling, *Int J Radiat Oncol Biol Phys* 88, 377-384, 2014.
- [3] Nakayama F, Yasuda T, Umeda S, et al.: Fibroblast growth factor-12 (FGF12) translocation into intestinal epithelial cells is dependent on a novel cell-penetrating peptide domain: involvement of internalization in the *in vivo* role of exogenous FGF12, *J Biol Chem* 286, 25823-25834, 2011.

Highlight

Irradiation responsive miRNA “miR-574-3p” delays cell growth by suppressing cell cycle-related gene “enhancer of rudimentary homolog (ERH)”

Ken-ichi Ishikawa, Atsuko Ishikawa,
Yoshimi Shoji, Takashi Imai

E-mail: k_jshi@nirs.go.jp

Introduction

Irradiation triggers a variety of cellular responses such as growth delay, DNA repair, apoptosis, and senescence. These responses are the result of activation, inactivation, interaction, or changes in the activity level of numerous proteins. Although many studies have indicated that the fate of irradiated cells is specific to the cell type, tumor type, irradiation type, and nature of the induced stress, the mechanism that regulates these cellular responses remains unclear.

Early cellular responses to irradiation are characterized by transcriptional regulation of genes [1]. In addition, during the last decade, small RNA molecules such as microRNAs (miRNAs) were demonstrated to play important roles in the regulation of gene expression in almost all vertebrates.

Recently, we found that X-ray irradiation of cells induced the expression of miR-574-3p, which, in turn, suppressed the production of the enhancer of rudimentary homolog (ERH) protein and delayed cell growth [2]. These findings provide important insight into the cellular responses to irradiation.

Results

1) Induction of miR-574-3p expression after irradiation

To explore the role of miRNA molecules in X-ray or carbon ion beam (C-ion)-induced changes in gene expression, we analyzed the miRNA expression profile of the A549 cell line, which derived from human lung adenocarcinoma, within a few hours of irradiation using miRNA arrays. After a 3-h exposure to 2-Gy X-ray irradiation, the cells showed induction of miR-574-3p (Fig.1). However, qRT-PCR showed no induction of miR-574-3p expression after C-ion irradiation with 1, 2, 5, or 10 Gy for 1 or 3 h, suggesting that induction of miR-574-3p might be specific to X-ray irradiation.

X-ray-induced induction of miR-574-3p was also detected in ONS76 (brain medulloblastoma) and SF126 (brain astrocytoma) cell lines, whereas it was not detected in C32TG (amelanotic melanoma). Expression of miR-574-3p was slightly suppressed in the NB1RGB (normal skin fibroblast) and HeLa (cervical adenocarcinoma) cell lines.

To study the biological significance of miR-574-3p induction, we transfected synthetic miR-574-3p or miR-574-3p antagonists,



which function as a suppressor of miRNA, into A549 cells. Cells transfected with the synthetic miR-574-3p had a significant delay in growth compared with the cells transfected with control cells (Fig.2).

Growth delay is a known cellular response to irradiation. To study the involvement of miR-574-3p in the growth delay induced by X-irradiation, we observed the growth of A549 cells transfected with miR-574-3p antagonists or synthetic miR-574-3p and subsequently irradiated with X-rays. As expected, the growth delay induced by X-irradiation was partially attenuated in cells transfected with miR-574-3p antagonists.

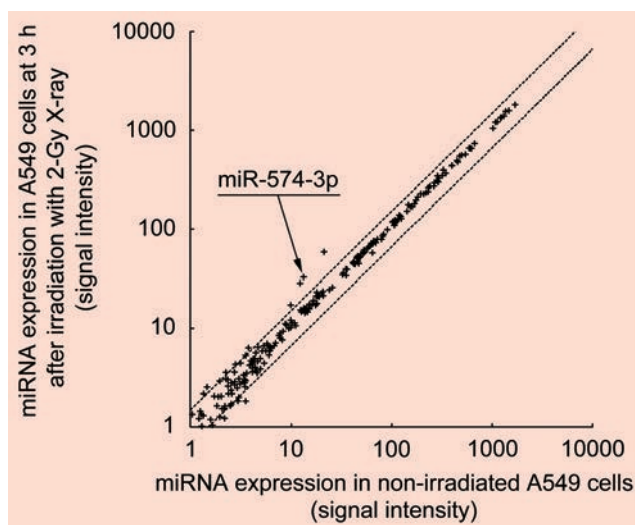


Fig.1 X-ray-responsive miRNA in A549 cells. The dotted lines indicate the thresholds of 1.5-fold change.

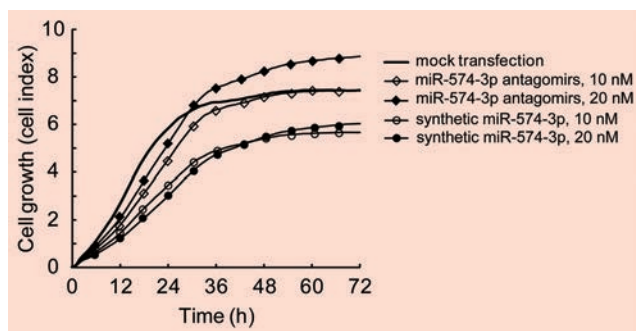


Fig.2 Delay in cell growth caused by overexpression of miR-574-3p in A549 cells

2) Suppression of ERH by miR-574-3p

To identify the target mRNA regulated by miR-574-3p, we compared the expression profile of mRNA in A549 cells transfected with synthetic miR-574-3p with that in cells transfected with miR-574-3p antagonirs by microarray analysis. Fifty-three mRNAs were down-regulated by at least 0.5-fold ($p < 0.001$) in cells overexpressing miR-574-3p compared to cells with miR-574-3p knocked down. Among the 53 targets identified, 8 genes have been focused on as potential candidate genes regulated by miR-574-3p, based on bioinformatics analysis. Among these 8 genes, only the enhancer of rudimentary homolog (ERH) is known to associate with cellular responses to genotoxic stress.

The enhancer of rudimentary (ER) gene was originally isolated from *Drosophila melanogaster* and found to participate in the pyrimidine metabolic pathway. Its human homolog, ERH, was identified later, and the nucleotide identity between the human and *Drosophila* genes is almost 80%. ERH is a multifunctional nuclear protein that mediates the cell cycle at the metaphase-anaphase transition and transcriptional regulation.

To test whether ERH expression is affected by miR-574-3p, the miRNA was transfected into A549 cells. Western blot analysis revealed that expression of the ERH protein was 0.68-fold lower in A549 cells transfected with the synthetic miR-574-3p than in the non-transfected cells. Interaction between miR-574-3p and the predicted sequence found in the 3'-UTR of the ERH mRNA was confirmed using luciferase assay (Fig.3).

To ascertain whether ERH directly affects cell growth, we transfected siRNA against ERH (siERH) or negative control oligonucleotides into A549 cells. As expected, cells transfected with siERH displayed a significant delay in growth compared with cells transfected with the negative control oligonucleotides, mock transfected cells, or non-transfected cells.

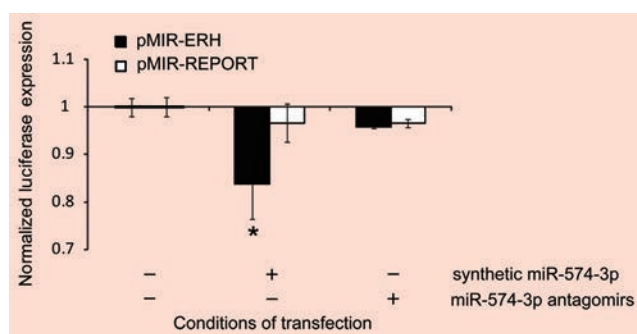


Fig.3 Luciferase reporter assay for binding of the modified ERH-3'-UTR with miR-574-3p.

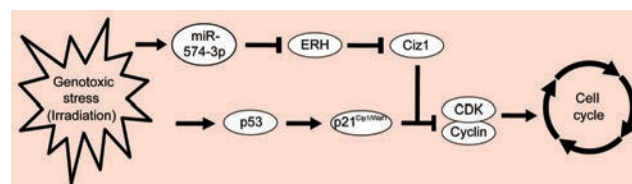


Fig.4 Proposed role of miR-574-3p in radiation-induced growth delay.

3) ERH regulates cell cycle progression

DNA damage caused by irradiation is known to arrest cell cycle progression through the activation of the tumor suppressor protein, p53, and subsequent induction of the cyclin kinase inhibitor, p21^{Cip1/Waf1}, which binds to and inhibits CDK-cyclin complexes. In addition to these important components involved in cell cycle control, many proteins also interact with p53 and p21^{Cip1/Waf1}. Cip1-interacting zinc finger protein, Ciz1, is one of these binding partner of p21^{Cip1/Waf1}. Ciz1 is aberrantly expressed in various types of tumors and is thought to be a tumor suppressor. Ciz1 is believed to facilitate the formation of the CDK-cyclinE-p21^{Cip1/Waf1} complex. Ciz1 induces the cytoplasmic localization of p21^{Cip1/Waf1} when it is up-regulated by DNA damage. Therefore, we infer that the CDK-cyclinE-p21^{Cip1/Waf1} complex is formed under the action of Ciz1 to arrest the cell cycle after DNA damage. Interestingly, Ciz1 has been characterized as a novel molecular partner for human ERH. We postulate that because ERH blocks the action of Ciz1, induction of miR-574-3p by DNA damage with subsequent reduction of ERH expression facilitates the formation of the CDK-cyclinE-p21^{Cip1/Waf1} complex. As a result, growth delay is maintained, thereby enabling the repair of DNA damage (Fig.4).

Conclusion

Many in vitro and in vivo studies have shown that gene expression profiles responding to X-ray or C-ion irradiations included common and specific gene expressions for each irradiation. In this study, miR-574-3p, which played an important role in cell cycle regulation after DNA damage, was induced by X-ray irradiation, but not by C-ion irradiation. The induction of miR-574-3p expression resulted in suppression of ERH expression and led to a delay in cell growth. Although further studies are necessary to elucidate the precise mechanism of miR-574-3p and its target gene ERH, our finding lends important insight to the cellular response to irradiation.

References

- [1] Ishikawa K, Koyama-Saegusa K, Otsuka Y, *et al.*: Gene expression profile changes correlating with radioresistance in human cell lines, *Int J Radiat Oncol Biol Phys* 65(1), 234-245, 2006.
- [2] Ishikawa K, Ishikawa A, Otsuka Y, *et al.*: A genotoxic stress-responsive miRNA, miR-574-3p, delays cell growth by suppressing the enhancer of rudimentary homolog gene in vitro, *Int J Mol Sci* 15(2), 2971-2990, 2014.

Highlight

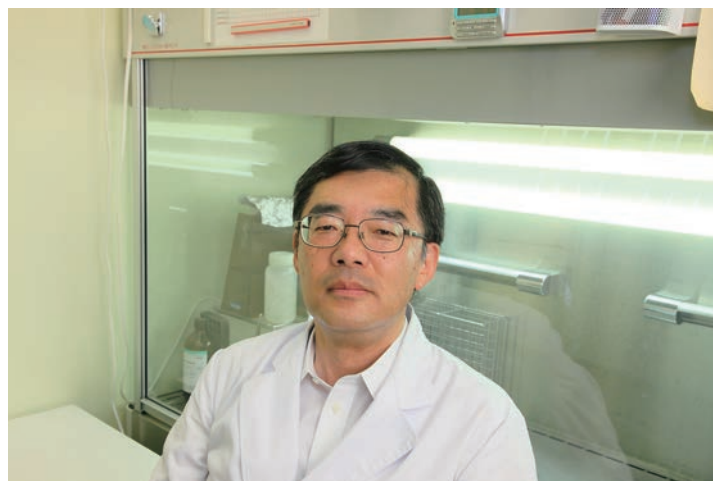
Enhanced lethal effect via bystander effect using carbon-ion microbeams simulating the 3D fast spot scanning system

Masao Suzuki

E-mail: m_suzuki@nirs.go.jp

Since 1994, a Phase I/II clinical study and cancer radiotherapy have been carried out using carbon-ion broad beams generated with the HIMAC. Now, a new treatment facility for advanced carbon-ion therapy has begun applying a 3D fast spot scanning system with pencil beams [1, 2]. To identify the biological effects of the 3D fast scanning carbon ion beams in vitro, we demonstrated the lethal effect of human tumor cell lines with different origins using the spot scanning irradiation system of carbon-ion microbeams generated with the Takasaki Ion Accelerators for Advanced Radiation Application (TIARA) in the Japan Atomic Energy Agency (JAEA). A radiation-induced bystander effect is described as the ability of cells that are not directly irradiated by a radiation beam but that are close to cells that are irradiated to show induced biological effects [3]. This bystander effect plays an important role in the mechanism(s) for heavy-ion radiosensitivity, especially for spot scanning irradiation. It is very powerful for understanding radiation-induced bystander effects to use a microbeam-irradiation system and we, therefore, have been doing a joint study with JAEA about biological responses using the heavy-ion microbeams.

Carbon-ion microbeams ($^{12}\text{C}^{5+}$, 220 MeV) collimated to 20 μm in diameter were generated with the HZ1 port at TIARA. Eight different human cell types harboring wild- or mutated-type *P53* gene were distributed by the Riken BioResource, the Health Science Research Resources Bank and the Institute for Fermentation in Japan. Two days before the irradiation approximately 8×10^5 exponentially growing cells were inoculated into separate microbeam dishes. These dishes were made of an acrylic resin ring with 36 mm diameter and had a 7.5 μm -thick polyimide film attached on the ring bottom. The irradiation was carried out using the 256 (16 \times 16)-cross-stripe-irradiation method (Fig. 1). In this irradiation condition, the percent of the number of total microbeam-irradiated cells to total plated cells on the dish was calculated as around 0.01%. The linear energy transfer (LET) of carbon-ion microbeams was estimated to be 103 keV/ μm at the sample position and the irradiation was carried out in each spot with 8 delivered ion beams (0.4Gy). Lethal effect was detected using a colony formation assay as reproductive cell death. In order to block up cell-cell communication, half of the sample dishes were treated with a



specific inhibitor of gap-junction mediated cell-cell communication (40 μM of γ -isomer of hexachloro-cyclohexane) one day before the irradiation.

We first examined the lethal effect and the gap-junction mediated bystander lethal effect using two tumor cell lines with the same origin transfected with either the wild-type *P53* gene (H1299/wtp53) or mutated-type *P53* gene (H1299/mp53) from a human non-small cell lung carcinoma cell line (H1299). The percent survival for the carbon-ion-microbeam irradiation (IR) in H1299/wtp53 cells was around 90%, while it was almost 100% in H1299/mp53 cells (Fig.2). We would expect the percent survival of 99.99% if the lethal effect was induced in only the directly irradiated cells, representing 0.01%, assuming no bystander effect. However, the percent survival in H1299/wtp53 cells was significantly lower than our expectation. We concluded that the lethal effect in the carbon-ion irradiated H1299/wtp53 cells was enhanced by the bystander effect. Moreover, it returned to around 100% when using the specific inhibitor of gap-junction mediated cell-cell communication.

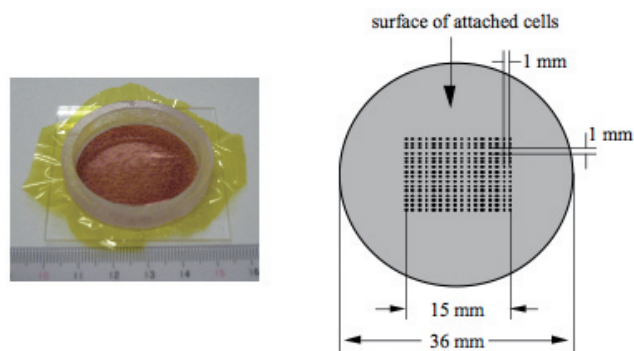


Fig.1 Photo of a dish and a schematic diagram for the 256 (16 \times 16)-cross-stripe method of the microbeam irradiations.

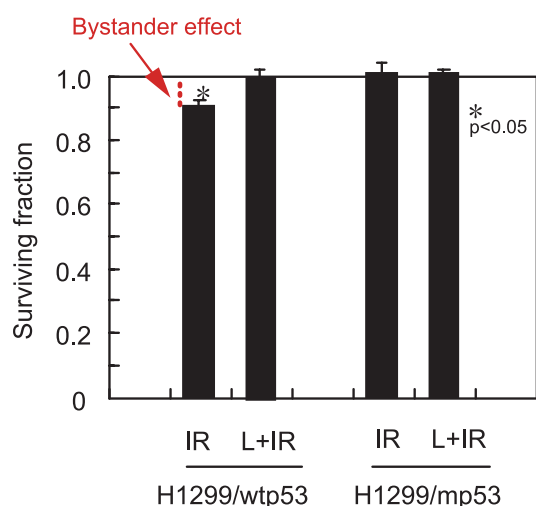


Fig.2 Bystander lethal effect in H1299/wtp53 and H1299/mp53 cells irradiated with carbon-ion microbeams (0.4Gy). IR, microbeam irradiated sample; L+IR, microbeam irradiated sample with a gap-junction inhibitor. The results are the means and standard errors from 6 independent beam times (* $p < 0.05$).

The observed bystander lethal effect was induced by the mechanism of gap-junction mediated cell-cell communication.

To generalize the result, we next examined the *P53*-dependent bystander lethal effect using 6 human cell lines with different origins, such as normal human skin fibroblasts (wild-type *P53* gene), brain astrocytoma (wild-type *P53* gene), lung adenocarcinoma (wild-type *P53* gene), melanoma (mutated-type *P53* gene), brain medulloblastoma (mutated-type *P53* gene) and brain gliosarcoma (mutated-type *P53* gene). The results clearly showed that the percent survival was 85-92% in the cells with wild-type *P53* gene and around 100% in the cells with mutated-type *P53* gene. Also, the reduced survival in the cells with wild-type *P53* gene returned to 100% when using the specific inhibitor of gap-junction mediated cell-cell communication (Fig.3). There was clear evidence that the spot irradiation of carbon-ion microbeams could induce the enhanced lethal effect in cells harboring wild-type *P53* gene via the gap-junction mediated bystander effect.

The results suggest that the spot scanning irradiation system of carbon ions enables us to kill tumor cells effectively and to provide tailor-made therapy depended on specific gene(s), such as *P53* gene status, considering the *P53*-dependent bystander lethal effect. Additionally, the study results will facilitate development of drugs that can enhance the bystander lethal effect in *P53*-mutated tumor cells.

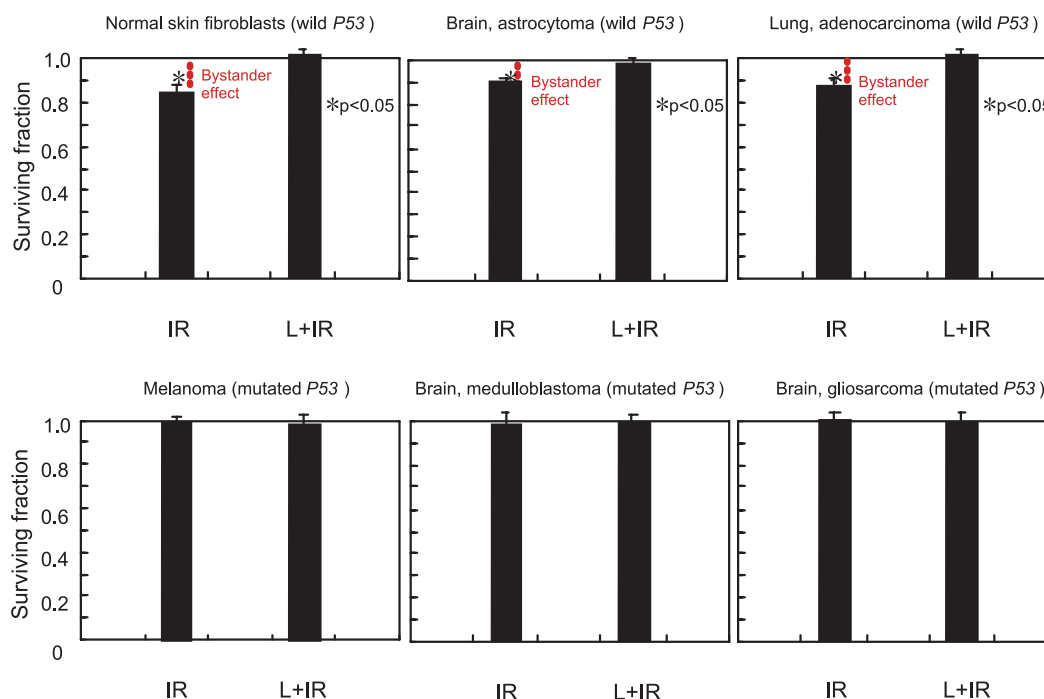


Fig.3 *P53*-dependent bystander lethal effect in 6 different human cell lines irradiated with carbon-ion micro-beams (0.4Gy). The treatment in the horizontal axis is the same as explained in the caption of Fig.2. The results are the means and standard errors from 6 independent beam times (* $p < 0.05$).

References

- [1] Furukawa T, Inaniwa T, Sato S *et al.*: Design study of a raster scanning system for moving target irradiation in heavy-ion radiotherapy, *Med Phys* 34, 1085-1097, 2007.
- [2] Furukawa T, Inaniwa T, Sato S *et al.*: Performance of the NIRS fast scanning system for heavy-ion radiotherapy, *Med Phys* 37, 5672-5682, 2010.
- [3] Autsavapornporn N, Suzuki M, Funayama T *et al.*: Gap junction communication in the propagation of bystander effects induced by microbeam irradiation in human fibroblast cultures: The impact of radiation quality, *Radiat Res* 180, 367-375, 2013.

Highlight

The Research Project with Heavy Ions at NIRS-HIMAC

Tsuyoshi Hamano

E-mail: hamano@nirs.go.jp

Since 1994 the Heavy-Ion Medical Accelerator in Chiba (HIMAC) at NIRS has been made available for use by researchers worldwide in the field of ion-beam sciences in addition to carbon-beam radiotherapy. There are four experimental halls (Physics, Biology, Secondary beam and Medium-energy caves) as well as five treatment rooms. During the daytime from Tuesday through Friday, HIMAC is operated for patient treatments. At night and on weekends the four halls can be used for various experiments with ion beams. The latter framework is specified as "The Research Project with Heavy Ions at NIRS-HIMAC". Table 1 shows typical beam characteristics which are available to users at the Physics cave.

NIRS accepts proposal submissions for the Research Project twice a year (basically in June and November). Information about the call for proposals can be seen on the NIRS website [1]. The Program Advisory Committee (PAC) for the Research Project reviews submitted proposals from the viewpoint of scientific merits and feasibilities. The Machine Time Committee allocates beam time in accordance with the review of the PAC, considering requests from proposers. The Program Coordinator Group supports researchers especially from external institutions. The researchers, whose accepted proposals employ HIMAC, are asked to make a report to NIRS including a list of publications of the work and to make a presentation at an annual meeting after the end of the fiscal year (FY).

Table 1 Typical beam characteristics available at HIMAC

Ion	Energy (MeV/u)							Intensity pps (particles / second)
He	100	180	230	-	-	-	-	$<1.2 \times 10^{10}$
C	100	180	230	290	350	400	430	$<1.8 \times 10^9$
N	100	180	230	290	350	400	430	$<1.5 \times 10^9$
O	100	180	230	290	350	400	430	$<1.1 \times 10^9$
Ne	100	180	230	290	350	400	600	$<7.8 \times 10^8$
Si	100	180	230	290	350	400	600	$<4.0 \times 10^8$
Ar	-	-	-	290	-	400	650	$<2.4 \times 10^8$
Fe	-	-	-	-	-	400	500	$<2.5 \times 10^8$



Fig.1 shows the numbers of accepted proposals as a function of year. FY 2013 had 137 proposals from medicine, biology and physics etc. that were accepted and a total beam time of 5282 hours was supplied. Fig. 2 shows contents of accepted proposals: the physics pie chart (a) includes medical physics, accelerator, atom & nuclear physics, chemistry and space sciences; and the biology pie chart (b) includes fundamental studies for cancer treatment, response of normal tissue, cell biology and molecular biology. 660 researchers, including 148 foreigners, were registered as participants from external institutions. Fig. 3 shows numbers of scientific reports such as original papers, proceedings, theses and oral presentations. For more details, the annual report [2] of the Research Project (partly in English) is available from the Program Coordinator (book or CD-ROM) and at the NIRS website (PDF file). It includes submitted reports and publication lists.

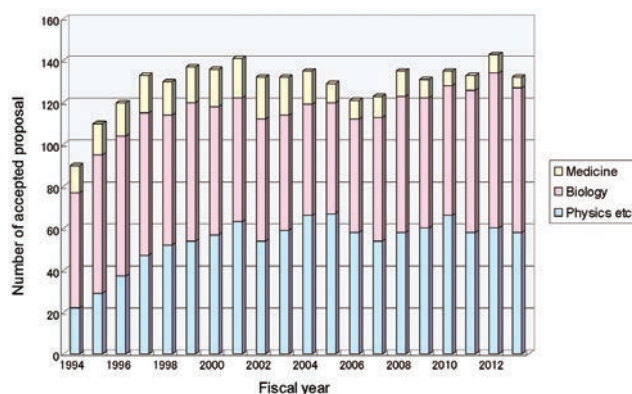


Fig.1 Numbers of accepted proposals as a function of fiscal year

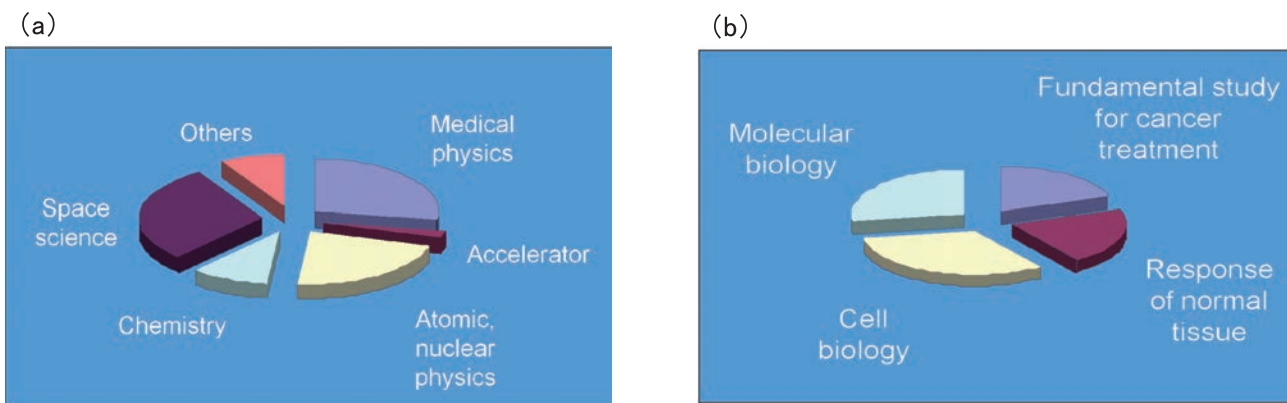


Fig.2 Contents of accepted proposals in physics (a) and biology (b) in FY 2013

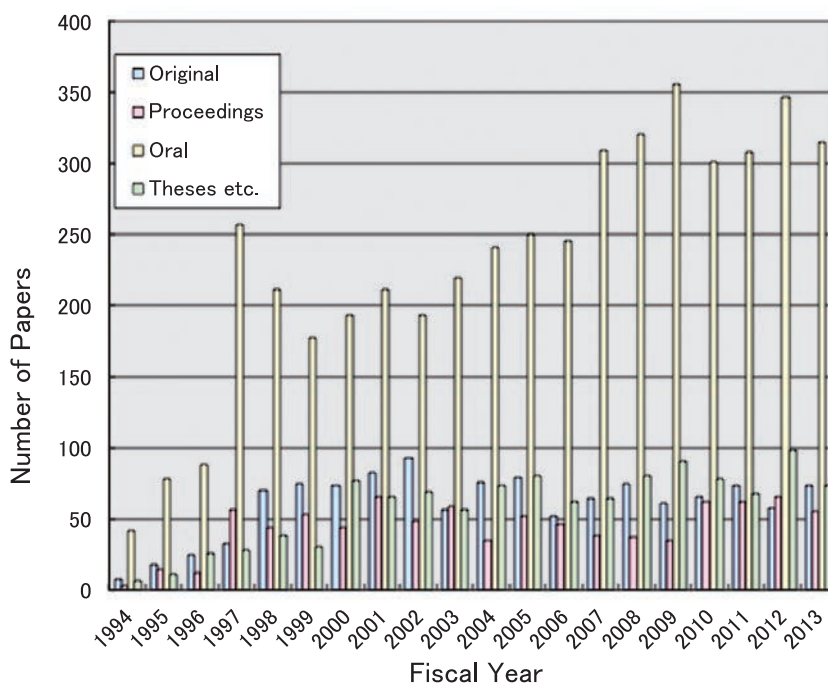


Fig.3 Number of scientific reports as a function of fiscal year

References

- [1] NIRS, <http://www.nirs.go.jp/information/application/26himac2014.shtml>
- [2] NIRS, 2012 Annual Report of the Research Project with Heavy Ions at NIRS-HIMAC, NIRS-M-260, Aug. 2013
<http://www.nirs.go.jp/publication/irregular/04.shtml>

Molecular Imaging Research for Functional Diagnosis

Yasuhisa Fujibayashi, Ph.D., D.Med.Sci.

Director of Molecular Imaging Center

E-mail: yfuji@nirs.go.jp

NIRS has a long history of research and development in clinical applications of radiation, especially in the field of nuclear medicine including positron emission tomography (PET), single photon emission tomography (SPECT) and internal radiation therapy. Based on these accomplishments, the Molecular Imaging Center (MIC) was established in 2006. At present, research carried out in the MIC is based on collaboration among diverse areas as follows:

- (1) Drug design for target-selective delivery (molecular probes), labeling of the molecular probes with a suitable radionuclide for diagnosis/therapy, and radionuclide production.
- (2) Development of three-dimensional quantum photon measurement systems such as PET and SPECT, including hardware and software.
- (3) Basic evaluation and clinical application for diagnosis/therapy of tumors, psychiatric and neurodegenerative disorders, and aging-related diseases such as inflammatory diseases.

The MIC also promotes research on magnetic resonance imaging (MRI), X-ray-CT imaging and optical imaging. These imaging techniques are an integral part of diagnostic imaging, so called multimodal imaging. Recently, PET-MR has been approved for clinical medicine, and development of its clinical applications will be a key task for MIC.

Molecular Probe Program

1) Radiolabeling technique

We used [^{11}C]methyl iodide, [^{18}F]fluoroethyl bromide and [^{18}F]fluorine ion to label a variety of precursors and thereby develop novel PET probes with various functional groups. [^{11}C]Formaldehyde was used to label an oligopeptide containing tryptophan hydrochloride. We found that the use of tetrabutylammonium fluoride could promote N- and O- [^{11}C]methylation reactions with [^{11}C]methyl iodide in dimethyl sulfoxide.

2) Development of novel molecular probes

We developed diverse PET probes for receptors, transporters and enzymes. Of these probes, [^{11}C]ITMM is undergoing clinical study for the imaging and quantitative analysis of mGluR1 in human brain. Further, neuroprotective effects were successfully monitored using PET with [^{11}C]ITMM. On the other hand, we devel-



oped several lipophilic ^{11}C -labeled compounds that will enter the brain and undergo glutathione conjugation to form hydrophilic and MRP1-specific radiometabolites in the brain.

3) Production of non-standard PET, beta-, and alpha radionuclides

We have developed two production systems for the useful radionuclides ^{68}Ge and ^{211}At .

4) Production of useful PET probes for clinical use

We routinely produce more than 70 PET probes for clinical and basic research. In fiscal year 2013, we established rapid and reliable production and quality control methods of three new PET probes and evaluated the toxicity and safety of these probes. We improved the production equipment, systems and documents to comply with the Japanese Society of Nuclear Medicine GMP standard for PET radiopharmaceuticals (JSNM GMP standard), and passed the audit from the auditing organization for the JSNM GMP standard.

5) Contribution to the quality control of clinical PET in Japan

We performed quantitative analyses and provided certificates for chemical impurities in several radiopharmaceuticals including [^{18}F]FDG formulations which are produced in greater than 80 PET facilities in Japan.

Biophysics Program

The Biophysics Program aims to develop next generation PET technologies and to develop the methods for quantitative analyses of *in vivo* imaging.

1) Imaging Physics Team

The Imaging Physics Team carries out research and development of novel technologies for next generation PET instrumentations and imaging algorithms. A depth-of-interaction (DOI) detector is a key device to get any significant improvement in sensitivity

while maintaining high spatial resolution. DOI measurement also has a potential to expand application of PET to new fields because it allows for more flexible detector arrangement. We are developing an OpenPET, which will lead to PET imaging during treatment. Following our first idea of a dual-ring geometry, we invented a single-ring geometry as the 2nd generation OpenPET. The DOI detector itself continues to evolve with the help of recently developed semiconductor photodetectors, often referred to as silicon photomultipliers (SiPMs). We are developing a SiPM-based DOI detector named X'tal cube to achieve sub-mm spatial resolution, which is reaching the theoretical limitation of PET imaging. We have developed a prototype for 1mm isotropic detector resolution, which equals the world record.

2) Imaging Physiology Team

The Imaging Physiology Team develops the methods for quantitative analyses of *in vivo* imaging obtained from PET, MRI, and optical imaging. In PET receptor imaging, a method for measurement of dopamine release by a single PET scan with multiple injections of [¹¹C]raclopride was developed. The kinetics of radioligands for neuroreceptors was evaluated using the graphic plot analysis previously developed in simulated brain tissue time-activity curves with various binding parameters. A semi-automated classification of vascular components in mouse brain from a two-photon laser scanning microscopy was developed to determine the ratio of each vascular component including artery, capillary, and vein in cerebral blood volume for correction of intravascular radioactivity in PET studies. The relation between autoregulatory vasodilatation due to stenocclusive vascular lesion and vascular response to hypercapnia in microvasculature was evaluated using two-photon laser scanning microscopy in mice.

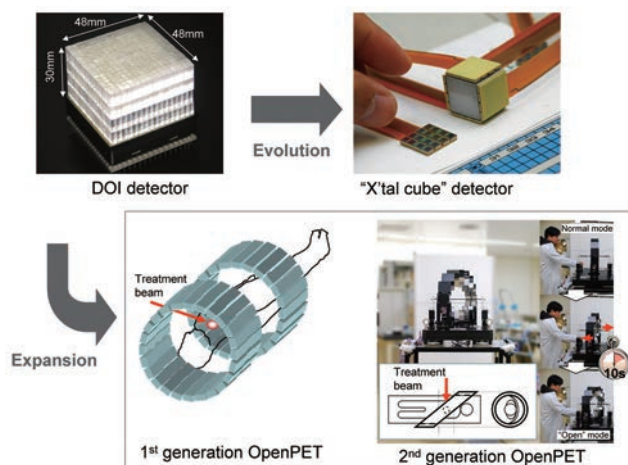


Fig.1 Developments of next generation PET technologies: the world's finest PET detector "X'tal cube" and the world's first open-type PET "OpenPET". A small type equipped with transformable mechanism was developed.

Diagnostic Imaging Program

1) Basic clinical research studies on pathophysiological imaging

We continued clinical research using the hypoxia PET probe, [¹⁸F]FAZA, to clarify the relationship between [¹⁸F]FAZA tumor uptake and responsiveness to treatment. In the radiation-induced thymic lymphoma model, early changes of bone marrow and thymus after irradiation were evaluated by PET and MRI to elucidate the key event related to carcinogenesis. For internal radiotherapy targeting a hypoxic microenvironment using [⁶⁴Cu]ATSM, we developed methods to increase the therapeutic effect and to reduce the side

effects. We proved that PET with [¹¹C]acetate can predict the responsiveness to treatment targeting fatty acid synthase (see the Highlight for details). We also developed a PET probe derived from aminolevulinic acid for prediction of the effect of photodynamic therapy.

2) Development of antibody/peptide probes for the targeted imaging of cancer-related molecules

For the targeted cancer imaging, we labeled antibodies against cancer targets such as CD144 (see the Highlight for details) and fibrin with ⁸⁹Zr and successfully carried out PET imaging in mouse xenograft models. In addition, experimental radioimmunotherapy was performed using ⁹⁰Y-labeled anti-transferrin receptor antibody in mice having pancreatic cancer xenografts. A peptide probe targeting $\alpha v \beta 3$ integrin, ⁶⁴Cu-labeled tetramer of cRGD, was applied to the pancreatic cancer model and we successfully visualized orthotopically-implanted cancer in the pancreas. A method to decrease high renal uptake of this probe was also established.

3) Development of MRI-based functional probes and nano-sized multi-functional probes and their application in various disease models

MRI-based functional probes to measure tissue redox status were applied for various disease models such as Parkinson's disease and we succeeded in detecting high production of reactive oxygen species. We developed a novel probe that accumulates in mucosal epithelium and applied it for the spontaneous colon cancer model. We also developed various nano-sized probes for the detection of very small cancers, LN metastases, resistance to treatment, and so on, and evaluated their usefulness in disease models.

Molecular Neuroimaging Program

The Molecular Neuroimaging Program focuses on pathophysiology of neuropsychiatric disorders including Alzheimer's disease, evaluation of drugs and the molecular mechanism of human behavior. From basic research using transgenic mice to clinical studies, we use PET, MRI, and laser microscopy to analyze the molecular function of disease.

The major topic in 2013 was the publication of a new tau ligand from basic research to clinical application. The study was originally started in the Neuromolecular team lead by Dr. Higuchi. He designed the structure of the new tau ligand PBB3 and labeled it with C-11 in collaboration with staff of the Molecular Probe Program. Then the clinical study was carried out by Clinical Neuroimaging Team; this presents a good example of collaboration with other teams and programs. We received a Japanese patent for the tau ligand within a year. The impact of the new tau ligand on the scientific community has been large and it was featured in the journals, *Nature* and *Nature Reviews Neuroscience*. We are currently starting several collaborative projects both within and outside Japan.

Other than the new tau ligand we have done several studies to evaluate drug effects. Norepinephrine transporter (NET) is being targeted as an important antidepressant. There have been limited reports about the occupancy of NET and the clinical threshold of the NET occupancy has not been clarified yet. We have measured the NET occupancy by antidepressants using (S,S)-[¹⁸F]FMeNER-D2. Based on the NET occupancy of the tricyclic antidepressant nortriptyline, we estimated that more than 50% occupancy would be needed for the clinical effect. This is the first report to indicate the clinical threshold of the NET occupancy.

Highlight

Imaging of activity of the ATP-binding cassette transporter ABCC1 in the lungs

Toshimitsu Okamura

E-mail: okamura@fml.nirs.go.jp

Background and objectives

The ATP-binding cassette (ABC) transporter ABCC1 serves as a primary active transporter using the energy from ATP hydrolysis. This protein has an unusually broad substrate specificity and eliminates numerous substances including lipophilic therapeutic agents and hydrophilic metabolites from cells or tissues. ABCC1 is expressed in many tissues, with a relatively high level in the lungs. The prominent expression of ABCC1 in the lungs may serve as a defense mechanism against exogenous and endogenous toxic compounds, and the alteration of ABCC1 expression is associated with certain lung diseases such as chronic obstructive pulmonary disease. Imaging of pulmonary ABCC1 activity would therefore be useful for elucidating pathological conditions of lung diseases. However, few reports are available on methods for imaging of ABCC1 activity in the lungs. Here, we introduce a paper that examines the feasibility of imaging pulmonary ABCC1 activity using 6-bromo-7- ^{11}C methylpurine (^{11}C]7M6BP) [1]. This compound has recently been developed as a probe for the assessment of cerebral ABCC1 activity and is found to be enzymatically converted to its GSH conjugate (GS-P), a substrate for ABCC1, in the brain [2].

Approach for imaging of pulmonary ABCC1 activity and probe requirements

Fig. 1 shows the model for imaging ABCC1 activity with a probe for positron emission tomography (PET), an imaging technique that can quantify the pharmacokinetics of the probe following injection. A PET probe diffuses into cells after intravenous injection and undergoes conversion to a hydrophilic substrate that is then extruded by ABCC1. In the early phase after injection, the radioactive species in cells are a mixture of the PET probe and the hydrophilic substrate but gradually they change to the hydrophilic substrate alone. Since it is unlikely that the hydrophilic substrate formed within cells is eliminated by simple diffusion, the rate of reduction in radioactivity would reflect pulmonary ABCC1 activity in vivo after the PET probe completely disappears. The PET probe [^{11}C]7M6BP should thus possess the following characteristics: high extraction to the lung tissue and efficient conversion to the GSH conjugate.

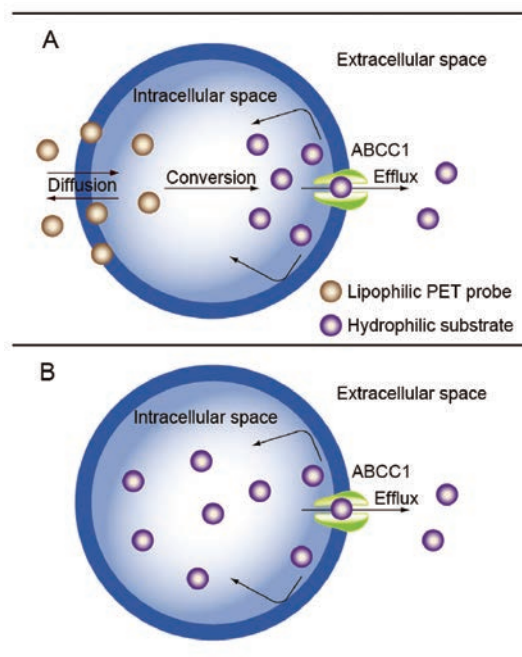


Fig. 1 Model for the imaging of ABCC1 activity

When a lipophilic probe is administered intravenously, it enters cells by simple diffusion. While a portion of the incorporated probe diffuses from the cells, the rest is converted into a hydrophilic substrate for ABCC1 (A). If the conversion to the substrate is rapid, the probe will no longer exist in cells or the lung tissue within a short time after its administration (B). In this situation, any decrease in radioactivity will depend on ABCC1 activity alone.

Major findings

In our approach, [^{11}C]7M6BP should enter the lung tissue by simple diffusion, whereas its GSH conjugate (GS-P) should not. To

confirm this, the uptake of the two compounds into the lungs was examined in wild-type mice. The PET probe [^{11}C]7M6BP showed high uptake in the lungs 1 min after injection. By contrast, the initial uptake of [^{35}S]GS-P in the lungs was low and comparable to that in the blood. The lung-to-blood ratio of [^{35}S]GS-P at 1 min after injection was much lower than that of [^{11}C]7M6BP, and the uptake of [^{35}S]GS-P into the lung via simple diffusion would thus be negligible.

The PET imaging of ABCC1 activity also requires that [^{11}C]7M6BP should be efficiently converted to [^{11}C]GS-P in the lung tissue. To test this, we analyzed the chemical form of radioactive compounds in the lungs 5 min after an intravenous injection of [^{11}C]7M6BP into the wild-type and *Abcc1*^{-/-} mice by HPLC. The parent compound [^{11}C]7M6BP completely disappeared from the lung tissue of the two strains of mice, and the radioactive species in the lungs were present primarily in the form of the GSH conjugate, although an unknown metabolite, which might be a degradation product of the GSH conjugate formed by metabolic enzymes, was observed in the lungs of the wild-type mice.

A PET study with [^{11}C]7M6BP was performed in wild-type mice, *Abcc1*^{-/-} mice and triple knockout mice lacking the genes for *Abcb1a/1b* (P-glycoprotein) and *Abcg2* (breast cancer resistance protein). Lung radioactivity in wild-type and *Abcc1*^{-/-} mice reached a maximum level immediately after the injection of [^{11}C]7M6BP. Thereafter, radioactivity was rapidly decreased from the lungs of wild-type mice, whereas it was mostly constant up to 60 min later in lungs of *Abcc1*^{-/-} mice. The efflux half-lives determined from the time-radioactivity curves during the period of 5 to 15 min were 6.3 min for the wild-type mice and 108 min for the *Abcc1*^{-/-} mice. A significant increase in the efflux half-life was observed in the lung tissue of *Abcc1*^{-/-} mice. The kinetics of [^{11}C]7M6BP in the lungs of *Abcb1a/1b*^{-/-}/*Abcg2*^{-/-} mice was quite similar to that of wild-type mice, and the lung radioactivity in the *Abcb1a/1b*^{-/-}/*Abcg2*^{-/-} mice was rapidly reduced after reaching a maximum level. PET summation images of wild-type, *Abcc1*^{-/-}, and *Abcb1a/1b*^{-/-}/*Abcg2*^{-/-} mice are shown in Fig.2. A high accumulation of radioactivity was observed in the lungs of *Abcc1*^{-/-} mice, whereas extremely low levels of radioactivity were found in the lungs of the wild-type and *Abcb1a/1b*^{-/-}/*Abcg2*^{-/-} mice.

Fig.3 shows the effects of MK571 (ABCC1 inhibitor) on the kinetics of [^{11}C]7M6BP in the lungs. The clearance of radioactivity from the lungs was delayed by the treatment with MK571 (100 mg/kg) compared with control mice. The high dose treatment (300 mg/kg) resulted in a further delay in the washout of radioactivity compared with the low dose treatment. The efflux half-lives were 6.9

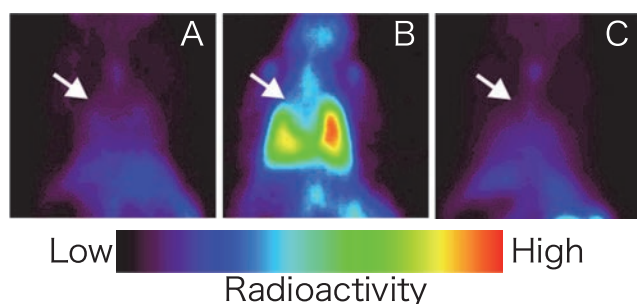


Fig.2 PET images after the administration of [^{11}C]7M6BP to wild-type (A), *Abcc1*^{-/-} (B), and (C) *Abcb1a/1b*^{-/-}/*Abcg2*^{-/-} mice. Coronal summed images from 0-60 minutes after the administration are shown. Arrows indicate lungs.

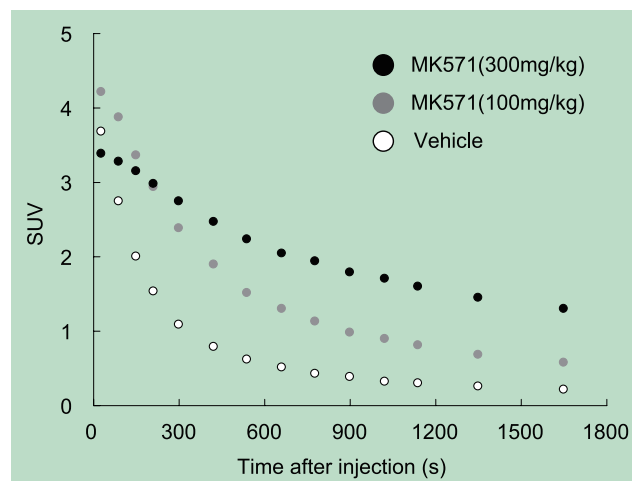


Fig.3 The effect of the ABCC1 inhibitor (MK571) on kinetics of [^{11}C]7M6BP in the lungs

min for the vehicle treatment, 7.9 min for the low dose (100 mg/kg) treatment, and 16 min for the high dose (300 mg/kg) treatment. There were significant differences in the efflux half-life between the control and low dose groups, and between the low and high dose groups

In conclusion, these results suggest that [^{11}C]7M6BP enters the lung tissue by simple diffusion after injection and becomes converted into the hydrophilic GSH conjugate, which is then specifically extruded by ABCC1; therefore [^{11}C]7M6BP allows for the imaging of *in vivo* ABCC1 activity in the lungs.

Future expectations

Overexpression of efflux pumps such as ABCC1 and ABCB1 is associated with drug resistance, which is one of the big problems in cancer treatment. The therapeutic efficacy could be enhanced by the coadministration of ABCC1 inhibitors with anticancer drugs, but the inhibitors may also result in inhibition of essential physiological functions of ABCC1 not only in the lungs but also in other tissues. It is hence desirable to estimate the degree of inhibition of pulmonary ABCC1 activity *in vivo* by inhibitors to enhance therapeutic effects and to lessen side effects. The PET probe [^{11}C]7M6BP is expected to be helpful for such an estimation. It could also be used for assessment of patients with lung diseases such as chronic obstructive pulmonary disease (COPD), which shows low expression of ABCC1 as compared with healthy controls [3]. Furthermore, recent reports suggest the association of single nucleotide polymorphisms in ABCC1 with lung function and inflammatory markers in COPD. The PET probe [^{11}C]7M6BP might be useful for investigating the relationship between ABCC1 activity and genetic polymorphisms, although further studies are required for the clinical use of [^{11}C]7M6BP.

References

- [1] Okamura T, Kikuchi T, Okada M, *et al.*: Imaging of activity of multidrug resistance-associated protein 1 in the lungs, *Am J Respir Cell Mol Biol* 49, 335-340, 2013.
- [2] Okamura T, Kikuchi T, Okada M, *et al.*: Noninvasive and quantitative assessment of the function of multidrug resistance-associated protein 1 in the living brain, *J Cereb Blood Flow Metab* 29, 504-511, 2009.
- [3] van der Deen M, Marks H, Willemse BW, *et al.*: Diminished expression of multidrug resistance-associated protein 1 (MRP1) in bronchial epithelium of COPD patients, *Virchows Arch* 449, 682-688, 2006.

Highlight

Development of radiolabeling technique for cyclic RGD peptide by using carbon-11 formaldehyde

Masayuki Hanyu

E-mail: hanyu@nirs.go.jp

Objectives

Some low molecular weight oligopeptides have been considered as potential imaging agent with good permeability properties that can permit rapid access to the target tissues. One of the main challenges of PET for radiochemists is the development of rapid synthetic methods for the introduction of short-lived positron-emitting radionuclides, such as carbon-11 ($T_{1/2} = 20.4$ min), into the peptide of interest. Several methods have been developed for the synthesis of ^{11}C -labelled oligopeptides using general ^{11}C -labelled agent such as $[^{11}\text{C}]\text{CH}_3\text{I}$ [1]. However, these require complex synthetic procedures to be carried out over long time periods relative to the short half-life of carbon-11, and this has limited their application. The development of procedures amenable to the synthesis of novel carbon-11 labeled agents for use as tracers in biomedical research is important to move PET imaging techniques forward.

$[^{11}\text{C}]\text{Formaldehyde}$ ($[^{11}\text{C}]\text{CH}_2\text{O}$) is a carbon-11 labeled agent for compounds required in PET studies. However, synthetic methods for $[^{11}\text{C}]\text{CH}_2\text{O}$ in the preparation of PET compounds have to be performed at very low temperature under rigid control. The use of $[^{11}\text{C}]\text{CH}_2\text{O}$ has not been developed to any great extent because the current labeling approaches using $[^{11}\text{C}]\text{CH}_2\text{O}$ are generally inaccessible. Hooker *et al.* [2] recently reported a simple and fast method for the preparation of $[^{11}\text{C}]\text{CH}_2\text{O}$. Furthermore, the treatment of tryptamine with $[^{11}\text{C}]\text{CH}_2\text{O}$ under acidic conditions provided $[^{11}\text{C}]\text{2,3,4,9-tetrahydro-1H-}\beta\text{-carboline}$ in a good radiochemical yield. We envisaged that the treatment of Trp with $[^{11}\text{C}]\text{CH}_2\text{O}$ under acidic conditions would provide $[1\text{-}^{11}\text{C}]\text{1,2,3,4-tetrahydro-}\beta\text{-carboline-3-carboxylic acid}$ ($[^{11}\text{C}]\text{Tpi}$) as well as several related analogues. Herein, we describe the manual and remote-controlled synthesis of $[^{11}\text{C}]\text{Tpi}$ -containing oligopeptide via a Pictet-Spengler reaction using $[^{11}\text{C}]\text{CH}_2\text{O}$ [3].

Over View

The synthesis of $[1\text{-}^{11}\text{C}]\text{Tpi}$ was initially examined under the conventional acid catalyzed Pictet-Spengler conditions using Trp and a solution of $[^{11}\text{C}]\text{CH}_2\text{O}$ in DMF (Fig.1.). The radiosynthesis of $[1\text{-}^{11}\text{C}]\text{Tpi}$ was conducted by mixing a solution of $[^{11}\text{C}]\text{CH}_2\text{O}$ in DMF with a solution of p-toluenesulfonic acid (TsOH) in DMF, and

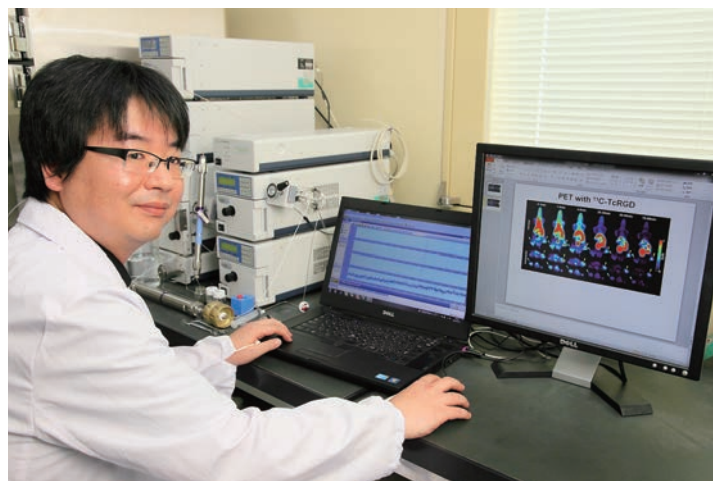


Table 1 Survey conditions for the preparation of $[1\text{-}^{11}\text{C}]\text{Tpi}^a$

Entry	Acid	Solvents	Substrate	RCY ^b (n=4)
1	TsOH (0.1 mmol)	DMF	Trp	42.3±3.2 %
2	TsOH (0.1 mmol)	H ₂ O	Trp	45.3±2.1 %
3	-	1 M HCl	Trp	44.8±2.9 %
4	-	H ₂ O	Trp•HCl	45.2±3.6 %

^a Reaction condition: $[^{11}\text{C}]\text{CH}_2\text{O}/\text{DMF}$ (37-370 MBq) 200 μl ; substrate (15 μmol); Solvents 200 μl ; reaction time 5 min; reaction temperature 100°C.

^b Determined by a radiochromatogram of the analytical HPLC.

using Trp instead of tryptamine according to the previously described method [2]. The desired product was obtained with a moderate radiochemical yield (Table 1, entry 1). The radiosynthesis was then conducted using an aqueous solution of TsOH because the Trp was poorly soluble in the TsOH/DMF solution at room temperature. These reaction conditions provided a similar result (Table 1, entry 2) to the initial conditions, indicating that the reaction between $[^{11}\text{C}]\text{CH}_2\text{O}$ and Trp in the DMF/water solution did not have any discernible impact on the radiolabeling of $[1\text{-}^{11}\text{C}]\text{Tpi}$. The choice of solvent used in this reaction was found to be particularly important because the synthesis of $[1\text{-}^{11}\text{C}]\text{Tpi}$ from $[^{11}\text{C}]\text{CH}_3\text{I}$ occurred over two steps but was conducted in one-pot. We proceeded to evaluate the Pictet-Spengler reaction using 1 mol/L HCl as the reaction solvent (Table 1, entry 3). Under these reaction conditions, the radiochemical yield of $[1\text{-}^{11}\text{C}]\text{Tpi}$ was found to be similar to those reported above (Table 1, entries 1-2). The Pictet-Spengler reaction proceeded smoothly when an aqueous solution of Trp•HCl was used without the addition of an acid catalyst to give the desired product in a 45.2% radiochemical yield (Table 1, entry 4).

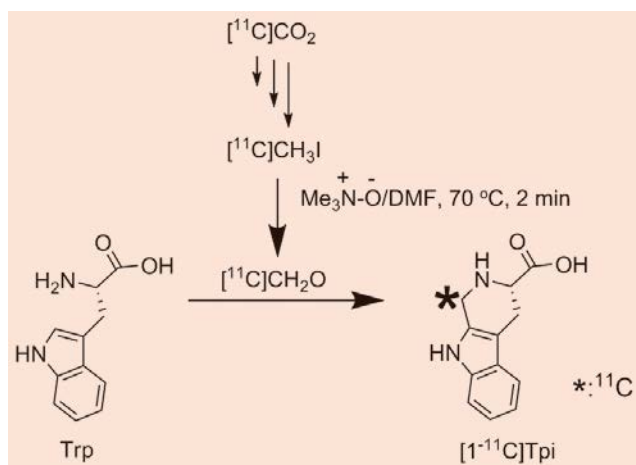


Fig.1 Radiolabeling method via the Pictet-Spengler reaction using $[^{11}\text{C}]\text{CH}_2\text{O}$.

The Pictet-Spengler reaction between $[^{11}\text{C}]\text{CH}_2\text{O}$ and $\text{Trp}\cdot\text{HCl}$ was found to proceed in the absence of an additional acid catalyst when the materials were heated in aqueous DMF. This procedure represents an effective radiolabeling method because it requires particularly mild conditions. The radiolabeling of bioactive oligopeptides containing $\text{Trp}\cdot\text{HCl}$ with $[^{11}\text{C}]\text{CH}_2\text{O}$ via a Pictet-Spengler reaction could therefore be a useful procedure.

Cyclic RGD peptides, such as $\text{cyclo}[\text{Arg-Gly-Asp-D-Tyr-Lys}]$, are potent antagonists for the $\alpha\text{v}\beta_3$ integrin receptor. A variety of different cyclic RGD peptides conjugated to a radioactive tracer have been reported for the PET imaging of tumors that over-express the $\alpha\text{v}\beta_3$ integrin receptor. With this in mind and to establish further potential uses for our new labeling method, we investigated the application of our direct labeling method using $[^{11}\text{C}]\text{CH}_2\text{O}$ to the model cyclic RGD peptide $\text{cyclo}[\text{Arg-Gly-Asp-D-Tyr-Lys}(\text{Trp})]$ hydrochloride (**1**). The reaction of compound **1** with $[^{11}\text{C}]\text{CH}_2\text{O}$ under the conventional manual synthetic procedure proceeded smoothly to give the desired product $\text{cyclo}[\text{Arg-Gly-Asp-D-Tyr-Lys}(1-[^{11}\text{C}]\text{Tpi})]$ ($[^{11}\text{C}]\text{Tpi-RGD}$, Fig.2.) with a radiochemical yield of $22.3\pm 4.3\%$ (not decay-corrected). Interestingly, the guanidino, phenolic hydroxy, carboxylic acid and amide groups of $[^{11}\text{C}]\text{Tpi-RGD}$ remained intact under the reaction conditions. Based on this result, it is therefore clear that this procedure could be particularly effective for the direct formation of cyclic C-C bonds for the radiolabeling of oligopeptides without the need for protecting groups.

Based on the reaction conditions determined in the current study, we proceeded to investigate the remote-controlled radiosynthesis of $[^{11}\text{C}]\text{Tpi-RGD}$ using an automatic production system to generate the $[^{11}\text{C}]\text{CH}_3\text{I}$. The one-pot synthesis of $[^{11}\text{C}]\text{Tpi-RGD}$ from $[^{11}\text{C}]\text{CH}_3\text{I}$ was successfully carried out using an automatic production system. From a starting point in the range of 21.0-22.2 GBq for the $[^{11}\text{C}]\text{CO}_2$, $[^{11}\text{C}]\text{Tpi-RGD}$ was obtained at the end of synthesis in the range of 0.8-1.4 GBq.

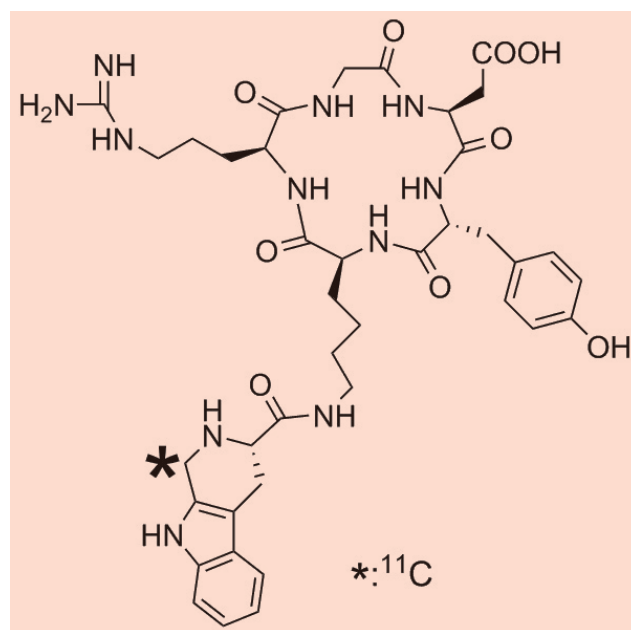


Fig.2 Structure of $\text{cyclo}[\text{Arg-Gly-Asp-D-Tyr-Lys}(1-[^{11}\text{C}]\text{Tpi})]$ ($[^{11}\text{C}]\text{Tpi-RGD}$)

The average time required for the synthesis was found to be 35 min from the end of the bombardment. The identity of $[^{11}\text{C}]\text{Tpi-RGD}$ was confirmed by its co-injection with authentic sample in an analytical HPLC system. The radiochemical purity of $[^{11}\text{C}]\text{Tpi-RGD}$ was found to be greater than 98% and its specific activity was 85.7 ± 9.4 GBq/ μmol .

In conclusion, we have successfully achieved the preparation of $[^{11}\text{C}]\text{Tpi-RGD}$ via a Pictet-Spengler reaction. This labeling reaction was completed under mild reaction conditions over a short reaction time in only one step using the HCl salt of the precursor having Trp on the terminal site, except for the C-terminal side, without the need for a protecting group. In addition, this labeling technique could be used to increase the overall utility of ^{11}C -labeled oligopeptides as PET probes because this method allows for the incorporation of carbon-11 into a cyclic C-C bond. This reaction could be readily applied to an automated radiolabeling platform using commercially available automated synthetic apparatus for $[^{11}\text{C}]\text{CH}_3\text{I}$. The results obtained in the current study can be extended to further studies aimed at the preparation of ^{11}C -labeled oligopeptides.

References

- [1] Henriksen G, Schottelius M, Poethko T, *et al.*: Proof of principle for the use of ^{11}C -labelled peptides in tumour diagnosis with PET, *European J Nucl Med Mol Imaging* 31, 1653-1657, 2004.
- [2] Hooker J. M, Schönberger M, Schieferstein H, *et al.*: Simple, Rapid Method for the Preparation of $[^{11}\text{C}]\text{Formaldehyde}$, *Angew Chem Int Ed* 47, 5989-5992, 2008.
- [3] Hanyu M, Takada Y, Hashimoto H, *et al.*: Carbon-11 radiolabeling of an oligopeptide containing tryptophan hydrochloride via a Pictet-Spengler reaction using carbon-11 formaldehyde, *J Pep Sci* 19, 663-668, 2013.

Highlight

Multimodal functional imaging of nigral dopaminergic neurons with PET and MRI

Hiroshi Kawaguchi

E-mail: kwgc@nirs.go.jp

Introduction

Positron emission tomography (PET) and magnetic resonance imaging (MRI) are useful diagnostic imaging technologies. PET visualizes internal biological processes of the neurotransmission system and cancer cell metabolism using radiotracers. MRI provides detailed anatomical structure of tissue with high spatial resolution (~ 1 mm in a clinical scanner) and great soft tissue contrast. In addition, MRI visualizes physiological information such as tissue microstructure via water molecule diffusion, local blood oxygenation change and accumulation of specific molecules that change magnetic properties of tissue. Because PET and MRI provide complementary information, the integrated analysis of metrics from these modalities will provide new interpretations on pathophysiology of diseases and improve diagnoses.

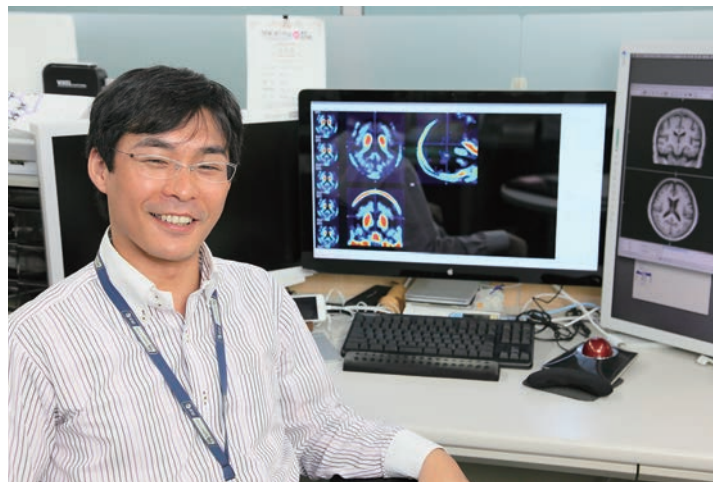
The central dopaminergic system is of great interest to investigate the pathophysiology of neurological diseases such as Parkinson's disease. The dopaminergic neurons are mainly located in the substantia nigra (SN) in the midbrain. Nigral dopaminergic neurons contain neuromelanin (NM) pigment that is synthesized from excess dopamine in cytosomes and stored in lysosome-like organelles with iron. The amount of iron is related to T1-shortening strength in MRI, which enables us to measure the NM concentration related signal [1]. There are also various radiotracers available for PET imaging of the human dopaminergic neuronal system [2]. The specific radiotracer binding to dopamine transporter (DAT) is found in SN. Assuming that DAT controls intracellular and extracellular concentrations of dopamine, the amount of DAT may be related to NM concentration in the SN.

To examine this hypothesis, we performed multimodal imaging with NM MRI and PET with [18 F]FE-PE2I, which selectively binds to the dopamine transporter, to measure dopaminergic neuronal functions in the SN.

Methods

1) Subjects

PET and MR Images were acquired from young healthy subjects (YHS: N=6), aged healthy subjects (AHS: N=6) and aged Parkinson disease patients (APD: N=7).



2) PET and MR images acquisition

A dose of [18 F]FE-PE2I was intravenously injected and sequential PET scans were performed for 90 min with a SET-3000 GCT/X (Shimadzu).

MR scan were performed with the MAGNETOM Verio 3.0T (Siemens). Anatomical T1-weighted images (T1WI) and NM MR images were acquired with a 3D MPRAGE sequence and a 2D fast spin echo sequence, respectively.

3) Image processing

The non-displaceable binding potential to dopamine transporter ($\text{DAT-BP}_{\text{ND}}$) was calculated from dynamic PET data acquired over 90 min with a simplified reference tissue model using the cerebellar gray matter as a reference region. In the NM MR image, the ratio of the pixel intensities in the SN and decussation of the superior cerebellar peduncles (R_{NM}) was calculated to assess NM content. The shape of each subject was normalized to a stereotactic template for each of the two age-matched healthy subject groups. The anatomical normalization of the subjects was performed by the DARTEL tool on SPM8 software package.

Results

Fig.1 shows images of the $\text{DAT-BP}_{\text{ND}}$ and R_{NM} averaged within each subject group around SN [3]. Both $\text{DAT-BP}_{\text{ND}}$ and R_{NM} showed higher intensity in SN than surrounding regions in the midbrain. The R_{NM} values were 1.18 ± 0.03 , 1.20 ± 0.02 and 1.17 ± 0.03 for YHS, AHS and APD, respectively. Similarly, the $\text{DAT-BP}_{\text{ND}}$ values in SN were 0.64 ± 0.06 , 0.44 ± 0.16 and 1.29 ± 0.04 for YHS, AHS and APD, respectively. Fig.2 is a scatter plot of $\text{DAT-BP}_{\text{ND}}$ versus R_{NM} [3]. Negative correlations between $\text{DAT-BP}_{\text{ND}}$ and R_{NM} were found (-0.11, -0.26 and -0.53 for YHS, AHS and APD, respectively), but the results were not statistically significant.

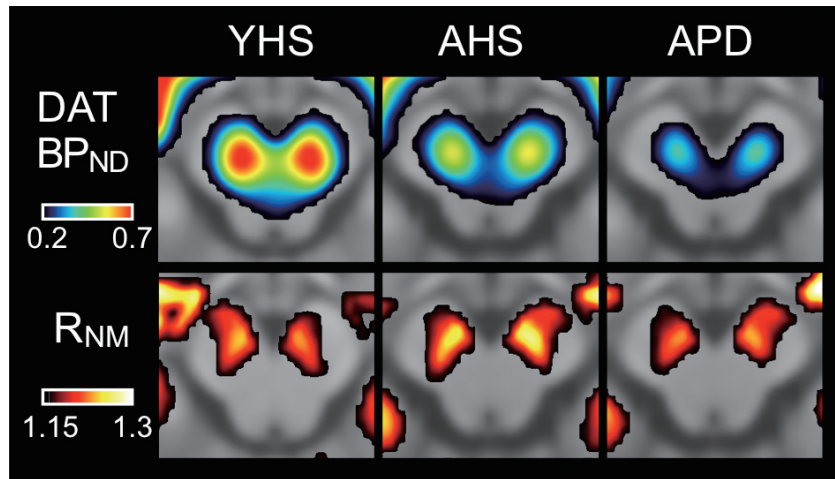


Fig.1 Image of the average DAT-BP_{ND} and R_{NM} for young healthy subjects (YHS), aged healthy subjects (AHS) and aged Parkinson's disease patients (APD). DAT-BP_{ND} and R_{NM} were superimposed on the averaged T1-weighted image [3].

Discussions

The age-related decrease of DAT-BP_{ND} and increase of R_{NM} were observed in healthy subject groups. Previous studies with post-mortem human samples showed normal aging leads to the increase of NM pigment and the decrease of DAT immunoreactive neurons in SN. These indicate an increase in NM accumulation and a loss of the DA neurons in SN with aging, which suggest that the aging effect should be considered when using these metrics in research analyses and diagnoses.

The DAT-BP_{ND} and R_{NM} of APD were lower than those of AHS, which indicates the loss of dopaminergic neurons in SN, behavior that is well known in the pathophysiology of Parkinson's disease. On one hand, there was an overlap for the APD and AHS when using either metric alone. On the other hand, there was a clear border for the two groups in the scatter plot of DAT-BP_{ND} and R_{NM}, which indicates the multimodal imaging produces more accurate measurements for the diagnosis of Parkinson's disease.

In the present study, small negative correlations were observed between DAT-BP_{ND} and R_{NM} for all subject groups but these were not statistically significant. In SN, DATs are located in neuronal dendrites and in the places where they were specifically transported. These localizations suggest that DAT modulates the intracellular and extracellular dopamine levels of nigral neurons. The NM apparently is synthesized by accumulation of cytosolic dopamine and DOPA, the precursor of dopamine, derivatives formed in the cytosol. The higher NM accumulation would be caused by the smaller DAT expression in SN neurons, which would be a reason for the small negative correlation between DAT-BP_{ND} and R_{NM}. The other possible factor concerned with NM accumulation would be the amount of vesicular monoamine transporter 2 (VMAT2) in a DA neuron. VMAT2 transports dopamine from cellular cytosol into synaptic vesicles. If VMAT2 is expressed highly, there would be less NM accumulating in neurons because the excess dopamine produces NM. A postmortem brain study in the literature has shown that there was an inverse relationship between VMAT2 immunostaining intensity and neuromelanin pigment in the SN.

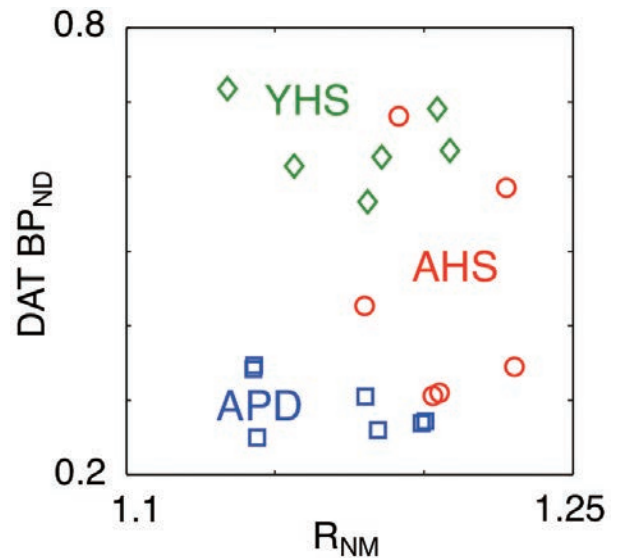


Fig.2 Relationship between DAT-BP_{ND} and R_{NM} [3].

In conclusion, our results suggest 1) the aging effect should be considered when using DAT-BP_{ND} and R_{NM}, 2) the multimodal imaging produces more accurate measurements for the diagnosis of Parkinson's disease, and 3) the R_{NM} provides information about the dopaminergic neuronal function in the SN that is supplementary to DAT-PET.

References

- [1] Sasaki M, Shibata E, Tohyama K, *et al.*: Neuromelanin magnetic resonance imaging of locus ceruleus and substantia nigra in Parkinson's disease, *Neuroreport* 17, 1215-1218, 2006.
- [2] Ito H, Takahashi H, Arakawa R, *et al.*: Normal database of dopaminergic neurotransmission system in human brain measured by positron emission tomography, *NeuroImage* 39, 555-565, 2008.
- [3] Kawaguchi H, Shimada H, Suzuki M, *et al.*: Relationship between neuromelanin-weighted MRI contrast and PET radiotracer binding to dopamine transporter in substantia nigra, *Proc ISMRM* 22, 1916, 2014.

Highlight

Development of the X'tal cube PET detector: the use of scintillator plates

Naoko Inadama

E-mail: inadma@nirs.go.jp

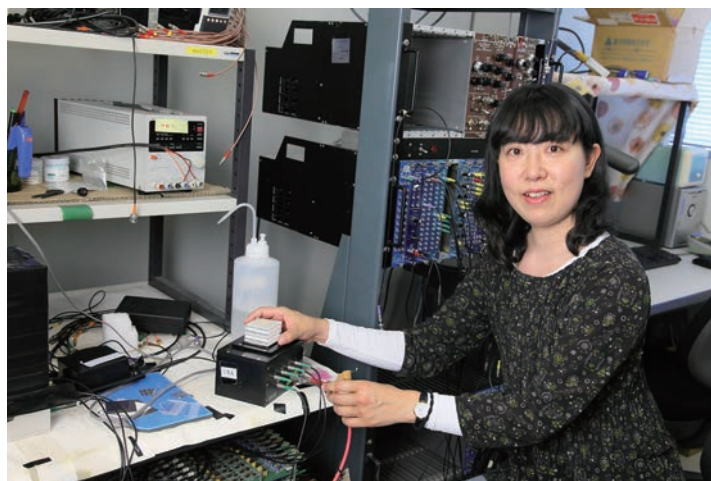
Introduction

X'tal (crystal) cube is the PET detector which has been developed by our team for the purpose of achieving high detector spatial resolution in all three dimensions while maintaining high sensitivity. Last year, we reported that we could resolve 1 mm difference of the radiation detected position in the X'tal cube by using a monolithic scintillator fabricated by laser processing. As the next stage, considering mass production, we newly proposed to use plate scintillators, which should contribute to easier construction of the X'tal cube and showed that an X'tal cube composed of the plate scintillators could have 2 mm detector spatial resolution [1]. In this study, we aimed for higher spatial resolution of 1 mm and measured performance of a prototype X'tal cube.

Structure of the prototype X'tal cube

Fig. 1(a) illustrates the structure of an X'tal cube. It is composed of a scintillation crystal block and 4×4 multi-pixel photon counters (MPPCs) on each crystal block surface. The MPPC is a photo-detector and is thin and small enough not to interfere in radiation detection even if it is coupled on the surface of the radiation entrance. The crystal block is segmented 3-dimensionally into small cubes whose size determines detector resolution. Unlike a general PET detector, there is no reflector between the segments so that scintillation light originating in a radiation detected segment spreads to all six surfaces and is detected by all MPPCs. Segment identification is then performed by a 3D position histogram in which the response corresponding to each crystal segment is made as a result of a simple Anger-type calculation with all the MPPC signals.

For scintillator, we used $\text{Lu}_{2(1-x)}\text{Y}_{2x}\text{SiO}_5$ (LYSO, $x = 0.1$, Crystal Photonics Inc.; USA). While all 3D segmentation in the crystal block was processed by laser previously, in the prototype X'tal cube, the crystal block was composed of the stack of LYSO scintillator plates segmented into the 2D array by laser processing (Fig. 1(a)). The surface of the LYSO plates was mechanically polished; this was a requirement for the laser processing. The LYSO plates were $18 \text{ mm} \times 18 \text{ mm}$ square and 1.0 mm thick and segmented into an 18×18 array of $1.0 \text{ mm} \times 1.0 \text{ mm}$ in the x and y directions. We stacked 18 of the LYSO plates in the z direction for



the crystal block. Between the plates, air gaps remained.

The MPPCs we used were model S10931-050P (Hamamatsu Photonics K.K., Japan; 3600 micro-pixels of $50 \mu\text{m} \times 50 \mu\text{m}$ size, 61.5 % fill factor; $3.0 \text{ mm} \times 3.0 \text{ mm}$ active area). They were coupled onto each crystal block surface with RTV rubber (KE420, Shin-Etsu Chemical Co., Ltd., Japan; 1.45 refractive index). The area between the MPPC active area was covered with reflector so as not to lose scintillation light. As the reflector, we used multilayer

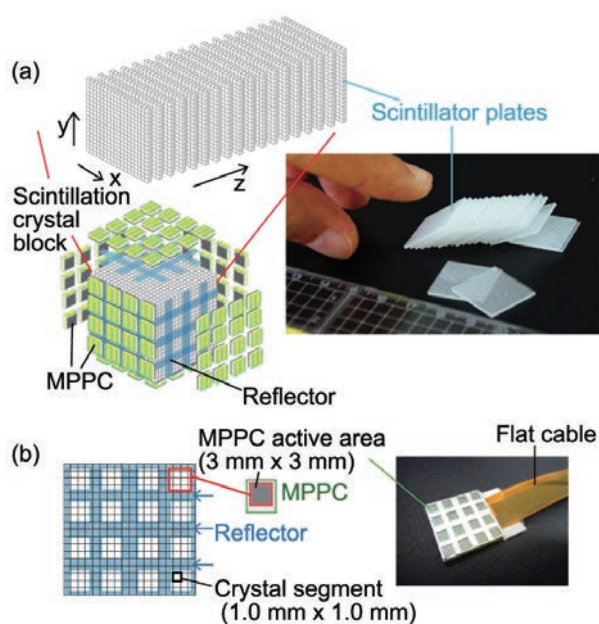


Fig. 1 (a) Structure of an X'tal cube. The crystal block for the prototype X'tal cube was composed of scintillator plates. (b) Location of MPPC active area on the crystal segment array.

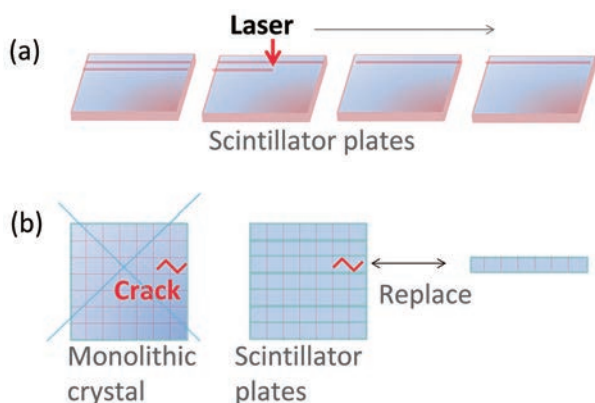


Fig.2 Advantages of using the scintillator plates: (a) in laser processing and (b) repair of the crystal block.

polymer mirrors (Sumitomo 3M, Ltd., Japan; 98% reflectivity, 0.065 mm thickness). The location of the 4×4 MPPC active areas on 18×18 crystal segments is indicated in Fig.1(b).

An advantage of using the scintillator plates is easier processing compared to a thick monolithic scintillation crystal because focusing the laser to an intended point is difficult deep into the scintillator. Additionally, we can process many scintillator plates at a time as shown in Fig.2(a). And in case a crystal block gets cracked, we can replace part of the crystal block using scintillator plates (Fig.2(b)).

Performance of the prototype X'tal cube

Fig.3(a) shows the 3D position histogram of the prototype X'tal cube obtained by uniform irradiation of gamma-rays from ^{22}Na point source. Response alignment is straight and that is advantageous in the process of segment identification such as creating look-up-tables. The scintillator parts where the response distribution is shrunk correspond to the plates covered with the reflector on their side faces (Fig.1(b)). Figs.3(b) and (c) are 2D position histograms extracted from the 3D position histogram at the expanded and shrunk parts, respectively. Outer responses of Fig.3 (c) are overlapped. However, because the overlap should be caused by the reflector, we expect that the use of array-type MPPCs which have little dead space between active areas will solve this problem.

Fig.4 shows energy performance of the crystal segments #1 to #4. #1 was located on a MPPC active area and #3 was covered with reflector. #2 and #4 were placed on the inner part of the segment lines of #1 and #3, respectively. Light outputs and energy resolutions are indicated with blue and pink characters, respectively. Light outputs are expressed as relative values to the output of the #1. #1 showed better performance. Despite inferior segment identification performance of #3 (Fig.3(c)), it showed comparable energy performance with #2 and #4. And although #4 was located far from the MPPCs, it showed similar light output to the other three segments.

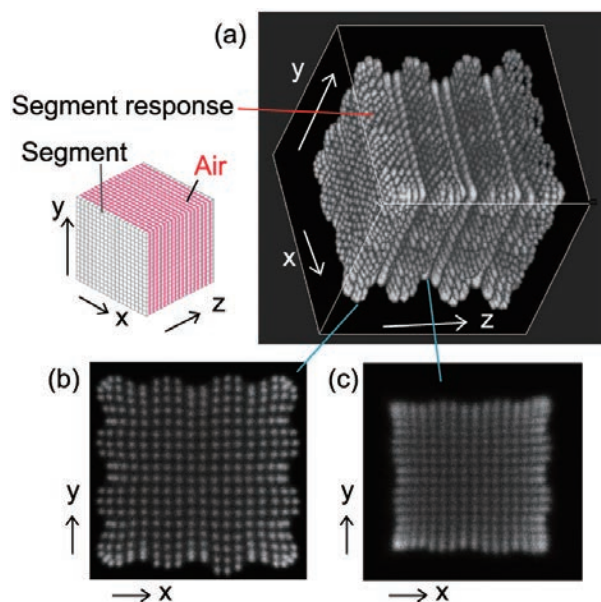


Fig.3 (a) 3D position histogram of the prototype X'tal cube. (b) 2D position histograms extracted from (a) at the expanded and (c) shrunk parts.

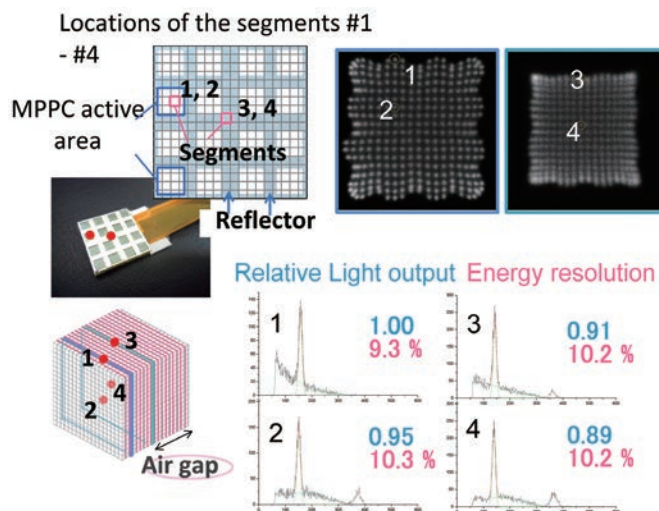


Fig.4 Pulse height distribution of the summed signals of all MPPCs for outer and center segments in the plate crystal block.

Conclusion

We examined the use of scintillator plates for the X'tal cube when the crystal segments become small cubes such as $1.0 \text{ mm} \times 1.0 \text{ mm} \times 1.0 \text{ mm}$. While the X'tal cube with the monolithic crystal block having 3D laser processing achieved segment identification of that size, the use of the scintillator plates caused degradation in segment identification at some outer parts (Fig.3). Energy resolution was around 10% independent of segment location and conditions: outer or inner part and direct or indirect coupling to MPPCs.

References

- [1] Inadama N, Moriya T, Hirano Y, *et al.*: X'tal Cube PET Detector Composed of a Stack of Scintillator Plates Segmented by Laser Processing, *IEEE Trans Nucl Sci* 61(1), 53-59, February 2014.

Highlight

Development of positron emission tomography probe for imaging CD147 expression in tumors

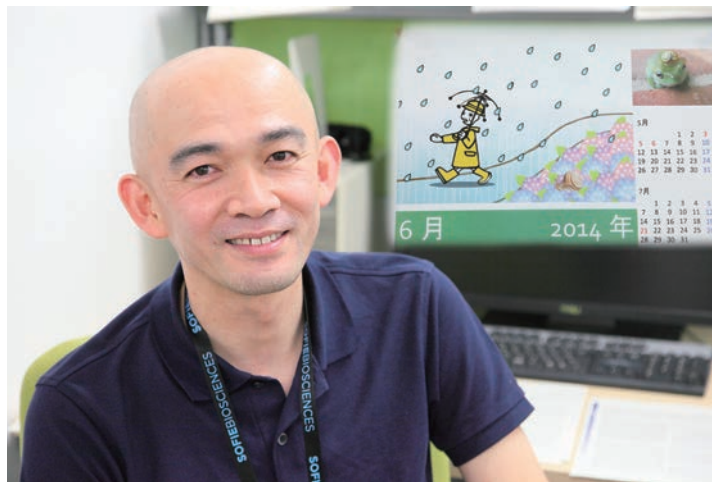
Atsushi Tsuji

E-mail: a_tsuji@nirs.go.jp

We have developed several antibody-based imaging probes for targeting tumors. Here, we focus on the radiolabeled anti-CD147 antibody 059-053 as a positron emission tomography (PET) probe in a pancreatic cancer model. We assessed its *in vitro* and *in vivo* properties in an article published in *PLoS One* in 2013 [1].

Pancreatic cancer is a commonly diagnosed cancer and the eighth leading cause of cancer deaths worldwide, accounting for 278,684 of the estimated new cancer cases and 266,669 of the estimated cancer deaths annually (GLOBOCAN 2008, <http://globocan.iarc.fr/>). Pancreatic cancer patients present only minor symptoms at a medical evaluation, and the silent nature of this disease that nothing is apparent until late in the disease progression contributes to a very poor prognosis. Only 7% of patients present with localized, potentially curable tumors at diagnosis and approximately 50% of pancreatic cancer patients are diagnosed at advanced stages of the disease. The overall 5-year survival rate among patients with pancreatic cancer is 6% in the United States. Therefore, additional effective anticancer therapy is required to augment and/or complement the present treatment strategies such as surgery and chemo/radiotherapy, especially for patients with metastatic cancer.

CD147 is a 55-kDa transmembrane protein of the immunoglobulin superfamily and expresses in many types of tumors including pancreatic cancer. CD147 induces expression of matrix metalloproteinases, such as MMP-1, MMP-2, MMP-9, MT1-MMP, and vascular endothelial growth factor. Overexpression of CD147 in breast cancer cells by expression vector transfection results in increased tumor growth and metastasis. These findings suggest that CD147 is involved in invasion, metastasis, angiogenesis and tumor proliferation, and therefore is a good candidate for targeted cancer therapy. Depletion of CD147 by RNA interference or specific antibody reduces the proliferation, invasion, metastasis of tumors and blood vessel formation, and therefore clinical trials of CD147-targeted therapy have been conducted. Although the incidence of CD147 expression is high (87%) in pancreatic cancer, some tumors do not express CD147 and thus are not suitable candidates for CD147-targeted therapy. It is therefore important to use a noninvasive imaging method to evaluate the CD147 status in an individual tumor at the time of treatment planning to select



appropriate patients for CD147-targeted therapy.

We recently isolated a novel fully human monoclonal IgG1 antibody designated as 059-053 against CD147 from a large-scale human antibody library constructed using a phage-display system that incorporated a highly efficient screening method termed isolation of antigen-antibody complexes through organic solvent, with living pancreatic cancer cells [2]. This antibody induces antibody-dependent cell-mediated cytotoxicity and inhibits cell proliferation of pancreatic cancer cells. We therefore radiolabeled 059-053, and evaluated the *in vitro* and *in vivo* properties as a new PET probe for imaging CD147-expressing tumors in a pancreatic cancer model.

First, we evaluated CD147 protein expression of four pancreatic cancer cell lines (MIA PaCa-2, PANC-1, BxPC-3, and AsPC-1) by western blotting and immunofluorescence staining to select a suitable cell line to assess radiolabeled 059-053. The MIA PaCa-2 cell line showed the highest expression as determined by western blotting and immunofluorescence staining analysis. In addition, we confirmed that MIA PaCa-2 cells formed subcutaneous and orthotopic tumors in nude mice and high CD147 expression in these tumors was determined by immunohistochemical staining. A4 cells showed no CD147 protein expression either *in vitro* or *in vivo*. We therefore chose MIA PaCa-2 cells as a positive control and A4 cells as a negative control for the following evaluation.

Next, we radiolabeled 059-053 with ^{125}I , ^{67}Ga , or ^{89}Zr and evaluated *in vitro* properties. Cell binding and competitive inhibition assays revealed that 059-053 bound specifically to MIA PaCa-2 cells with high affinity, but not to A4 cells. The immunoreactive fraction of radiolabeled antibodies was more than 0.8, indicating that the loss of immunoreactivity by radiolabeling procedures was minimal. The internalization assay showed that protein-bound fractions in culture medium rapidly increased after incubation at

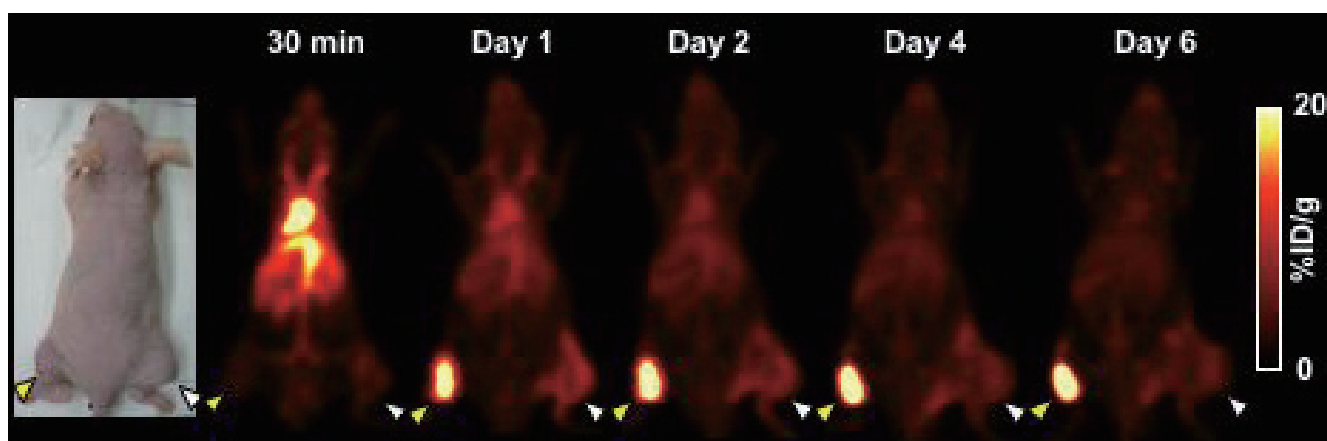


Fig.1 Serial PET images (maximum-intensity-projection) of a nude mouse bearing MIA PaCa-2 (yellow arrowhead) and A4 (white arrowhead) xenografted tumors at 30 min, and days 1, 2, 4, and 6 after intravenous injection of 3.7 MBq [^{89}Zr]059-053. (From the reference [1])

37°C, and the internalized fraction was low. This suggests that CD 147-antibody complex is easily detached from the plasma membrane under the conditions/procedures of this internalization experiment. In this study, although we employed ^{67}Ga in place of ^{89}Zr for the internalization assay, this result is thought to be consistent with that using ^{89}Zr -labeled antibody because desferrioxamine, used as a chelate in this study, forms complexes with both these radiometals, and their desferrioxamine complexes are known to be stable *in vitro* and *in vivo*, and the *in vivo* distribution has been reported to be similar between ^{67}Ga - and ^{89}Zr -labeled antibodies. In contrast to the results of internalization assay, the *in vivo* distribution studies demonstrated that uptake of [^{89}Zr]059-053 in MIA PaCa-2 tumors was very high and increased with time, suggesting that the CD147-antibody complex did not detach from the membrane *in vivo*. Furthermore, the difference in tumor uptake patterns between [^{89}Zr]059-053 and [^{125}I]059-053 strongly suggests that radiolabeled 059-053 was internalized in cells after binding to CD147 on the cell surface *in vivo*. Taken together, trypsinization of cells probably caused the results we observed in the internalization assay, even though the duration of trypsinization was made as short as possible to minimize damage to CD147 on the cell surface by trypsin. *In vivo* distribution and serial PET studies demonstrated that [^{89}Zr]059-053 highly accumulated in MIA PaCa-2 tumors, but not in A4 tumors (Fig.1). This suggests that [^{89}Zr]059-053 is a promising PET probe for the detection of CD147-expressing tumors and in the selection of appropriate patients for anti-CD147 therapy. However, because our anti-CD147 antibody 059-053 does not bind to mouse CD147, our results in the murine model may not fully predict the distribution in human patients. CD147 expression is reported to be high in most cancer tissues, but it is limited in normal tissues. Scintigraphy with ^{131}I -labeled anti-CD147 F(ab')₂ in patients with hepatocellular carcinoma has shown lower uptake in normal organs than in hepatocellular carcinoma tissues. Therefore, the anti-CD147 antibody 059-053 is expected to show low accumulation in normal organs of patients, although further clinical study will be necessary to precisely evaluate normal organ uptake.

Subcutaneous tumor models are powerful tools for oncological investigations, but these models cannot always mimic clinical

findings. For example, the tumor microenvironment influences cell migration such that orthotopic xenografts give rise to a higher incidence of metastatic lesions than do subcutaneous xenografts. We conducted PET/CT imaging in the orthotopic pancreatic tumor mouse model and demonstrated that [^{89}Zr]059-053 visualized orthotopically implanted tumors. Thus, [^{89}Zr]059-053 could be useful for studies investigating CD147-targeted therapy efficacy or the metastatic process in orthotopic pancreatic cancer models.

CD147 highly expresses not only in pancreatic cancer but also in many other types of cancers, such as glioma, ovarian cancer, renal cell carcinomas, bladder carcinoma, and hepatocellular carcinoma. Moreover, its increased expression is associated with poor prognosis in several cancers, such as breast, cervical, liver, colorectal, and bladder cancers, and it is considered to be caused by increased metastatic rates and treatment resistance. In the present study, we showed that [^{89}Zr]059-053 uptake in major organs was low. Taken together, [^{89}Zr]059-053 could detect CD 147-expressing tumors not only in the pancreas but also in other organs, and it could be used to assess the metastatic potential and treatment resistance of these tumors, although further studies will be necessary to prove these potential uses.

In conclusion, we radiolabeled a fully human anti-CD147 monoclonal antibody 059-053 and evaluated its *in vitro* and *in vivo* properties for use as a new CD147-targeted PET imaging probe in a model of pancreatic cancer. [^{89}Zr]059-053 highly accumulated in CD147-expressing tumors and clearly visualized subcutaneously and orthotopically implanted xenografts. PET with [^{89}Zr]059-053 is a promising noninvasive imaging method to provide useful information for the selection of appropriate cancer patients who could gain benefits from CD147-targeted therapy, although further clinical studies are necessary.

References

- [1] Sugyo A, Tsuji AB, Sudo H, *et al.*: Evaluation of ^{89}Zr -labeled Human Anti-CD147 Monoclonal Antibody as a Positron Emission Tomography Probe in a Mouse Model of Pancreatic Cancer, *PLoS One* 8, e61230, 2013.
- [2] Kurosawa G, Akahori Y, Morita M, *et al.*: Comprehensive screening for antigens overexpressed on carcinomas via isolation of human mAbs that may be therapeutic, *Proc Natl Acad Sci USA* 105, 7287-7292, 2008.

Highlight

Fatty acid synthase is a key target in multiple essential tumor functions: [1-¹⁴C]acetate PET to predict the targeted therapy outcome

Yukie Yoshii

E-mail: yukiey@nirs.go.jp

Fatty acid synthase (FASN) is a key enzyme in fatty acid synthesis from acetyl CoA. FASN is over-expressed in several human cancers, including prostate, breast, lung, ovary, bladder, stomach, oral cavity and melanoma, and the over-expression is known to be associated with poor prognosis. In recent years, inhibitors of FASN has been developed and reported to have antitumor activity. Orlistat, a selective inhibitor of FASN, is one of those poised for clinical use, particularly since orlistat is already used as an over-the-counter drug for obesity in the United States and European Union. Thus, FASN-targeted therapy is expected to be effective against FASN-expressing tumors, which show malignant behaviors. However, large variations in FASN expression levels in individual tumors have been observed by pathological studies, and methods to predict FASN-targeted therapy outcome before treatment are required to reduce unnecessary treatment.

Development of the method to predict FASN-targeted therapy outcome

Here, we show the method to predict FASN-targeted therapy outcome using [1-¹⁴C]acetate PET [1-3]. First, we examined relationships between uptake of radiolabeled acetate, FASN expression, and sensitivity to orlistat treatment *in vitro* with human prostate cancer cell lines (LNCaP, PC3, 22Rv1, and DU145) (Fig.1). From the [1-¹⁴C]acetate uptake study, high uptake of [1-¹⁴C]acetate was observed in LNCaP cells, while that in PC3 and 22Rv1 was lower, and that in DU145 was very low (Fig.1A). FASN expression showed a similar trend to that observed in the uptake of [1-¹⁴C]acetate (Fig.1B) and LNCaP cells showed higher FASN expression compared to the other cell lines. There was a strong positive correlation between uptake of [1-¹⁴C]acetate and FASN expression. Fig.1C shows % cell viability after orlistat treatment *in vitro*. Under the low dose orlistat treatment at 12.5 μ M, LNCaP cells, which had shown high uptake of [1-¹⁴C]acetate and FASN expression, showed a significant decrease in % cell viability, but there were no significant decreases in % cell viability in other cell lines. With 25 μ M orlistat treatment, besides LNCaP cells, PC3 and 22Rv1 cells, which had shown relatively low uptake of [1-¹⁴C]acetate and FASN expression, showed a significant decrease in % cell viability, while DU145 cells, which had shown very low up-



take of [1-¹⁴C]acetate and FASN expression, showed no decrease in cell viability. With over 50 μ M orlistat treatment, all cell lines examined showed a significant decrease in % cell viability, but the changes in DU145 cells were moderate. There was a significant negative correlation between % cell viability, and uptake of [1-¹⁴C]acetate and FASN expression, respectively, under low-dose orlistat treatment at 12.5 μ M. Thus, our data demonstrated higher sensitivity to orlistat treatment in the cells with higher FASN expression and uptake of acetate.

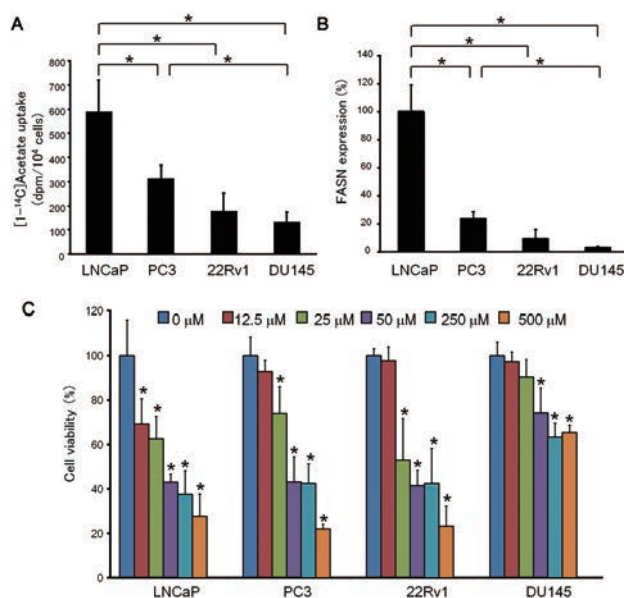


Fig. 1 *In vitro* study on relationships between uptake of radiolabeled acetate, FASN expression, and sensitivity to orlistat treatment

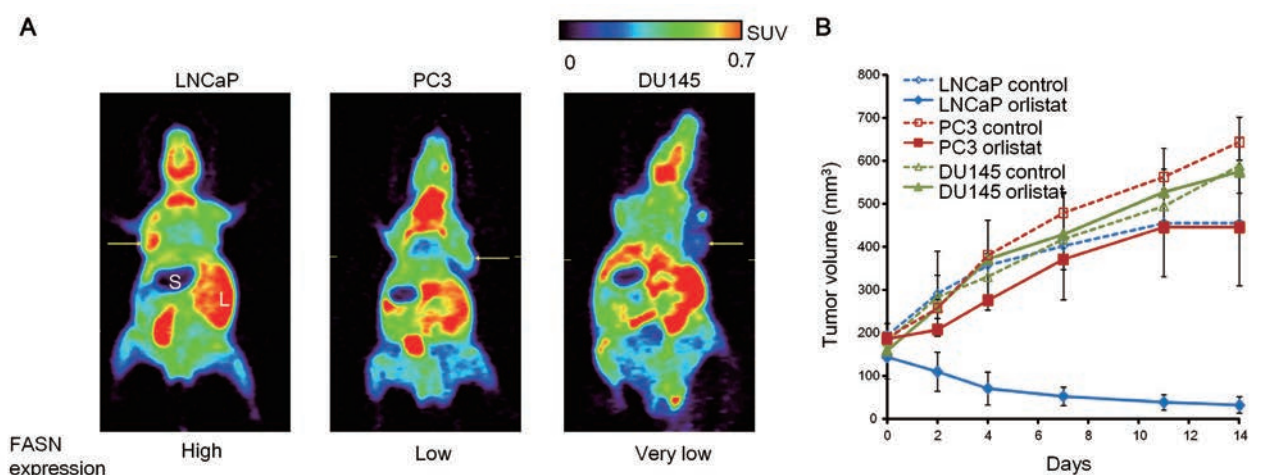


Fig.2 *In vivo* study; [^{14}C]acetate PET and FASN-targeted therapy with orlistat

Next, we conducted an *in vivo* study with mice bearing LNCaP (high FASN expression), PC3 (low FASN expression), or DU145 (very low FASN expression) tumors. To examine absolute uptake of radiolabeled acetate in these xenograft tumors, we performed a biodistribution study. As a result, at 30 min after injection of [^{14}C] acetate, LNCaP tumors (0.27 ± 0.05 %ID/g) showed 2.2-fold higher uptake of [^{14}C]acetate than PC3 tumors (0.13 ± 0.01 %ID/g; $P < 0.01$) and 5.5-fold higher uptake than DU145 tumors (0.06 ± 0.01 %ID/g; $P < 0.001$). Then, a small animal PET study with [^{11}C]acetate was also done. The images demonstrated the same tendency as the biodistribution study; [^{11}C]acetate showed clear tumor accumulation in LNCaP tumors, while moderate or low accumulation of [^{11}C]acetate was observed in PC3 and DU145 tumors (Fig.2A). We further examined sensitivity of FASN-targeted therapy with orlistat in each tumor model *in vivo* (Fig.2B). We observed that tumor volume in LNCaP tumors treated with orlistat had decreased markedly at day 14. In contrast, PC3 and DU145 tumors showed progressive increases in tumor volume even after orlistat treatment. No serious body weight loss and side effects were observed during treatment. Therefore, our *in vivo* data demonstrated that uptake of radiolabeled acetate reflects sensitivity of FASN-targeted therapy with orlistat and that FASN-targeted therapy with orlistat is highly effective against tumors with high FASN expression indicated by high uptake of radiolabeled acetate.

Collectively, our data demonstrated that [^{11}C]acetate PET is a useful tool to predict FASN-targeted therapy outcome.

Mechanisms of FASN-targeted therapy

In addition, how FASN inhibition affects tumor progression still remains unclear. In this study, we therefore examined mechanisms of FASN inhibition to provide the treatment strategy of FASN-targeted therapy [1-2]. First, we established FASN knockdown LNCaP cells by transduction of short-hairpin RNA against FASN and investigated the detailed characteristics by analyses on morphology and cell behavior and microarray-based gene expression profiling (Fig.3). We found that FASN inhibition not only suppressed cell proliferation but also prevented pseudopodia formation and suppressed cell adhesion, migration, and invasion, which are essential for tumor progression. FASN inhibition also suppressed genes involved in production of intracellular second mes-

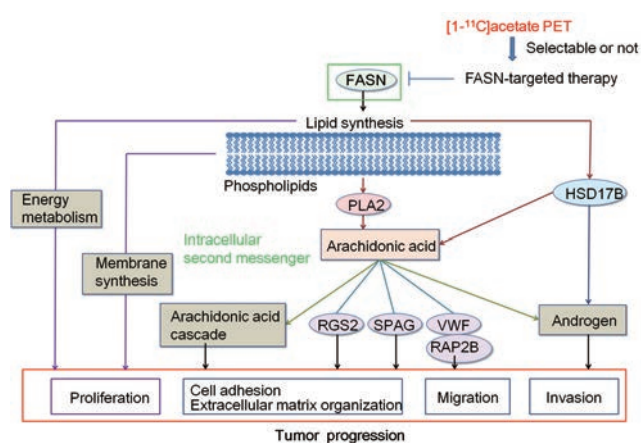


Fig.3 Mechanisms of FASN-targeted therapy

senger arachidonic acid and androgen hormones, both of which have a function to promote tumor progression. This indicates that FASN-targeted therapy could be an effective treatment to suppress multiple tumor essential functions involved in tumor progression and metastasis in prostate cancers.

In summary, our study suggests that [^{11}C]acetate PET could be a powerful tool to accomplish personalized FASN-targeted therapy by non-invasive visualization of tumor acetate uptake and selection of responsive tumors. The FASN-targeted therapy could be an effective treatment strategy to suppress multiple mechanisms related to tumor progression in cancers selected by [^{11}C]acetate PET.

References

- [1] Yoshii Y, Furukawa T, Saga T, *et al.*: Acetate/acetyl-CoA metabolism associated with cancer fatty acid synthesis: overview and application, *Cancer Letters* in press, 2014.
- [2] Yoshii Y, Furukawa T, Oyama N, *et al.*: Fatty Acid synthase is a key target in multiple essential tumor functions of prostate cancer: uptake of radiolabeled acetate as a predictor of the targeted therapy outcome, *PLOS ONE* 8, e64570, 2013.
- [3] Yoshii Y, Waki A, Furukawa T, *et al.*: Tumor uptake of radiolabeled acetate reflects the expression of cytosolic acetyl-CoA synthetase: implications for the mechanism of acetate PET, *Nucl Med Biol* 36, 771-777, 2009.

Highlight

In-vivo visualization of tau pathology in living mouse model and patients with Alzheimer's disease and related neurodegenerative tauopathies

Masahiro Maruyama, Hitoshi Shimada,
Ming-Rong Zhang, Tetsuya Suhara,
and
Makoto Higuchi

E-mail: marum@nirs.go.jp

Background

Intracellular inclusions of pathological tau fibrils are hallmark lesions in Alzheimer's disease (AD) and associated tauopathies, and there has been a growing interest in the mechanistic links between fibrillar tau accumulation and neuronal deterioration. Characteristic symptoms of tauopathies are known to be associated with regional distribution of fibrillary tau lesions. *In-vivo* tau imaging would accordingly facilitate precise clinical diagnosis of tauopathies and objective staging of the disease in living patients on a neuropathological basis. Here, we aimed at developing a positron emission tomographic (PET) imaging agent capable of capturing tau inclusions in patients with AD and non-AD tauopathies.

Methods

1) *In-vitro* screening for candidate tau imaging probes using brain slices of tau transgenic (Tg) mice and human tauopathies

Brain sections were generated from Tg mice for a human tau isoform (T34) with the P301S mutation causative of familial tauopathy (PS19 mice) [1]. We also used slices of the brains provided by University of Pennsylvania. These samples were labeled with fluorescent chemicals potentially reacting with tau aggregates, and their binding to tau lesions was assessed by confocal microscopy. Affinity of these compounds with tau inclusions was further proven by immunohistochemical staining of the same sections by a phosphorylated tau antibody (AT8).

2) *In-vivo* two-photon fluorescence imaging and quantitative PET imaging for tau Tg mice

Fluorescence signals from the intravenously administered candidate tau imaging probe which was selected by the above-mentioned *in-vitro* screening were captured by *in vivo* two-photon laser scanning microscopic imaging of the spinal cord of laminectomized PS19 mice. To demonstrate transfer of the probe from blood vessels into the brain parenchyma, Sulforhodamine 101 (MP Biomedicals), a blood vessel marker, was intraperitoneally administered before intravenous injection of the probe.

PET scans of mice anesthetized by isoflurane were performed using a microPET Focus 220 animal scanner (Siemens Medical



Solutions). The probes radiolabeled with ^{11}C were intravenously injected from the tail vein, and each mouse was scanned for 90 min. Scan data were analyzed using PMOD image analysis software (PMOD Technologies) with reference to an anatomical MRI template. After completion of PET imaging, mice were dissected, and brain sections were stained by FSB (1-fluoro-2,5-bis(3-carboxy-4-hydroxystyryl)benzene), a prototypical chemical compound recognizing fibrillar tau inclusions. A ^{11}C -labeled probe conceived to be the most suitable for *in vivo* PET imaging was then applied to the following clinical assays.

3) Clinical human PET imaging

A clinical study was approved by the Ethics and Radiation Safety Committees, NIRS. Written informed consent was obtained from the subjects or their family members. PET scans were conducted with a Siemens ECAT EXACT HR+ scanner (CTI PET Systems). Individual MRI data were coregistered to the PET images using PMOD software (PMOD Technologies). Volumes of interest were drawn on the coregistered MR images and were transferred to the PET images. To analyze the distribution of amyloid and tau lesions, PET scans with ^{11}C -labeled tau probe and an amyloid radioprobe, [^{11}C]Pittsburgh Compound-B ([^{11}C]PIB) were conducted for the same individuals, including patients with AD and non-AD tauopathies and age-matched nondemented controls.

Results and Discussion

1) Generation of new ligands for diverse tau inclusions in a mouse model and human tauopathies

We screened an array of fluorescent chemicals for candidate tau imaging agents by microscopically assaying their reactivities with tau inclusions on brain slices from PS19 mice and patients with AD and diverse other tauopathies. Chemical properties of the

name	AD		Pick disease		PS19 mouse	
	compound	Phospho-tau IHC	compound	Phospho-tau IHC	compound	Phospho-tau IHC
PBB1						
PBB2						
PBB3						
PBB4						
PBB5						

Fig.1 Binding of a new series of tau probes (PBBs) to tau lesions of model mouse and human tauopathies.

PBB: phenyl/pyridinyl-butadienyl-benzothiazoles/benzothiazoliums
IHC: Immunohistochemical stain

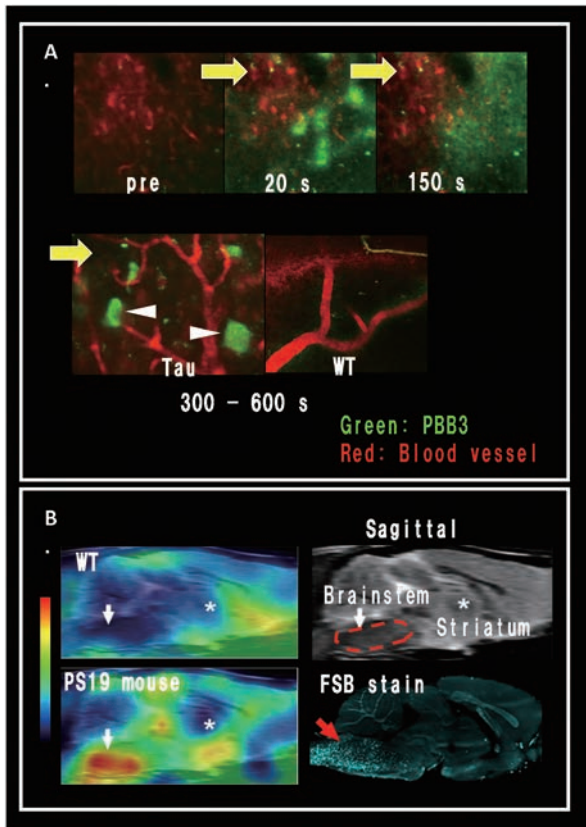


Fig.2 A. Real-time microscopical PBB3 fluorescence imaging of tau lesions. B. Pre-clinical assessment of $[^{11}\text{C}]\text{-PBB3}$ PET imaging. FSB: 1-Fluoro-2,5-bis(3-carboxy-4-hydroxystyryl)benzene

compounds, including structural dimensions and hydrophilicities, were found to be correlated with affinity and selectivity for tau inclusions in a wide range of tauopathies. Based on this observation, we developed a new class of fluorescent tau ligands, phenyl/pyridinyl-butadienyl-benzothiazoles/benzothiazoliums (PBBs), for multimodal optical and PET visualization of diverse tau inclusions in brains of living patients including AD and mice modeling these disorders (Fig. 1) [2].

2) *In-vivo* two-photon laser scanning fluorescence microscopy and microPET imaging of model mice for characterization of tau probes

Fluorescence signals of a pyridinated PBB, PBB3, which was injected from the tail vein were rapidly penetrated into the brain as

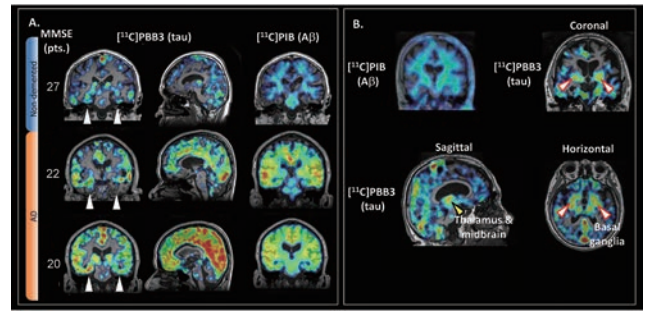


Fig.3 A. PBB3 accumulation corresponding with disease severity in AD. B. PIB and PBB3 image of a case of corticobasal syndrome.

MMSE : Mini-Mental State Examination PIB : Pittsburgh Compound-B

assessed by real-time *in-vivo* two-photon laser scanning microscopy. Labeling of putative intraneuronal tau inclusions (arrowhead: Fig.2-A) was found in PS19 mice at 3-5 min after intravenous PBB3 injection but not in wild-type mice.

PET imaging of PS19 mice demonstrated increased retention of $[^{11}\text{C}]\text{PBB3}$ in the brainstem of PS19 mice enriched with abundant tau lesions, which was postmortally confirmed by FSB staining, in contrast to low-level radioactivity in the same region of wild-type mice (arrowhead: Fig.2-B). The target to reference contrast of $[^{11}\text{C}]\text{PBB3}$ was the highest among the radiolabeled PBBs examined in this study.

3) Detection of tau pathologies in living patients with AD and non-AD tauopathy by $[^{11}\text{C}]\text{PBB3-PET}$

We then applied $[^{11}\text{C}]\text{PBB3}$ to a clinical PET study, and found intense PBB3 signals retained in the medial temporal region of AD subjects but not elderly controls. By contrast, $[^{11}\text{C}]\text{PIB}$ produced minimal binding to this area relative to other neocortical regions [3], supporting the selectivity of $[^{11}\text{C}]\text{PBB3}$ for tau aggregates versus amyloid. In addition, distribution of $[^{11}\text{C}]\text{PBB3}$ binding spread from the hippocampal formation to the entire limbic system and subsequently to the extensive neocortical areas in transition from normal aging to advanced AD (arrowhead: Fig.3-A), indicating the utility of $[^{11}\text{C}]\text{PBB3-PET}$ data as an objective measure of the disease progression. Furthermore, increased $[^{11}\text{C}]\text{PBB3}$ signals were found in a corticobasal syndrome patient who was negative for $[^{11}\text{C}]\text{PIB-PET}$. Moreover, the area showing intense PBB3 signals corresponded to the putative focus of the clinical symptoms (arrowhead: Fig.3-B).

While ^{11}C -labeled ligands are advantageous for performing tau and amyloid PET scans in a single day and for reducing radioactive exposure, ^{18}F -labeled PBB3 derivatives are also being developed to ensure wider availability. *In-vivo* visualization of tau lesions would thus serve pre-clinical and clinical needs for diagnostic and therapeutic assessments of tauopathies, leading to further investigation of the molecular etiology of these neurodegenerative disorders.

References

- [1] Yoshiyama Y, Higuchi M, Zhang B, *et al.*: Synapse loss and microglial activation precede tangles in a P301S tauopathy mouse model. *Neuron* 53, 337-351, 2007.
- [2] Maruyama M, Shimada H, Suhara T, *et al.*: Imaging of tau pathology in a tauopathy mouse model and in Alzheimer patients compared to normal controls. *Neuron* 79, 1094-108, 2013.
- [3] Braak H, Braak E :Neuropathological staging of Alzheimer-related changes, *Acta Neuropathol* 82, 239-259, 1991.

Highlight

Antidepressants and norepinephrine transporter in the brain: Clinical positron emission tomography studies using (S,S)-[¹⁸F]FMeNER-D₂

Harumasa Takano

E-mail: suhara@nirs.go.jp (contact person)

Introduction

Depression is one of the most common psychiatric disorders, and its lifetime prevalence is estimated to be around 10%. It has also been reported as one of the most burdensome diseases worldwide. Antidepressants have been developed since the 1960's; central monoamines, including dopamine, serotonin, and norepinephrine, are closely involved in the pathophysiology of depression and most antidepressants demonstrate their efficacy through these systems. Norepinephrine (NE) plays crucial roles in various cognitive functions such as arousal, attention, emotion, and motivation. The norepinephrine transporter (NET) is one of the major targets of some antidepressants such as certain tricyclic antidepressants (TCAs) and serotonin and norepinephrine reuptake inhibitors (SNRIs). The NET selective drug atomoxetine is used to treat attention-deficit hyperactivity disorder (ADHD).

Development of (S,S)-[¹⁸F]FMeNER-D₂

Although PET probes to evaluate the serotonin transporter (5-HTT) and the dopamine transporter (DAT) have been developed since the late 1990's, the development of NET-specific probes was delayed because of the lack of suitable probes. In the mid 2000s, a highly selective NET probe, (S,S)-[¹⁸F]FMeNER-D₂ (Fig. 1), an analog of reboxetine, was developed at the Karolinska Institute in Sweden. We have developed a less invasive method for the quantification of NET binding in the brain [1] and utilized it in a variety of clinical studies (Fig. 2).

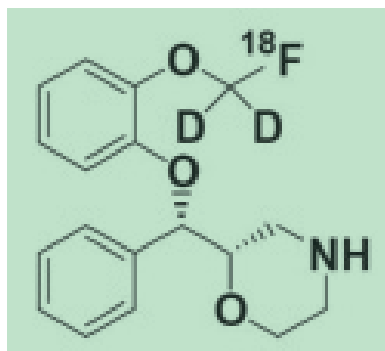


Fig. 1 Structure of (S,S)-[¹⁸F]FMeNER-D₂

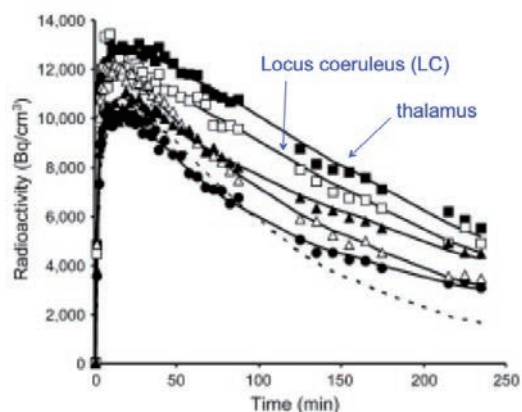


Fig. 2 Time activity curves of (S,S)-[¹⁸F]FMeNER-D₂ in brain regions

NET occupancy of antidepressants

Central drug occupancy indicates how drugs act on the target site in the brain, and it is obtained using the following formula:

$$\text{Occupancy (\%)} = 100 \times (\text{BP}_{\text{reference}} - \text{BP}_{\text{drug}}) / \text{BP}_{\text{reference}}$$

where $\text{BP}_{\text{reference}}$ is the binding potential (BP) of the reference (mean for healthy volunteers or baseline) and BP_{drug} is the BP of the patients with drug treatment (or BP of subjects after drug challenge).

NET occupancy by nortriptyline

Nortriptyline is a NET-selective TCA that has been widely used for the treatment of depression. Previous PET studies have demonstrated that serotonin transporter occupancy of over 80% is needed for the clinical efficacy of SSRIs [2, 3]; however, there have been no reports of NET occupancy in patients treated with NET-selective antidepressants. After we confirmed the dose-dependent NET occupancy in the thalamus of healthy subjects following a single dose of nortriptyline using PET and (S,S)-[¹⁸F]FMeNER-D₂ [4], we investigated NET occupancy in patients with depression who were taking various repeated doses of nortriptyline [5]. Reference data for the calculation of occupancy was obtained from age-matched healthy controls (Fig. 3). The result demonstrated approximately 50-70% NET occupancy resulting from the administration of 75-200 mg/day of nortriptyline. The estimated effective dose (ED_{50}) and concentration (EC_{50}) required to induce 50% occupancy was 65.9 mg/day and 79.8 ng/mL, respectively. Since the minimum therapeutic level of plasma nortriptyline for the treatment of depression is 70 ng/mL [6], our data show that this plasma nortriptyline level corresponds to approximately 50% NET occupancy measured using PET. This suggests that the central NET occupancy of more than 50% would be appropriate for nortriptyline treatment in patients with depression (Fig. 4).

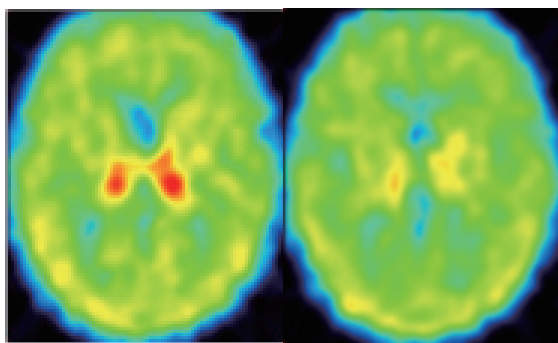


Fig.3 Summated transverse images of (S,S)-[¹⁸F]FMeNER-D₂ at the level of the thalamus for a subject at baseline (left) and after nortriptyline administration (right)

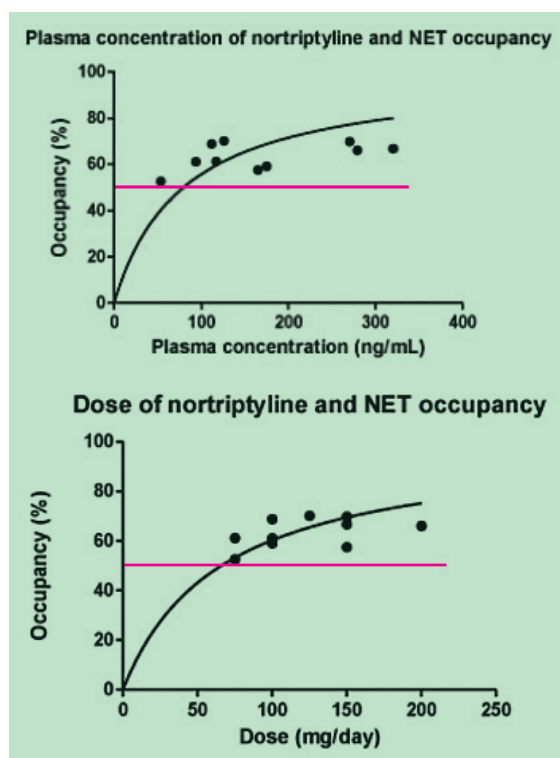


Fig.4 Estimated central NET occupancy for daily dose (top) and plasma levels of nortriptyline (bottom) in patients with depression

NET and 5-HTT occupancy by milnacipran

Similarly, we estimated both NET and 5-HTT occupancies in the brain using (S,S)-[¹⁸F]FMeNER-D₂ and [¹¹C]DASB, respectively, in patients with depression taking various doses of milnacipran, an SNRI [7]. As Fig.5 illustrates, the occupancy of both NET and 5-HTT was approximately 40% for milnacipran at 100 mg/day, the dose most commonly administered to patients with depression. Considering the reported minimum therapeutic occupancy for NET and 5-HTT, the results for milnacipran were low for both transporters. Taken together with reports that the clinical efficacy of milnacipran is improved with higher doses (150-300 mg/day), the clinical dose prescribed for milnacipran might currently be too low, although we cannot exclude the possibility of an interaction between NET and 5-HTT.

Future Directions and Conclusion

Thus far, there have been no reports on NET binding in patients with depression before the initiation of treatment, and this informa-

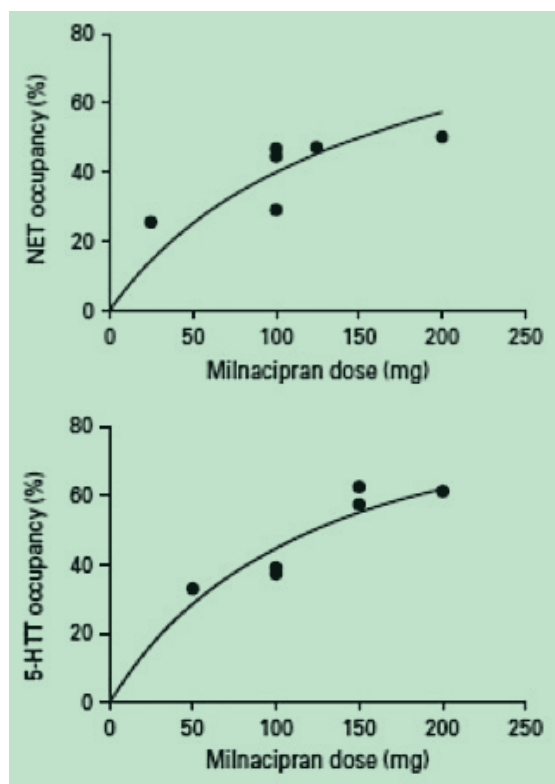


Fig.5 Estimated central NET (top) and 5-HTT (bottom) occupancy and daily dose of milnacipran in patients with depression

tion could likely clarify the pathophysiology of depression and the pathogenesis of clinical symptoms, in terms of norepinephrine neurotransmission. In addition, careful observation of any changes in symptoms and cognitive function is required following a course of treatment. Molecular imaging techniques such as PET provide us with opportunities to explore the mechanisms of action of pharmacotherapies in neuropsychiatric disorders and obtain information that is helpful for clinical practice.

References

- [1] Arakawa R, Okumura M, Ito H, *et al.*: Quantitative analysis of norepinephrine transporter in the human brain using PET with (S,S)-[¹⁸F]FMeNER-D₂, *J Nucl Med* 49, 1270-1276, 2008.
- [2] Meyer JH, Wilson AA, Sagrati S, *et al.*: Serotonin transporter occupancy of five selective reuptake inhibitors at different doses, *Am J Psychiatry* 161, 826-835, 2004.
- [3] Suhara T, Takano A, Sudo Y, *et al.*: High levels of serotonin transporter occupancy with low-dose clomipramine in comparative occupancy study with fluvoxamine using positron emission tomography, *Arch Gen Psychiatry* 60, 386-391, 2003.
- [4] Sekine M, Arakawa R, Ito H, *et al.*: Norepinephrine transporter occupancy by antidepressant in human brain using positron emission tomography with (S,S)-[¹⁸F]FMeNER-D₂, *Psychopharmacology* 210, 331-336, 2010.
- [5] Takano H, Arakawa R, Nogami T, *et al.*: Norepinephrine transporter occupancy by nortriptyline in patients with depression: a positron emission tomography study with (S,S)-[¹⁸F]FMeNER-D, *Int J Neuropsychopharmacol* 17, 553-560, 2014.
- [6] Hiemke C, Baumann P, Bergemann N, *et al.*: AGNP consensus guidelines for therapeutic drug monitoring in psychiatry: update 2011, *Pharmacopsychiatry* 44, 195-235, 2011.
- [7] Nogami T, Takano H, Arakawa R, *et al.*: Occupancy of serotonin and norepinephrine transporter by milnacipran in patients with major depressive disorder: a positron emission tomography study with [¹¹C]DASB and (S,S)-[¹⁸F]FMeNER-D, *Int J Neuropsychopharmacol* 16, 937-943, 2013.

Research on Radiation Protection

Kazuo Sakai, Ph.D.

Director of Research Center for Radiation Protection

E-mail: kzsakai@nirs.go.jp

Overview

The primary aim of the Research Center for Radiation Protection is to provide a scientific basis for radiation protection and safety. Toward this goal, radiation exposure from various sources is measured, the dose-effect relationships for various endpoints are examined, and the mechanisms underlying the effects are investigated. The Research Center disseminates its research results to promote public understanding of radiation effects and to encourage the enactment of more reasonable regulations concerning the use of radiation. The scope of its activities is not limited to Japan. It has been appointed a Collaborating Centre by the International Atomic Energy Agency and the appointment was renewed this year for the next four years.

The Research Center consists of the Planning and Promotion Unit, three research programs (Radiobiology for Children's Health Program, Radiation Risk Reduction Research Program, and Regulatory Science Research Program) and one Research and Development Team; the activities in each of these programs and the team are summarized below.

Activities across the whole center

Since the TEPCO Fukushima Daiichi Nuclear Power Plant (NPP) accident (March 11, 2011), the Center has organized telephone consultations which have been carried out with the help of other NIRS members. The number of consultations has reached almost 19,000.

In FY2013, the 6th International Systems Radiation Biology Workshop was held on March 5-7, 2014 as a Research Center Symposium, conjointly with DoReMi (Low Dose Research towards Multi-disciplinary Integration, supported by the EC). More than 100 researchers including 14 from foreign institutes participated in this symposium. Various research results were presented and discussed, which are related to low dose radiation effects, including studies on tumor cell proliferation and progression and mathematical analyses of the mechanism of carcinogenesis. Not only frontier research findings were presented, but also recovery operations for the Fukushima NPP accident and risk communication about radiation effects were also discussed. The symposium was very fruitful for the Center and all participating organizations.



At the close of the symposium, we invited 5 researchers for peer review on our research activities in the most recent 3 years. Prior to the review meeting, a research report was sent to each reviewer. At the review meeting, program leaders made presentations on their research activities, followed by discussion with the reviewers. A review report was immediately compiled, and reviewers finalized the review report, giving us a lot of useful suggestions and encouragement.

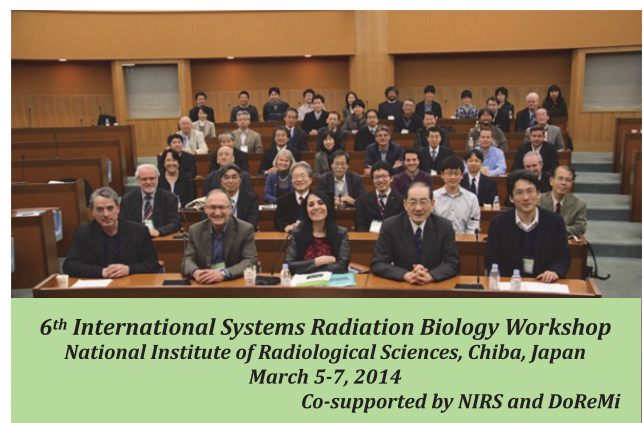


Fig. 1 Participants in the Research Center Symposium

Radiobiology for Children's Health Program

1. Background and Objectives of the Research Program

In this era of low birthrate and prolonged longevity in Japan, concerns about the safety of fetuses and children have been growing. Progressive increases in the use of medical radiation for children have recently forced the ICRP, IAEA and WHO to draft global initiatives on radiation protection of children.

This program carries out studies using mice and rats to provide information on the risk of cancer due to radiation exposure during fetal and childhood periods. Our studies focus on the effects of high linear energy transfer (LET) radiations i.e., neutrons and heavy ions, on fetuses and children. The ultimate objective of this research group is to propose weighting factors for both age-at-exposure and radiation quality to support the framework of radiation protection.

2. Approach to Reach the Objectives

Mice and rats were exposed to gamma rays from a ^{137}Cs source at a dose rate of 0.6 Gy/min. Carbon ion exposure was performed using the Heavy Ion Medical Accelerator in Chiba (HIMAC) (energy, 290 MeV/u; LET, 13 keV/ μm). For routine carbon ion radiotherapy, 13 keV/ μm approximates the LET of the therapy beam passing through normal tissue ahead of the tumor volume. Fast neutrons (2 MeV average energy) were generated by a Be(d,n)B reaction from the Neutron Exposure Accelerator System for Biological Effect Experiments (NASBEE) and administered at a dose rate of 0.025 Gy/min.

Life shortening was investigated in B6C3F1 mice of both sexes, which are the standard strain for toxicology research. For assessment of cancer risk, various animal models for not only hematopoietic neoplasms but also solid tumors at specific sites were used.

3. Results

3.1. Lifespan shortening

Life shortening (LS) is considered as a reasonable endpoint to estimate the risk of radiation because it is representative of the total radiation effects. The results obtained are as follows:

- Female mice appeared to be more susceptible to radiation-induced lifespan shortening than male mice. The effect of gamma rays on lifespan shortening of neonate or infant mice was more pronounced than that of adult mice. Surprisingly, irradiation at the late fetal stage had little influence on lifespan shortening.
- Carbon ions were more potent in reducing lifespan than gamma rays. When acute non-cancer effects were excluded, RBE values were almost the same regardless of the age-at-exposure.
- Neutrons were extremely potent in reducing lifespan compared to gamma rays and carbon ions. The largest RBE for neutrons was observed when irradiated in utero as compared to later life stages.

3.2. Cancers

There are susceptible age windows for radiation carcinogenesis, which are organ dependent. Most organs show high radiation sensitivity in perinatal or infant stages, but the lungs and acute myeloid leukemia show susceptible age windows in the adult stage.

Lung: As are the results of epidemiological studies on atomic bomb survivors, irradiating Wistar rats resulted in an increase of the incidence and the hazard ratio of adenocarcinoma and squamous cell carcinoma in a dose dependent manner. The cancer risk for X-rays at infancy was lower than that at puberty and adulthood. Array CGH analysis revealed that copy number loss was more frequent in tumors developed after infant irradiation than those after later age groups.

Mammary gland: Female SD rats of various ages (3, 13 and 17 dpc; and 1, 3, 7 and 15 weeks after birth) were exposed to gamma rays, carbon ions or fast neutrons. All animals were screened weekly for mammary carcinoma by palpation until they

were 90 weeks old. Fetal and mature (15-week-old) rats were resistant to radiation induction of mammary carcinomas. Dose responses to gamma rays were similar among the groups irradiated 1, 3 and 7 weeks after birth. The effects of carbon ion and neutron irradiation increased with increasing age-at-exposure. RBE values of carbon ions were 0.2, 1.3 and 2.8 for rats irradiated at 1, 3 and 7 weeks of age, respectively. The RBE values for neutrons were much higher than that for carbon ions regardless of age at exposure.

Kidney: Although the kidneys are one of the organs with low susceptibility to radiation carcinogenesis, the precise risks of kidney cancer after childhood exposure to radiation remain to be quantified. Perinatal exposure to radiation increased the incidence of renal cell carcinoma in Eker rats, which harbor a germ-line mutation in one of the alleles of the *Tsc2* gene. But atypical tubules, which are premalignant lesions of kidney cancers, were induced at higher rates in adult rats than neonatal rats. This indicates that malignant progression is much faster when irradiated at the perinatal age than at the adult age.

The frequencies of LOH at the wild-type allele of *Tsc2* were 38%, 29% and 60% in the unirradiated group and the group irradiated at 19 dpc and post-natal day 5, respectively. The pattern of LOH on chromosome 10 indicated that an interstitial-type LOH at the *Tsc2* locus was only observed in radiation-induced renal tumors. Sequence analysis of *Tsc2* in the LOH-negative tumors showed frame-shift mutations, deletion mutations and a missense mutation of *Tsc2*. Altogether, about 90% of the spontaneous tumors and 60% of the radiation-induced tumors showed inactivation of wild-type *Tsc2*.

Radiation Risk Reduction Research Program

1. Background and Objectives of the Research Program

Cancer susceptibility after exposure to radiation differs depending on individuals. Age and gender are known factors causing individual differences in radiation sensitivity. Smoking has also been identified to elevate the individual sensitivity to α -particles. In addition to these well-defined factors, there are other potential factors which have been suggested to modulate radiation sensitivity of individuals. First, variable efficiency of DNA repair resulting from single nucleotide polymorphisms (SNPs) located in genes for DNA repair-related proteins is thought to cause individual differences in radiation sensitivity. Second, there is evidence suggesting that individual radiation sensitivity is modulated by life styles; especially the calorie intake has been shown to have a significant impact on radiation carcinogenesis in laboratory animals.

The purpose of this program is to identify factors, whatever genetic and epigenetic, causing individual differences in radiation sensitivity, and also to present a possible way to reduce individual radiation risks by artificially regulating these factors.

2. Approach to Reach the Objectives

We consider that finding SNPs in the human population that impair DNA repair factors is critical to identify high risk groups and to establish a finely-tuned justification for radiation protection of these individuals. In the repair of DNA double strand breaks (DSBs) in animal cells, multiple protein factors are recruited and accumulated at the DSB site. If some factors have amino acid substitutions or deletions produced by SNPs which cause inability to accumulate at the DSB site, such factors would be considered no longer functional, and the cells would be hypersensitive to radiation. In order to identify such SNPs, we established a micro-

scope system that enables us to detect accumulation of GFP-tagged protein factors at the DSB sites produced by micro-irradiation of live cells with a laser beam. By examining ability to accumulate GFP-tagged variously-mutated DNA repair factors, we searched for amino acids substitutions and deletions that caused functional failure of DNA repair factors. At the same time, we searched the database for SNPs which could produce equivalent amino acid substitutions or deletions.

3. Research Results

We first investigated *Ku70* which plays an important role in non-homologous end-joining (NHEJ) which is a major DNA repair mechanism of mammals. Using a *Ku70*-deficient epithelial cell line, we could show that the ectopically-expressed EGFP-tagged *Ku70* accumulated at DSBs immediately when DSBs were produced by micro-irradiation with the laser. A series of deletion mutants of *EGFP-Ku70* was constructed, and we could identify several domains, including the N-terminal, DNA-binding and Ku80-binding domains, deletion of which caused inability of the factor to accumulate at the DSB. In addition, we could show that a single mutation at leucine 385 abolished the ability to accumulate at DSBs. This result indicated that SNPs associated with a loss of leucine at 385 are candidate biomarkers of radiation sensitivity.

We further analyzed a second DNA repair factor *Rad52* which plays an essential role in another DNA repair mechanism, homologous recombination. We observed that deletion of the eight amino acids of the C-terminal end completely abolished the recruitment of *Rad52* to DSBs. Importantly, it was previously reported that three human SNPs bring about deletions of the C-terminal end of *Rad52*, suggesting that these SNPs are candidate biomarkers of radiation sensitivity.

Radiation-induced DNA damages are repaired mainly by NHEJ in mammalian cells, but this is not a mechanism with high fidelity. Then we examined whether individual sensitivity to stochastic effects of radiation may be reduced by artificial inhibition of NHEJ pathways in cases that it is planned to expose an individual to low level radiation. In order to explore the feasibility of this idea, we analyzed the frequency of radiation-induced mutation at *HPRT* gene locus using various cell lines deficient in NHEJ-related genes. As a result, mutation frequencies in these cells were found to be lower than that in their parental cells. This observation is considered to be the result of an enhanced cell killing. However, it may be considered that the radiation-protective strategy by inhibition of NHEJ pathways may be beneficial in the case where deterministic effects caused by a critically large number of cell death events are negligible.

4. Significance and Relevance

The impact of various factors on individual radiation sensitivity is currently being investigated in Europe and the US to provide a scientific basis for protection of high risk groups from radiation. However, it is important to note that some factors such as lifestyles and genetic polymorphisms are different between races and/or cultures, so that the research on these factors should be promoted in Japan separately. Thus, our research program had great significance and relevance. As well, we are planning to establish possible ways to reduce individual radiation risks by artificially regulating these factors. This strategy may be referred to as "active radiation protection" showing a possible style for next generation radiation protection.

Regulatory Science Research Program

1. Background and Objectives of the Research Program

Radiation protection research is the science that applies the actual practice of radiation protection. In many cases, however, these results cannot be used as they are. Thus, it is important to process the scientific knowledge in a suitable form to apply each practice and provide it to government regulatory agencies and to society.

Objectives of this program are to investigate the necessary information for development of radiation safety standards and guidelines, and to propose scientifically based measures for radiation regulation and policy aiming at a more reasonable system of radiation protection.

Based on international trends, in Japan, we should give priority to discussion of the regulation of radon and NORM (naturally occurring radioactive materials). From the viewpoint of impacts of the Fukushima NPP accident, the accurate risk assessment for low dose radiation and effective communication of the risk are required from both government organizations and society.

2. Approach to Reach the Objectives

The program carries out studies on evaluation of occupational and public exposures from natural radiation sources such as radon, NORM and cosmic rays. Collected data on industrial use of NORM and cosmic-ray exposure when flying in air craft are accumulated in databases and published. The program is also developing techniques to reduce indoor radon exposure and to standardize radon measurements; these are thought to be urgent tasks for near-future regulation of indoor radon in Japan.

The information collected includes health effects of residents in high background areas, residents in Semipalatinsk (the nuclear weapons test site in the former USSR), atomic bomb survivors, and victims of the Chernobyl accident. The collected information is used for reviews of epidemiological studies and analysis as a base for radiation risk assessment. Using the results of basic studies related to the effects of radiation on the environment and health, the program is developing models of the mechanisms by which radiation affects the environment and organisms.

To reduce anxiety about the effects of radiation and answer people's questions about radiation protection measures, the program is analyzing the current situation of risk communication and developing tools for better communication.

3. Research Results

3.1. Measures for regulation and optimization of exposures from natural radiation

Regarding indoor radon exposure, the efficiency of mitigation methods using under-floor ventilation was investigated in a Japanese traditional wooden house. International comparison of radon measurements was carried out for their standardization. Occupational exposure due to utilization of NORM was studied to obtain the relationship between activity concentration of the materials and dose received by various workers, which is useful information to set the exemption criteria for the NORM level. The measurement system for cosmic rays in a facility on the top of Mt. Fuji was developed to evaluate the sudden increase of dose due to solar flares.

3.2. Policy for radiation regulation based on radiation risk

In order to propose a radiation protection policy with due consideration of social rationality, the program has made a comprehensive analysis of epidemiological data using advanced statistics analysis and has also developed an effective method for risk

communication. A tool for risk assessment using the latest risk information was developed to estimate radiation risk among a specified group of exposed people. The contents of the telephone consultations opened at NIRS after the Fukushima NPP accident were analyzed.

3.3. Measures for environmental protection

To develop new standards for environmental protection against radiation exposure, we carried out analysis of the transfer of radioactive materials to animals using a dynamic model. The results of the assessment showed higher activity concentration in a standard animal than that estimated by a model using a static value for the transfer factor.

3.4. Activities other than research

As activities other than research, members of the program have handled considerable numbers of requests from regulatory bodies responsible for radiation protection of the public against exposure to radioactive materials due to the Fukushima NPP accident. Members of the program also have cooperated in activities of international organizations, especially UNSCEAR.

R&D Team for Biospheric Assessment for Waste Disposal

The aim of the team's current project is to provide environmental transfer parameters for radiation dose assessments from radionuclides released from radioactive waste disposal sites. To obtain suitable parameters for the Japanese biosphere, this team has been carrying out three tasks: (1) Constructing the database of environmental transfer parameters (TFs and Kds) considering climate change; (2) estimating the effects on microbial activities for the transfer parameters of ^{14}C in soil-plant systems; and (3) collecting the environmental transfer parameters of important radionuclides (Pu, Am, Th and Cl) by ultra-high sensitivity analysis. Some details of these are given below.

1. Constructing the database of environmental transfer parameters (TFs and Kds) considering climate change

A literature survey was conducted to estimate the effect of warm and cool temperatures on soil-to-plant transfer factors (TFs) compared to those for temperate areas. According to the IAEA Technical Report Series No.472 (TRS-472), TF of Cs increased with decreasing temperature. A literature survey of Japanese TF-Cs of brown rice showed this trend as well. Additionally, 20 samples of leafy vegetables and associated soils were collected in the southern part of Japan this year to compare the TF change with leafy vegetables grown under warm conditions. The concentrations of 20 elements in the vegetables and soils were determined and were compared with our previous data. Although there were no differences between the new data and our previous data in soils, the concentrations of Si, Co, Ni, Cd and Cs in vegetables showed differences which were more than a factor of two. More detailed study is needed; more elemental concentration data at major-to-trace levels will be added next year to provide more information.

The effective half-lives of radio-Cs in fruit trees and the concentration ratios of Cs-137 of wild animals and fishes in Fukushima Prefecture were collected to understand the behavior of Cs in the

environments under the non-equilibrium condition to get apparent equilibrium constant values in transition.

2. Estimation of the effects on microbial activities for the transfer parameters of ^{14}C

It has been recognized that ^{14}C (T1/2: 5,730 years) is one of the dominant radionuclides affecting exposure dose from TRU wastes. The measurement method for gaseous chemical species containing ^{14}C released from soil was investigated. A new method to quantify the gasification of ^{14}C from soil was also studied, focusing on microbial activity. In our previous study, it was revealed that soil microorganisms strongly affected the chemical form changes of ^{14}C in low molecular weight organic carbon compounds. Thus respiration activity of soil microorganisms was measured using the INT Formazan reaction.

Although individual mechanisms of ^{14}C changes with time were studied, it is necessary to connect laboratory study results and field observations. Thus construction of a realistic ^{14}C model is necessary, but in our previous model, the gasification process had a single parameter though it should be affected by both temperature and CO_2 concentration in the air. A literature survey was conducted to obtain default parameter data on uptake of carbon by rice plants from the ambient air. Then the model was updated and sensitivity tests were carried out to see the applicability of the newly included parameter values.

3. Collecting the environmental transfer parameters of important radionuclides (Pu, Am, Th and Cl) by ultra-high sensitivity analysis

This year, our study focused on the development of highly sensitive analytical methods for the determination of Pu isotopes and Cl in soil samples. For Pu analysis, we compared the sensitivities of two sector-field ICP-MS instruments, the Element 2 and the newly introduced Element XR. Due to the newly developed jet-interface in the Element XR, a factor of 10 sensitivity improvement is achieved compared with the Element 2. Combined with a high-efficiency samples introduction system (Aridus II), a sensitivity of 100 M cps/ppb U or Pu was obtained, which provides the required sensitivity for Pu isotope analysis of rice samples which we expect to conduct next year. To determine Pu isotopes in soil samples, we developed a two-stage anion-exchange chromatographic separation procedure, in which extremely high U decontamination factor of 2×10^6 was achieved. The troublesome UH^+ interference was completely eliminated. An analytical method for accurate determination of Pu isotopes in soil samples was established, and applied to the determination of ^{239}Pu and ^{240}Pu in school ground soil samples collected in the 1970s to obtain the background data on Pu contamination in school ground soils in central-east Japan. For soil Cl analysis, two methods, water extraction-IC measurement and TMAH extraction-ICP-MS analysis, were evaluated. The obtained results showed that for samples with a Cl concentration higher than 100 mg/kg, good agreement between these two methods was obtained, while for the samples with Cl concentrations lower than 100 mg/kg, the concentration of Cl obtained with the TMAH-ICP-MS analysis method was higher than that of the water extraction-IC measurement method. Further work is planned for next year to complete establishment of the sensitive Cl analytical method.

Highlight

Root uptake of radiocesium by a vegetable growing on various potting mixes

Nobuyoshi Ishii

E-mail: nobu@nirs.go.jp

Potting mix is often composed of a variety of soils such as akadama-tsuchi, kuro-tsuchi, and so on. In this study, root uptake of radiocesium (^{134}Cs , ^{137}Cs) was evaluated for mini cabbage plants grown on potting mixes with different concentrations of radiocesium. Three potting mixes were prepared that contained kuro-tsuchi and akadama-tsuchi mixed with one other radiocesium contaminated material: leaf-mold (at two radiocesium concentrations) or sludge. (Akadama-tsuchi was contaminated with radiocesium, but radiocesium in kuro-tsuchi was below the detection limit.) Mini cabbage plants were grown using the three mixtures. At the harvest date, the concentrations of radiocesium in the mini cabbage edible plant parts were below the new standard limit for general foods in Japan, that is, 100 Bq kg^{-1} wet. The highest soil-to-plant transfer factor of 0.69 (dry weight basis) was observed for the potting mix composed of contaminated akadama-tsuchi, kuro-tsuchi, and slightly contaminated leaf-mold. Akadama-tsuchi is the most commonly used material for potting mixes, and thus it may be necessary to pay attention to the radiocesium contamination in akadama-tsuchi.

Introduction

The Fukushima Daiichi Nuclear Power Plant (FDNPP) was severely damaged by events that followed the magnitude 9.0 earthquake and the subsequent huge tsunami of March 11, 2011. Radionuclides, which were released because of the plant damage, have contaminated the environment, and among the radionuclides deposited on the surface soil, relatively long-lived radionuclides, such as radiocesium (^{134}Cs , ^{137}Cs), would be taken up by agricultural crops. Intake of agricultural crops contaminated with radionuclides causes internal radiation exposure.

The safety of most agricultural crops has been ensured by a new standard limit for radionuclides in foods, which was enforced by the Japanese government on April 1, 2012. However, measurement of radiocesium in crops, which were harvested from home gardens, has not been carried out before their consumption in many cases. To ensure safety and security, it is important to obtain a better understanding of transfer of radiocesium to crops from the ingredients of commercial potting mixes.



Potting mixes often contain a variety of Ingredients such as akadama-tsuchi, kuro-tsuchi, leaf-mold, and so on. Sludge from drinking water treatment plants is also a material for potting mixes, but Japanese government has started to regulate the shipping of the sludge, which contains more than 400 Bq kg^{-1} of radiocesium, in order to minimize radiation dose from the contaminated sludge to the public. Potting mix ingredients have different chemical compositions, therefore, transfer of radiocesium from soil to agricultural crops would differ by each ingredient. In this study, the transfer of radiocesium from these ingredients to edible parts of mini cabbage plants was studied [1].

Materials and methods

Akadama-tsuchi, kuro-tsuchi, and two kinds of leaf-mold (slightly contaminated leaf-mold and heavily contaminated leaf-mold) were purchased from a gardening center in 2011. Sludge was obtained from a drinking water treatment plant in Saitama Prefecture. The concentrations of radiocesium in each ingredient are listed in Table 1. The presence of ^{134}Cs in these ingredients (except for kuro-tsuchi which was below the detection limit) suggests contamination from radiocesium released by the FDNPP accident.

Table 1 Concentration of radiocesium in each ingredient of potting mixes

Ingredient	Concentration (Bq/kg-dry)	
	^{134}Cs	^{137}Cs
Akadama-tsuchi	1.6.E+01	2.4.E+01
Kuro-tsuchi	DL*	4.5.E+00
Slightly contaminated leaf-mold	5.5.E+00	5.1.E+00
Heavily contaminated leaf-mold	9.9.E+03	1.5.E+04
Sludge	6.7.E+03	1.0.E+04

* Detection limit: less than $2.7 \times 10^1 \text{ Bq/kg-dry}$

Table 2 Radiocesium concentrations of the samples and TF

Number of potting mix	Ingredient*	Concentration (Bq kg ⁻¹ -dry)						TF**
		Potting mix		Edible part		Core part		
		¹³⁴ Cs	¹³⁷ Cs	¹³⁴ Cs	¹³⁷ Cs	¹³⁴ Cs	¹³⁷ Cs	
1	Slightly contaminated leaf-mold	1.3.E+01	2.1.E+01	1.1.E+01	1.4.E+01	3.2.E+01	2.9.E+01	0.686
2	Hevily contaminated leaf-mold	9.6.E+02	1.5.E+03	1.9.E+02	2.7.E+02	2.1.E+02	2.8.E+02	0.189
3	sludge	1.4.E+03	2.1.E+03	1.4.E+02	2.0.E+02	3.1.E+01	1.5.E+02	0.094

*All potting mixes contained Akadama-tsuhi, Kuro-tsuhi, and chemical fertilizer.

**TF: the ratio of ¹³⁷Cs in the edible part of mini cabbage (Bq kg⁻¹-dry) to its concentration in potting mix (Bq kg⁻¹-dry).

Three kinds of potting mixes were prepared by using these materials. First, the same volumes of akadama-tsuhi and kuro-tsuhi (1:1) were mixed well (base soil). Thirty grams chemical fertilizer (8% nitrogen, 8% phosphorus, and 8% potassium by weight) was mixed into 8-L base soil. To grow the mini cabbage plants, a certain amount of the slightly contaminated leaf-mold (300 mL), the heavily contaminated leaf-mold (200-mL dry), or sludge (300-mL) was mixed into 500-mL base soil containing chemical fertilizer. These mixes were identified as potting mixes No.1, 2, and 3, respectively.

Two pots were filled with each of the three mixes and one seedling of mini cabbage (*Brassica oleracea Capitata*) was planted in each pot. The plants were grown for 79 days under natural light. The temperature was controlled at 25 ± 5°C during the cultivation period. Mini cabbages were harvested on June 27, 2012 and divided into edible and core parts. These parts and potting mixes were separately dried and powdered using a grinder for the analysis of radiocesium.

The concentration of radiocesium in the samples was quantified using a germanium detecting system (Seiko EG&G). The measurement values were corrected to harvest date.

The soil-to-plant transfer factors (TFs) were calculated as the ratio of the radiocesium concentration in the edible part of mini cabbage (Bq kg⁻¹ dry weight) to its concentration in potting mix (Bq kg⁻¹ dry weight)

Results and discussion

The radiocesium concentrations of the samples at the harvest date are summarized in Table 2. Radiocesium was detected in edible and core parts which suggested that root uptake of radiocesium occurred for this vegetable. It was found that the plant samples obtained from the plants grown in the potting mix with the highest radiocesium concentration, did not have the highest amount of radiocesium. Potting mix No.3 had the highest radiocesium concentration of 3.5 × 10³ Bq kg⁻¹, while the highest radiocesium concentration in the edible and core parts of the plant were observed with the potting mix No.2. These results suggest that the transfer of radiocesium from soil to plants is affected by the ingredients for potting mix.

The radiocesium concentrations were compared between edible and core parts (Table 2), and a significant difference (*t*-test, *P* < 0.05) was found for the mini cabbage grown in the potting mix No.1. Removal of the core parts and not eating them may reduce the radiocesium ingestion. On the other hand, Ban-nai et al.[2] showed that there were no differences in the concentration of

¹³⁷Cs between edible and other parts of cabbage, and thus more studies on the distribution of radiocesium in crops is necessary.

To compare the transfer of ¹³⁷Cs among the different potting mix samples, TF values were calculated using the concentration of ¹³⁷Cs in edible parts and the potting mixes (Table 2). The values varied among the samples, and the highest value was obtained for the mini cabbage harvested from the potting mix No.1. The main source of ¹³⁷Cs for the potting mix No.1 was akadama-tsuhi. Probably, ¹³⁷Cs in akadama-tsuhi would be more readily available to mini cabbage compared to that in leaf-mold and sludge. Akadama-tsuhi is inorganic volcanic soil and has minute holes allowing water retention. These holes may be responsible for the high TF value. Since akadama-tsuhi is the most commonly used soil in commercial potting mixes in Japan, attention should be paid to the radiocesium contamination of akadama-tsuhi.

Tsukada and Hasegawa [3] reported that the geometric mean of TF values of ¹³⁷Cs for cabbage which was harvested in Aomori Prefecture during the early 1990s was 0.026 and that its 95% confidence interval was from 0.0021 to 0.33. These contaminations of ¹³⁷Cs resulted from the atmospheric nuclear weapon tests in the 1960s and the Chernobyl accident in 1986. Therefore, it would appear that it is relatively hard to transfer ¹³⁷Cs from soil to cabbage by an aging effect. As expected, the TF value for the potting mix No.1 sample exceeded the 95% confidence range, and the TF values for the potting mixes No. 2 and No. 3 were higher than the geometric mean of the previously reported TF values [3]. TF values in this study would decrease with time.

The Japanese government has enforced the new standard limit for radionuclides in general foods (100 Bq kg⁻¹). This standard is based on the concentration on fresh weight basis. Radiocesium concentrations reported here were on dry weight basis, therefore, the values were converted to the concentrations on fresh weight basis. The radiocesium concentrations in edible parts were 4.9 Bq kg⁻¹ for the potting mix No.1, 65.1 Bq kg⁻¹ for the potting mix No.2, and 61.9 Bq kg⁻¹ for the potting mix No.3. In each crop part sample, the concentrations of radiocesium were below 100 Bq kg⁻¹ of fresh weight.

References

- [1] Ishii N, Tagami K, Kawaguchi I, et al.: Root uptake of radiocesium by a mini cabbage growing on various potting soils, *Jpn J Health Phys* 48, 150-155, 2013.
- [2] Ban-Nai T, Muramatsu Y, Yanagisawa K: Transfer factor of some selected radionuclides (radioactive Cs, Sr, Mn, Co and Zn) from soil to leaf vegetables, *J Radiat Res* 36, 143-154, 1995.
- [3] Tsukada H, Hasegawa H: Soil-to-plant transfer factor of Cs-137 and other elements in cabbage plants, *J Radioanal Nucl Chem* 252, 219-224, 2002.

Highlight

Ecological half-lives of radiocesium in some marine biota caught offshore of Fukushima Prefecture

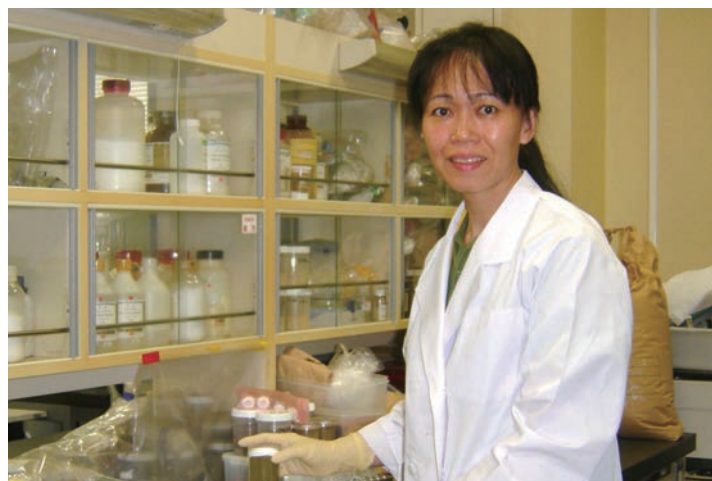
Keiko Tagami

E-mail: k_tagami@nirs.go.jp

A large amount of radiocesium was discharged in the Fukushima Daiichi Nuclear Power Plant (FDNPP) accident of March 2011. This highlight describes the use of open-source food monitoring data to evaluate ecological half-lives (T_{eco}) of radiocesium in some marine biota caught offshore of Fukushima Prefecture. Data were collected in two regions (north and south) with respect to the FDNPP site to obtain the regional ^{137}Cs concentration decreasing trend and then, the estimated T_{eco} in marine biota were obtained. T_{eco} values were then compared with biological half-life (T_b) estimated in laboratory settings. The ratios of T_{eco} to T_b were inconsistent among different groups of marine species. The T_{eco}/T_b ratios for brown seaweeds and bivalves were each approximately 1, however for demersal fish ratios ranged from 4.3 to 15. The reasons for the different ratios of T_{eco} to T_b may be attributed to environmental and ecological factors, such as different trophic levels and metabolic changes.

Definition of ecological half-life

The time required for the biological elimination of 50% of a radionuclide from a living plant or animal body is called the biological half-life (T_b). When the radionuclide is actually taken into a living body, both physical decay and biological elimination occur together; therefore, the term 'effective half-life (T_{eff})', is used which is



expressed as $1/T_{\text{eff}} = 1/T_p + 1/T_b$. However, in a natural environment, when radioactive contamination occurs, it is important to investigate how long the radionuclide persists in a population of a certain species, because the rate is influenced by ecological factors, including both abiotic and biotic factors. Ecological niche affects the radionuclide fate in a food web for example. For such cases, the term 'ecological half-life' (T_{eco}) has been used. In this study, the term T_{eco} is used to describe the time required for a 50% decline of a radionuclide in a population in a natural ecosystem.

T_{eco} typically has short-term and long-term components. The first component likely reflects the biological elimination rate of the radionuclide, while the second component likely reflects the biogeochemical cycles of the radionuclide in the ecosystem. Thus, eventually, the radionuclide concentration reaches a dynamic equilibrium between organisms and the ecosystem, and also decreases as a result of physical decay. However, in this study, only

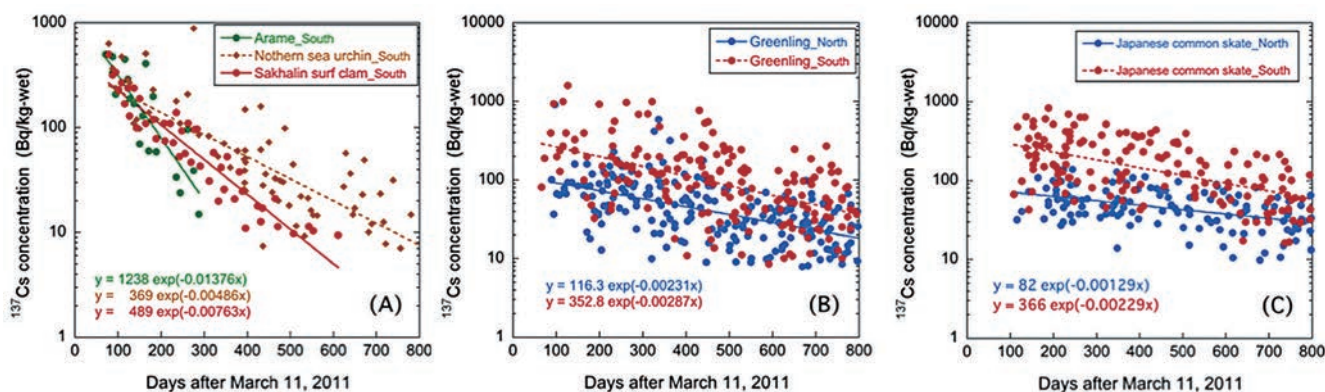


Fig.1 Time trend of ^{137}Cs concentrations in edible part of marine species collected offshore of Fukushima Prefecture (Bq/kg-wet) after March 11, 2011. (A) *Arame*, northern sea urchin and Sakhalin surf clam in the southern region and (B) greening, and (C) Japanese common skate in both regions.

Table 1 Ecological half-life (T_{eco}) of ^{137}Cs for each species caught off Fukushima.

Species	North				South			
	n	Correlation coefficient	Probability	T_{eco} days	n	Correlation coefficient	Probability	T_{eco} days
<i>Arame</i>	-	-	-	-	19	-0.854	<0.0001	50
Abalone	-	-	-	-	17*	-0.913	<0.0001	51
Skahalín surf clam	-	-	-	-	61	-0.937	<0.0001	91
Northern sea urchin	-	-	-	-	98	-0.791	<0.0001	143
Sand crab	-	-	-	-	17	-0.969	<0.0001	97
Greenling	200	-0.554	<0.0001	300	181	-0.533	<0.0001	244
Flatfish	256	-0.565	<0.0001	310	268	-0.464	<0.0001	357
Marbled sole	244	-0.402	<0.0001	452	184	-0.479	<0.0001	281
Japanese common skate	166	-0.428	<0.0001	539	196	-0.520	<0.0001	303

* Data up to 300 days after March 11, 2011 was used. -: no data.

the short-term component was calculated because the data collection period was not long enough to estimate the long-term component. Thus, T_{eco} is estimated by $\ln 2 \cdot \lambda_{eco}^{-1}$, where λ_{eco} is the ^{137}Cs ecological loss rate in a population and it is obtained from the slope of the exponential decline in ^{137}Cs concentration in the population over time.

Data sources

Open-source ^{137}Cs concentration data for edible marine biota caught offshore of Fukushima Prefecture together with the sample collection date were taken from monthly food monitoring reports provided on the website of the Ministry of Health, Labour and Welfare of Japan (http://www.mhlw.go.jp/shinsai_jouhou/shokuhin.html). ^{137}Cs concentration data for a total of about 170 edible marine species have been reported, however, the sampling intervals were random and not consistent among different species. Thus, we selected 16 species which had data available from March 11, 2011 through the end of December 2012 (651 days), and we calculated the T_{eco} values [1]. In the same manner, the results for nine species were obtained using data collected up to 800 days after March 11, 2011 and they are reported here. The data were then separated into two regions based on the relative direction of the sampling locations with respect to the FDNPP site: a northern region (Shinchi-cho, Soma-shi, Minami Soma-shi) and a southern region (Iwaki-shi).

Ecological half-lives of ^{137}Cs in marine biota

The collected ^{137}Cs activity concentration data (Bq/kg-wet) for each species of each region were plotted on a logarithmic scale against time and some examples are shown in Fig.1. In the north-

ern region, there were not enough ^{137}Cs data to calculate T_{eco} for *Arame*, abalone, Skahalín surf clam, northern sea urchin and sand crab possibly due to the radiocesium concentration in seawater north of the FDNPP site being lower than that south of the site in March 2011, immediately after the radionuclide releases. The calculated T_{eco} values are listed in Table 1 together with the correlation coefficient between ^{137}Cs concentration (as logarithmic values) and time; good correlations were found with $p < 0.0001$ by the t-test for all species. As shown in Fig.1, decreasing rates were similar for both regions. The ratio of T_{eco} (north/south) for four fish species ranged from 0.9 to 1.8.

The T_{eco}/T_b ratios are listed in Table 2. These ratios varied between the different major groupings, e.g., being about 1 for brown seaweed and bivalves, and 4.3-15 for demersal fish. After the FDNPP accident, ^{137}Cs concentration in the surface water decreased by a factor of 1000 between April to May 2011; this prompt and continuous advection due to currents, may, to some extent, have created similar conditions to those of laboratory experiments on T_b . Thus T_{eco} s for seaweeds and shellfish results were similar to T_b s. Although ^{137}Cs in most seaweeds, molluscs and crustaceans became lower than the detection limit within 800 days after March 11, 2011, ^{137}Cs concentrations in demersal fish were still being measured, which caused higher T_{eco}/T_b ratios. In the long-term under which equilibrium conditions were reached, no biomagnification would occur because the water to marine species ^{137}Cs concentration ratios were almost the same among various species [2]. However, in the short-term after the accident, an apparent biomagnification might occur due to trophic levels and metabolic changes accompanying with growth; as the trophic level increases, prey have higher ^{137}Cs concentration for longer time periods.

It is important to measure T_b to know elimination mechanisms, however, T_b cannot indicate the actual phenomena. Investigating T_{eco} of various species is necessary to understand the uptake and elimination mechanisms of ^{137}Cs in marine biota in the actual field.

References

- [1] Iwata K, Tagami K, Uchida S: Ecological half-lives of radiocesium in 16 species in marine biota after the TEPCO's Fukushima daiichi nuclear power plant accident, *Environ Sci Technol* 47, 7696-7703, 2013.
- [2] Tagami K, Uchida S: Marine and freshwater concentration ratios ($CR_{wo-water}$): review of Japanese data, *J Environ Radioactiv* 126, 420-426, 2013.

Table 2 Comparison of field data (T_{eco}) and laboratory data (T_b).

	Species, T_{eco}	Species, T_b	T_{eco}/T_b
Seaweeds	<i>Arame</i> 50	Bladderwrack 54	0.93
Shellfish (Bivalves)	Sakhalín surf clam 91	Scallop 75	1.2
Demersal fish	Flatfish 310-357	Flatfish 24 (avg.)	13-15
	Marbled sole 281-452	Plaice 65	4.3-7.0

Highlight

Cancer prevention by adult-onset calorie restriction after infant exposure to ionizing radiation in B6C3F1 male mice

Yi Shang

E-mail: shangyi@nirs.go.jp

Introduction

It is well known that children are more susceptible to carcinogenic effects of radiation as compared with adults. Epidemiological studies of atomic bomb survivors, patients undergoing radiation-based medical treatments and victims of nuclear power plant accidents show that exposure at a young age results in higher risk of cancer compared with exposure during adulthood. Thus, there is a critical need to make efforts for assessing risk and developing prevention strategies for radiation-induced cancer after childhood exposure.

Calorie restriction (CR) has been known to increase mean lifespan by decelerating the rate of aging and inhibiting tumor formation in a variety of species. CR has been reported to decrease occurrence of not only spontaneous but also chemical carcinogen-induced tumors in rodents and non-human primates. CR has also been reported to have effects on radiation-induced leukemias [1], but data on tissues other than bone marrow are lacking. Although CR has been proposed as a strategy for preventing cancers, CR during childhood is not appropriate because of the potential malnutrition and disrupted endocrine function. A recent report using a chemical carcinogen-induced mouse skin tumor model shows that CR during the cancer promotion phase is more effective than during the tumor initiation phase [2]. Because radiation-induced carcinogenesis is thought to be a relatively long-term process, we propose that adult-onset CR during the tumor promotion/progression phase could be a valuable strategy in the prevention of tumors after childhood exposure to ionizing radiation.

In this highlight, we show that adult-onset CR is effective for suppressing late-occurring tumors in both non-irradiated and irradiated mice. However, CR was less effective for early-occurring radiogenic tumors such as thymic lymphoma (TL) and early-occurring non-TL [3].

Results

1. Effect of calorie restriction on lifespan

Changes in overall survival ratio are shown in Fig.1. Irradiation resulted in statistically significant lifespan shortening by 38%. Irrespective of irradiation, CR significantly extended the overall lifespan of the non-irradiated and 3.8 Gy irradiated groups by

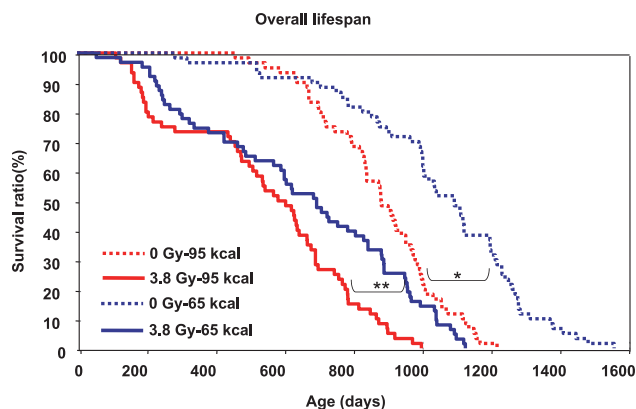


Fig.1 Kaplan-Meier curves that represent survival ratios for all experimental groups. The statistical significance of the differences in survival among groups was evaluated with the log-rank test. $P < 0.05$ was considered significant. *: 0 Gy-95 kcal vs 0 Gy-65 kcal; **: 3.8 Gy-95 kcal vs 3.8 Gy-65 kcal.

19.6% and 19.2%, respectively. The lack of a difference between the lifespan extension between non-irradiated and 3.8 Gy irradiated groups indicates that CR contributes to lifespan extension through mechanisms that are independent of radiation effects.

2. Effect of calorie restriction on cancer prevalence

In this study, several types of cancers were detected. TL and early-occurring non-TL, which were the main causes of early death, were seen only in the irradiated groups. After one year, late-occurring non-TL, liver, and lung tumors were detected in both non-irradiated and irradiated groups.

Specifically, the incidence of TL in the 3.8 Gy-95 kcal group was 20.0%, and the incidence in the 3.8 Gy-65 kcal group was 14.3%.

CR appeared to improve TL-free survival although the difference was not statistically significant.

Lymphomas that originated from lymphoid tissues other than the thymus, such as the lymph nodes or spleen (collectively called here non-TL), appeared to be classified into two types with respect to tumor development time: early and late. The two types were separated by the onset times and the time lag for these two lymphomas was >200 days. We analyzed early- and late-occurring non-TL separately. The incidence of early-occurring non-TL in the irradiated groups on both diets was ~10%. Early-occurring non-TL-free survival were not statistically affected by CR. The incidence of late-occurring non-TL in non-irradiated mice was 48.3% in the 95 kcal group and 20% in the 65 kcal group. The incidence of late-occurring non-TL in the irradiated groups was unexpectedly reduced from 16.7% to 9.5% in the 65 kcal group. CR significantly improved the late-occurring non-TL-free survival in both the non-irradiated and irradiated groups.

The predominant liver tumor type observed was hepatocellular carcinoma (HCC). Exposure to 3.8 Gy at 1 week of age significantly increased the incidence of HCC from 13.3% to 46.7% in the 95 kcal group and from 15.0% to 31.7% in the 65 kcal group, suggesting that liver tumors are radiogenic. CR significantly improved HCC-free survival in both the non-irradiated and 3.8 Gy irradiated groups.

The predominant lung tumor type was adenocarcinoma; we detected no effect of radiation on its incidence. In the 95 kcal groups, radiation did not increase adenocarcinoma incidence, while in the 65 kcal groups, adenocarcinoma incidence was even lower in the 3.8 Gy group than in the non-irradiated group. The effect of CR was evident in the 3.8 Gy groups: the incidence of lung adenocarcinoma was reduced from 25.0% in the 95 kcal group to 6.3% in the 65 kcal group. CR significantly increased the lung adenocarcinoma-free survival in both the non-irradiated and 3.8 Gy irradiated groups.

3. Risk of the various tumor types: Cox proportional hazard analysis

Multivariate Cox proportional hazard analysis was performed to assess the hazard ratio (HR) of cancer development (3.8 Gy vs. 0 Gy or 65 kcal vs. 95 kcal). Table 1 shows the HRs of cancer risk (3.8 Gy vs. 0 Gy) for various organs in the 95 kcal and 65 kcal groups. Radiation affected overall lifespan equally in the two diet groups. CR reduced HRs in a tissue-dependent manner. The tu-

Table 1 Summary of hazard ratio (HR) for major tumors

	Radiation vs. 0 Gy		Calorie vs. 95 kcal	
	95 kcal	65 kcal	0 Gy	3.8 Gy
Overall lifespan	4.22	4.48	0.33	0.54
Lifespan of tumor-free mice	4.37	7.96	0.18	0.46
TL	ND	ND	ND	0.65
Early-occurring non-TL	ND	ND	ND	0.88
Late-occurring non-TL	2.30	2.89	0.10	0.18
HCC	12.92	20.89	0.23	0.25
Lung adenocarcinoma	6.20	3.79	0.16	0.13

ND: not detected

mors most affected by CR were non-TL and lung tumors followed by HCC. CR also affected overall lifespan and lifespan of tumor-free mice. The effect in the 3.8 Gy irradiated group was smaller than that in non-irradiated groups, suggesting that CR is less effective for radiation-associated diseases. This was mainly because early-occurring radiogenic TL and non-TL were not highly influenced by CR.

Summary

We showed here that irrespective of CR, 3.8 Gy of X-ray exposure shortened lifespan by 38%, and irrespective of irradiation CR extended lifespan by 20%. Adult-onset CR reduced the risk of hepatocellular carcinoma, late-occurring non-TL, and lung tumors but not TL or early-onset non-TL. The ability of CR to prevent late-occurring tumors was the same for non-irradiated and irradiated mice, indicating that the mechanism(s) by which CR influences cancer is independent of irradiation. In summary, adult-onset CR significantly inhibits late-occurring tumors in a tissue-dependent manner regardless of infant radiation exposure.

References

- [1] Yoshida K, Inoue T, Nojima K, *et al.*: Calorie restriction reduces the incidence of myeloid leukemia induced by a single whole-body radiation in C₃H/He mice, *Proc Natl Acad Sci USA* 94, 2615-9, 1997.
- [2] Birt DF, Pelling JC, White LT, *et al.*: Influence of diet and calorie restriction on the initiation and promotion of skin carcinogenesis in the SENCAR mouse model, *Cancer Res* 51, 1851-4, 1991.
- [3] Shang Y, Kakinuma S, Yamauchi K, *et al.*: Cancer prevention by adult-onset calorie restriction after infant exposure to ionizing radiation in B6C₃F₁ male mice, *Int J Cancer* in press.

Highlight

Effect of age at exposure on hematopoietic stem and progenitor survival

Kentaro Ariyoshi, Yoshiya Shimada

E-mail: ariyoshi@cc.hirosaki-u.ac.jp or y_shimad@nirs.go.jp



Introduction

In recent years, there has been a growing concern in society about the risks associated with exposure to ionizing radiation, especially for children. With respect to radiation-induced cancer, studies of atomic bomb survivors and other cohort studies suggest that age at exposure modifies the radiation effects on cancer mortality. The relative risk of acute lymphocytic leukemia (ALL) is higher after childhood exposure than adult exposure, while the risk of acute myeloid leukemia (AML) remains constant or increases slightly increasing age at exposure. Animal studies also have shown that the incidence of radiation induction of AML is minimal when irradiation is carried out during in utero or infancy periods, but it reaches a maximum when irradiation occurs as an adult. Recent studies postulated that AML arises from hematopoietic stem cells (HSCs), suggesting that HSCs are also the target of radiation-induced AML. Despite the increase in knowledge of stem cell biology, there is still little information on the role of age in radiation effects of stem cells.

In the present study, we aimed to clarify the effect of age at exposure on HSC survival after radiation and the association of survival with the age effect on radiation-induction of AML. This work has been published in *Radiation Research* [1].

Results

Survival of CFUs after radiation exposure

Female C3H/He mice, which are prone to radiation-induced myeloid leukemia, were irradiated with various ages (1, 3, 8, and 14 weeks after birth) with ^{137}Cs γ rays at 0, 2, 4, and 6 Gy, and the number of HSCs in bone marrow tissue was evaluated using the CFU-S assay. Also, the number of hematopoietic progenitor cells was evaluated using the *in vitro* CFC assay, for CFU-granulocyte macrophages (CFU-GMs) and burst-forming unit-erythroid cells (BFU-Es) and CFU-granulocyte, -erythrocyte, -monocyte, and -megakaryocyte (CFU-GEMM). The number of the CFU-S was significantly reduced in 1-week-old mice as compared with the older mice after 2 Gy exposure (Fig.1A). Also, the numbers of CFU-GM and BFU-E colonies from 1-week-old mice were significantly reduced as compared with the mice at other ages after radiation exposure (Figs. 1B, 1C). No significant changes were observed in

CFU-GEMM (Fig.1D), which might be because the number of colonies was so small.

Expression of chemokine and cytokine genes

By using microarray analysis, we compared gene expression profiles of bone marrow tissues from mice sham irradiated or 2 Gy irradiated at 1 week and 8 weeks of age. Principal component analysis (PCA) indicated that gene expression profiles could be distinguished by age at exposure, and also time after exposure (Fig.2A). Pathways were differentially affected by time after exposure among different age groups, and 25 pathways including chemokine pathways were identified (Fig.2B). Then, by qPCR, we compared expression levels of several radio-protective chemokines or cytokines in bone marrow tissues between mice sham irradiated and those 2Gy irradiated at 1-week and 8-weeks of age. Among these, expressions of *Csf2* and *Fgf1* changed negligibly in the 1-week-old mice, while their expression in the 8-weeks-old mice increased significantly after irradiation (Figs. 2C, 2D). Also time-dependent increases in expressions of *Kitl* (Fig.2E) and *Il1b* (Fig.2F) after irradiation were observed in the 8-weeks-old mice, although the increase in *Il1b* expression was not statistically significant.

Summary

In this study, we demonstrated that an increased radio-resistance in adult HSCs might result from the induction of radio-protective cytokines, such as *Csf2*, *Fgf1* and *Kitl*, and possibly *Il1b*, after radiation exposure. Our findings imply that increased radio-resistance in adult HSCs may be associated with an increased risk of AML.

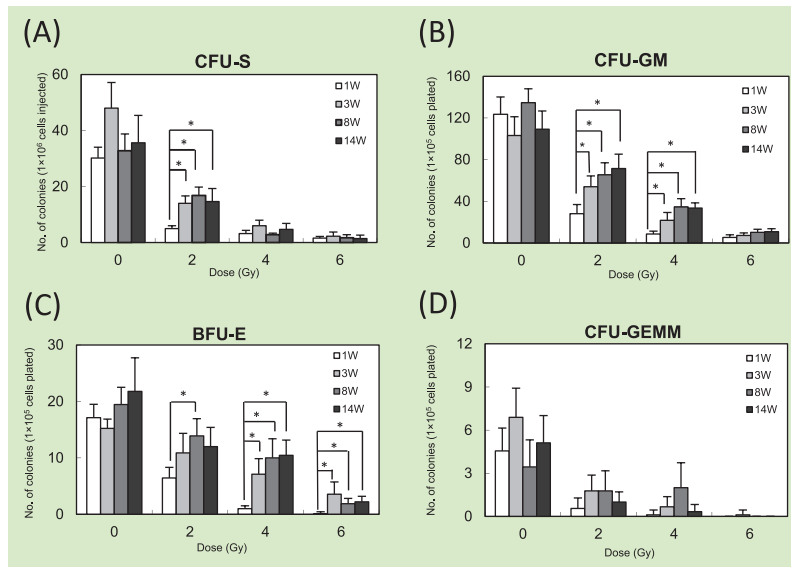


Fig.1 Effect of radiation exposure on survival of HSCs and hematopoietic progenitor cells. The numbers of colonies of CFU-S (A), CFU-GM (B), BFU-E (C) and CFU-GEMM (D) of 1, 3, 8, and 14-weeks-old mice after exposure to 0, 2, 4 and 6 Gy of γ -rays are shown. The asterisks mark differences that are statistically significant ($p < 0.01$).

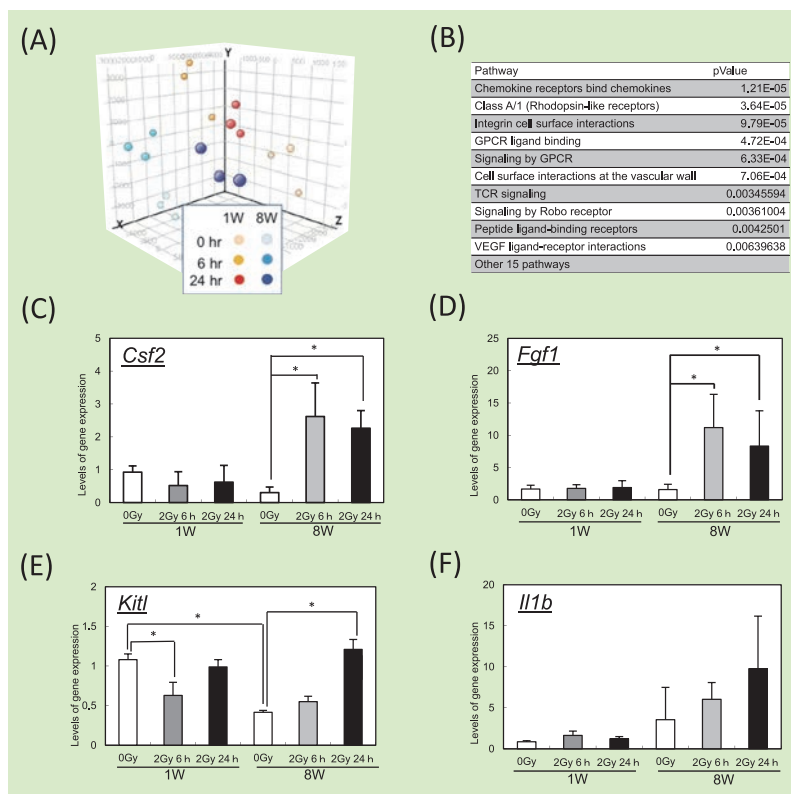


Fig.2 Array expression profile and radio-protective cytokine/ chemokine gene expression in bone marrow tissues. PCA of bone marrow tissue samples from 1-week-old and 8-weeks-old mice after 0 h, 6 h and 24 h after 2 Gy exposure (A). Pathways affected by time after exposure among different age groups (B). qPCR analysis of radio-protective chemokine or cytokines: *Csf2* (C), *Fgf1* (D), *Kitl* (E) and *IL1b* (F) in bone marrow tissues. The asterisks mark differences that are statistically significant ($p < 0.01$).

References

- [1] Ariyoshi K, Takabatake T, Shinagawa M, *et al.*: Age dependence of hematopoietic progenitor survival and chemokine family gene induction after gamma irradiation in bone marrow tissue in C3H/He mice, *Radiation Research* 181, 302-313, 2014, doi: <http://dx.doi.org/10.1667/RR13466>.

Highlight

Generation of breast cancer stem cells by steroid hormones in irradiated human mammary cell lines

Guillaume Vares

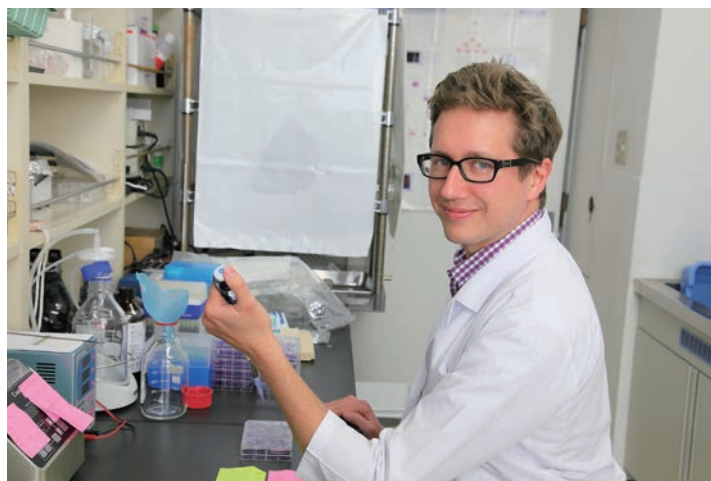
E-mail: vares@nirs.go.jp

Breast cancer risk factors

Worldwide, breast cancer represents 16% of all cancer incidences among women and 13.7% of cancer deaths. Although breast cancer rates have traditionally been lower in Japan than in the United States, breast cancer incidence is expected to rise significantly. It was shown that women who had received medium or high-dose ionizing radiation to the chest (for example, as treatments for other cancers, such as Hodgkin's lymphoma) have a relative risk of breast cancer between 2.1 and 4.0. By age 45 years, up to 20% of women exposed to chest ionizing radiation for a pediatric malignancy are diagnosed with breast cancer. New data are coming to light indicating that even low dose exposures (such as diagnostic chest X-rays for tuberculosis or pneumonia) might raise this risk. Sex steroid hormones such as estrogen and progesterone play a crucial role in the development and homeostasis of the mammary gland, by regulating proliferation, differentiation and apoptosis. Evidence from the last few decades supports the idea that accumulated exposure to steroid hormones (for example in post-menopausal women under hormonal replacement therapy) is also a risk factor for breast cancer. The interplay between steroid hormones and radiation-induced risks has been described in a number of studies. For example, we have shown that progesterone protects cultured mammary cells against radiation-induced apoptosis and increases the number of proliferating cells containing chromosomal damage [1]. However, our knowledge of hormonal action in the irradiated breast is far from complete and new discoveries are challenging some established paradigms.

Cancer stem cells

Recently, a lot of attention has been given to a small population of malignant cells thought to be responsible for tumor maintenance and initiation of relapse. These cancer stem cells (CSCs) possess the ability to self-renew (thus to form tumors) and to cause the different lineage of cancer cells comprising a tumor. Breast CSCs were first observed by Al Hajj et al. [2], who described the existence of a subpopulation of CD44⁺CD24^{low}ESA⁺ lineage⁺ human breast cancer cells capable of initiating tumors in immune-deficient NOD/SCID mice. CSC populations have been



defined using several combinations of cell-surface markers, such as CD44⁺CD24⁻, or by measuring cellular activities, such as the expression of aldehyde dehydrogenase (ALDH). In a recent study, it was shown that breast cancer cell lines contain breast CSCs. CSCs may arise from normal stem cells, or from a differentiated progenitor, which acquired self-renewal abilities. CSCs are thought to be radio-resistant and have a distinct molecular signature.

Steroid hormones in the breast

Both estrogens and progesterone have strong proliferative effects on stem/progenitor cells. Several studies have shown that progesterone regulates genes (Notch pathway genes DLL-1, DLL-3, IL6, PRSS2, Interleukins IL6 and IL8 and others) is potentially involved in stem cell regulation. Estrogen was recently shown to stimulate CSC expansion through FGF signaling. It was also shown that radiation exposure or steroid hormones can contribute to the initiation of epithelial-to-mesenchymal transition (EMT) and the expansion of CSCs subpopulation. However, to date, the potential involvement of steroid hormones in the radiation-triggered EMT is unknown. New developments have also brought light onto the molecular mechanisms of hormonal action. In the normal human breast, nuclear estrogen and progesterone receptors (ER and PR, respectively) are expressed in only 15 to 30% of the luminal epithelial cells and not in other cell types. It is thought that receptor-containing cells secrete paracrine factors that influence the proliferation and activity of nearby receptor-negative cells. Recent investigations have shown that cultured MCF10A normal epithelial cells that do not express PR are nonetheless responsive to progesterone. Furthermore, CSCs can be generated during the transformation of MCF10A cells.

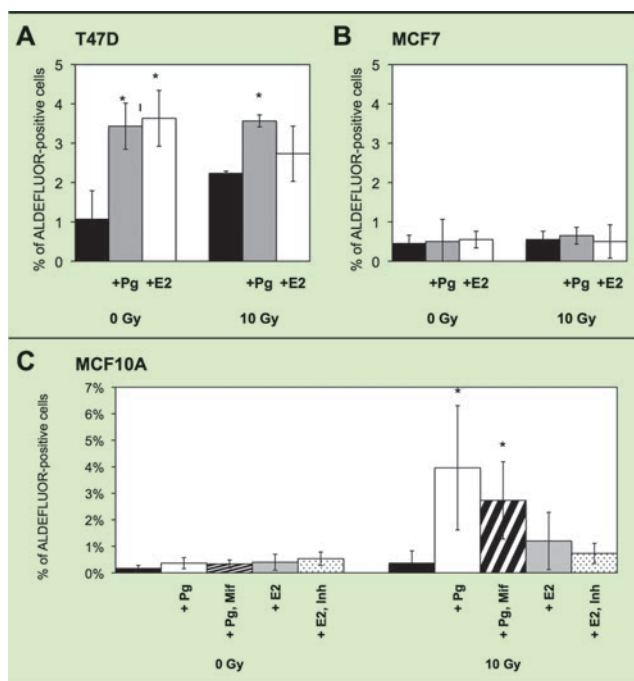


Fig.1 Proportion of CSCs after irradiation and steroid hormone treatment. The percentages of ALDH+ T47D (A), MCF7 (B) and MCF10A (C) cells were evaluated by flow cytometry three days after irradiation. Hormonal treatment was performed two days before irradiation and every day afterwards. Pg: progesterone, Mif: mifepristone, E2: estrogen, Inh: PD173074. Results are representative of at least three independent experiments. Error bars represent standard deviation. Asterisks denote significant differences (t-test, * $p < 0.05$, ** $p < 0.01$).

Ionizing radiation and steroid hormones generate cancer stem cells

In order to evaluate whether the modulation of radiosensitivity and radiation-induced breast cancer risk might involve CSCs, we measured the proportion of ALDH+ (Fig.1) and CD44+/CD24-cells in cultured breast cell lines [3]. Depending on the cell line, both exposure to ionizing radiation (X-rays) and steroid hormone treatment (progesterone and estrogen) could stimulate the expansion of CSCs. These CSCs exhibited higher tumorsphere-forming abilities and increased radioresistance. In irradiated MCF10A cells, progesterone action was independent of PR expression.

In MCF10A cells, progesterone triggers oxidative stress as well as cancer- and stemness-associated miRNA regulations

The stimulation of reactive oxygen species levels by progesterone in MCF10A cells is consistent with earlier reports showing increased mitochondrial activity (observed as increased mitochondrial potential) and the subsequent inhibition of Fas-induced apoptosis. In addition to non-genomic effects, progesterone directly triggered miRNA regulations (such as the downregulation of miR-22-3p and miR-29c-3p and the upregulation of miR-328 and miR-98-5p) consistent with cancer-related processes and stemness (Fig.2).

Conclusion

Progesterone directly triggered miRNA regulations and modulated the radiosensitivity of normal breast epithelial cells lacking the expression of PR, suggesting that the classical model of hor-

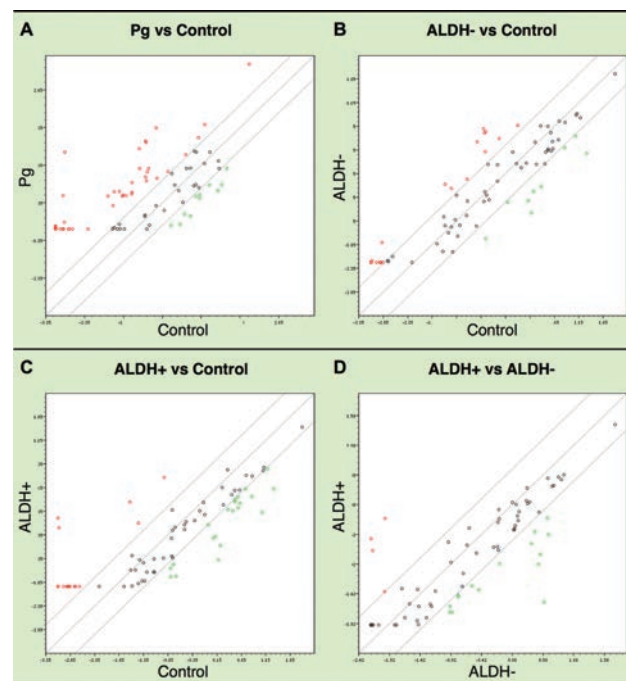


Fig.2 Comparative microRNA expression levels in MCF10A cells. Each scatter plot shows microRNA expression levels (logarithmic scale) for two experimental groups: cells exposed to progesterone treatment alone (Pg) vs non-irradiated cells (Control) (A), ALDH- cells (after irradiation and progesterone treatment) vs Control (B), ALDH+ cells (after irradiation and progesterone treatment) vs Control (C), ALDH+ cells vs ALDH- cells (D). The outer diagonal lines indicate 4-fold differences in microRNA expression. Each microRNA is represented by a circle.

monal paracrine action in the normal breast may need to be completed. Furthermore, the combination of progesterone treatment and radiation exposure was capable of generating CSCs and might trigger or contribute to cancer initiation events.

Our results suggest that progesterone might influence radiation-induced breast cancer risk by generating tumor-initiating breast CSCs. In order to decrease the potential risks of breast cancer resulting from chest ionizing radiation exposure, it might be useful to take into account the variability of progesterone levels during the menstrual cycle and between individuals. Our results also shed additional light on elevated breast cancer risks in women treated with hormone replacement therapy. Further investigations are needed to better understand the mechanisms involved in PR-independent progesterone action in the normal breast and the generation of CSCs after exposure to ionizing radiation, in particular in the low-dose range.

References

- [1] Vares G, Ory K, Lectard B, *et al.*: Progesterone prevents radiation-induced apoptosis in breast cancer cells, *Oncogene* 23(26), 4603-13, 2004.
- [2] Al-Hajj M, Wicha MS, Benito-Hernandez A, *et al.*: Prospective identification of tumorigenic breast cancer cells, *Proc Natl Acad Sci USA* 100(7), 3983-88, 2003.
- [3] Vares G, Cui X, Wang B, *et al.*: Generation of breast cancer cells by steroid hormones in irradiated human mammary cell lines, *PLoS One* 8(10), e 77124, 2013.

Highlight

Most hydrogen peroxide-induced histone H2AX phosphorylation is mediated by ATR and is not dependent on DNA double-strand breaks

Takanori Katsube

E-mail: tkatsu@nirs.go.jp

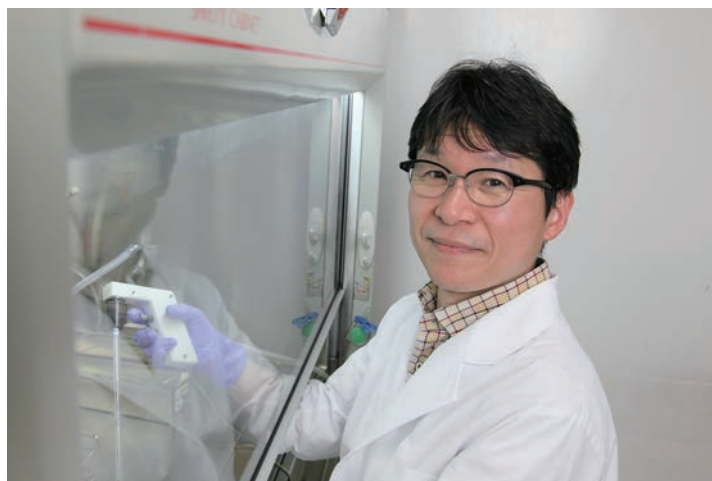
DNA double-strand breaks (DSBs) are the most serious damage to cells exposed to ionizing radiation (IR). The nuclear foci of phosphorylated histone H2AX (γ H2AX) are frequently used as a marker to monitor induction and repair of DNA double-strand breaks (DSBs) following exposure to IR or other DNA damaging agents. However, our recent study showed that γ H2AX foci induced by oxidative stress in hydrogen peroxide (H_2O_2)-treated cells are not associated with DSBs.

DSBs and γ H2AX

H2AX is a variant form of the nucleosomal protein, histone H2A. H2AX is phosphorylated on its S139 site by ataxia telangiectasia mutated (ATM), a member of the phosphatidylinositol-3 kinase-like kinases (PIKKs), in response to DSBs (Fig.1 A). Phosphorylated H2AX, called γ H2AX, makes a binding site for many components of the DNA damage response (DDR). The induction of γ H2AX around DSBs can be detected as ' γ H2AX foci' under a microscope with immunocytochemistry and utilized as a highly sensitive way to monitor the induction and repair of DSBs. Traditional techniques, such as pulsed-field gel electrophoresis or chromosome analysis, usually require Gy-order doses to detect IR-induced DSBs, whereas γ H2AX analysis can be utilized with a milli Gy-order dose. Therefore, γ H2AX analysis has become the most popular tool to detect DSBs in radiation biology. However, the formation of γ H2AX foci does not solely correlate with DSB formation under certain conditions. ATM- and Rad3-related (ATR), another PIKK, is activated in response to replication stress-induced single-stranded DNA (ssDNA), which, in turn, phosphorylates H2AX (Fig.1 B). Therefore, there are some limitations in γ H2AX analysis to monitor DSBs at least in S-phase cells.

Oxidative stress induces γ H2AX in a different manner to IR

Non-homologous end-joining (NHEJ) is the prominent pathway for DSB repair in mammalian cells. To better understand the roles of NHEJ in DDR to IR in humans, we characterized a series of mutant cell lines deficient for NHEJ-related genes generated by gene targeting in the human cell line HCT116 [1]. *XRCC4* is one of the key components of NHEJ and the *XRCC4*-deficient (*XRCC4*^{-/-})



cells are seriously incompetent in the repair of DSBs. Consistent with the close relationship between γ H2AX foci and DSBs, X-ray-induced γ H2AX foci disappeared more slowly in *XRCC4*^{-/-} cells than in parental HCT116 cells [1]. Remarkably, γ H2AX induced by oxidative stress in H_2O_2 -treated HCT116 and *XRCC4*^{-/-} cells displayed several different features from those induced by IR [2]. Firstly, oxidative stress-induced γ H2AX commonly appeared as gross nuclear-wide immunoreactive signals but did not as distinct 'foci' (Fig.2 A-L). Secondly, oxidative stress-induced γ H2AX decreased as fast in NHEJ-deficient *XRCC4*^{-/-} cells as in NHEJ-proficient HCT116 cells (Fig.2 M, N). If γ H2AX is correlated with DSB formation and repair, it would decrease more slowly in *XRCC4*^{-/-} cells than in HCT116 cells. Lastly, γ H2AX appeared in a biphasic mode following oxidative stress in both HCT116 and *XRCC4*^{-/-}

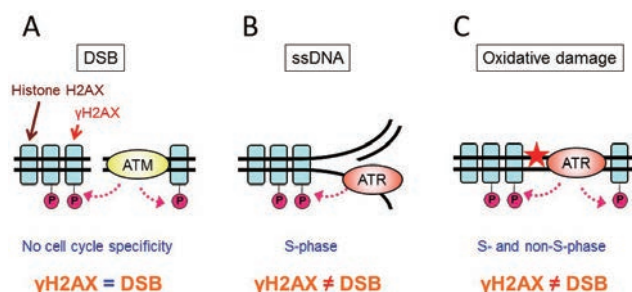


Fig.1 Schematic representation of γ H2AX inducing pathways in response to DNA damages. (A) ATM mediates the phosphorylation of H2AX in response to DSBs. This process can take place in every cell phase. (B) ATR mediates H2AX phosphorylation in response to ssDNA mostly arising from replication fork stalling during the S-phase. (C) Hydrogen peroxide or oxidative stress induces γ H2AX, which is mediated by ATR and not dependent on DSBs.

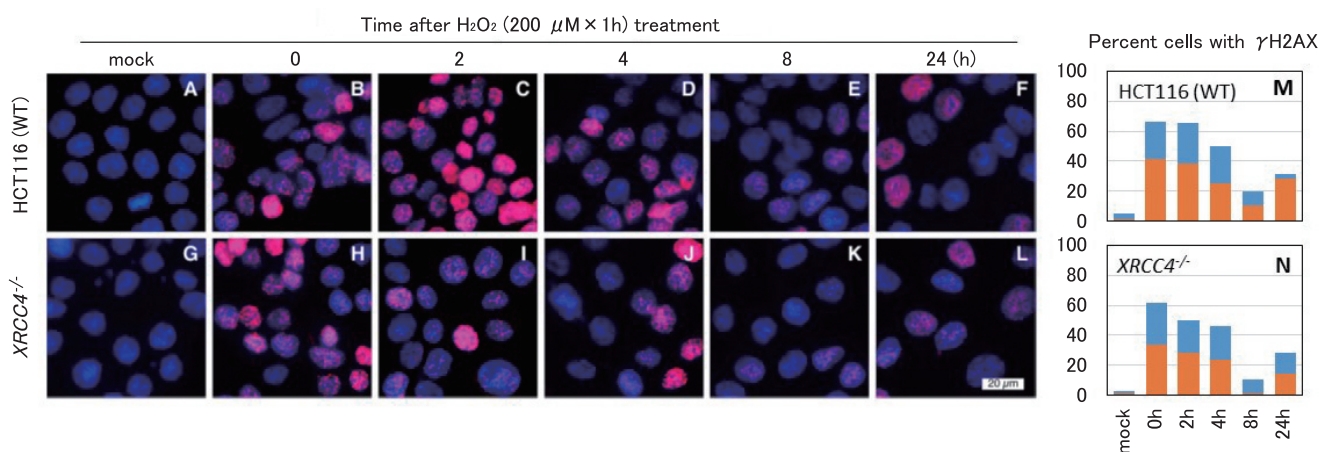


Fig.2 Nuclear foci formation and loss of γ H2AX in HCT116 (A-F) and its NHEJ-deficient derivative, $XRCC4^{-/-}$ cells (G-L), following exposure to H_2O_2 . Cells were treated with $200 \mu M H_2O_2$ for 1 h, further incubated in complete medium, fixed at indicated time points and then immunostained with an anti- γ H2AX antibody (red). Nuclei were counterstained with DAPI (blue). Scale bar = $20 \mu m$. (M, N) Cells with γ H2AX expression were examined at each time point. Orange columns indicate cells with an intense γ H2AX signal extending over half the area of the nucleus. Blue columns show cells with more than 5 γ H2AX foci. More than 189 cells were scored for each time point of both cell types. Modified from figures in [2].

cells (Fig.2). Reinduction of γ H2AX foci was a unique observation for cells exposed to H_2O_2 and was not observed in cells exposed to IR. This result suggested that γ H2AX foci observed in H_2O_2 -treated cells must be induced by a different mechanism than those in cells exposed to IR.

ATR is the major kinase inducing γ H2AX following oxidative stress

ATM and ATR are the main kinases that phosphorylate H2AX in the damage response to DSBs or ssDNA, respectively (Fig.1 A and B). To examine the participation of these kinases in the damage response following the H_2O_2 ($200 \mu M$) treatment, we analyzed the induction of γ H2AX in the presence of specific inhibitors of ATM or ATR (Fig.3). When cells were cultured with a ATM inhibitor (ATMi, KU-55933), γ H2AX was underexpressed immediately after the 1 h treatment (0 h), while its expression was equivalent to that in control cells without a kinase inhibitor 2 h after the treatment or later. The reappearance of γ H2AX was not affected by ATMi 24 h after the treatment. On the other hand, the phosphorylation of H2

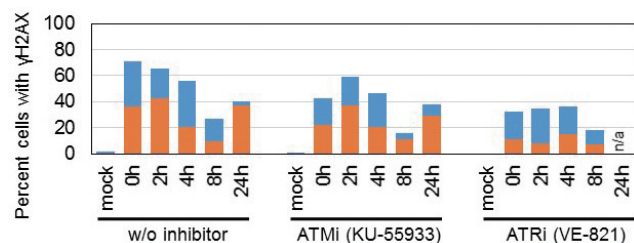


Fig.3 Impact of ATM and ATR on the formation of γ H2AX following the H_2O_2 treatment. HCT116 cells were treated with H_2O_2 ($200 \mu M$) for 1 h in the presence of ATM or ATR inhibitors (KU-55933 or VE-821, respectively). γ H2AX analysis was performed and the percent of cells with γ H2AX expression was shown as described in Fig.2. Orange columns indicate cells with an intense γ H2AX signal and blue columns show cells with more than 5 γ H2AX foci. Data for 24 h after the H_2O_2 treatment with VE-821 were not available because most cells were lost during the immunostaining process. Modified from figures in [2].

AX in responses to H_2O_2 was largely disturbed by the presence of ATR inhibitor (ATRi, VE-821). A very large fraction of cells at 24 h after the H_2O_2 treatment with ATRi became detached from glass coverslips during the immunostaining process of the fixed sample, most probably because of cell death. Western blot analyses of prominent substrates for ATM or ATR showed that ATR was activated but ATM was not by $200 \mu M H_2O_2$ (details are in [2]). These results demonstrated the predominant participation of ATR, rather than ATM, in the oxidative stress response. Cell cycle analysis by pulse labeling of S-phase cells with 5-ethynil-2'-deoxyuridine revealed that the γ H2AX was induced in both S- and non-S-phase cells following the H_2O_2 treatment (details are in [2]). Therefore, γ H2AX must be induced in different mechanisms in response to replication stress and to oxidative stress (Fig.1 B and C).

Conclusion

The present study demonstrated the biphasic induction of γ H2AX following oxidative stress-induced by the H_2O_2 treatment. The initial and later inductions of γ H2AX were primarily mediated by ATR and both were unlikely to associate with DSBs. Reinduction of γ H2AX 24 h later can be associated with cellular senescence, because oxidative stress closely associates with organismal aging. Oxidative stress also contributes to many aspects in biological responses to IR, such as inflammation. Hence, we cannot rule out the possibility that oxidative stress induced γ H2AX affected the results of γ H2AX analysis monitoring DSBs following IR. To improve the reliability of γ H2AX analysis, further understanding for γ H2AX induction following oxidative stress is needed.

References

- [1] Katsube T, Mori M, Tsuji H, *et al.*: Differences in Sensitivity to DNA-damaging Agents between $XRCC4^{-/-}$ and Artemis-deficient Human Cells. *J Radiat Res* 52, 415-424, 2011.
- [2] Katsube T, Mori M, Tsuji H, *et al.*: Most hydrogen peroxide-induced histone H2AX phosphorylation is mediated by ATR and is not dependent on DNA double-strand breaks. *J Biochem*, doi: 10.1093/jb/mvu021,2014.

Highlight

Radiation monitoring at the summit of Mt. Fuji for the study of high-altitude radiation environment

Kazuaki Yajima

E-mail: k_yajima@nirs.go.jp

Introduction

Aircrews are exposed to elevated levels of cosmic radiation at aviation altitudes because the dose rate of cosmic radiation increases with altitude. The ICRP has recommended in ICRP Publication 60 that the cosmic radiation exposure of commercial jet crews should be included in the category of occupational exposure. The Radiation Council of the Japanese government established a guideline for the management of cosmic radiation exposure of air crews in 2006. From 2007 NIRS started to help airlines to assess the annual dose of their aircrews to follow the guideline. The aviation route doses which are used for the assessment of the aircrew annual effective doses are calculated by the NIRS as a contracted service using an originally developed program called "JISCARD EX" [1]. The guideline requests the airlines to prepare an appropriate correspondence to the additional dose due to solar flares by using a forecasting method such as a space weather forecast. Actually, outbreaks of solar flares do not directly cause an additional dose to aircrews, but a dose increasing phenomenon called Ground Level Event (GLE), which occurs when energetic solar particles emitted by solar flares arrive at the Earth's atmosphere, cause it. GLE has occurred once a year during the past 70 years on average.

The purposes of this study are to improve the reliability of the evaluation of aircrew doses using numerical model calculations and to prepare for evaluation of the additional dose at a GLE outbreak. From 2007 we started cosmic radiation measurements at the Mt. Fuji automated weather station (Fig. 1) with the support of the NPO "Valid Utilization of Mt. Fuji Weather Station". This weather station is 3,776 m above sea level, and is a suitable observatory for high-altitude cosmic radiation studies [2, 3]. From 2010, construction began for a radiation monitoring system that can be used for annual continuous observations at the Mt. Fuji automated weather station. In this highlight, we outline the radiation monitoring system and summarize some of the monitoring data obtained by it in 2013.

Materials and methods

The radiation monitoring system was installed on the second floor of the Mt. Fuji automated weather station. It consists of a



moderator-type neutron rem meter (FHT 762 WENDI-2, Thermo Fisher Scientific Inc.), a data logger / controller (NM10, Melex Ltd.), a long-distance wireless local area network (WLAN) router, a directional Uda-Yagi antenna and two types of battery power units with Li-ion batteries and lead-acid batteries, respectively. A photo of the radiation monitoring system is shown in Fig. 2. The Wendi-2 is suited to measure cosmic-ray induced neutrons (cosmic neutrons) since it responds to a wide energy range from 25 meV to 5 GeV. A long-distance WLAN receiving system composed of the long-distance WLAN router, the directional Uda-Yagi antenna, and a data receiving program which runs on a Windows PC and a CATV Internet connection device was installed in the Fuji observatory of Nagoya University. The two directional Uda-Yagi antennas were precisely set oppositely facing each other. The distance between the Mt. Fuji automated weather station and the Fuji obser-



Fig. 1 A photo of the Mt. Fuji automated weather station on the summit of Mt. Fuji at an altitude of 3,776 m.

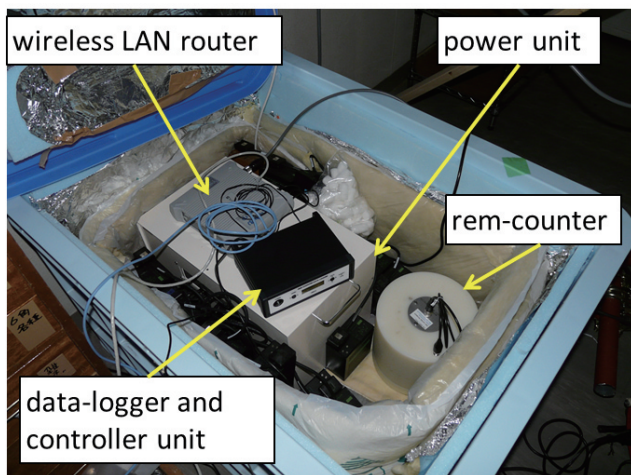
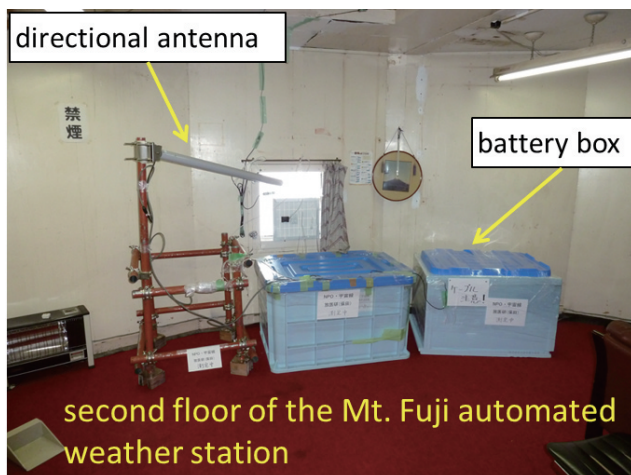


Fig.2 The photo of the radiation monitoring system which was installed on the second floor of the Mt. Fuji automated weather station.

vatory is about 13 km. The radiation monitoring system connects the long-distance WLAN receiving system via the long-distance WLAN, and the monitored data at the Mt. Fuji automated weather station are sent to the data receiving program which runs on a Windows PC at the Fuji observatory. The long-distance WLAN receiving system has an Internet connection. Therefore at NIRS, we can obtain the data monitored at the Mt. Fuji automated weather station.

Results and discussion

Fig.3 shows the neutron count per hour (cph) measured using the WENDI-2 at the Mt. Fuji automated weather station from August 22, 2013 to March 12, 2014, and the atmospheric pressure there during the same period. The atmospheric pressure data were obtained from the Japan Meteorological Agency web site. The reason for measuring neutrons in this study is that cosmic neutrons are the main contributor to cosmic radiation exposure. In the measurement period, the measured neutron count rate changed with approximately 20% variance between 100 - 150 cph. In general, we consider the neutron count rate changes gently. A negative correlation is clearly seen between the neutron count rate and the atmospheric pressure. This is because the absorption in the atmosphere of cosmic neutrons increases as the upward atmosphere thickens.

Monthly averages of the change in a day of the neutron count

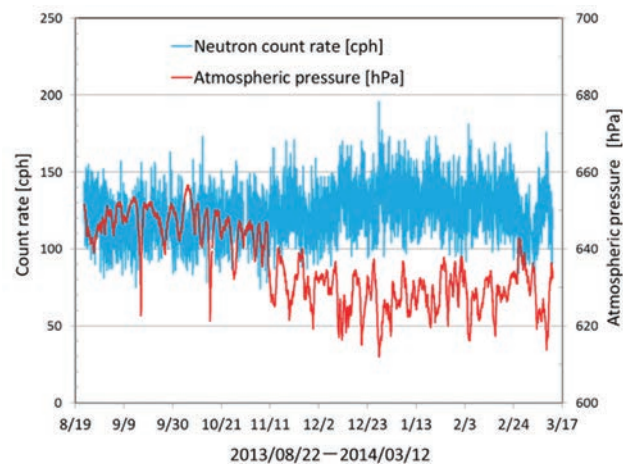


Fig.3 The neutron count per hour measured using the WENDI-2 at the Mt. Fuji automated weather station from August 22, 2013 to March 12, 2014, and the atmospheric pressure there for the same period.

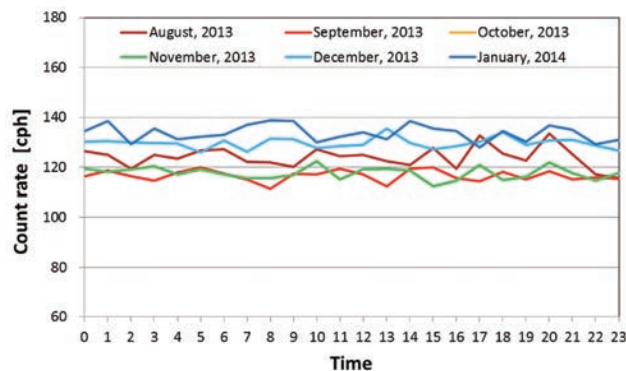


Fig.4 Monthly averages of the change in the day of the neutron count rate from August 2013 to January 2014.

rate from August 2013 to January 2014 are shown in Fig.4. A difference in neutron count rate level according to the month was apparent. No correlation was seen between the neutron count rate and the change in a day.

At present, the atmospheric pressure seems to have a dominant effect on the change of the neutron count rate. We intend to investigate other factors which may be buried in the atmospheric pressure influence in the future. The current monitoring system may detect a GLE with more than 40% of increases in counting rate per hour. We think that the accomplishment of the annual continuous monitoring is a prior problem now because no one knows when a GLE will occur.

References

- [1] Yasuda H, Sato T, Yonehara H, *et al.*: Management of cosmic radiation exposure for aircraft crew in Japan, *Radiat Prot Dosim* 146, 123-125, 2011.
- [2] Yajima K, Yasuda H: Measurement of cosmic-ray origin neutrons using a scintillation detector at the summit of Mt. Fuji, *Radiat Meas* 46, 1724-1727, 2011.
- [3] Yasuda H, Yajima K, Yoshida S: Dosimetry of cosmic radiation in the troposphere based on the measurements at the summit of Mt. Fuji, *Proc Radiochim Acta* 1, 67-70, 2011.

Highlight

Methodological extensions of meta-analysis with excess relative risk estimates

Kazutaka Doi, Yoshiya Shimada,
Hidenori Yonehara, Shinji Yoshinaga

E-mail: kazutaka@nirs.go.jp

Introduction

Excess relative risk (ERR) is categorized as a relative excess measure and is often used as an effect measure in the analyses of radiation epidemiological data. If ERR values have been derived from a linear dose-response analysis, they are often expressed as a relative increase in rates per unit dose, e.g., ERR per Gy. In this highlight, we refer to ERR per Gy as ERR for simplicity.

Numerous studies have shown that the ERR of solid tumors per unit of radiation is much higher in children than adults, meaning children are more sensitive to the carcinogenic effects of radiation than adults. The exceptions to this finding are cancers of several sites. However, the dose-response relationship between radiation and the long-term effects of radiation in childhood are poorly quantified. In addition, the small numbers of subjects in each study have limited evaluation of the risk of second malignant neoplasms (SMNs) after radiotherapy.

Previously, we evaluated the risk of SMN using a meta-analysis of nine studies in which ERR estimates were presented [1]. However, such a small number of eligible studies available restricted detailed quantitative evaluations. Additional studies in which risk estimates were expressed in terms of relative risks such as rate ratio, hazard ratio, or odds ratio per several dose categories were available; however, due to non-comparability of data, these studies were not included in the meta-analysis.

The objective of the present work was to develop a method to calculate ERR estimates from other forms of risk estimates. Using this new method, we conducted a meta-analysis of 26 studies and examined additional detailed evaluations of SMN risk according to study characteristics. We especially focused on age-related variability of radiation effects.

Method

We proposed a method for estimating ERR from studies in which relative risk estimates such as odds ratio, incidence rate ratio, or hazard ratio are calculated by dose category. We consider a study in which relative risk estimates for several dose categories are available. We assume the relative risk estimate, confidence limits, and representative dose for each dose category are available. The standard error (SE) of the estimate is calculated from



the relative risk estimate and confidence limits. Regarding the relative risk estimate and representative dose as data, we fit a linear regression model in which the intercept is fixed at 1 and the slope of the model corresponds to ERR (Fig.1). The SE of the estimate is obtained through a parametric bootstrap method.

Meta-analysis of second malignant neoplasms risk in childhood cancer survivors

Relevant studies were identified by a systematic search of the literature using the PubMed database (from 1950 to 2009). We used Medical Subject Headings (MeSH), a large controlled vocabulary developed for indexing journal articles and books on the

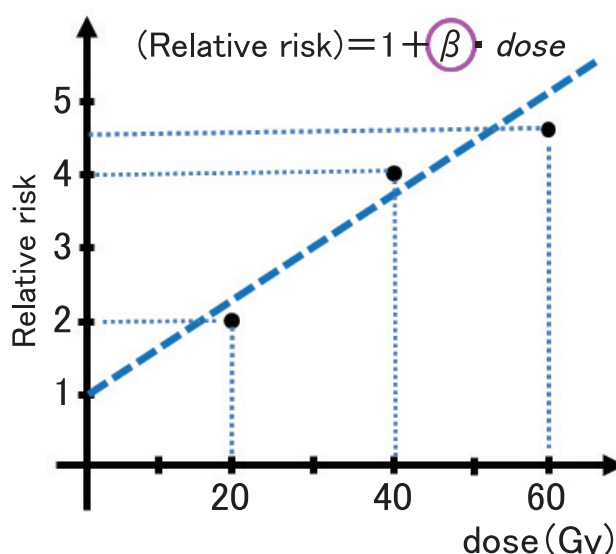


Fig.1 Illustration of our method: The slope of the regression model corresponds to ER

life sciences, to retrieve studies indexed using the MeSH terms “neoplasms, second primary” and “radiotherapy.” After performing the initial search using these MeSH terms, additional studies were retrieved with a standard keyword search using the terms “paediatric/pediatric” or “childhood.” The computer search was supplemented by hand-searching reference lists of already retrieved papers. The titles and abstracts of all studies were scanned to exclude irrelevant publications.

The following inclusion criteria were used to determine the studies for the meta-analysis: (1) the endpoint of the study should be SMN risk among childhood cancer survivors, (2) the study design should be either a cohort study or a case-control study, (3) risk estimates should be expressed in terms of ERR (or ERR was calculable from category-specific risk estimates including rate ratio, hazard ratio, and odds ratio), and (4) sufficient data should be present in the publications to enable estimation of the SE of the ERR estimates. If the publication was an earlier report of data that was subsequently updated in another article, it was excluded from the analysis.

Generally, logistic regression analysis is utilized for case-control studies, and Poisson and Cox regression analyses are utilized for cohort studies, and risk estimates obtained from these regression models are stated as an odds ratio, rate ratio, or hazard ratio. Following our previous study that included randomized controlled trials (risk ratio), case-control studies (odds ratio), and cohort studies (rate ratio), we treated ERR estimates from odds ratios, rate ratios, and hazard ratios equally and included them in the meta-analysis.

Result

We selected 198 studies in the first step of the systematic literature search using MeSH terms and keywords. Of these, we excluded 180 studies that did not satisfy all of the inclusion criteria. We added 10 studies to the pool of eligible studies by conducting a hand search. Two studies, one that used data reported earlier but included in a subsequent article and one that used identical data, were excluded. Eventually, we identified 26 epidemiological studies. Among these studies, ERR estimates were available for 15 studies, and ERR estimates were calculable for 11. There is a study in which ERR estimates for more than one site are available, and we ultimately included 27 ERR estimates in the meta-analysis gleaned from the 26 eligible studies.

The results from the meta-analysis are presented in Table 1. The overall ERR using all studies included in the meta-analysis was 0.60 (95% CI: 0.30, 1.20; n = 27). The overall estimate of ERR from

the cohort studies was 1.22 (95% CI: 0.45, 3.33; n = 13), and that from the case-control studies was 0.30 (95% CI: 0.12, 0.73; n = 14). The overall estimate of ERR from European studies was 0.74 (95% CI: 0.30, 1.83; n = 20), from the North American studies was 0.28 (95% CI: 0.07, 1.17; n = 5), and from both European and North American studies was 0.46 (95% CI: 0.06, 3.10; n = 2). The overall estimates of ERR according to SMN sites were as follows: thyroid, 3.01 (95% CI: 1.09, 8.35; n = 7); bone and soft tissue, 0.48 (95% CI: 0.03, 7.30; n = 4); breast, 0.31 (95% CI: 0.16, 0.59; n = 4); brain, 1.51 (95% CI: 0.10, 23.09; n = 4); and leukemia, 0.38 (95% CI: 0.004, 37.88; n = 2). The overall estimate of ERRs available in the original papers was 0.99 (95% CI: 0.43, 2.25; n = 16), and that calculated by the proposed method was 0.25 (95% CI: 0.08, 0.84; n = 11).

In the meta-regression model, which included age at primary cancer diagnosis as a covariate of main interest, the regression coefficient was -0.159 (95% CI: -0.293, -0.024), indicating a significant decrease in ERR with an increase in the age at primary cancer diagnosis (0.85 times [95% CI: 0.75, 0.98] per year). The analysis, which included the site of the SMN as a covariate in addition to the age at primary cancer diagnosis, also revealed a trend of decreasing ERR with increasing age at primary cancer diagnosis (0.92 times [95% CI: 0.78, 1.08] per year); however, this trend was not statistically significant.

Discussion

We proposed a method for calculating ERR estimates from dose category-specific risk estimates. Using this method, the number of studies included in the meta-analysis was increased from 15 to 27, thus enabling us to perform a separate analysis based on type of SMN. We could also quantify the dependence of ERR on the age at primary cancer diagnosis.

The increased number of studies included in the meta-analysis enabled us to evaluate the separate estimate for each type of SMN. The risk estimates of childhood thyroid cancer exposed to radioiodine after the Chernobyl accident have varied from 5.5 (95% CI: 3.1, 9.5) to 8.4 (95% CI: 4.1, 17.3), depending on the risk model[2]. The pooled risk estimate from five cohort studies of childhood thyroid cancer including studies of atomic bomb survivors and medically irradiated children is 7.7 (95% CI: 2.1, 28.7) [3]. In our work, the overall estimate for thyroid was 3.01 (95% CI: 1.09, 8.35; n = 7), and compatible with these studies.

With the methods developed to calculate ERR, we have conducted a meta-analysis that includes a greater number of studies about SMN risk among childhood cancer survivors than was previously possible. From the detailed evaluation, some factors which may explain heterogeneity were suggested, such as age at which the cancer is first diagnosed. For further evaluation of how the age impacts ERR, further studies should include patients who are irradiated in adulthood in addition to childhood.

References

- [1] Doi K, Mieno MN, Shimada Y, *et al.*: Risk of second malignant neoplasms among childhood cancer survivors treated with radiotherapy: meta-analysis of nine epidemiological studies, *Paediatr Perinat Epidemiol* 23, 370-379, 2009.
- [2] Cardis E, Kesminiene A, Ivanov V, *et al.*: Risk of thyroid cancer after exposure to ¹³¹I in childhood, *J Natl Cancer Inst* 97, 724-732, 2005.
- [3] Ron E, Lubin JH, Shore RE, *et al.*: Thyroid cancer after exposure to external radiation: a pooled analysis of seven studies, *Radiat Res* 141, 259-277, 1995.

Table 1 Results from the meta-analysis

	ERR estimate	95% CI
Overall (n = 27)	0.60	0.30-1.20
Cohort studies (n = 13)	1.22	0.45-3.33
Case-control studies (n = 14)	0.30	0.12-0.73
European studies (n = 20)	0.74	0.30-1.83
North American studies (n = 5)	0.28	0.07-1.17
European and north American (n = 2)	0.46	0.06-3.10
Thyroid (n = 7)	3.01	1.09-8.35
Bone and soft tissue (n = 4)	0.48	0.03-7.30
Breast (n = 4)	0.31	0.16-0.59
Brain (n = 4)	1.51	0.10-23.09
Leukemia (n = 2)	0.38	0.004-37.88
ERR available (n = 16)	0.99	0.43-2.25
ERR calculated (n = 11)	0.25	0.08-0.84

Research on Radiation Emergency Medicine

Katsushi Tajima, Ph.D.

Director, Planning and Promotion Unit, Research Center for Radiation Emergency Medicine

E-mail: tajima@nirs.go.jp

Introduction

Radiation emergency medicine research programs are aimed at providing the best possible treatment to anyone involved in radiation accidents, anytime and anywhere. All of our efforts are made to attain this ultimate goal. Specifically, we are focusing our efforts on three projects (Fig. 1). The first project is directed toward developing and modifying the most appropriate methodologies for evaluating radiation exposure, especially contamination by actinides accompanied by trauma. The term “actinide” refers to 14 heavy-metal elements (atomic numbers 90 - 103) with unique behavior, including high radioactivity and alpha-ray emission. The second project is aimed at exploring and supplying effective drugs to reduce the radiotoxicity and metallic toxicity of internal actinide contamination. In Japan, only NIRS has been authorized to accept these two projects using actinides, including uranium and plutonium. The third project is targeted at the application of mesenchymal stem cells (MSCs) as regenerative medicine to treat radiation exposure injuries. MSCs can differentiate into various normal tissues and support regeneration of damaged tissue. Tissue regeneration failure is characteristic of radiation injury, and therefore, the application of MSCs to treat this injury is reasonable.



Here, we outline our proposed research projects with special emphasis on their significance.

1. Research project for radiation dosimetry

Accurate and rapid dose evaluations are needed in radiation accidents, especially in those involving patients who are expected to be highly exposed. One of the challenging tasks is the dose evaluation for internal contamination with actinides as represented by plutonium (Fig. 2). Most of the actinides are alpha emitters and it is difficult to quantify their radioactivity once they are incorporated into the body. We have been developing new measuring techniques to meet requirements in radiation emergency medicine, such as a high throughput bioassay method using an inductively-coupled plasma mass spectrometer (ICP-MS) and an

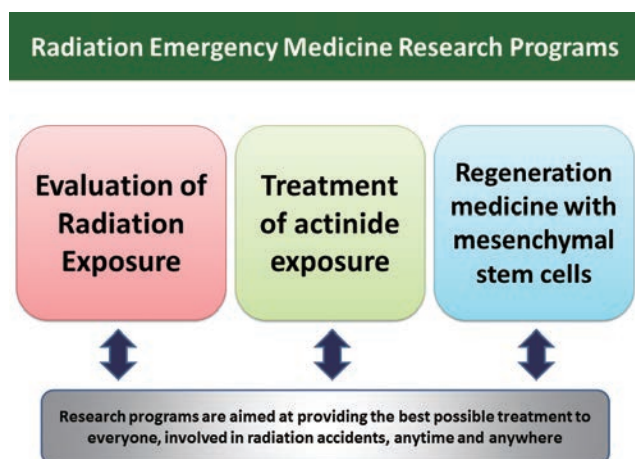


Fig.1 Outline of Radiation Emergency Medicine Research Programs

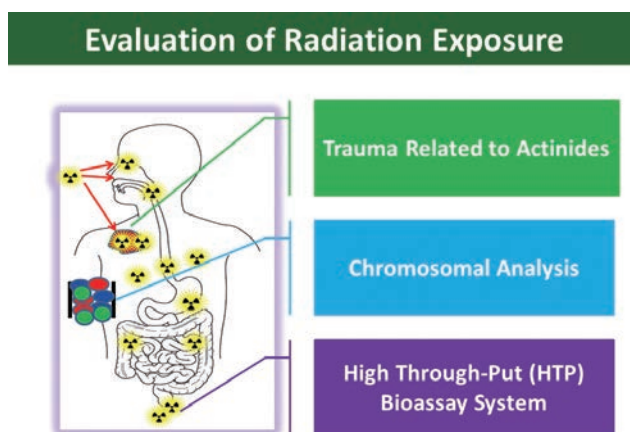


Fig.2 Research Project for Radiation dosimetry

automated organic destruction system and a rapid actinide measuring method for various samples using X-ray fluorescence instruments. We also have been studying a computational calibration technique for in vivo counters measuring the actinides, a biokinetic model that can be used in actinide internal contamination with chelation therapy, and so on.

Chromosomal analyses are also useful methods for evaluating radiation exposure. These methods are used to evaluate specific chromosome aberrations as eventual outcomes from biological reactions derived from radiation exposure. Chromosomal translocation may be stable in peripheral blood cells for a long period of time, and thus exposure doses can be retrospectively evaluated. We will modify these established methods.

2. Research project on the treatment of actinide exposure

Actinides have high alpha-ray radioactivity and a relatively long half-life. Once an actinide enters the body, it is retained in the target organ where it has radiologic and metallic toxic effects for a long time. The treatment strategy comprises two or three steps (Fig.3). The initial step should be designed to remove the actinide by local resection. This procedure is not always possible for every accident case, however, due to widely or deeply contaminated lesions or unresectable body areas. In this case, only a chelating reagent such as diethylenetriaminepentaacetic acid (DTPA) is currently available. The pharmacokinetics of free-DTPA indicates that it has a short half-life in peripheral blood (about 1 hour) and poorly penetrates into cells. Therefore, we require new drug classes, new agents, and new uses of the currently available agents for use in actinide-related accidents.

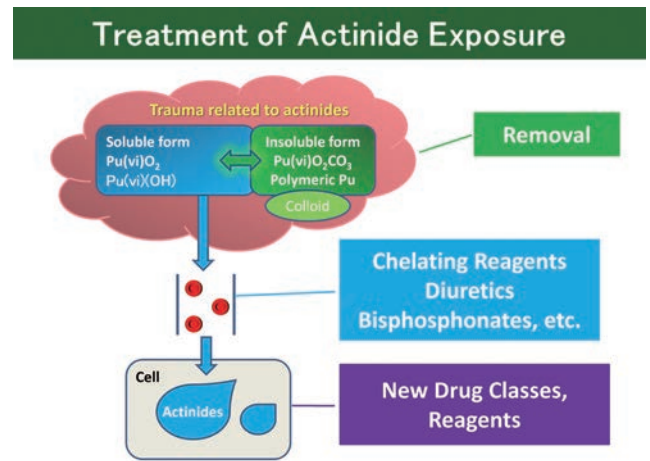


Fig.3 Research Project for Treatment of Actinide Exposure

3. Research project on regeneration medicine with mesenchymal stem cells

Radiation-injured tissues are characteristically resistant to tissue regeneration. In effect, tissue regeneration requires tissue stem cells that differentiate into normal cells suitable to repair or replace the damaged tissues. In a number of animal models, MSCs injected into the radiation-injured tissues might contribute to tissue regeneration mainly through humoral factors or cell-to-cell contacts (Fig.4). Therefore, we will investigate the molecular mechanisms of MSCs, and work to obtain beneficial molecules and evaluate the efficacy and safety of these molecules in vivo using animal models, for eventual application in a clinical setting.

Regeneration medicine with mesenchymal stem cells

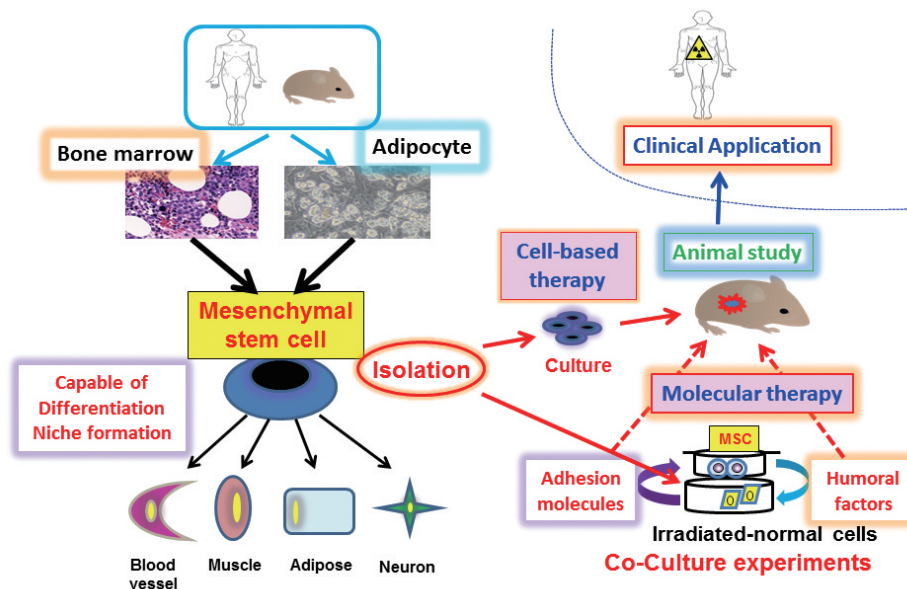


Fig.4 Research Project for Regeneration Medicine with Mesenchymal Stem Cells

Highlight

Radiation increases the cellular uptake of exosomes through CD29/CD81 complex formation

Katsushi Tajima

E-mail: tajima@nirs.go.jp

Exosomes, bilipid membrane vesicles (30-100 nm in diameter) that originate in multi-vesicular bodies and are released into the extracellular milieu upon fusion with the plasma membrane, are attracting increased attention. Exosome secretion is a cellular mechanism for delivering cargo to mediate intercellular communication and to affect biologic function by the exchange of proteins and lipids, or the delivery of genetic materials to recipient cells. Exosomes are also involved in various other cellular functions and pathophysiologic states, and thus they could potentially provide a new approach for detecting noninvasive disease and predicting disease progression. Moreover, exosomes have properties that can be exploited for therapeutic interventions as a new drug delivery system and a novel therapeutic tool under various conditions, including cancer, inflammation, ischemia, and regeneration.

Tumor cells and their cancer-associated microenvironment, comprising fibroblast-like cells, the extracellular matrix, and inflammatory cells, secrete exosomes between them, allowing for crosstalk that leads to the promotion or inhibition of tumor progression, but the precise mechanism of communication is poorly understood. Mesenchymal stem cells (MSCs), clusters of multipotential fibroblast-like cells present in every organ as well as in the tumor stromal microenvironment, have regenerative and protective effects for injured tissues, and they inhibit or promote tumor metastasis with their secreted exosomes, but the underlying mechanism is not clearly understood. Potential applications of MSCs and their secreted exosomes are currently attracting attention in a number of medical fields, such as oncology, immunology, and radiation therapy.

Radiation and drug therapy are currently the main therapeutic tools for a number of diseases. Radiation therapy not only acts on target cells, but also affects the stromal microenvironment. Thus, understanding how radiation affects cellular uptake and the secretion of exosomes between target cells and stromal cells is crucial.

Recent studies of exosome biogenesis revealed that exosomes originate from endosomal proteins involved in membrane trans-



port and fusion in processes requiring heat shock proteins, integrins, and tetraspanins, and that the source of exosomes defines their function. For therapeutic applications of exosomes, especially those derived from MSCs, the target cells must effectively internalize the exosomes. Several mechanisms of exosome uptake involving their surface molecules have been described and two distinct modes of internalization have been suggested (Fig. 1). In monocytes and macrophages, exosome internalization depends on the actin cytoskeleton and phosphatidylinositol 3-kinase regulated by dynamin2, and non-phagocytic cells require an energy-dependent pathway, including caveolae, macropinocytosis, and clathrin-coated vesicles. The effects of radiation on exosome uptake processes, however, remain unknown. More detailed knowledge of the mechanisms of cellular uptake and the effects of radiation on these processes is needed to promote the effective use of exosomes and MSCs as potential therapeutic tools. A better understanding of the processes involved will be instructive for modifying exosomes to be preferentially targeted in pathologic conditions by bioengineering. We have addressed several essential questions relating to the basic cellular uptake of exosomes and how radiation regulates that process, with a focus on target cell ligands. Our findings revealed that radiation leads to the colocalization of integrin (CD29) and tetraspanin (CD81) and increases the cellular uptake of exosomes (Fig. 2) [1].

References

- [1] Hazawa M, Tomiyama K, Saotome-Nakamura A, *et al.*: Radiation increases the cellular uptake of exosomes through CD29/CD81 complex formation, *Biochem Biophys Res Commun*, doi.org/10.1016/j.bbrc.2014.03.067.

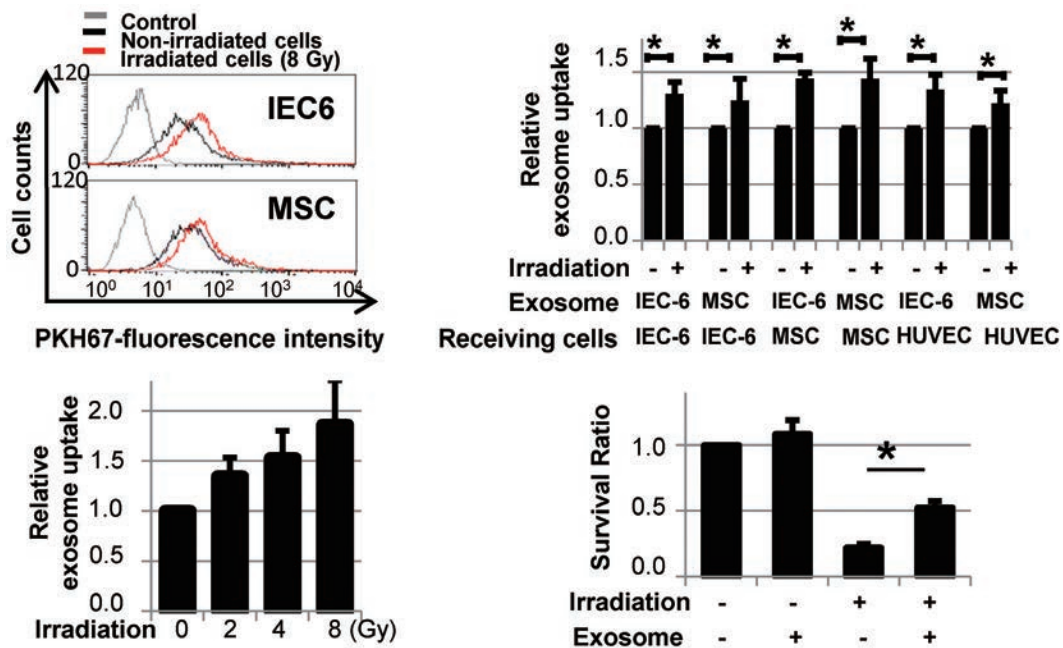


Fig.1 Radiation increases the cellular uptake of exosomes and effect of exosomes on irradiated cell viability. (A) Irradiated-recipient cells (8 Gy) and labeled-exosomes from MSC were incubated for 16 hours. Representative cytograms were shown. (B) 2 to 8 Gy irradiated-cells were incubated with the labeled-exosomes for 16 hours, and analyzed by FCM. (C) The radiation-induced cellular uptake of exosomes was not dependent on the recipient cell type. The experiments were performed three times. Value represent mean +/- SD. Non-irradiated control group was set to 100%, and mean fluorescent intensity was calculated. * $p < 0.05$ versus non-irradiated control group: Mann-Whitney Utest. (F) Exosomes from MSCs were added and incubated with previously irradiated cells (8 Gy) for 24 hours. Viable cells were detected by the trypan blue exclusion method. The cell viability experiments were repeated three times. Data are normalized to non-irradiated control group cells. All experiments were repeated three times. * $p < 0.05$.

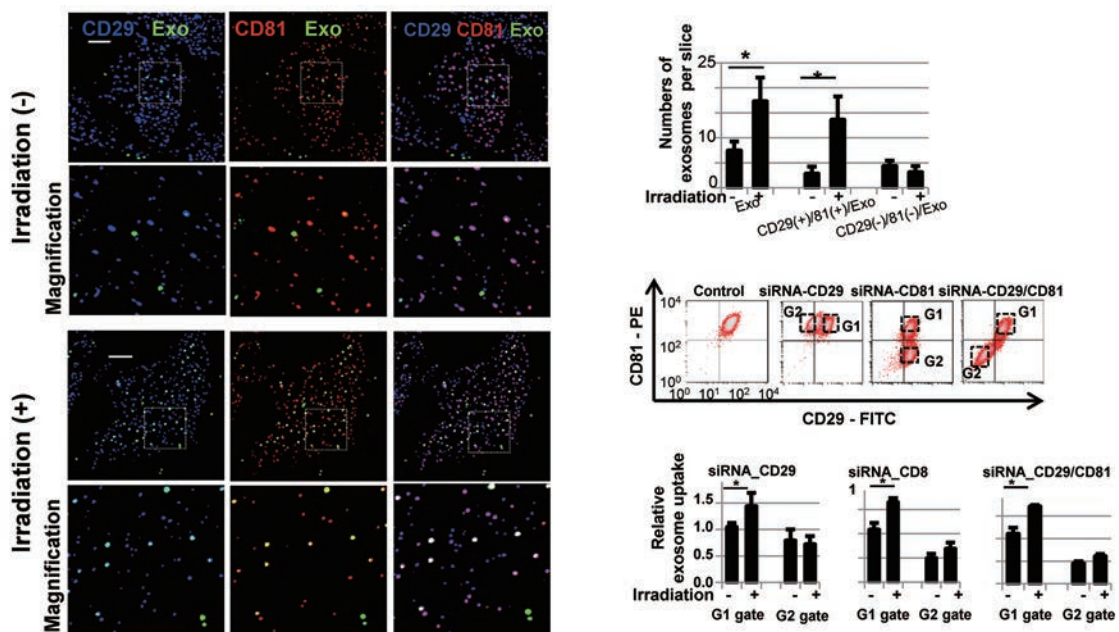


Fig.2 Exosomes bind to the CD29/CD81 complex. (A) 8 Gy irradiated cells were incubated with CellVue-labeled exosomes for 1 hour, and washed three times with PBS and fixed in 4% paraformaldehyde. Antibodies against CD29 and CD81 were reacted without cells permeabilization. Exosomes (green) more colocalized CD29 (blue) and CD81 (red) on radiation exposure. Exosomes preferentially bind to the CD29/CD81 complex, leading to merged signals (white). Representative figures were shown. (B) Histograms showed the numbers of attached-exosomes per slice (1 slice = 1 cell). Exosome column: the number of exosomes+ (green) signals per slice, exosome+/CD29+/CD81+ column: the numbers of three merged signals (white) per slice, other column: the numbers of exosome+/CD29(-)/CD81(-) signals per slice. The numbers of each column were based on 8 images from three independent experiments. * $p < 0.05$ by Student t-test. White bar: 10 mm. (C) The transient gene knockdown experiments against CD29 and CD81. MSCs were transfected with siRNA for 48 hours, and cell surface CD29/CD81 and exosomes uptake assay were performed with or without radiation. In this assay, an intact-cell population (G1-square gate: control) and an impaired-cell population (G2-square gate: knockdown) were divided. Each population was analyzed. (D) CD29 and/or CD81 knockdown abolished the radiation induced-effects on exosomes. All experiments were repeated four times. Control si RNA knockdown was set to 100%. * $p < 0.05$ by Student t-test.

Highlight

Preparation of agarose beads containing Prussian blue and magnetite for internal decorporation of radiocesium

Izumi Tanaka, Hiroshi Ishihara

E-mail: tanaka_i@nirs.go.jp, ishihara@nirs.go.jp

Objectives

Radiocesium nuclides generated during nuclear fission are contained in used nuclear fuels and nuclear wastes. For people who work in or around nuclear-related plants, there is some risk of accidental absorption of a large amount of radiocesium. The risk of internal contamination also present, since improper operations or acts of terrorism can result in release of ^{137}Cs from the strongly reinforced containers that are used in industries and in hospitals as gamma-ray sources. When internal radiocesium contamination occurs in humans, and the committed dose of the internal exposure reaches more than 300 mSv [1], decorporation treatment by the use of Prussian blue should be considered. Although Radiogardase[®] is available as an approved drug, improvement of the drug preparation is possible. We propose an example drug preparation of Prussian blue for radiocesium decorporation, based on the current concept to minimize the risk with the use of a drug.

Introduction

Cesium is an alkaline metal and it exists as an ionic water-soluble form in the body. Ingested radiocesium moves rapidly into the circulation system, is distributed in the body, and is accumulated in cells. Due to the difference in the tissue-specific retention time, cesium migrates among organs via the circulation system. Because intracellular cesium in skeletal muscle cannot be easily excreted, the biological half-time of the body-burden is long. The major excretion pathway of intracorporeal radiocesium is via the urinary excretion system from the circulation system. Although certain amounts of radiocesium are secreted into the gastrointestinal (GI)-tract, most of the radiocesium is reabsorbed in the intestine and returned to the circulation system. When insoluble carrier that can tightly bind with the radiocesium flows through the GI-tract cavity to become feces, the total excretion rate of radiocesium is enhanced. The reinforcement of the excretion pathway accelerates total excretion of radiocesium, and contributes to a decrease in the level of internal exposure. In the ^{137}Cs internal contamination accident in Goiania in 1987, Prussian blue was given to patients as the insoluble carrier to remove radiocesium, and its efficacy has been proven [2].



Radiogardase[®] capsule, the only approved drug for humans for radiocesium decorporation, have been developed in 1970s. However, with the current pharmaceutical concept that seeks the comfort of patients and protection of nursing staff and the natural environment, the drug is considered to have two problems. First, a Radiogardase[®] capsule contains multiform rectangular parallelepiped and rigid minerals in various sizes from approximately 0.1 μm to 5 mm of Prussian blue crystals (chemical formula: $\text{Fe(III)}_4[\text{Fe(II)}(\text{CN})_6]^{3-} \cdot 14 \text{ to } 16 \text{ H}_2\text{O}$), and this physical form is irritating to the mucosal tissue of the GI-tract in the patients. Second, after treatment of a patient, radioactive air-borne particles may be produced from the patient's excreted feces which contain nano-sized crystals bound with radiocesium. This occurs because the Prussian blue crystals in the radioactive feces are not always stable based on the chemical equilibrium of the crystal coordination lattice.

Results

To address these points, we made a hydrogel preparation of Prussian blue and magnetite [3]. Prussian blue nanocrystals (PBNC, $\text{Fe(III)}_4[\text{Fe(II)}(\text{CN})_6]^{3-} \cdot 200 \text{ to } 300 \text{ H}_2\text{O}$, approximately 100 nm in size) and magnetite [$\text{Fe(II)Fe(III)}_2\text{O}_4$] coated with silica (final average diameter of 350 nm) were dissolved into molten agarose gel. The spherical form of the gel was prepared by emulsification with sorbitan tristearate, water-in-oil detergent, in mineral oil as solvent. After sedimentation of gel in a magnetic field, oil and the detergent were removed. Fig.1 shows the spherical form preparation of agarose with Prussian blue and magnetite (APBM) particles with diameters from 10 to 100 μm .

Binding capacity (Fig.2a) with radiocesium in vitro for Radiogardase[®], PBNC or APBM was the same. Decorporation rate of PBNC or APBM in vivo was measured in mice which were internally contaminated with ^{137}Cs by oral administration. Fecal excre-

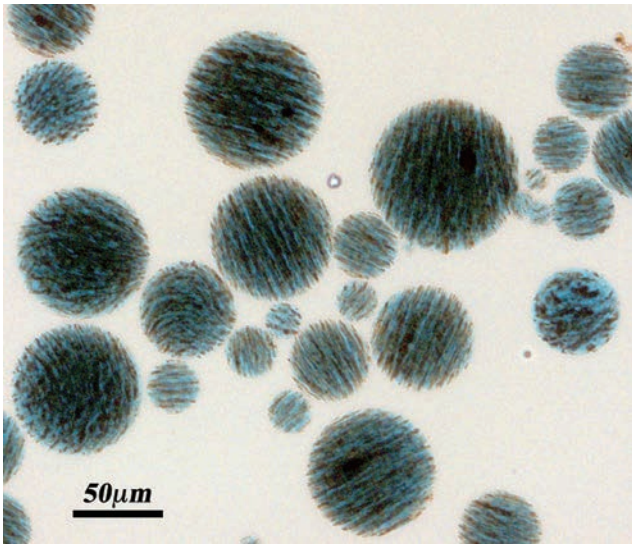


Fig.1 Agarose with Prussian blue and siliconized magnetite (APBM) particles.

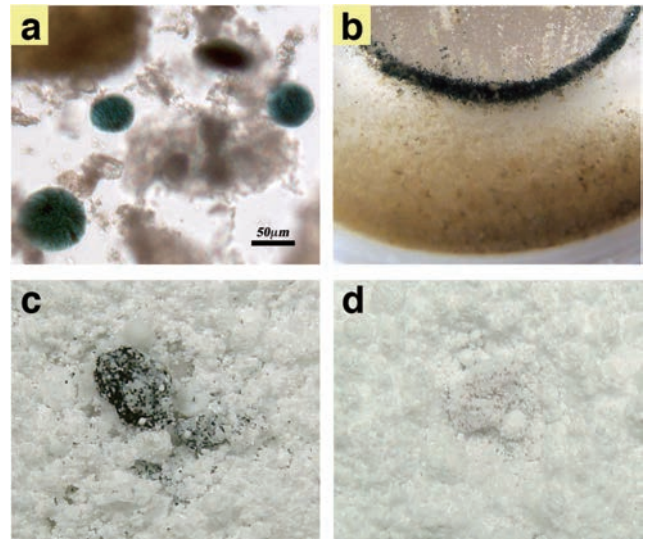


Fig.3 Photos of materials in the waste disposal process. a. APBM particles in the waste. b. Recovering of APBM particles from the waste using a magnet. c, d. APBM-particle waste before (c) and after (d) incineration at 800°C with zeolite.

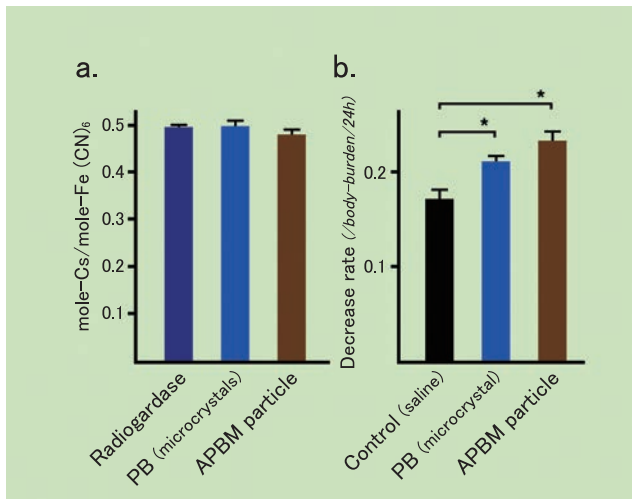


Fig.2 Adsorption of radiocesium by Prussian blue preparations. a. Prussian blue preparations were incubated at 37°C with CsCl containing ¹³⁷Cs at pH7.0 in vitro. The binding rates were calculated from the radioactivity in the supernatant. b. For the in vivo experiment, mice injected with ¹³⁷Cs were orally administrated with Prussian blue preparations (equivalent to 8.5 mg of 14 to 16 H₂O hydrate crystal of the coordination complex of Fe(III)₄[Fe(II)(CN)₆]₃ per kg body weight for 3 times in a day). The decrease rates of body-burden in 24h were compared. Bar: standard deviation, *: p<0.01 (Least significant difference).

tion rate was drastically enhanced by PBNC or APBM, while urinary excretion rate was decreased. Totally, the body-burden of radiocesium was significantly decreased by the treatments of PBNC

or APBM (Fig.2b).

The radioactive excreta were used as a sample of radioactive medical waste in a waste disposal site, to verify the utility of the methods, i.e. suppression of air-borne particles from the waste. The radioactive feces from mice were emulsified with benzethonium chloride as cationic detergent, and the APBM particles kept their shape in the suspension (Fig.3a). The radiocesium-bound APBM particles could be collected in a magnetic field (Fig.3b). Amounts of ¹³⁷Cs in the residue of the emulsified feces were minimal, suggesting further binding of free-radiocesium in urine occurred during the emulsification of the waste. When the collected APBM particles with debris of feces were incineration at 800°C with zeolite (SiO₂/Al₂O₃=6), radiocesium remained in the solid phase suggesting it was translocated from Prussian blue to the zeolite. All of the materials were ashed and stabilized (Fig.3c), so that they could be handled and stored in a waste disposal facility. The procedures may be applied to the treatment of excreted waste to suppress the release of radiocesium during long-term storage.

References

- [1] The Health Protection Agency, U.K.: Use of Prussian Blue, <http://www.hpa.org.uk>.
- [2] Melo DR, Lipsztein JL, Oliveira CAN, *et al.*: ¹³⁷Cs internal contamination involving a Brazilian accident, and the efficacy of Prussian blue treatment, *Health Phys* 66, 245-252, 1994.
- [3] Tanaka I, Ishihara H, Yakumaru H, *et al.*: Polyvinyl alcohol hydrogel preparations containing nanoparticles of magnetite and Prussian blue derivatives for internal decorporation of ¹³⁷Cs (*manuscript in preparation*)

Highlight

Accuracy investigation of whole body counters operated in Fukushima Prefecture

Takashi Nakano, Osamu Kurihara,
Eunjoo Kim

E-mail: nakano@nirs.go.jp

A whole body counter (WBC) is one of the *in vivo* measurement instruments that detect photons emitted from radionuclides in the body and also quantify the body content of the radionuclide identified. The basic principle of the WBC is to make relative measurements to a phantom imitating radioactivity in the whole-body or in a particular organ. Thus, it is necessary to calibrate the WBC using an appropriate phantom that contains a known amount of radionuclides.

In recent years, NIRS has been requested to perform an accuracy investigation of WBCs that have been operated in Fukushima Prefecture to measure radionuclides in residents exposed during the 2011 Fukushima Daiichi Nuclear Power Plant accident.

Here, we describe preliminary results of the accuracy investigation of 36 WBCs during FY 2012 to 2013.

The accuracy investigation of WBCs

The accuracy investigation in this work used a set of four BOMAB (Bottle MANikin aBSorption) phantoms specified by the ANSI standard [1]. These four phantoms are owned by NIRS and each contains one of three radioactive sources (Ba-133, Cs-137, or Co-60) or water (as a blank source). The radioactivities of the radionuclides in these phantoms were guaranteed by JCSS (Japan Calibration Service System); for example, the extended uncertainty of the radioactivity is 6.5% ($k=2$) for Cs-137. As shown in the photo of Fig. 1, each BOMAB phantom consists of 10 cylindrical or elliptical cylindrical containers and imitates a reference male with a height of 177 cm and a total weight of 70 kg.

The phantom was placed at a prescribed position in the WBC and the accuracy investigation was performed by estimating the



Fig. 1 Photo showing the exterior of an adult male BOMAB phantom



relative bias of each WBC. The relative bias was estimated by comparison between the observed value obtained by the WBC and the certificated value of the phantom (as a reference). In this accuracy investigation, 36 WBCs (stand type, 28; chair type, 8) were investigated.

Results and discussion

Figs. 2 and 3 show the relative bias results of Cs-137 for 36 WBCs and Co-60 for 33 WBCs (3 WBCs were excluded that could not identify Co-60) operated in Fukushima Prefecture. We confirmed that almost all the WBCs were appropriately calibrated, and they satisfied the bias test criteria described in the literature [2]. Of particular interest is the difference in the distribution of the relative biases between Cs-137 and Co-60. The distribution has positive-negative symmetry for Cs-137, whereas it is biased toward the negative side for Co-60. This result suggests that the counting efficiency value for Co-60 tends to be somewhat underestimated in many WBCs. A probable reason for this is that a portion of the γ -rays (1,460 keV) from K-40 (natural radionuclide) are measured and attributed to being from Co-60 (1,333 keV) in the calibration because of the relatively poor resolution of the NaI(Tl) detectors that are generally used in commercial WBC products.

From this accuracy investigation, we determined the relative bias results for both Cs-137 and Co-60 were within the range -15% to +15%. This is attributed to the fact that most of the foreign WBCs operated in Fukushima Prefecture after the nuclear accident were produced by one US company. These foreign WBCs had been calibrated by a secondary phantom that gives a similar counting efficiency to that of a BOMAB phantom. Meanwhile, in the case of the WBCs from domestic companies, it seems to be due to using a calibration factor which was adjusted to the counting efficiency according to the NIRS-owned BOMAB phantoms in

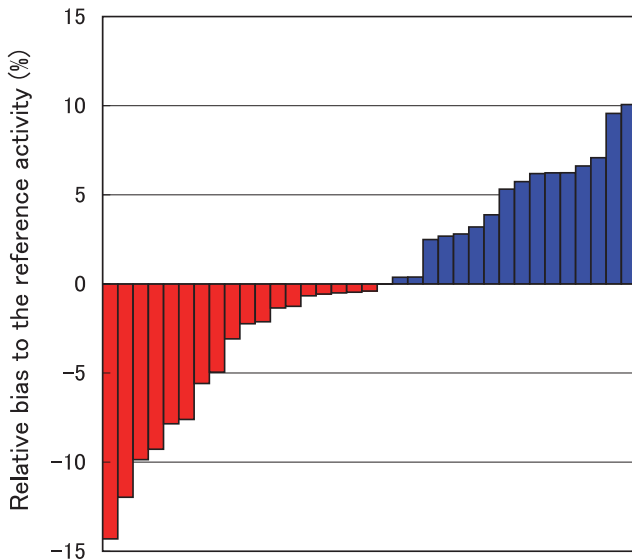


Fig.2 Relative biases to the reference activity of the Cs-137 BOMAB phantom for 36 WBCs operated in Fukushima Prefecture

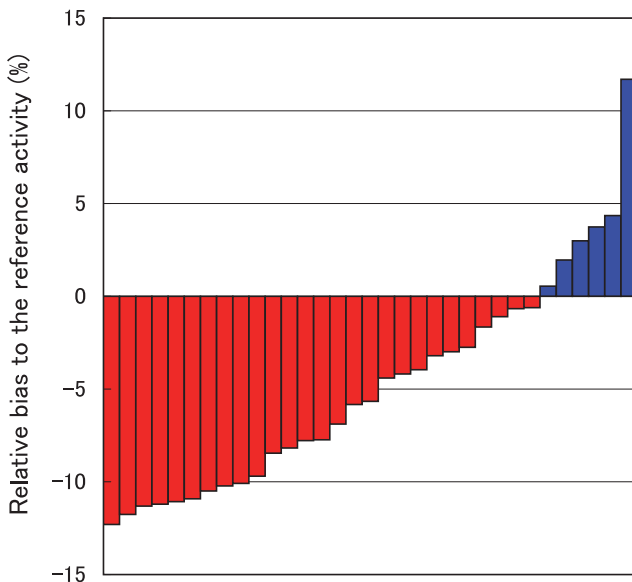


Fig.3 Relative biases to the reference activity of the Co-60 BOMAB phantom for 33 WBCs operated in Fukushima Prefecture

the past calibration. Software packages for spectrum analyses have been improved to allow compensation for an environmental background effect. Moreover, it seems that WBC operators have been more careful to carry out background measurements and the energy calibration.

Recent issues

WBCs have been developed mainly for individual monitoring of internal exposure to workers in nuclear related facilities. Thus, the WBCs have normally been calibrated using only a phantom imitating an adult male. However, after the accident, it has been necessary to measure internal doses to members of the public. Especially, there has been a growing need to perform accurate meas-

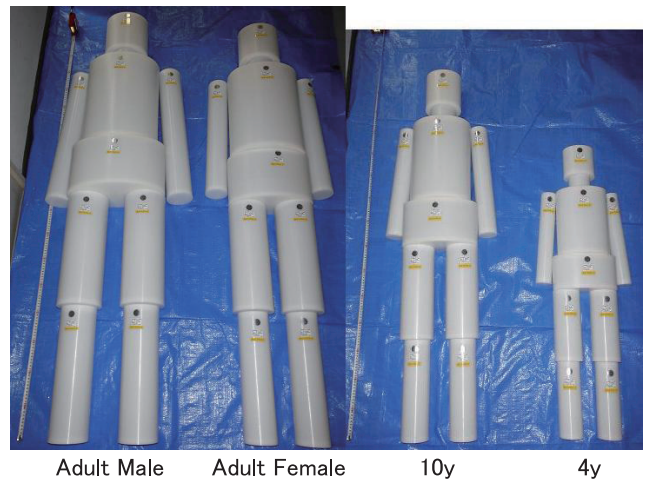


Fig.4 Photos showing the exterior of the family BOMAB phantoms

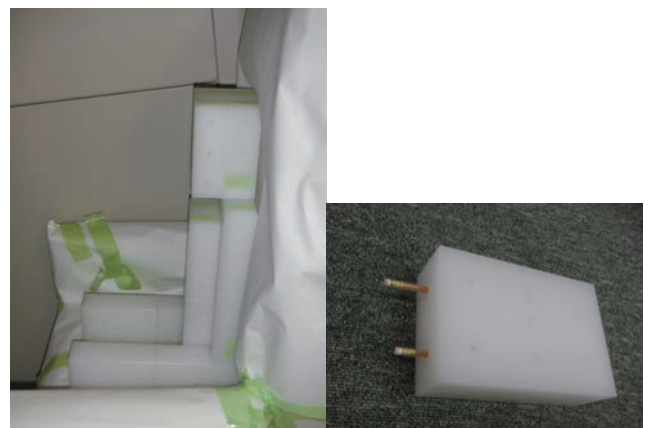


Fig.5 IGOR phantom for 2-year-child and the component block

urements for small children with the WBCs.

In order to evaluate the dependency of counting efficiency of the WBC on the body size, we prepared a set of a BOMAB phantom family consisting of Adult Male, Adult Female, 10-y Child and 4-y Child (Fig.4) models, and an IGOR phantom imitating various body shapes [3] (Fig.5).

A number of WBCs have been operated at various institutions in Japan. However, as another issue for the WBCs, a national standard on the specifications of a calibration phantom for WBCs has not been established. Although it is difficult to propose a new calibration standard phantom through a consensus process for the entire country, an ANSI-based BOMAB phantom would be able to be used as a de facto standard for this purpose.

References

- [1] America National Standard: Specification for the Bottle Manikin Absorption Phantom, ANSI/HPS N13.35-1999, 1999.
- [2] America National Standard: Performance Criteria for Radiobioassay, ANSI /HPS N13.30-1996, 1996.
- [3] Kovtun A N, Firsanov V B, Fominykh V I, et al.: Metrological Parameters of the Unified Calibration Whole-Body Phantom with Gamma-Emitting Radionuclides, *Radiat Prot Dosim* 89, 239-242, 2000.

Highlight

Biodosimetry of restoration workers for Fukushima Daiichi Nuclear Power Station accident

Yumiko Suto, Miho Akiyama, Momoki Hirai

E-mail: y-suto@nirs.go.jp

Summary

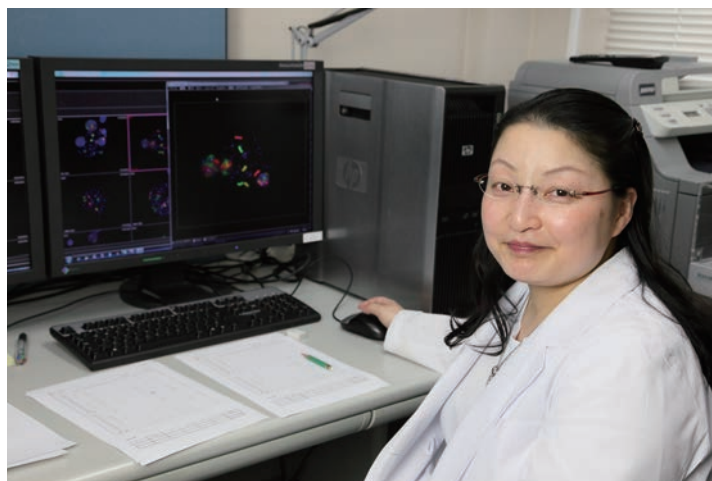
The nuclear accident of the Fukushima Daiichi Nuclear Power Station (NPS) was caused by the combined disaster of the Great East Japan Earthquake and the subsequent tsunamis on March 11, 2011. As the national core center for radiation emergency medical preparedness and response, NIRS received all nuclear workers who were engaged in emergency response tasks at the NPS and suspected of being over-exposed to acute radiation. Biological dosimetry by dicentric chromosome assay (DCA) was helpful for medical triage and management of the workers.

Biological dose assessment (biodosimetry)

When a radiation accident or unplanned radiation exposure occurs, biodosimetry based on cytogenetic assays is used to estimate the absorbed dose in the exposed individual to get useful information for the medical triage and management of radiological casualties with suspected acute radiation syndrome (ARS). Nowadays more cytogenetic assays to measure chromosomal aberrations, such as micronuclei (MN) in bi-nucleated cells, premature chromosome condensation (PCC), and fluorescence in situ hybridization (FISH), are available. However, the DCA using patients' peripheral blood lymphocytes is still considered to be the 'gold standard' for biodosimetry for radiation emergency medicine. In fact DCA has been used in previous serious radiation accidents such as the Chernobyl accident in 1986, the Goiania accident in 1987, the JCO criticality accident in 1999, the Bulgaria accident in 2011 and the Fukushima Daiichi Nuclear Power Plant accident in 2011 [1].

DCA of the restoration workers for the Fukushima Daiichi NPS accident

From March 21 to July 1, 2011, we examined blood samples obtained from a total of 12 restoration site-workers by DCA according to the International Atomic Energy Agency (IAEA) and the International Organization for Standardization (ISO) protocols. After 48 h of peripheral blood lymphocyte culturing, more than 1,000 metaphases were captured for dicentric scoring with the aid of two sets of automated cytogenetic imaging systems. Biological doses were estimated based on our dose-response curve for



dicentric induction by in vitro ^{60}Co irradiation at 11 dose points (Table 1; Fig.1). Fourteen age-matched and occupationally non-exposed healthy individuals were also examined as controls.

Among the workers, no individuals showed values exceeding the dose limit of 250 mGy (Table 2). When considering a 95% upper confidence limit of dose estimates, the value was below 300 mGy, which is lower than the lower limit level of medical triage for acute radiation syndrome (1 Gy) (Table 2). These results corroborate the fact that no ARS occurrences were observed among the workers examined. Interestingly, the estimated values were in good agreement with those of physically estimated doses made by personal dosimeters (Fig.2).

Table 1 Dose-response curve data for the dicentric chromosome assay (DCA) [1].

Dose (Gy)	No. of cells	Dicentric equivalent counts ^a	Yield	V/m^b
0	5000	1	0.0002	1
0.1	5003	11	0.0022	1.180
0.25	2606	30	0.0115	0.989
0.5	2107	68	0.0323	0.968
0.75	1674	101	0.0603	0.980
1	1112	102	0.0917	0.968
1.5	720	129	0.1792	0.993
2	415	128	0.3084	0.897
3	277	162	0.5848	0.776
4	117	122	1.0427	0.866
5	245	394	1.6082	0.816

^a The number of centromeres minus one in a multi-centric chromosome equals the dicentric equivalent count.

^b Variance to mean ratio. The p values of goodness of fit test for the Poisson distribution at every dose points were $p > 0.05$, except for the 0.1-Gy dose point ($p < 0.05$) at which one cell possessing two dicentrics was unexpectedly observed.

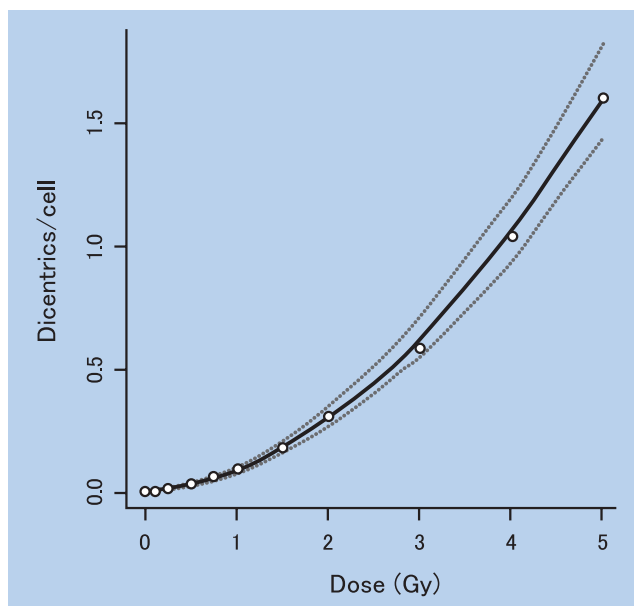


Fig.1 Dose-response curve for the dicentric chromosome assay (DCA). $Y = (0.00015 \pm 0.00017) + (0.0302 \pm 0.0044) \times D + (0.0588 \pm 0.0028) \times D^2$; Y, dicentric yield; D, dose (Gy); p value of goodness of fit test: $p = 0.73$. Dotted lines denote 95% confidence limits. (Modified from [1].)

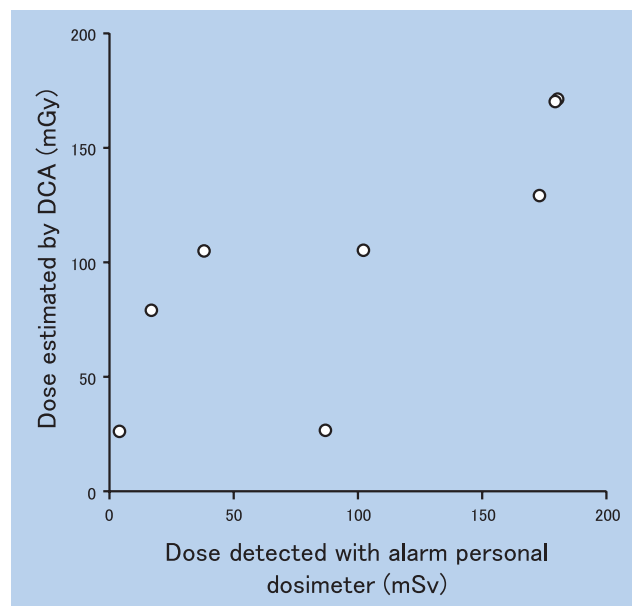


Fig.2 Correlation between physical doses detected with alarm personal dosimeters (APDs) and biological doses estimated by the dicentric chromosome assay (DCA). The following linear regression was obtained: $[\text{physical dose (mSv)}] = [\text{biological dose (mGy)}] \times [1.03 \pm 0.33] - [7.07 \pm 37.70]$ ($p < 0.05$) [1].

Table 2 Results of biological dosimetry of restoration workers for the Fukushima Daiichi Nuclear Power Station accident examined by the dicentric chromosome assay (DCA) and records of physical dosimetry detected with alarm personal dosimeters (APDs). [1]

ID ^a	APD record (mSv) ^a	No. of metaphases scored	Dicentric equivalents counts (DIC) ^b	DIC per metaphase	Dose estimated by DCA (mGy)	95% LCL ^c (mGy)	95% UCL ^d (mGy)
Fu-3	179	1003	7	0.00698	170	77	298
Fu-4	180	1000	7	0.00700	171	77	299
Fu-5	173	1000	5	0.00500	129	45	255
Fu-6	87	1036	1	0.00097	26	0	137
Fu-7	38	1005	4	0.00398	105	29	230
Fu-8	102	1013	4	0.00395	105	29	229
Fu-9	unknown	1035	6	0.00580	146	59	271
Fu-10	17	1037	3	0.00289	79	14	199
Fu-11	4	1042	1	0.00096	26	0	136
Fu-12	unknown	1004	2	0.00199	55	3	174

^a Detailed data and information of the alarm personal dosimeter (APD) record of each worker will be published elsewhere.

^b The number of centromeres minus one in a multi-centric chromosome equals dicentric equivalent count.

^c Lower confidence limit.

^d Upper confidence limit.

A second DCA was performed for 6 out of 12 individuals at one-year follow-up health examinations. Every one of these individuals showed either a decreasing tendency or the same values as obtained from the first examinations, inferring their good recovery.

For better dose assessment in a future emergency

DCA requires two-day peripheral blood lymphocyte culturing before starting metaphase chromosome analyses to estimate biological doses. Other biological assays described above also have drawbacks with respect to the time needed to obtain dose estimates for rapid decision on the right line of medical treatment. Therefore, alternative technologies that suit requirements for triage biodosimetry are needed.

Now we are developing a method, "prematurely condensed dicentric chromosome (PCDC) assay", for rapid medical triaging of acute exposed patients by using our modified protocol for detection of cell-fusion mediated premature chromosome condensa-

tion [2] and the FISH technique with pan-centromeric and telomeric peptide nucleic acid (PNA) probes [3]. The PCDC assay has the potential for evaluating exposed radiation doses in as short as six hours after the collection of peripheral blood specimens.

The need for improved cytogenetic research strategies adopted for mass-casualty management should also be reconsidered.

References

- [1] Suto Y, Hirai M, Akiyama M, *et al.*: Biodosimetry of restoration workers for Tokyo Electric Power Company (TEPCO) Fukushima Daiichi Nuclear Power Station accident, *Health Physics* 105, 366-373, 2013.
- [2] Suto Y, Akiyama M, Hirai M, *et al.*: A modified protocol for accurate detection of cell fusion-mediated premature chromosome condensation in human peripheral blood lymphocytes, *Cytologia* 78, 97-103, 2013.
- [3] Suto Y, Hirai M, Akiyama M, *et al.*: Sensitive and rapid detection of centromeric alphoid DNA in human metaphase chromosomes by PNA fluorescence *in situ* hybridization and its application to biological radiation dosimetry, *Cytologia* 77, 261-267, 2012.

Development of Fundamental Technologies in Radiological Science

Shinichi Kuroki

Director of Research, Development and Support Center

E-mail: skuroki@nirs.go.jp

The Research, Development and Support Center

The Research, Development and Support Center was established in 2011 to support and promote research activities of NIRS.

This center performs basic and advanced research and development necessary for the activities of the NIRS such as R&D in the field of technology for radiation generators, radiation detection technology, and radiation biology. It also supports researchers by providing users a comfortable environment in which they make use of research facilities such as the radiation generators and in supplying experimental animals, and so on. In addition to these activities, it maintains safety of all working environments and manages buildings in the NIRS campus, the NIRS computer network system and the NIRS library.

This center consists of one unit and three departments: the Planning and Promotion Unit, Department of Technical Support and Development, Department of Safety and Facility Management, and Department of Information Technology. The unit and each department are briefly introduced as follows.

The Planning and Promotion Unit

The Planning and Promotion Unit functions as the secretariat of the center and is the hub linking all the sections of the center with the NIRS administrative sections such as the Department of Planning and Management and the Department of General Affairs and the other centers.

The Department of Technical Support and Development

The Department of Technical Support and Development provides services to users for performing various experiments such as management of the facilities for radiation generators and many devices used for experiments. This department also develops radiation detectors with new technologies, researches radiation biology, and supports researchers in conducting animal experiments of the highest level quality.

This Department has three sections: Radiation Engineering Section, Radiation Measurement Research Section and Laboratory Animal and Genome Sciences Section.

The Radiation Engineering Section maintains the facilities for radiation generators and many devices which are used for experi-



ments. There are seven gamma-ray generators, six X-ray generators and two Cockcroft-Walton accelerator systems which consist of proton accelerators and beam-lines. One of the Cockcroft-Walton accelerator systems is used to generate neutron fluxes for research experiments on the biological effects of low dose radiation (**NASBEE**; a neutron exposure accelerator system for biological effect experiments). The other Cockcroft-Walton accelerator system has three beam-lines; two beam-lines are used as atomic element analyzers (**PASTA**; PIXE analysis system and tandem accelerator) and the third beam-line is used to deliver a single particle proton targeting an individual cell (**SPICE**; single particle irradiation system to cell). Both these systems were damaged in the March 2011 Great East Japan Earthquake. The latter system experienced more serious damage; the vacuum condition of the accelerator itself broke, the magnets for steering and focusing proton beams were moved from their original positions and some beam-lines were badly bent. The members of the Radiation Engineering Section fixed them which took about 10 months. These radiation generators are used not only by NIRS researchers but also by researchers from outside NIRS.

The synchrotron accelerator HIMAC is used for carbon ion radiotherapy for cancer and there are also three cyclotron accelerators used for radio-pharmacy development related to molecular imaging. HIMAC and these cyclotrons are managed and maintained by the Department of Accelerator and Medical Physics of the Research Center for Charged Particle Therapy.

The Radiation Measurement Research Section develops various radiation detectors. After the Fukushima Daiichi Nuclear Power Plant accident occurred, the section began developing some detectors for surveying high level radiation areas in Fukushima Prefecture: these are a gamma-camera which can selectively detect radiation from the ^{137}Cs radioisotope and a detector system which

can find hot-spots where very high levels of radiation are located. We are aiming at commercializing these items.

The Laboratory Animal and Genome Sciences Section supports researchers in conducting animal experiments of the highest level quality. Seven species of animals for animal experiments are available. In this section, we breed more than 15,000 mice and 2,000 rats a year and have developed genetically modified mice in order that researchers can conduct even more advanced experiments. Since some mice and rats are bred in SPF conditions, it is very important to sterilize the area periodically and keep it clean all the time. We control the SPF areas very strictly.

R&D Infrastructure Platform Program

In 2013, the research subject from NIRS, "Business use of various radiation fields related to humans", was selected as the R&D Infrastructure Platform Program by the Ministry of Education, Science and Technology (MEXT). This Platform Program is aimed at promoting usage of advanced research equipment and facilities of universities and public research institutes by researchers from industry-government-academia and supporting network formation.

Under this program, advanced facilities of NIRS such as PASTA, SPICE, NASBEE and the other radiation generators are provided for use to industry-government-academia researchers with steadfast support. This program will strengthen the research activities in the fields of life science, human science, and human environment related science.

The Department of Safety and Facility Management

The Department of Safety and Facility Management is responsible for keeping working environments safe and providing safe and comfortable conditions for all research activities. It has four sections: Safety and Risk Management Section, Safety Control Section, Radiation Safety Section, and Facility Management Section.

The Safety and Risk Management Section is in charge of planning and promotion of safety, providing NIRS's employees with educational training for maintaining safety and security, and maintaining general safety in the NIRS campus and buildings and so on. Especially it is responsible for risk management including making and revising the Emergency Preparedness Plan of NIRS and implementing drills for nuclear and radiological emergencies in Japan. In 2013 this section started work to establish a more systematic risk management structure at NIRS under the risk management committee.

The Safety Control Section is in charge of safety for genetic modification of experimental animals, safety for handling chemical agents and harmful substances, workplace safety, environment protection, preventing and extinguishing fire, and so on.

In NIRS, about 1,600 persons including its direct employees, researchers from outside NIRS, and contracted workers are registered as radiation workers who can work in the 20 radiation controlled areas in NIRS. NIRS must instruct them regarding radiation safety and security before entering a radiation-controlled area for the first time. There are more than 400 kinds of radioisotopes used for experiments on radiobiology, radiation medicine and so forth. And NIRS also has many radiation generators as mentioned above. All items concerned with radiation have to be controlled strictly by rules. The Radiation Safety Section is charged with controlling all of them in accordance with the rules.

The Radiation Emergency Medicine Cooperative Research Fa-

cility (REMCRF) has one building in which the use of actinide nuclei is allowed for research on radiation emergency medicine. This facility is the only one of its kind in Japan in which researchers can use, for instance, plutonium in animal experiments. Therefore, this building has to be strictly controlled to keep the inside of the building at a negative pressure according to the radiation safety law. In this case, the ventilation system of the building is maintained by the Radiation Safety Section in cooperation with the Promotion Section for REMCRF of the Research Center for Radiation Emergency Medicine instead of the Facility Management Section because of existence of the strict rules.

There are about 50 buildings on the NIRS campus. The Facility Management Section maintains the buildings and their equipment such as elevators, air conditioners, etc., and the campus infrastructures such as electric power lines, telephone systems, gas lines, water supply lines, and so on. NIRS was established in 1957, so some buildings are very old and a few were damaged considerably in the March 2011 earthquake. Some of them have had to have seismic strengthening. Construction of a new building used for human resource development was completed under the supervision of this section and this building was opened in May 2013. This section has also been managing construction of another new building to be used for environmental radiation research on the consequences of the Fukushima Daiichi Nuclear Power Plant accident. And also in 2013, the section started construction of a high voltage electric booster station which will replace the old one.

The Department of Information Technology

The computer network system is one of the main infrastructures of NIRS. This network system has more than 1,200 users daily and about 3,500 computers are connected to it. The Department of Information Technology is responsible for maintenance and development of the computer network system. This department has two sections: Information Systems Section and Research Information Section.

The Information Systems Section is responsible mainly for hardware and software to control the computer network system. This section established the network system and now revises it. One of the most important missions of this section is to secure information security. Users of this system must observe the Information Security Policy of NIRS and other documents under the policy. In 2013, this policy was strengthened to prevent information leakage. And to keep security more effectively, an e-learning exercise to educate users was implemented in the summer and an e-learning self-inspection was carried out by each user in the winter.

The Research Information Section is responsible mainly for the other information system related matters especially user support of the system. The administrative sections have many computer-aided service systems, for instance, personnel management, accounting procedures, patent database, etc. These service systems are maintained by the relevant section in principle, but the Research Information Section has undertaken various jobs such as improving the service systems or adding new functions to them. This section also has developed an institutional repository to replace the conventional database system used for registration of achievements of NIRS research activities. This repository was released to NIRS users in December 2013. In addition, this section is also managing the library of NIRS and publications such as a research reports, proceedings and so on prepared at NIRS.

Highlight

Verification of shielding method with water-filled materials for space radiation protection

Satoshi Kodaira

E-mail: koda@nirs.go.jp

The International Space Station (ISS) crew is constantly exposed to space radiation consisting of various charged particles. The radiation dose comes mainly from protons and helium ions, while the contribution of heavy components (up to iron ions) leads to an increase in dose equivalent due to the high LET (linear energy transfer) with high quality factor related to the relative biological effectiveness. Moreover, primary highly energetic charged particles produce secondary particles such as fragments and neutrons. The radiation dose level varies depending on the solar activity, and orbital parameters such as altitude, attitude and shielding distribution in the ISS [1]. Therefore, dose monitoring is needed to control the crew's health and safety. The effective dose limits of a 10 yr career for astronauts are recommended as 400 mSv (female) and 700 mSv (male) for 25 yr olds [2]. The radiation risk of astronauts in the ISS is controlled under such recommended limitations with actual dose measurements. Future crew members will be exposed to much higher dose of space radiation for up-coming long-term missions on Mars. However, following the current practice, the radiation protection still depends on using materials with the thickness of a few g/cm^2 for vehicle walls and the internal instruments installed in the ISS. In this work, we have verified the dose reduction effects for space radiation by using the additional water shielding material ("protective curtain") of stack boards consisting of hygienic wipes and towels which have been stored in the ISS.

The hygienic materials were assembled into a protective curtain with 4 layers, which corresponds to the additional water shielding thickness of $6.3 \text{ g}/\text{cm}^2$. The total mass of the protective curtain was 67 kg, and it was installed along the outer wall of the starboard crew cabin in the Russian Service Module as shown in Fig.1c.

For the measurements, twelve dosimeter packages (#1- #12) consisting of thermoluminescence detectors (TLDs) and CR-39 plastic nuclear track detectors were installed in the module from June 16, 2010 to November 26, 2010. The exposure duration was 163 days. Half of the packages were located on the surface of the protective curtain and the other half were on the crew cabin wall behind or alongside the protective curtain. The dose reduction effect by the protective curtain was experimentally verified by the



dose variations among the 6 location pairs.

The LET spectra for packages #3 (shielded) and #4 (unshielded) measured by CR-39 are shown in Fig.2. As seen from the figure, the flux in the shielded package was degraded compared with that of the unshielded one, and was the same as the rest of the package locations (#1, #2 and #5 - #12) in Fig.3. The mean absorbed dose and dose equivalent rates for all packages were measured as $327 \mu\text{Gy}/\text{day}$ and $821 \mu\text{Sv}/\text{day}$ for the unshielded packages and $224 \mu\text{Gy}/\text{day}$ and $575 \mu\text{Sv}/\text{day}$ for the shielded packages, respectively. The dose reduction rate in dose equivalent was found to be $37 \pm 7 \%$ except for packages #5 - #8, which was consistent with the calculated results in the spherical water phantom by PHITS. The data from the packages #5 - #8 showed minute effects by the protective curtain because those packages were additionally shielded by a thick glass window ($5 \text{ g}/\text{cm}^2$) installed on the vehicle wall.

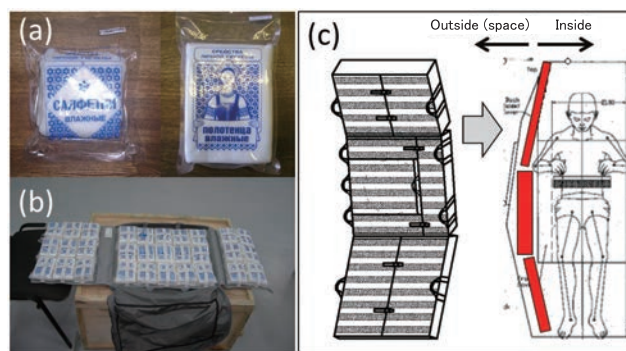


Fig.1 Protective curtain [3]. (a) Hygienic wipes and towels, (b) a stack board and (c) a schematic drawing of the stack board and its installation in the ISS.

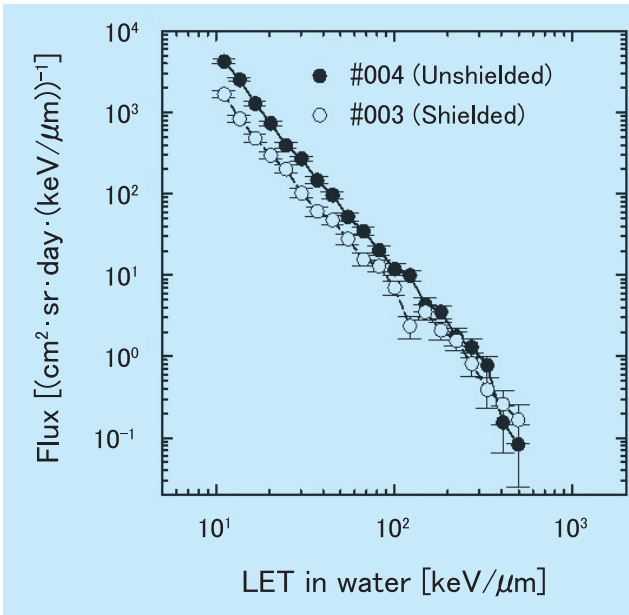


Fig.2 LET spectra for packages #3 (shielded) and #4 (unshielded) measured by CR-39 [3].

The mean dose reduction due to the low LET ($<10 \text{ keV}/\mu\text{m}$) and high LET ($\geq 10 \text{ keV}/\mu\text{m}$) components were $37 \pm 2 \%$ and $37 \pm 11 \%$ in dose equivalent, respectively, and the contributions by the low and high LET components were found to be comparable in the observed dose reduction rate. Representative cosmic rays such as $<90 \text{ MeV}$ protons, $<160 \text{ MeV/n}$ carbon and $<400 \text{ MeV/n}$ iron would be absorbed in water with the thickness of $6.3 \text{ g}/\text{cm}^2$. There would be a small contribution to the dose from residual, more penetrating fragments, while the primary particles would be absorbed in the protective curtain. The protective curtain would be effective shielding material for not only trapped particles with several 10 MeV but also for low energy galactic cosmic rays with several 100 MeV/n . Moreover, the neutron components are measured as recoiled proton tracks in the LET spectrum. Thus the obtained dose reduction effects include partial neutron dose reduction by the water shielding.

We found that proper use of the protective curtain could effectively reduce the space radiation dose for crew living in the space station and extend the long-term missions to Mars in the future. The details of this work have been published in [3].

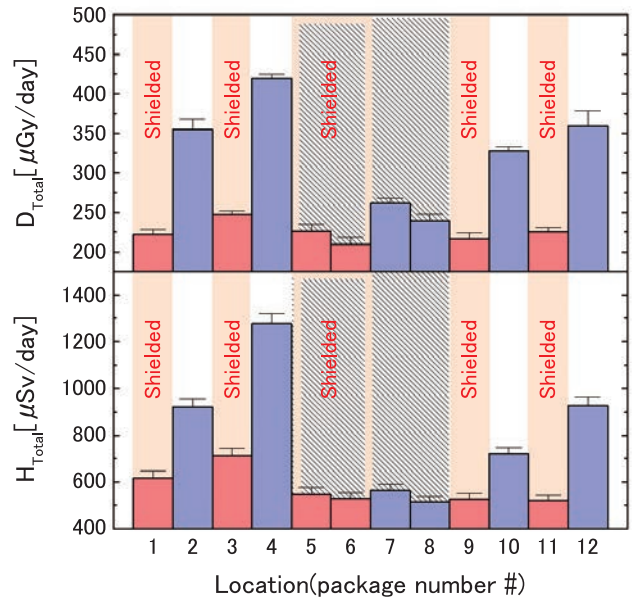


Fig.3 Variations of absorbed dose and dose equivalent rates as a function of the location of dosimeter packages [3]. Packages #5 - #8 shaded with diagonal lines were additionally shielded with a thick glass window.

References

- [1] Kodaira S, Kawashima H, Kitamura H, *et al.*: Analysis of radiation dose variations measured by passive dosimeters onboard the International Space Station during the solar quiet period (2007-2008), *Radiat Meas* 49, 95-102, 2013.
- [2] NCRP Report No.142. National Council on Radiation Protection, Bethesda, MD, 2002.
- [3] Kodaira S, Toloček RV, Ambrozova I, *et al.*: Verification of shielding effect by the water-filled materials for space radiation in the International Space Station using passive dosimeters, *Adv Space Res* 53 1-7, 2014.

Highlight

Development of a novel method for prediction of mouse embryo viability

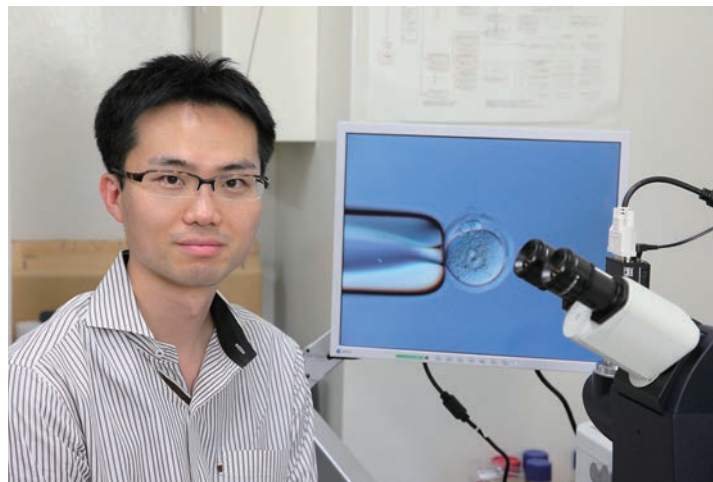
Satoshi Tsukamoto

E-mail: s_tsuka@nirs.go.jp

Embryo quality is crucial for a normal pregnancy and it is usually checked by microscopic observation. However, the morphology of the embryo is not perfectly correlated with the potential for embryo viability. For example, there are cases in which embryos with poor morphology develop normally after implantation. Our present study focuses on autophagy, which plays an important role during preimplantation embryo development. We have developed a method that allows for *in vivo* observation of embryonic autophagic activity. Using this developed method, we found that embryos with high autophagic activity were more likely to develop through embryogenesis. This is the first study to evaluate embryo quality from this point of view. Because there is a possibility that autophagy is also important in human embryos, we believe that this method to monitor embryo quality will be useful for infertility treatment.

Currently, 1 out of 40 people who give birth in Japan have used assisted reproductive technologies (ART) such as *in vitro* fertilization (IVF). However, because the success rate for childbirth is low (10%), IVF is often repeated, creating both a burden for the mother and an increased economic burden. The success of IVF is affected by various factors, but the reduced quality of embryos is one of the most important. Recent studies have suggested that there may be reduced quality of the ovum due to aging. Although IVF can be used to successfully produce several fertilized oocytes (embryos), only one can be implanted transferred into the mother's body, thus it is important to determine the quality of an embryo in order to produce a normal pregnancy. Generally, the quality of the embryo is evaluated based on observation of its morphology under a microscope. However, embryo morphology is not necessarily directly correlated with viability because there are implanted embryos with morphological defects that develop

The time from fertilization to implantation is 5 days in humans and 4 days in mice, and there are various internal changes in the embryos during this period. In particular, it is important that maternally derived factors such as mRNAs/proteins that accumulated during oogenesis, be degraded immediately after fertilization. If this degradation does not progress correctly, the remaining ma-



ternal components can affect further embryonic development.

Autophagy is a cytoplasmic degradation process which is mediated by lysosomes and conserved in many species from yeast to humans. The process of autophagy is classified broadly into four steps: autophagic induction, cytoplasmic sequestration, lysosomal fusion, and degradation [1]. During the process of autophagy, cytoplasmic components are sequestered by double-membrane structures, called autophagosomes. Since the sequestration by autophagosomes occurs randomly, an autophagosome may include not only proteins but also cellular organelles such as mitochondria and peroxisomes. Finally, autophagosomes fuse with the lysosomes, which results in the degradation of the sequestered components. The basic physiological functions of autophagy are the generation of amino acids for cellular metabolism and the maintenance of cellular quality. Given that autophagy is a bulk degradation system, autophagy may also play a role in extensive cellular remodeling during early embryonic development. In 2008, we reported that autophagy was highly activated immediately after fertilization. Autophagy-deficient embryos died before implantation [2]. Those findings first highlight the pivotal role of autophagy during early embryogenesis. In other words, normal embryonic development can only occur with functional autophagic activity.

There are several methods used to assess autophagic activity in cells. For example, cell fixation and immunostaining use antibodies to biochemically visualize the protein localization or expression levels of autophagy related proteins, such as LC3 which is an autophagosome marker. However, because the cells are dead in these methods, they cannot be used in live embryos where viability must be maintained. In the present study, we fo-

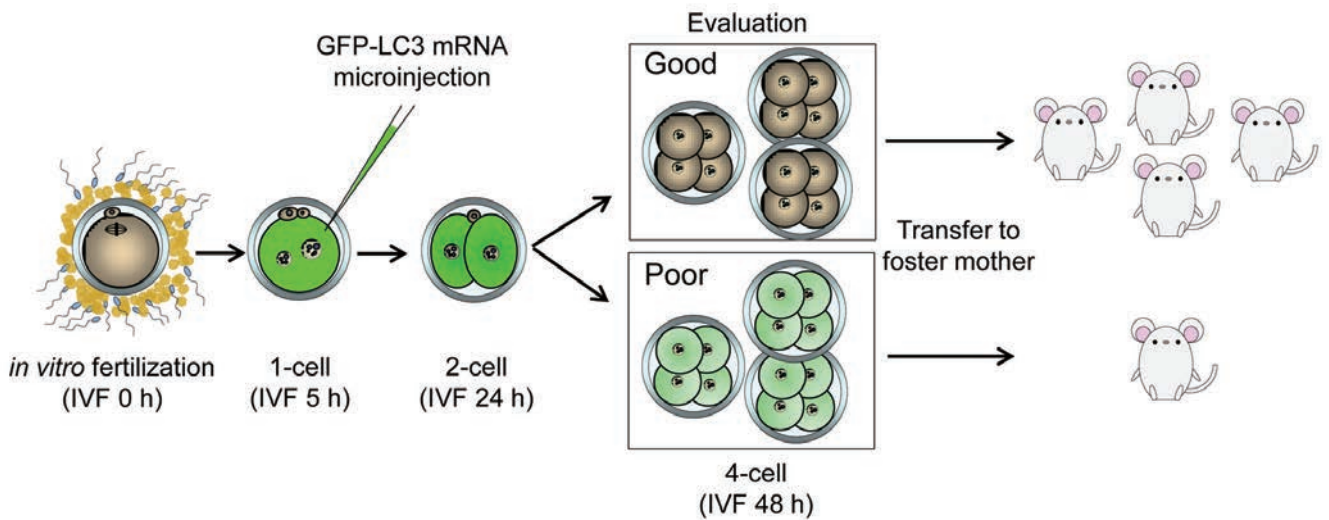


Fig.1 In order to monitor autophagic activity in individual live-embryos, mRNA encoding GFP-LC3 protein was microinjected into the 1-cell embryos. Those embryos were grouped into 2 groups (Good and Poor) based on the GFP-LC3 fluorescence at the 4-cell stage, 48 hours after *in vitro* fertilization. Those embryos were transferred to foster mothers separately and followed to compare the further embryonic development. More embryos were able to develop to full-term from the Good group, indicating that embryogenesis after implantation can be predicted by monitoring embryonic autophagic activity.

cused on LC3, a versatile marker of autophagy. Because this protein is selectively degraded in an autophagy-dependent manner, the degradation level of LC3 correlates with the autophagic activity. To monitor autophagic activity in live embryos, mRNA encoding LC3 fused to GFP (GFP-LC3) was microinjected into the 1-cell embryos and its fluorescence level was observed under constant fluorescence conditions. We found that the GFP-LC3 fluorescence was stable in the 2-cell stage 24 hours after fertilization, but was rapidly degraded on reaching the 4-cell stage (48 hours after fertilization). Degradation level of GFP-LC3 at the 4-cell stage was used as a marker to categorize the embryos into 2 groups (embryos with degraded GFP-LC3 were termed Good, and embryos with less degraded GFP-LC3 were termed Poor) and those groups were tested for further embryonic development. We found that those embryos classified as Good were easier to implant and developed embryogenesis better than those embryos classified as Poor (Fig.1) [3]. These results demonstrate that monitoring of autophagic activity can be used to select for embryos with high developmental potential.

Our study shows that successful embryogenesis can be predicted in advance by imaging the autophagic activity of individual embryos. By combining the monitoring of autophagic activity with conventional morphology-based microscopic analysis, a high-quality embryo (easily continuing through embryonic development) can be correctly selected from among a number of successfully fertilized eggs. However, because microinjection of GFP-LC3 in human embryos is currently ethically restricted, development of an alternative method for evaluating the activity of autophagy needs to be considered in the future. In addition, it is important to investigate the molecular mechanisms to regulate autophagic activity in early embryos, and to develop chemical-based methods to control the level of autophagic activity (enhancing the quality of the embryo).

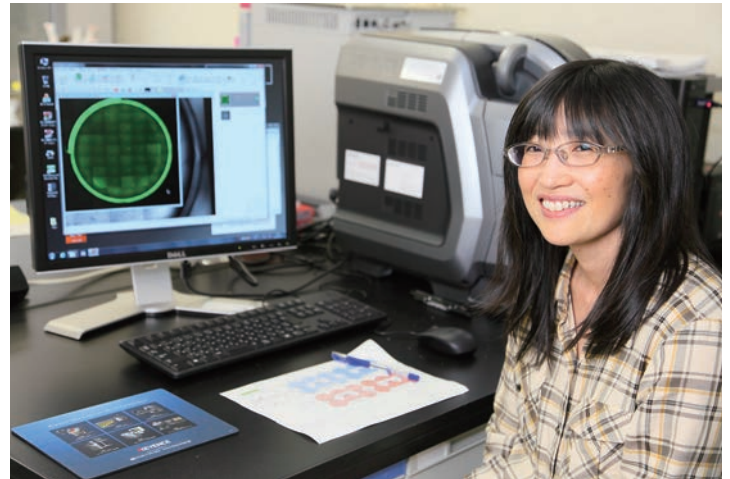
References

- [1] Mizushima N: Autophagy: process and function, *Genes Dev*, 21, 2861-73, 2007.
- [2] Tsukamoto S, Kuma A, Murakami M, *et al.*: Autophagy is essential for pre-implantation development of mouse embryos, *Science*, 321, 117-20, 2008.
- [3] Tsukamoto S, Hara T, Yamamoto A, *et al.*: Fluorescence-based visualization of autophagic activity predicts mouse embryo viability, *Sci Rep*, 4, 4533, 2014.

Highlight

A genome-wide analysis of point mutations in embryonic stem cells and induced pluripotent stem cells

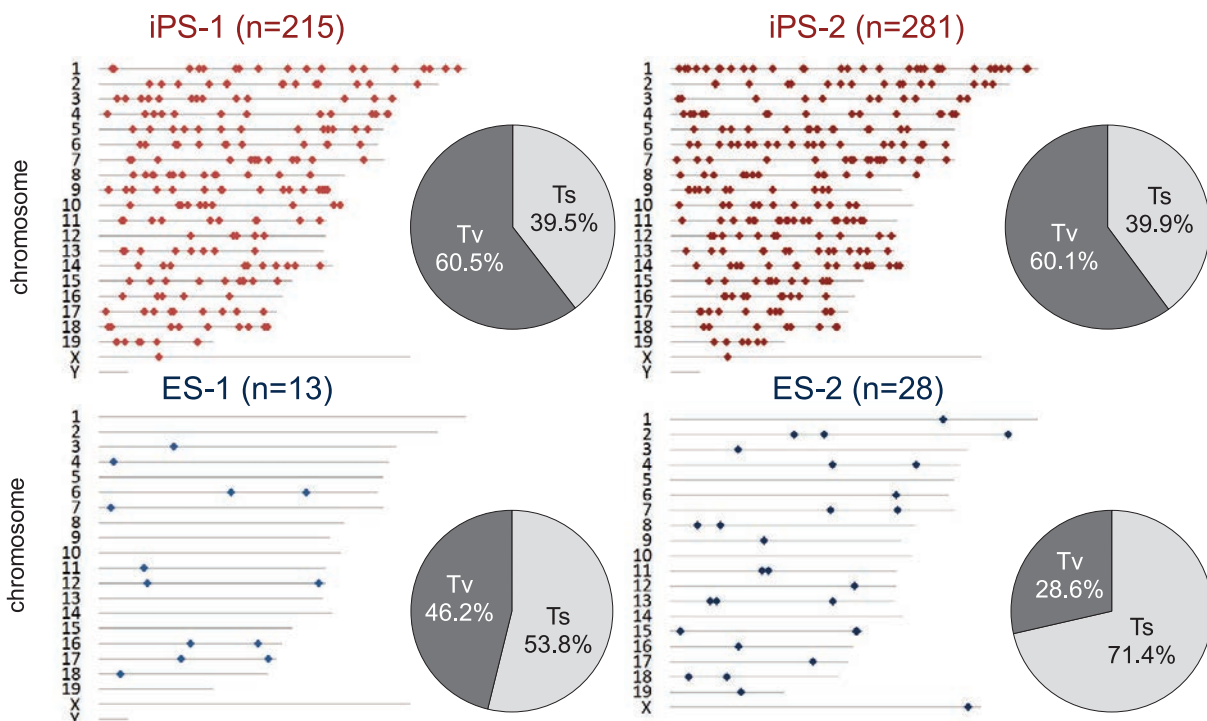
Ryoko Araki, Mayumi Sugiura,
Yuko Fujimori-Hoki, Misato Sunayama,
Masahiro Uda, Miki Nakamura, Masumi Abe
E-mail: a_ryo@nirs.go.jp



The induced pluripotent stem cell (iPSC) system holds great promise for regenerative medicine but its underlying molecular mechanisms have remained elusive. In contrast, the embryonic stem (ES) cell is the golden standard among pluripotent stem cells and has long history in both basic and applied research areas. Therefore, it is an interesting and important issue to know whether or not iPSCs and ES cells are the same type of pluripotent stem cells.

First, we have focused on the point mutation in iPSC genome,

especially in genome integration-free iPSCs [1]. Using also C57 BL/6 mouse, several integration-free iPSC lines were established



Ts: transition mutation
(purine → purine, pyrimidine → pyrimidine)
Tv: transversion mutation
(purine ↔ pyrimidine)

Fig.1 Point mutations and base substitution profile identified in iPSC and ESC lines.

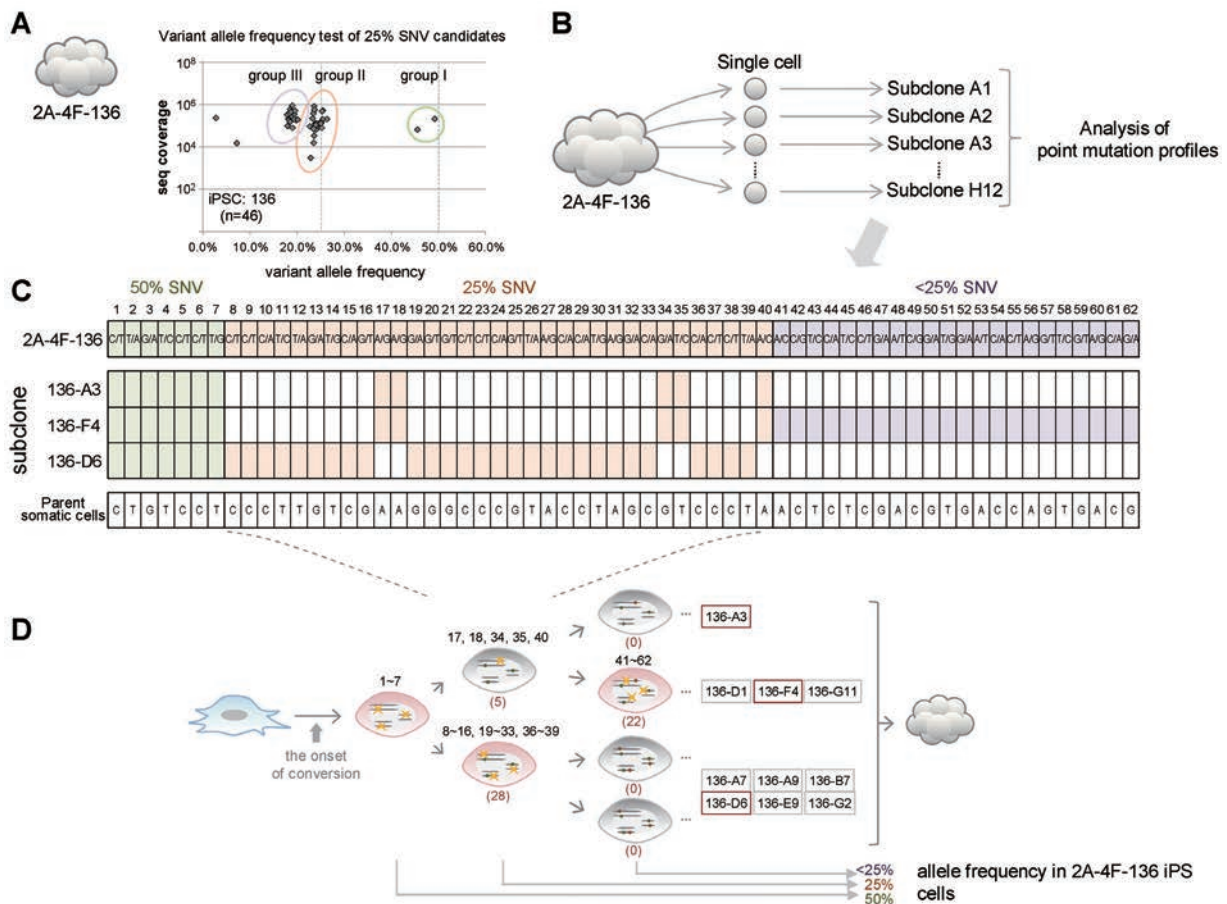


Fig.2 (A) Frequencies of each variant allele for SNV candidates of 2A-4F-136 iPSC screened using deep sequencing. (B) Schematic of single clone isolation and establishment from the 2A-4F-136 line. (C) Point mutation in each sub-clone. Heterogeneity of point mutations in the original line was seen. (D) Schematic of time course of point mutation appearance.

with the four factors, Oct3/4, Sox2, Klf4 and c-Myc (4F) in plasmid vectors from MEF [2]. The MEF was derived from a single embryo, not litter mates, to remove the intra-strain SNPs, which could be false positives of point mutations. Then, the whole genome sequencing (WGS) on the three such integration-free iPSC lines and their parent somatic cells was conducted and about 300 point mutations were identified in each genome (Fig.1) [3]. Sanger sequencing verified the results. In addition, no common SNV was observed between different iPSC lines, suggesting that these are not pre-existing SNVs in their parent cells. Indeed, ultra-deep sequencing did not detect any SNVs in the parent MEF fraction. Next, we focused on the point mutations in ES cells. To achieve a comprehensive point mutation analysis of ES cells, the genomes of both parents from which blastocysts were prepared are essential as controls. In this study, we established ES cell lines from an inbred mouse strain, C57BL/6, along with the preparation of the genomes of both parents. Their full developmental ability was confirmed by aggregation experiments [2]. On the ES lines and on their parent genomes we conducted WGS. As a result, we identified 10 to 30 point mutations in ES cell genomes, and the results were confirmed by Sanger sequencing. Importantly, the frequencies were $\sim 1/10$ of those observed in iPSCs genomes, in which more than hundreds of point mutations have been observed (Fig.1)[2]. In addition, we found a difference in their profile between iPSCs and ES cells: transversion-predominant for iPSCs and transition-predominant for ESCs (Fig.1).

Subsequently, to ensure the presence of iPSC generation-associated point mutations, we performed the variant allele frequency test. Then we observed a considerable number of SNVs at less than 50% allele frequency, indicating a presence of 25% and 12.5% allele frequency point mutations (Fig.2A). Similar SNVs were also observed by a deep WGS; a clear peak appeared at an allele frequency around 25% in addition to the peak at 50% frequency. Because pre-existing SNVs must be observed as 50% allele frequency, our observation shows the important facts that 25% or less of the SNVs were not pre-existing ones and that substantial numbers of point mutations occurred during the conversion process, especially in their initiation steps, of iPSC generation. We concluded our study by the investigation of sub-lines derived from single cells in an iPSC colony (Fig.2B). The heterogeneity of the point mutation patterns within an iPSC clone was seen (Fig.2C) and it reflected the history of the emergence of each mutation (Fig.2D).

References

- [1] Jincho Y, Araki R, Hoki Y, *et al.*: Generation of genome integration-free induced pluripotent stem cells from fibroblasts of C57BL/6 mice without c-Myc transduction, *J Biol Chem* 285, 26384-26389, 2010.
- [2] Araki R, Uda M, Hoki Y, *et al.*: Negligible immunogenicity of terminally differentiated cells derived from induced pluripotent or embryonic stem cells, *Nature* 494, 100-104, 2013.
- [3] Sugiura M, Kasama Y, Araki R, *et al.*: Induced Pluripotent Stem Cell Generation-Associated Point Mutations Arise during the Initial Stages of the Conversion of These Cells, *Stem Cell Reports* 2, 52-63, 2014.

Fukushima Project Headquarters

Satoshi Yoshida, Ph.D.

Deputy Director

E-mail: s_yoshid@nirs.go.jp

In order to support restoration and revitalization of Fukushima Prefecture following the nuclear accident at the Fukushima Daiichi Nuclear Power Plant (NPP), the Fukushima Project Headquarters was established in May 2012. The headquarters manages three research projects, Project for Human Health, Radiation Effect Accumulation and Prevention Project, and Project for Environmental Dynamics and Radiation Effects which were chosen after consideration of the major concerns of people living in the prefecture. The headquarters also manages other activities of NIRS related with the NPP accident.

The Project for Human Health started an epidemiological investigation with the cooperation of first responders who worked at Fukushima Daiichi NPP controlling the accident in the early stage. The project will monitor their health long-term by referring to their certificates of health and by asking for their medical history and information about their lifestyle such as smoking and drinking habits, etc. The information is being collected in a database to analyze the correlations between health conditions and the doses they received. The database structure and functions have been designed, and special attention was given to security of the collected information for long-term follow-up. More than 600 workers have been registered in the database along with the data of a baseline questionnaire survey. The findings from the follow-up study are expected to be used in workers' health care, as well as in future planning of radiation protection measures for emergency situations.

The project also developed the NIRS external dose estimation system for Fukushima residents to estimate the external effective doses for the first four months after the Fukushima Daiichi NPP accident. This system has been adopted in the Fukushima Health Management Survey, which is a long-term health management survey for all people of Fukushima Prefecture, conducted by Fukushima Medical University, and the estimated results were provided to the Fukushima residents, individually. This task can be very useful as the first approximation of the external effective doses to Fukushima residents by the accident.



The Radiation Effect Accumulation and Prevention Project aims to elucidate the effects of low-dose-rate radiation and its underlying mechanism, and then to provide possible measures to mitigate the risks based on findings using animal models. In order to answer the major questions determined from the concerns of Fukushima residents, the project conducts the following three research programs. 1) Effects of the low-dose-rate radiation on life shortening and cancer induction are being examined for juvenile exposure in comparison with adult exposure, to confirm if the dose-rate effect for children is the same as that for adults. 2) Accumulation of radiation effects in the stem cells of the skin and mammary glands is being evaluated, to clarify if the dose-rate effect can be explained in part by the reduced accumulation of radiation-induced damage in stem cells or by the elimination of damaged stem cells. 3) Inhibitory effects of calorie restriction and anti-oxidant food ingredients on radiation-induced cancer are being investigated, to provide possible approaches to reduce the cancer risk after childhood exposure by subsequent control of diet.

The Project for Environmental Dynamics and Radiation Effects started the following two research programs related with the environmental contamination in Fukushima. 1) Estimation of radiation doses for Fukushima residents from surrounding ecosystems, and providing countermeasures to minimize the received dose. On coming back to their homes, many of the evacuees are afraid of encountering high radiation doses from the contaminated environment and from the ingestion of radioactive materials from foods and water. In order to estimate long-term radiation doses of the residents from the surrounding environment during their daily life, the project started dose-estimation-oriented collection of environmental samples considering the migration of radioactive materials

in the environment. 2) Assessment of radiation effects on non-human biota in contaminated ecosystems. High contamination levels of the environment suggest possible effects of radiation on non-human biota. Although drastic effects such as the “red forests” in contaminated Chernobyl areas have not been observed, long-term studies are required to estimate the environmental effects. The project is collecting biological samples such as pine, wild mouse, and salamander in heavily contaminated areas, and is estimating radiation effects using different endpoints (e.g. growth rate, reproduction and chromosome aberration).

In addition to the projects, the headquarters manages the following activities in order to relieve the anxiety of people and to support research activities of the projects. 1) Development of an automated procedure for the dicentric chromosome aberration assay, and estimation of background frequency of the dicentric chromosome of Japanese. 2) Supporting the construction of new buildings and facilities for researches. 3) Telephone consultation. This consultation was started on March 13, 2011, and operated by NIRS's staff members by turn for 24 hours a day, seven days a week for the first two weeks from March 17, 2011. It continues to be run but with a reduced size, and a total of about 19,000 telephone calls have been received so far.

In the following highlight, three research topics are introduced from two research projects, the Radiation Effect Accumulation and Prevention Project and the Project for Environmental Dynamics and Radiation Effects.

Highlight

Effects of chronic γ -irradiation on the Tohoku hynobiid salamander, *Hynobius lichenatus*

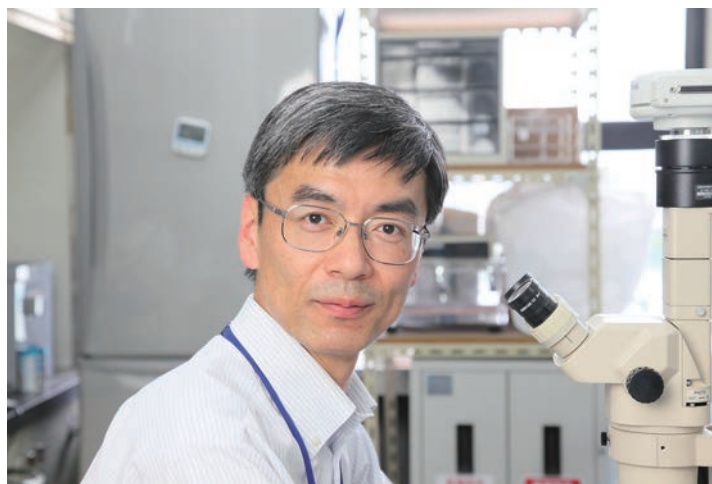
Shoichi Fuma

E-mail: fuma@nirs.go.jp

Introduction

Tremendously large amounts of radionuclides were released into the environment following the Fukushima Dai-ichi Nuclear Power Plant accident in March 2011. As a result, large areas in east parts of Japan from Kanto to Tohoku districts, but mainly in Fukushima Prefecture, were contaminated to varying degrees with the released radionuclides. Radiation effects on non-human biota inhabiting the contaminated areas have therefore been a concern since the accident [1].

The Tohoku hynobiid salamander, *Hynobius lichenatus* (order Caudata, class Amphibia; Fig.1) is suitable for field investigation of radiation effects on non-human biota, because this species is expected to be sensitive to radiation [2] and it inhabits the northern part of the Abukuma Mountains, which were among the most heavily contaminated areas by the accident. We started field stud-



ies on this salamander just after the accident. On the other hand, we also did a chronic irradiation experiment in the laboratory, because there were no data on effects of chronic irradiation on Caudata. In the present study, *H. lichenatus* was chronically γ -irradiated during the embryonic, larval and juvenile stages, and effects on growth and survival as well as histological changes were investigated [3].

Materials and methods

In May 2012, egg sacs of *H. lichenatus* were collected in the Aizu district, which was a less contaminated area in Fukushima Prefecture. Each embryo was separated from the egg sacs, and reared in water. External γ -irradiation was started in the NIRS ^{137}Cs irradiation facility. The irradiation was continued until the juvenile stage for 450 days at dose rates of 32, 150, 490, 4,600 and 18,000 $\mu\text{Gy h}^{-1}$.

Larvae were also reared in water, and aquatic oligochaetes *Tubifex tubifex* were given as food.

Juveniles metamorphosed from the larvae were reared in plastic containers filled with wet sphagnum moss, and larvae of moth *Galleria mellonella*, sow bugs *Porcellionides pruinosus* and larvae of cricket *Acheta domestica* were given as food.

Observation was made to check survival and metamorphosis. Weight of juveniles was measured. Histological examinations were performed in the liver, spleen, skin and intestine in accordance with routine methods.

Results and discussion

Chronic irradiation at 32, 150 and 490 $\mu\text{Gy h}^{-1}$ did not significantly affect survival (Fig.2) and growth such as age at metamorphosis (Fig.3) and weight of juveniles. No morphological aberrations and histological damages were observed.

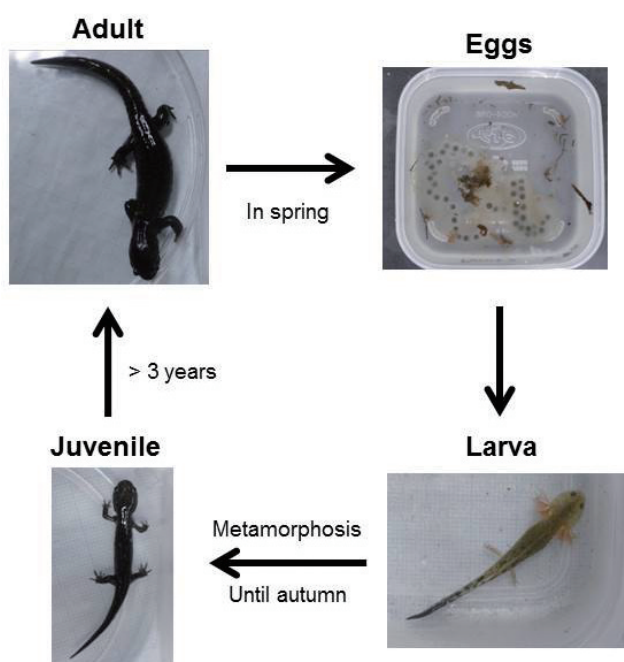


Fig.1 Life cycle of *H. lichenatus*

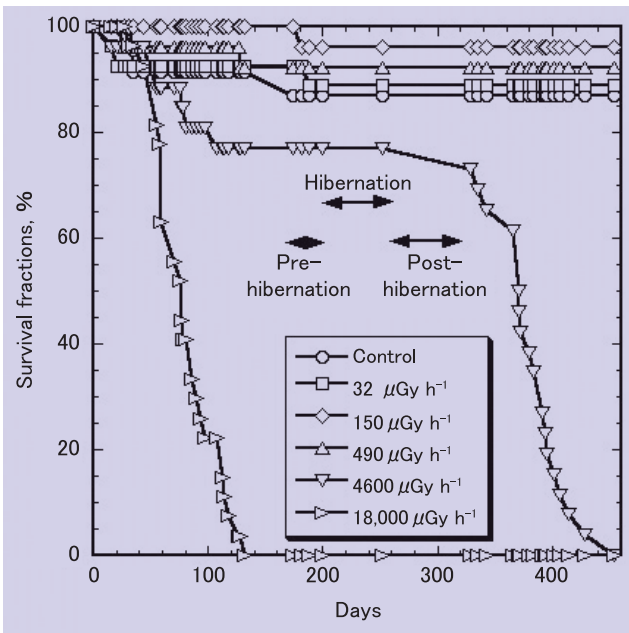


Fig.2 Survival curve of chronically γ -irradiated *H. lichenatus*^[3]

At 4,600 $\mu\text{Gy h}^{-1}$, growth was severely inhibited. Metamorphosis was delayed (Fig.3), and weight of juveniles was lighter than that of controls. All the individuals irradiated at this dose rate died, mostly at the juvenile stage (Fig.2). Subcutaneous haemorrhage was observed in some dead juveniles. The median life span was 371 days, during which a total dose (chronic LD_{50}) was 42 Gy. In the liver, the number of haematopoietic cells was significantly reduced in the living juveniles, and these cells disappeared in the dead juveniles. In the spleen, mature lymphocytes were depleted in the living larvae, and almost all the haematopoietic cells disappeared in the dead juveniles. These results suggest that this salamander died due to acute radiation syndrome, i.e., haematopoietic damage and subsequent sepsis caused by immune depression. The death would also be attributed to skin damage inducing infection.

At 18,000 $\mu\text{Gy h}^{-1}$, growth inhibition and morphological aberrations such as thickset bodies and development failure of hind limbs were observed in the larvae. Subcutaneous haemorrhage was also observed. All the individuals irradiated at this dose rate died at the larval stage due to multiple organ failure (Fig.2). The median life span was 77 days, and chronic LD_{50} was 28 Gy.

At 490 $\mu\text{Gy h}^{-1}$ or lower dose rates, growth and survival of *H. lichenatus* were not significantly affected over 450 days. For this relatively short period, this result supports validity of all the guidance dose rates proposed by various organisations (e.g., IAEA, UNSCEAR, US DOE, Environment Agency UK and Environment Canada) and programmes (e.g., FASSET, ERICA and PROTECT)

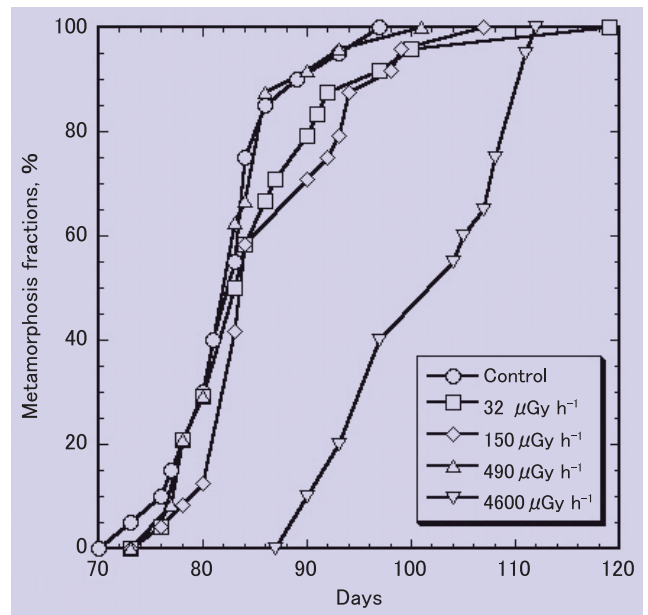


Fig.3 Metamorphosis fraction of chronically γ -irradiated *H. lichenatus*^[3]

for protection of amphibians and taxonomic groups or ecosystems including amphibians, which range from 4 to 400 $\mu\text{Gy h}^{-1}$.

However, considering the relatively long life span, i.e., longer than 14 years, of this salamander, the results obtained in this study may not support all of these guidance dose rates. Assuming that LD_{50} of chronic exposure is also 42 Gy at lower dose rates than 4,600 $\mu\text{Gy h}^{-1}$, a median lethal dose rate can be estimated to be less than 340 $\mu\text{Gy h}^{-1}$ ($=42 \times 10^6 \mu\text{Gy} / 14 \text{ y} / 365 \text{ d} / 24 \text{ h}$) for the whole life of this salamander. This estimation suggests that most of the guidance dose rates, ranging from 4 to 200 $\mu\text{Gy h}^{-1}$, would protect this salamander but the highest one, i.e., 400 $\mu\text{Gy h}^{-1}$ proposed by IAEA, UNSCEAR, US DOE and Environment Agency UK, may not on the whole life scale. Further long-term irradiation experiments are required for the definitive conclusion.

The dose rate-response relationship obtained in this study and dose rates estimated in the field study, which will be published in the near future, enable assessment of radiation risks to this salamander in the contaminated areas in Fukushima.

References

- [1] Schiermeier Q: Wildlife Threatened by Fukushima Radiation, *Nature News*, doi:10.1038/news.2011.326, 2011.
- [2] Fuma S, Watanabe Y, Kawaguchi I, et al.: Derivation of Hazardous Doses for Amphibians Acutely Exposed to Ionising Radiation, *J Environ Radioact* 103, 15-19, 2012.
- [3] Fuma S, Une Y, Ihara S, et al.: Effects of Chronic γ -Irradiation on Growth and Survival of the Tohoku Hynobiid Salamander, *Hynobius lichenatus*, *J Environ Radioact* 135, 84-92, 2014.

Highlight

Radionuclides in the marine environment off the coast of Fukushima Prefecture after the TEPCO Fukushima Daiichi Nuclear Power Station accident

Tatsuo Aono

E-mail: t_aono@nirs.go.jp

Introduction

It is necessary to clarify behaviors of the atmospheric and oceanic releases and the dispersion of artificial radionuclides in the marine environment after the TEPCO Fukushima Daiichi Nuclear Power Station (FDNPS) accident. Many and various types of monitoring measurements were carried out in the marine environment after this accident, but only the gamma-emitting radionuclides iodine-131(¹³¹I) and radioactive cesium (¹³⁴Cs and ¹³⁷Cs) which have high radioactivity were reported. The pre-accident levels of ¹³⁷Cs activities in seawater and sediments were 1-2 mBq/L and 1 Bq/kg-dry, respectively. The activities of ¹³⁴Cs + ¹³⁷Cs in seawater were observed to be more than 10 kBq/L around FDNPS at the end of March 2011, and measurements showed that they had decreased gradually to 1-2 mBq/L in the past few months, approaching the pre-accident levels. On the other hand, higher activities of ¹³⁴Cs + ¹³⁷Cs in sediments have been reported off the Fukushima coastal area in the Pacific Ocean.

Sampling off the coast of Fukushima

The activities of radionuclides in marine biota off Fukushima, including plankton and benthos, were investigated to determine the variation in radioactivity. The aims of the present study were to examine the temporal and spatial changes in radioactivity and to investigate the distribution and behavior in the marine environment after this accident. Samples collected in the marine environment included seawater and sediments and also marine biota such as plankton, benthos, fish and shellfish. They were collected with a plankton net, dredge sampler, and trawl net during cruises of some research vessels and by fishing ships. Radioactive Cs in filtered seawater was determined with the ammonium phosphomolybdate (AMP) /Cs compound method [1]. Detection limits of ¹³⁴Cs and ¹³⁷Cs were 1 mBq/L in seawater, respectively. Collected marine biota samples were classified into species, and some kinds of fish and shellfish were separated into some parts, such as the edible (muscle), viscera and bony parts, etc. These parts were dried with a vacuum drying machine, homogenized, and packed into a plastic container (U-8). The ¹³¹I activities could not be measured as ¹³¹I had been volatilized by heat from the biological sample. Radioactivity was determined by gamma-ray spectrometry using a



HPGe detector (GX-2019; Canberra). The radionuclide activities of seawater, sediment and biota on the sampling date were calculated with the correction of the decay. Detection limits of ¹³⁴Cs, ¹³⁷Cs and ^{110m}Ag in sediment and marine biota samples were all within 1 Bq/kg [wet weight (wet wt)].

The activities of radionuclides in marine environment

The observed artificial gamma-emitting radionuclides in marine biota include not only ¹³⁴Cs and ¹³⁷Cs but also ^{110m}Ag. Artificial radionuclides such as ¹³⁴Cs, ¹³⁷Cs, ¹⁴¹Ce, ¹⁴⁴Ce, ¹⁰³Ru, ¹⁰⁶Ru, and ^{110m}Ag were reported in Mediterranean seagrass after the Chernobyl accident [2]. However, ¹⁴¹Ce, ¹⁴⁴Ce, ¹⁰³Ru, and ¹⁰⁶Ru were not observed in the FDNPS fallout. ^{110m}Ag, is a short half-life radionuclide (249.8 d), and it was observed in the fallout, soil and sediments around eastern Japan. Marine biota that were used as foodstuffs before the accident were collected off Onahama (Fukushima, Prefecture) in June and December 2011, and their radionuclide activities are shown in Fig.1. The radioactivity of ¹³⁴Cs + ¹³⁷Cs in marine products ranged from 11 to 132 Bq/kg (wet wt) in June 2011 and from less than 1 to 135 Bq/kg (wet wt) in December 2011. ^{110m}Ag activity was not detected in fishes collected in December 2011, although this activity was observed in the viscera of squid, crab, and fish collected in June 2011. It is considered that the activity of ^{110m}Ag in fish and plankton gradually decreased with time because the half-life of ^{110m}Ag is 249.8 days. However, no cesium radioactivity was observed in squid and crab. It is well known that mollusca and crustacea concentrate silver in their visceral parts. The bottom-dwelling biota such as shellfish and benthos had high activities of Cs and Ag one year after the accident. The average cesium activity in seawater was 0.20 Bq/L in June 2011, which gradually decreased to 0.03 Bq/L in December 2011 around the sampling area. The Cs activity in seawater decreased ten-fold

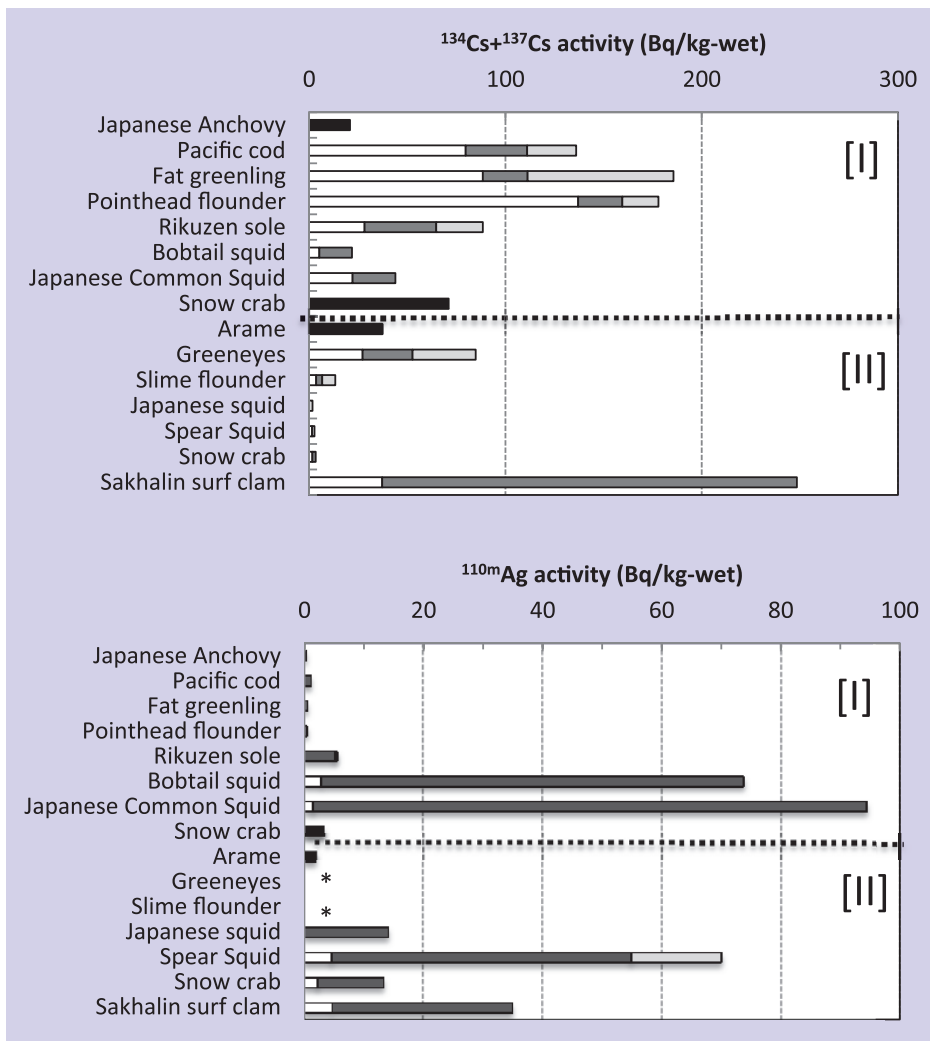


Fig.1 Radioactivity in each part of the marine organisms. *Black bars*, whole body; *open bars*, muscle (edible parts); *dark bars*, viscera; *light gray bars*, bony parts, and ***; lower than the detection limit. Samples were collected in June (I) and December (II), 2011.

during 6 months, and consequently activity in the marine organisms also dropped. On the other hand, the decrease of ^{110m}Ag activity in mollusks could be observed to be almost that of the physical half-life time. Furthermore, the Cs activities in plankton and seawater off Onahama in 2012 were from 40 to 130 Bq/kg (wet wt) and from 3 to 91 Bq/L, respectively. It is thought the decrease of activity of these radionuclides in marine organisms depends on differences in the mechanisms of accumulation and metabolism.

The CR [concentration ratio = activity in biota (Bq/kg (wet wt))/ activity in seawater (Bq/kg or Bq/L)] is usually represented in terms of the concentration in biota relative to that of seawater for modeling purposes [3]. This value of cesium in marine organisms was calculated with the activity of cesium in seawater (Table 1).

Table 1 Concentration ratio of cesium (CR-Cs) in marine biota.

	This study		TRS-422
	n	Estimated CR-Cs	CR-Cs
Fish	7	3.2E+02	1.0E+02
Mollusks	3	3.1E+02	6.0E+01
Crustaceans	1	7.6E+01	5.0E+01
Macroalgae	1	1.3E+03	5.0E+01
Plankton	12	6.9E+01	4.0E+01

The estimated CR of cesium (CR-Cs) in marine organisms ranged from $2.6\text{E}+1$ in the muscle part of squid to $1.0\text{E}+4$ in clam viscera. Large differences in CR-Cs in different parts of marine organisms were not observed. The estimated CR-Cs values in plankton were $5.8\text{E}+1$ to $1.5\text{E}+3$ in 2012. These values were higher than the reported CRs of fish, crustaceans, mollusks, and macroalgae in TRS-422, $1.0\text{E}+2$, $5.0\text{E}+1$, $6.0\text{E}+1$, and $5.0\text{E}+1$, respectively. These resulting values ranged from $5.8\text{E}+1$ to $7.8\text{E}+2$, and they were higher than the CR-Cs values ($2.0\text{E}+1$ to $4.0\text{E}+1$), but also similar to the Kd -Cs value in TRS-422 [3]. It was suggested that the rapid change in radioactivity in seawater and the resuspension of particles from the sediments led to high CRs of Cs after the FDNPS accident.

References

- [1] Aoyama M, Hirose K: Radiometric Determination of anthropogenic radionuclides in seawater samples, *Radioact in the Environ* 11,137-162, 2008.
- [2] Calmet D, Charmasson S, Gontier G: Chernobyl radionuclides in the Mediterranean seagrass *Posidonia oceanica*, 1986-1987, *J Environ Radioact* 13, 157-173, 1991.
- [3] IAEA: Sediment distribution coefficients and concentration factors for biota in the marine environment, Vol. 422, Technical reports series, *International Atomic Energy Agency*, 1985.

Effects of gamma-rays on hair follicle regeneration in mice

Kimihiko Sugaya

E-mail: k_sugaya@nirs.go.jp

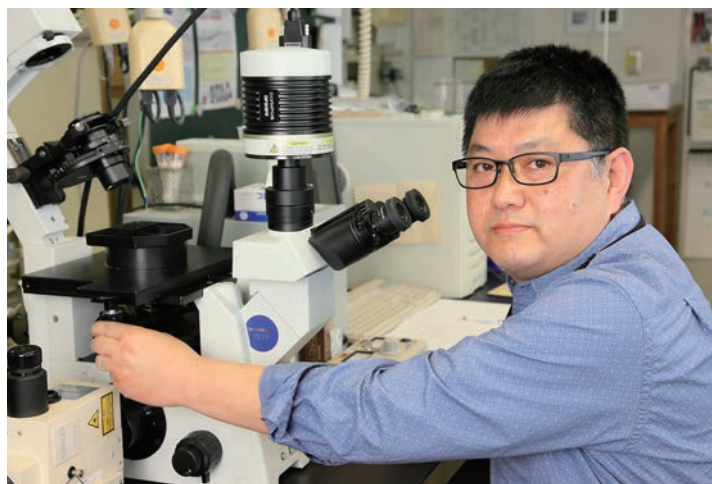
Summary

The effects of ionizing radiations on somatic stem cells largely remain unclear. Hair follicles are self-renewing structures that reconstitute themselves throughout the hair cycle, which is comprised of the following phases: anagen (growth), catagen (regression) and telogen (resting), suggesting the presence of their own stem cells. The whole bodies of C57BL/10JHir mice in the 1st telogen phase were irradiated with γ -rays. Mice were examined for effects on hair follicles, including their number, morphology and pigmentation in the 2nd anagen phase. Decreased hair follicle density and induction of curved hair follicles were observed in the dermal skin of irradiated mice. In addition to these keratinocyte-derived anomalies, melanocyte-derived anomalies including white hair and hypopigmented hair bulbs were found. The decrease in hair follicle density and the increase in the frequency of hypopigmented hair bulbs were dependent on the dose of γ -rays. These results suggest that γ -rays damage stem cells and progenitors for keratinocytes and melanocytes, thereby affecting the structure and character of regenerated hair follicles. The density of hair follicles and pigment production in hair bulbs are established as criteria for the effects of γ -rays on the hair cycle.

Introduction

The current radiological protection system assumes complete accumulation of the stochastic effect of the ionizing radiation. If long-lived tissue stem cells are a target of the radiation carcinogenesis, this model system appears to be rational, though epidemiologic studies do not necessarily support this idea.

To verify this idea, hair follicles may be a good experimental system, because they are self-renewing structures that reconstitute themselves, which suggests the presence of their own stem cells. The hair cycle consists of three phases: anagen (growth), catagen (regression) and telogen (resting) (Fig. 1A). *In vivo* and *in vitro* studies have revealed that keratinocyte and melanocyte stem cells are present in the bulge of the hair follicles in both mice and humans. The bulge region provides the insertion point for the arrector pili muscle and marks the lowermost permanent portion of the hair follicle during the hair cycle. Regeneration of hair follicle structure begins with keratinocyte and melanocyte progenies



derived from keratinocyte and melanocyte stem cells present in the hair bulge. In mice, the 1st and 2nd hair cycles are synchronized and proceed in waves all over the body.

Ionizing radiations, such as X-rays and γ -rays, affect mammalian keratinocytes, melanoblasts, melanocytes and fibroblasts dur-

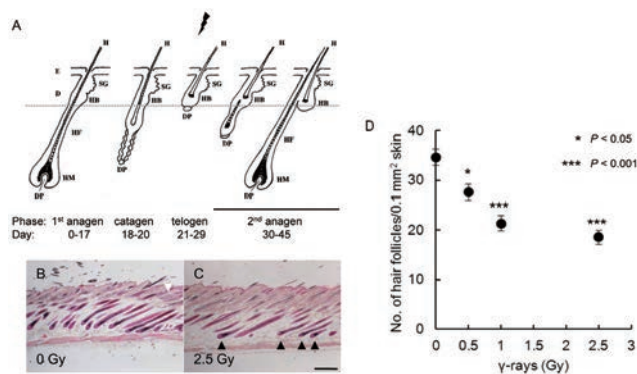


Fig. 1 Histological sections of the dorsal skin of control and irradiated mice at the 2nd anagen phase. (A) Diagram showing the hair cycle in mice. Abbreviations: H, hair shaft; E, epidermis; D, dermis; SG, sebaceous gland; HB, hair bulge; HF, hair follicle; HM, hair matrix; DP, dermal papilla; Arrow, γ -irradiation; the region above the dotted line indicates the permanent portion of hair follicles. (B) A section of control skin contains 10 hair follicles of the 2nd hair cycle. The white arrowhead indicates a typical hair of the 1st hair cycle. (C) Gamma-irradiation (2.5 Gy) decreased the density of hair follicles in the skin. Only 4 hair follicles of the 2nd hair cycle were observed in this section. Scale bar, 100 μ m. (D) Quantitative analysis of the effect of γ -rays on hair follicle density in the 2nd anagen phase. Error bars indicate the standard error. *P* values for comparisons of control mice (0 Gy) were calculated by two-tailed Student's *t*-test for comparison of groups of unequal size. This figure was modified from a figure in [1].

ing all stages of development. In embryonic mice exposed to ionizing radiations, patches of pigment-less white hair (white spots) can be found in the mid-ventrum of offspring. However, it is not fully understood whether keratinocyte and melanocyte stem cells in the bulge of postnatal skin are affected by this exposure. While there are a few reports showing the changes of hair with regard to the hair cycle after γ -irradiation, a reduction in the diameter of irradiated hair follicles has been demonstrated in humans and mice. These circumstances prompted us to investigate in detail how ionizing radiations affect the regeneration of hair follicles by evaluating changes in the number and morphology of hairs and by observing changes in the frequency of abnormal hair follicles due to defects in keratinocytes and melanocytes.

Results

1) Effects of γ -rays on hair follicle structure

Since newly formed hair follicles are derived solely from keratinocyte and melanocyte stem cells, we hypothesized that damage caused in keratinocyte and melanocyte stem cells in the 1st telogen could be detected as a phenotype of descendant hair follicle structures in the 2nd anagen (Fig.1A). Histological sections of mouse dorsal skin showed mature hair follicles at the 2nd anagen with some regressed hair follicles at the 1st anagen (Fig.1B). In mice exposed to 2.5 Gy γ -rays, there was a decrease in the number of hair follicles per 0.1 mm² skin section in the 2nd hair cycle (Fig.1C). Gamma-rays at doses of 0.5 Gy and 1 Gy also caused a significant decrease in the number of hair follicles per 0.1 mm² skin (Table 1). Hair follicle density decreased as the dose increased (Fig.1D). Interestingly, the decreasing rate appeared to reach a plateau at a dose of 1 Gy. An additional malformation was observed in the induction of curved hair follicles. One or two constrictions in the hair follicles were seen in the curved follicles, even in mice exposed to 0.5 Gy γ -rays, whereas no abnormalities were seen in control mice. The frequency of curved hair follicles in irradiated mice was significantly different to that in the control group (Table 1). However, these differences did not appear to be dose-dependent. These results suggest that γ -rays affected hair follicle number and structure in the 2nd anagen phase when stem cells and committed progenitors for keratinocytes were irradiated in the 1st telogen.

2) Effects of γ -rays on pigmentation of regenerated hair follicles

Next, we analyzed histological sections of the dorsal skin with regard to anomalies derived from melanocyte stem cell, such as the frequency of white hairs and hypopigmented hair bulbs (Table 1). Histological sections confirmed the presence of white hair shafts in the growing hair follicles of mice exposed to 0.5 Gy γ -rays, whereas no white hairs were found in control mice. However, the frequency of white hairs was very low and the differences between control and irradiated mice were not significant (Table 1).

Table 1 Effects of γ -rays on hair development in mice

Dose (Gy)	No.	No. of hair follicles/0.1 mm ² skin	Frequency of curved hair follicles (%)	Frequency of white hairs (%)	Frequency of hypopigmented hair bulbs (%)
0	28	34.56±1.61	0	0	0
0.5	29	27.54±1.62*	5.63±1.85**	0.50±0.31	1.40±0.47*
1	28	21.34±1.53***	3.58±1.19**	0.10±0.10	5.23±1.08***
2.5	30	18.57±1.44***	7.18±2.30*	0.63±0.27	18.42±5.05**

Errors are the standard errors. Asterisks indicate statistically significant difference from control (* P < 0.05, ** P < 0.01, *** P < 0.001). This table was modified from a supplementary table in [1].

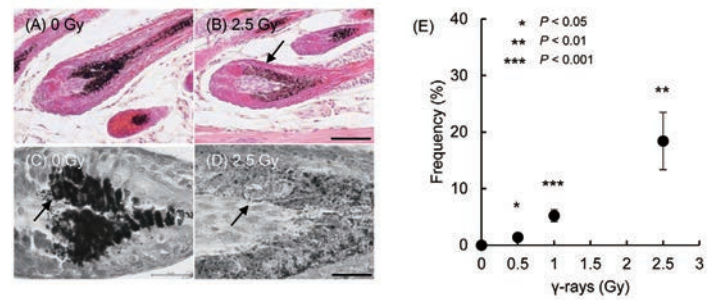


Fig.2 Effect of γ -rays on the development of progenies of melanocyte stem cells. (A, B) Mice exposed to 2.5 Gy γ -rays possess hair bulb melanocytes with extremely reduced pigmentation (B, arrow) in contrast to the heavily pigmented hair bulbs of control mice. Scale bar, 50 μ m. (C, D) Higher magnification views of hair bulbs of control and irradiated mice. Mice exposed to 2.5 Gy γ -rays possess hair bulb melanocytes with fewer and smaller melanosomes compared with control melanocytes, though melanosomes were mature. Arrows indicate hair bulb melanocytes. Scale bar, 20 μ m. (E) Quantitative analysis of the effect of γ -rays on the frequency of hypopigmented hair bulbs. Error bars indicate the standard error. P values for comparisons of control mice (0 Gy) were calculated by two-tailed Student's t -test for comparison of groups of unequal size. This figure was modified from a figure in [1].

We also studied the degree of pigmentation of hair bulb melanocytes. Histological sections of control mice contained fully pigmented melanosomes in the hair bulb (Fig.2A). However, mice exposed to 2.5 Gy γ -rays possessed hair bulb melanocytes with extremely reduced pigmentation (Fig.2B). The number of hair bulb melanocytes did not appear to be reduced. Melanosomes in irradiated hair bulbs appeared mature but they were much fewer in number and smaller in size in the exposed mice than they were in the control mice (Figs.2C, D). In contrast to the frequency of white hairs, the frequency of hypopigmented hair bulbs increased in a dose-dependent manner and reached more than 18% (Fig.2E). There was a significant increase in the frequency of hypopigmented hair bulbs, even in skin exposed to 0.5 Gy γ -rays (Table 1). These results suggest that γ -irradiation affects stem cells and committed progenitors for melanocytes at the 1st telogen and, as a result, inhibits the formation of melanosomes at the 2nd anagen.

Conclusion

The decrease in the density of hair follicles in the skin at the 2nd anagen and the increase in the frequency of hypopigmented hair bulbs are dependent on the dose of γ -rays. Furthermore, these irradiations induced abnormal hair follicle curvature and white hairs, suggesting that γ -irradiation in the 1st telogen strongly affects regeneration of hair follicles, which are produced by the progenies of keratinocyte and melanocyte stem cells, in the 2nd anagen.

References

- [1] Sugaya K, Hiribe T: Exposure to gamma-rays at the telogen phase of the hair cycle inhibits hair follicle regeneration at the anagen phase in mice, *Int J Radiat Biol* 90, 127-132, 2014.

Research on Evaluation of Medical Exposure

Yoshiya Shimada, Ph.D.

Director, Medical Exposure Research Project

E-mail: y_shimad@nirs.go.jp

In this midterm plan at NIRS, the Medical Exposure Research Project (MER-project) has the mission to investigate the frequencies and doses of domestic medical radiation uses, both diagnostic and therapeutic. The data are being collected in collaboration with local hospitals and academic societies. These data will be stored into a planned national database of medical exposure and used for both scientific and practical bases for the justification and optimization of radiation protection in medicine. They will be also provided to the UNSCEAR global survey project.

Five studies have been currently undertaken. (i) Estimations of examination frequencies and organ doses in X-ray CT, PET, PET/CT, and heavy ion particle therapy in collaboration with local hospitals and academic societies. (ii) Organ dose estimations of patients who received radiotherapy for cervical cancers and prostate cancer for the risk of secondary cancer. (iii) Study of radiobiology in radiation use in medicine. (iv) Development of the method for risk-benefit communications in medicine. (v) Running an organization for the exchange of information on radiation protection in medicine. The results obtained are as follows.

(1) The data of frequencies and dose (DICOM) in CT examination are being collected in collaboration with local hospitals such as the National Center for Child Health and Development (NCCHD) Hospital and the Chiba Children's Hospital in addition to the academic bodies including the Japanese Society of Radiation Oncology, Japanese Society of Radiological Technology, Japan Radiological Society and Japan Association of Radiological Technologists. In the Chiba Children's Hospital, data have also been extensively collected, and the data for the most recent 4 years on CTDI and DLP were summarized (see Highlight). In FY 2013, we started the survey of CTDIvol and DLP in two additional hospitals. Phantom measurements of organ doses have been continued in four hospitals as the basic data for optimization.

(2) For estimation of organ dose in radiotherapy of cervical cancers, a physical pelvic phantom was developed. The dose of organs in the pelvic region, i.e., colon, rectum, uterus and ovaries, which are monitored with gel dosimeters, are being estimated in the contemporary treatment protocol for cervical cancer. In addition,



tion, organ doses outside the pelvic region have been measured using the adult anthropomorphic phantom. The dose of an organ close to the cervical cancer site such as kidney and stomach was as high as 1 Gy. In addition, the dose of surrounding organs such as colon and rectum during prostate cancer therapy with HIMAC was also examined, and revealed to be much lower than that with IMRT, suggesting superiority of HIMAC for the reduction of secondary cancers. For PET diagnoses, the basic physiologically-based pharmacokinetic model (PBPK model) was made to consider the physiological differences among patients.

(3) The dose collection system and database are under development. Importance of tracking dose of the patients with a medical radiation exposure history, which is the concept behind the IAEA's "Smart Card/SmartRadTrack project", has been maintained. We developed the system that enables transfer of the DICOM data of different manufacturers into one database.

(4) WAZA-ARI is the web-based dose calculator of medical exposures in X-ray CT examinations, which has been developed by Oita University of Nursing and Health Sciences and the Japan Atomic Energy Agency (JAEA). It has been installed in the web server of NIRS, and opened to the public for trial use (Fig. 1-3). WAZA-ARI includes the simulation data of equivalent doses and effective doses for voxel phantoms of the Japanese male and female developed by JAEA, and voxel phantoms of 0, 1, 5, 10, 15 year old children developed by Florida University for X-ray CT examinations. It also includes the data of adults of different body shapes (normal, fat, fatter and thin bodies for male and female) developed by JAEA. The users can estimate the organ doses by inputting the exposure conditions such as the kind of CT machine, tube voltage, tube current, beam width, scan range, rotation time,



Fig.1 Login page for users

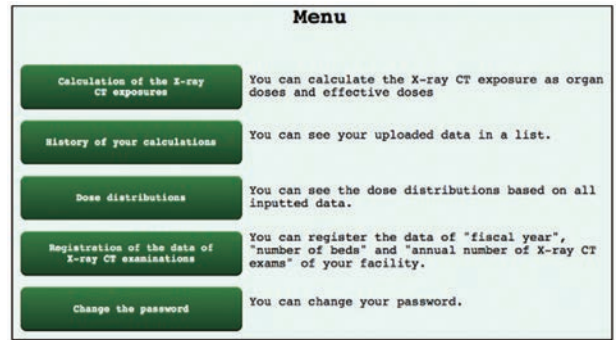


Fig.2 Menu page to select the functions of WAZA-ARI II

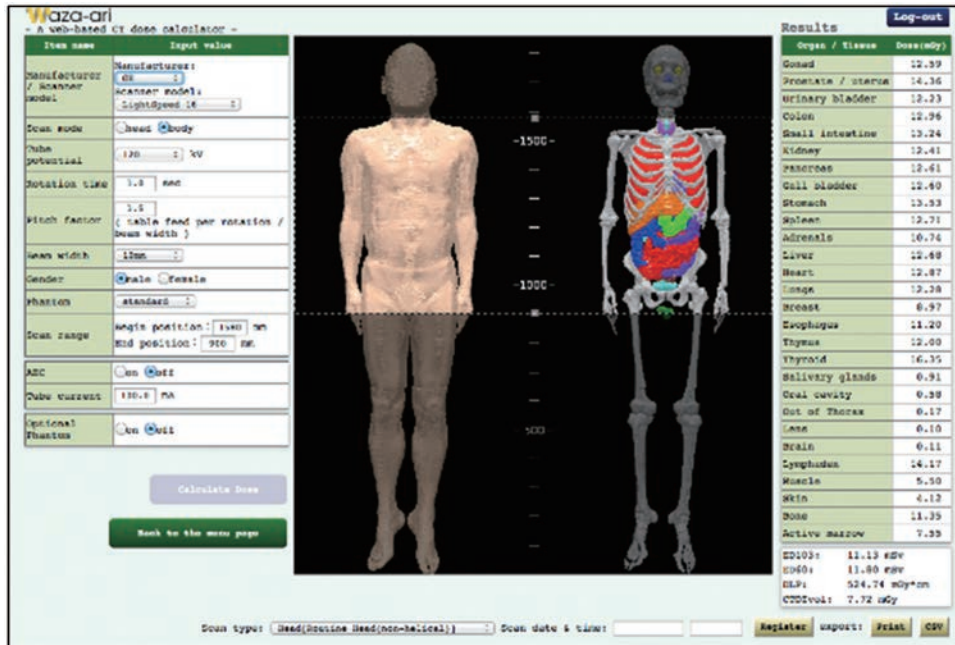


Fig.3 Example of the dose calculation result screen for each X-ray CT examination



Fig.4 The booklet of radiological examinations prepared for parents and the of the RCR booklet (iRefer) translated into Japanese.

pitch factor, etc. WAZA-ARI has the merit that it can do calculations by using not MIRRD-type phantoms but voxel phantoms, via the internet.

(5) For radiation risk communications, a booklet for parents (Fig.4), who are taking care of children with some illnesses, was issued in collaboration with medical staff in the Chiba Children's Hospital. During its preparation, the awareness of radiation dose of CT was raised for some physicians and they have started to look for ways to reduce the dose and examination frequency. To aid in making the best use of clinical radiology, the booklet *iRefer, making the best use of clinical radiology* (7th version), issued by the Royal College of Radiologists (RCR) was translated into Japanese (Fig.4).

(6) For nation-wide exchange of information on medical exposures, the general meeting of the Japan Network for Research and Information on Medical Exposure (J-RIME) was held in April 2013. Four working groups (Protection for pediatric patients, Smart Card system, Nation-wide survey, and Publicity) were approved to work among J-RIME members. Four academic societies reported that collecting exposure data for modalities such as CT, plain X-ray examination, and dental radiography is now being undertaken. The J-RIME has published the 5th issue of the newsletter "Limelight".

Highlight

Evaluation of extra-pelvic organ doses in radiotherapy of uterine cervical cancer

Kuniaki Nabatame

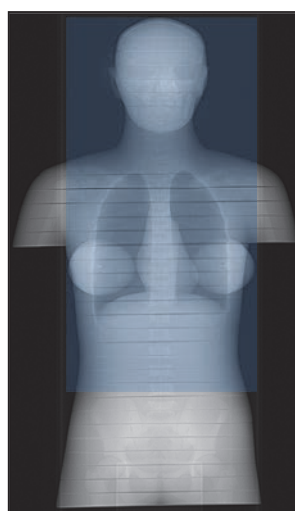
E-mail: nababox@nirs.go.jp

Introduction

Patients with uterine cervical cancer generally have received surgery, radiotherapy or their combinations for over 50 years in Japan. In addition, in 1990s, concurrent chemoradiotherapy (CCRT) also have become in wide use. Recently, the incident of cervical cancer has a peak in 30's - 40's in Japan. However, since its prognosis is basically better compared to other cancers, many patients survive for a long period of time. Consequently, there is great concern in a risk of secondary cancers for the patients received radiotherapy. In National Institute of Radiological Sciences (NIRS), a follow-up study for cervical cancer patients is in progress since 1961. In order to assess the risk of secondary cancer after radiotherapy for cervical cancer, it is essential to estimate the dose of not only the target but also the non-target organs. Therefore, we measured organ doses using anthropomorphic phantom under the same condition of photon radiotherapy for the uterine cervical cancer patient. Due to a wide range of unequal distribution of organ doses, we used both glass dosimeter and gel dosimeter. In this study, we report doses in organ outside of pelvis.

Methods

Measurements were performed with radio-photo luminescence glass dosimeters (RPLGDs), which were set in an adult anthropomorphic phantom. The sizes of RPLGD are 1.5mm in diameter and 12mm in length, which is suitable to be inserted in the anthropomorphic phantom (Fig.1). According to typical treatment protocols for the uterine cervical cancer treatment in NIRS (Tables 1 and 2), treatment plans for phantom were determined using treatment planning systems by an experienced radiation oncologist. Basically, for the uterine cervical cancer treatment, an external-beam radiotherapy (EBRT) and an intracavitary brachytherapy (ICBT) are paired or solo. The linear accelerator (Clinac21EX, Varian) was used for EBRT. The irradiation conditions are shown in Table 2. ICBT was performed with micro Selectron-HDR (Nucletron) and Ir-192 source placed to the location of uterine cervix (Fig.2).



Organ	No. of RPLGD
brain	6
brain stem	1
pituitary gland	1
lens	4
salivary gland	7
pharynx	5
thyroid	3
thymus	4
esophagus	2
lung	14
breast	4
heart	16
spleen	4
stomach	4
liver	5
pancreas	2
adrenal gland	4
kidney	4

Fig.1 Number of sites of inserted glass dosimeters for the dose measurement of each organ.

Table 1 Doses of external beam radiotherapy and intracavitary brachytherapy for each stage of cancer.

	EBRT		ICBT
	Whole pelvis	Center shielding	High dose rate
Stage I	20 Gy	30 Gy	24 Gy
Stages II, III	30 Gy	20 Gy	24 Gy
Stage IV	40 Gy	10 Gy	18 Gy
Postoperative	50 Gy	--	--



Fig.2 Photos of the set-ups for external irradiation (left) and internal irradiation (right).

Table 2 Energy of X rays, number of ports and irradiation field.

Energy	No. of portals	Irradiation field
6MV	parallel opposing ports (2 ports)	whole pelvis
6MV	4-field box technique (4 ports)	whole pelvis
6MV	parallel opposing ports (2 ports)	center shielding
10MV	parallel opposing ports (2 ports)	whole pelvis
10MV	4-field box technique (4 ports)	whole pelvis
10MV	parallel opposing ports (2 ports)	center shielding

Results and Discussion

Absorbed organ doses for two energies of X-rays for field configurations in the EBRT are determined. The measured organ doses ranged from 0.5 to 20mGy per Gy at the isocenter depending on the organ of interest. The organ dose factors in ICBT are

also calculated. It was less than 10mGy per Gy at the reference point. The total absorbed organ doses of the patient at each cancer stage were estimated to about 20~1000mGy. The organs close to the target were heavily exposed. The doses for stomach, kidney, and adrenal gland exceeded 800mGy. There is no difference among the protocols and stage of cancer. Considered the ERR/Gy is relatively high for kidney and stomach in female A-bomb survivors, we need to pay more attention to the second cancer after radiotherapy for cervical cancer.

Conclusion

This study reveals that doses of extra-pelvic organs of the standard treatment regimen for uterine cervical cancer patients.

Pediatric CT dose study at a tertiary children's hospital

Yoshihiro Nakada

E-mail: y-nakada@nirs.go.jp

Introduction

ICRP has proposed the diagnostic reference level (DRL) as an optimization tool for managing the dose from medical imaging procedures. DRL is established as a dose at the third quartile value of the distribution of mean doses of some common procedures in a number of hospitals and institutions [1]. These values should be reviewed regularly as they contribute to the safe management and optimization of doses. Several countries have established and proposed a national DRL, however, Japan has not. Recently, the data set on CT scans for adult patients from 80 institutions in Gunma Prefecture reported [2]. However, there is no study presenting a national DRL or a LDRL for pediatric CT in Japan. The aim of our study was to assess the local dose for pediatric CT examinations in a single children's hospital, which is a major tertiary care and referral center. This was achieved by sampling the dose parameters (CTDIvol and DLP) of each CT examinations across several age groups.



Materials and methods

We used the hospital information system (HIS) to retrospectively identify pediatric patients who had undergone head, chest, abdominal, cardiac, temporal bone, neck, face/sinuses, lumbar, and pelvis CT during the 4 years from October 2008 to July 2011. Retrospective review of picture archiving and communication system (PACS) showed that 4,801 CT examinations (Male, 2,767 Female, 2,034) and patient number were 2,546 (Male, 1,443 Female, 1,103). The patients were categorized into four age groups: <1 year, 1- to <5 years, 5- to <10 years and 10- to <15 years. The data collected were age and sex of the patients, CT protocols, number of CT examinations, and dates of the examinations. The CT scanner was the GE Light Speed VCT with 64 rows. Collected CT parameters were the scanning mode (axial for head and helical for chest and abdomen), tube voltage (kVp), tube current (mA), beam width, table travel per rotation for helical scan, CTDIvol and DLP.

We calculated effective dose by three methods. The first method is the measurements by using an anthropomorphic phantom representing a 3 month old, a 1-year old or 6-year old child and glass dosimeter (FGD). FGD were placed in the phantom in organs and tissues based on the effective dose definition of ICRP Publications 60 and 103. The second method is calculation by Monte Carlo simulation, using ImpACT and CT-Expo. The third method is multiplication coefficient (k-factor) of ICRP Publication 102 [3] by DLP.

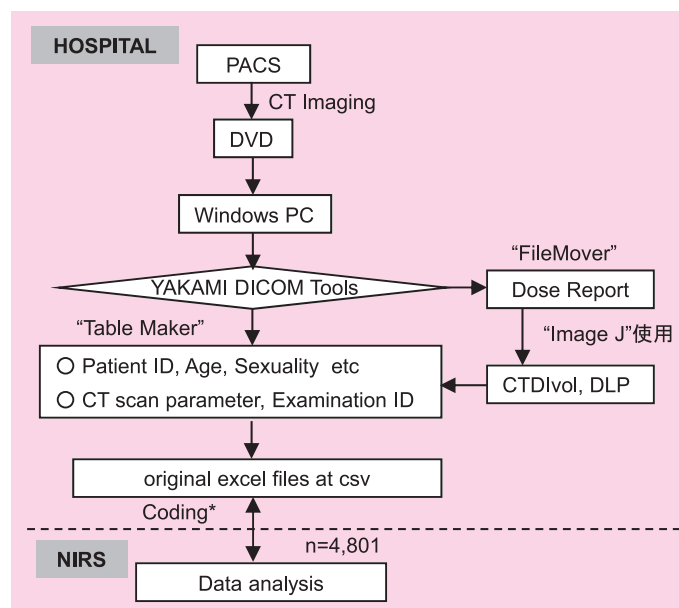


Fig.1 Flow of fact-findings

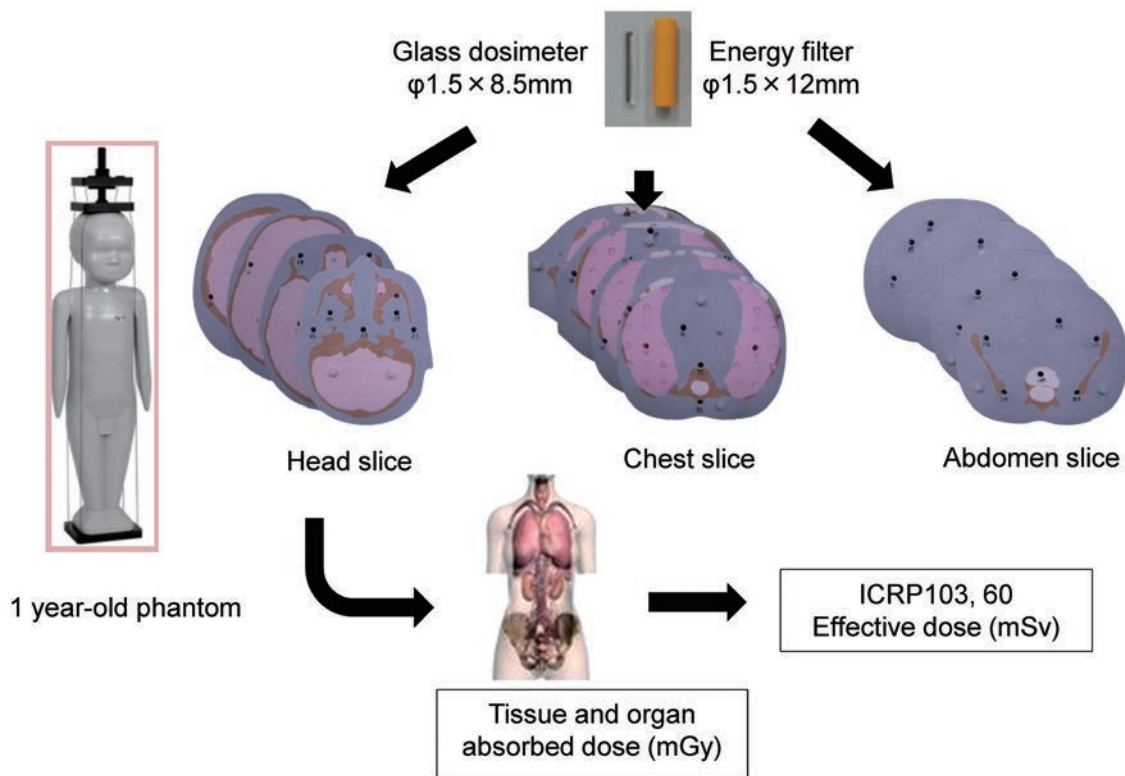


Fig.2 1 year-old anthropomorphic phantom dosimetry system

Results

The head CT was the most common, among all CT examinations. Among all head CT scans, two thirds were a non-helical scan and one third was helical scan. The chest CT and abdominal CT accounted for 6.2% and 6.6%, respectively. It is of note that the number of cardiac CT and temporal bone CT were greater than chest and abdominal CTs, which is characteristic for this children's hospital. The head CT was the most frequent among infants in the age of less than 1 year after birth. Similarly, cardiac CT was also predominant among children less than 1 year of age. There are two peak ages for temporal bone CT examinations; the first year and at 6-7 years of life. Temporal bone CT is a useful tool for the diagnosis of congenital hearing loss. A parent notices an auditory defect in a child as an infant or soon after going to elementary school. Repetition frequency of CT scans for head, chest, abdomen, heart and temporal bone were 2.0, 2.3, 1.9, 2.4, and 1.2, respectively. There was no age difference in the examination number per patient for temporal bone.

CTDIvol for head was done more often than for any other anatomical sites and increased with increasing age of patients. CTDIvol of chest and abdomen remained unchanged between ages less than 10 years old, but abruptly increased at ages >10 by 2-fold. CTDIvol for cardiac CT was 2 - 3 times larger than chest CT in every age group. As for the reason why CTDIvol value is high, unlike usual chest CT scan, cardiac CT is performed with larger scan times for contrast enhancement of the blood vessel. Age dependent increase in CTDIvol value was the most evident for cardiac CT. CTDIvol of temporal bone CT was constant throughout age examined. Age dependence of DLP showed the similar tendency as CTDIvol.

Effective dose (ED) calculated with anthropomorphic phantom and FGD for head decreased with age. It ranged from 1.5-3.1 mSv, which depends on the use of tissue weighting factors of

ICRP 60 or ICRP 103. EDs for chest CT increased with age.

They were 2.1-3.7 mSv. EDs for abdomen were similar among different age groups. They ranged 4.0-5.1 mSv. Generally, ED calculated using tissue-weighting factors from ICRP 103 was higher than that from ICRP 60. ED estimated by monte carlo simulation by 0.8-fold to 1.3-fold from ED calculated by FGD depending on the examination site.

There are several limitations in our study. First, our study population consisted of pediatric patients from single hospital, and our finding might not represent the actual pediatric CT radiation exposure among more hospitals, especially general hospitals. This is because the children's hospital has competent staffs specializing in children. Only 43% of the installed CT systems in the USA adjust the CT protocol for children resulting in unnecessary high radiation exposure. Thus, more hospitals should be encouraged to participate in the national dose survey. Owing to the rapid evolution of CT technology, CT radiation dosage protocol needs to be resurveyed to create an up-to-date DRL every 2 to 3 years.

In conclusion, this dose survey for pediatric CT found most of the CTDIvol and DLP in head, chest and abdomen were either similar or still below the DRLs recently published from six countries. Further studies are required, including more participating hospitals and efforts by academic bodies, in order to establish a national DRL to standardize the pediatric protocol in Japan.

References

- [1] International Commission on Radiological Protection. Managing patient dose in computed tomography, ICRP Publication 87. Annals of the ICRP: 30(4). Pergamon Press, Oxford, 2001.
- [2] Fukushima Y, Tsushima Y, Takei H, *et al.*: Diagnostic reference level of computed tomography (CT) in Japan, *Radiat Prot Dosim*151(1), 51-7, 2012.
- [3] International Commission on Radiological Managing patient dose in multi-detector computed tomography (MDCT). ICRP publication 102. Annals of the ICRP: 37(1). Pergamon Press, Oxford, 2007.

International Open Laboratory at NIRS (Second Term)

Ryuichi Okayasu, Ph.D.

Scientific Secretary

E-mail: rokayasu@nirs.go.jp

The second term NIRS International Open Laboratory (IOL) was started in April 2011 with four new units and its term was completed in March 2014 after three years of active international collaborative research activities. Dr. Makoto Akashi was named Director of the second term IOL and the operation was assisted by two Vice Directors (three in the third year). Recently an article regarding the second term IOL was published in the special issue of *Journal of Radiation Research* (Okayasu R. *J. Radiat. Res.* 55: i 68-i69, 2014.), and we encourage readers to see this article to learn more about this exciting program. Since 2013-2014 is the final year for the second term IOL, we had international peer reviews on the progress and accomplishments of all four units. Eight international experts in the field of radiation sciences were chosen to review four units and the reviews were performed by correspondence at the end of 2013. IOL units received seven "Excellent (S)"



grades and one "Very Good grade (A)", indicating that the second term IOL was evaluated with extreme enthusiasm. Moreover, many reviewers recommended IOL be continued if the funds are available.

We also had the final report meeting for the second term IOL on the 29th of January 2014 at NIRS. All of IOL's five Distinguished Scientists (DSs) participated as well as many attendees from in-



Fig.1 NIRS second term IOL final report meeting on January 29, 2014.

side and outside of NIRS. In this final meeting, four unit leaders presented their valuable research accomplishments and the five DSs also shared their recent findings, mainly those that resulted from IOL collaborations. We had very useful and in depth discussions on various subjects which were initiated through the IOL program. We have received many positive comments for the meeting and a substantial number of people outside of NIRS suggested that the IOL program be continued. A photo taken during this final meeting is shown in Fig. 1.

In order to summarize what we have performed during the second three year term, we have published a small report describing research activities from four second term IOL units. In this publication, detailed descriptions of research accomplishment from each unit are given as well as information on international visitors through the IOL program, publications (peer-reviewed and oth-

ers), meeting presentations, and external grant funding, etc. In addition this publication provides the results of international peer reviews with actual comments from the reviewers as well as posters from four large IOL meetings since 2011. We also have sponsored an international exchange activity within NIRS called "Friday Afternoon Get-together" almost every month, and some information on this gathering is also given in this publication. Fig.2 shows the cover of this small book on the final report of the second term IOL.

In conclusion, the NIRS IOL has significantly contributed to the advancement of international collaborations and exchanges, and the continuation of a similar international research program is desirable to advance research accomplishments within the Institute and beyond.

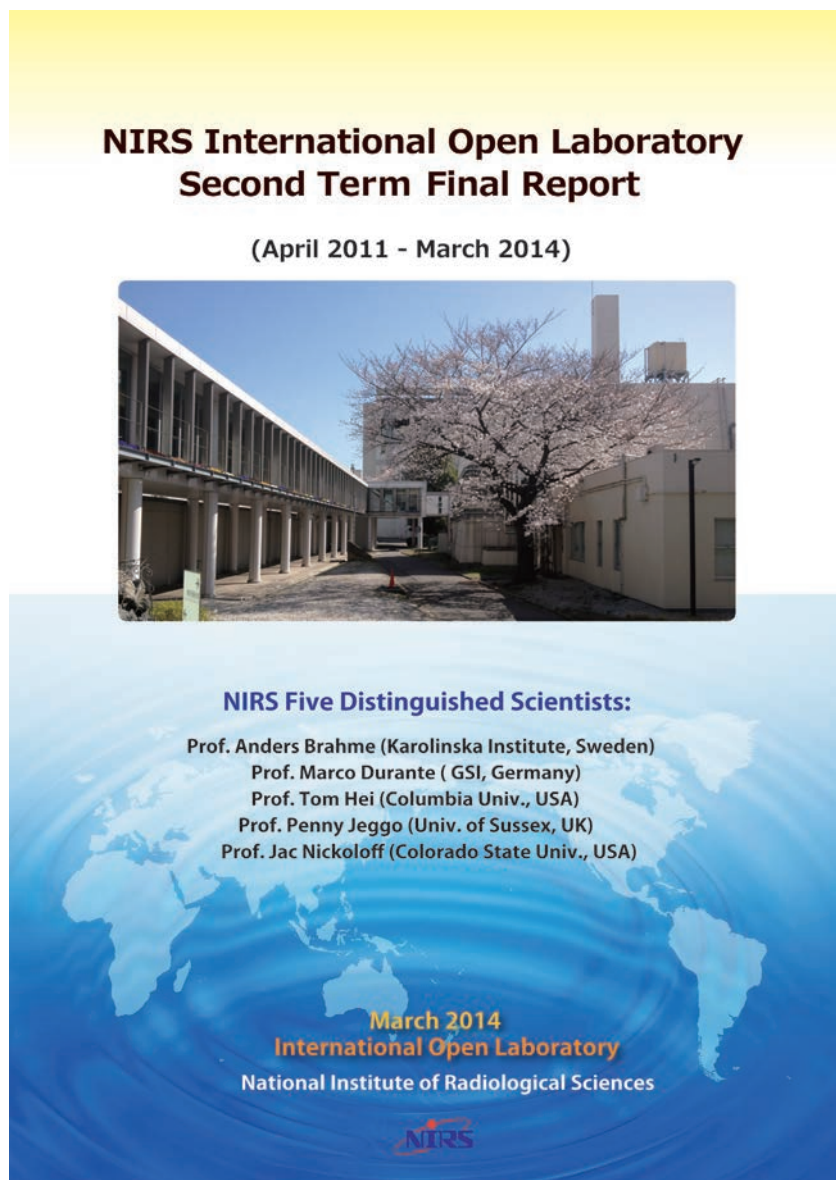


Fig.2 Cover of NIRS IOL Second Term Final Report

Radiation Response Model Research Unit

**Naruhiko Matsufuji, Anders Brahme,
Taku Inaniwa, Marta Lazzeroni, Bengt Lind,
Annelie Meijer, Masao Suzuki,
Chew Ming Tsuey, Mami Wada,
Takeshi Murakami**

E-mail: matufuji@nirs.go.jp

The Radiation Response Model Unit aims at understanding the biological response in fractionated C-ion RT as well as to explain the splendid clinical efficacy of C-ion. Working with the world-famous medical physicist Prof. Brahme and his laboratory in the Karolinska Institutet, the Unit carried out research activities for 2 terms, representing a total of 6 years. In the second term, which included FY2013 we focused on the following themes:

- Consideration of biologically optimized ion RT and the Repairable Conditionally Repairable (RCR) model
- Cell survival response of normal tissue to fractionated irradiation
- Repair kinetics to be implemented into the biological model used in ongoing C-ion RT
- Cell survival response of malignant tumor cells (GBM)

Some details are shown below.

Cell survival response to fractionated irradiation [1]

Radiation therapy is usually carried out on a fractionated irradiation basis to avoid serious side effects. C-ion RT is no exception; however, due to its superior dose localization to the tumor, hypofractionation is considered to be feasible. In fractionated therapeutic irradiation strategies, repair is thought to be completed before the subsequent irradiation. In other words, the dose response is considered to be identical among irradiations. In order to understand the response, we carried out an *in vitro* fractionated irradiation experiment with carbon ion beams that mimicked the clinical schedule with human cells. Two human normal cell lines, NB1RGB (normal human skin fibroblast cell line) and HFL-I (normal embryonic lung fibroblast cell line) were chosen and irradiated with C-290 MeV/n beam. The cells were irradiated at two different irradiation depths where the dose-averaged LET was approximately 13 and 75 keV/μm, respectively. The cells were almost 100% confluent by the first day of irradiation. For the fractionations, doses of 0.15-5.5 Gy were delivered to each cell flask placed at the isocenter for the single-, two-, three-, or four-dose fractionated irradiation over a 24-h interval. For the delayed assay, the cells were incubated for 24 h post-irradiation to determine cell survival as a function of the delayed plating time. A delayed-assay experiment was also conducted with the cells in



order to reveal the extent of damage repair. These experiments were carried out also with X-rays as a reference for the carbon beam. The results were analyzed by integrating the damage repair process into the linear-quadratic (LQ) model as shown below:

$$\log S_n = -n \left\{ \gamma (\alpha d + \beta d^2) + \beta d^2 h_n(\theta) \right\}.$$

Here, n is the number of irradiations, d is the fraction size [Gy], γ reflects the extent of PLDR (potentially-lethal damage repair) and $h_n(\theta)$ corresponds to the accumulation of SLD(sub-lethal damage).

Through the fractionated-irradiation experiment, we found that the cell survival in the fractionated irradiation cannot be explained as a simple repeat of a single irradiation, *i.e.*, the additional PLDR and SLDR factors as shown above are necessary to reproduce the data by the LQ model. Table 1 summarizes the SLDR and PLDR parameters. Concerning the SLDR, the SLD was completely repaired for X-rays, but about 30% of the SLDs were left unrepaired following exposure to 75 keV/μm carbon ions. The γ values derived by best fits were almost identical with those de-

Table 1 PLDR and SLDR indexes (γ and θ) of NB1RGB and HFL-I cells for X-ray or carbon beams

		α [Gy ⁻¹]	β [Gy ⁻¹]	γ	θ
NB1RGB	X-ray	0.59±0.17	0.05±0.02	0.46±0.00	0.09±0.06
	Carbon 13 keV/μm	0.43±0.05	0.01±0.01	0.67±0.05	0.00±0.00
	Carbon 75 keV/μm	1.32±0.04	<0.001	0.79±0.06	0.30±0.02
HFL-I	X-ray	0.43±0.14	0.06±0.02	0.47±0.04	<0.001
	Carbon 13 keV/μm	0.68±0.07	0.03±0.02	0.36±0.09	0.12±0.14
	Carbon 13 keV/μm	1.21±0.04	<0.001	0.93±0.06	0.34±0.13

rived from the delayed assay except for the HFL-I for 13 keV/ μm . In this study, the cross term between the PLDR and SLDR was not taken into consideration, which likely caused the discrepancy. The other possibility is that the repair capacity could change over time during fractionated irradiation, while we assumed a fixed repair capacity.

Consideration of repair kinetics in therapeutic model [2]

In the previous study, we assumed that PLDR and SLDR were constant as a function of time. Successively we investigated the kinetics of the repair. Concerning the biological model for C-ion RT, a pragmatic model has been originally developed and used, and recently the microdosimetric kinetic model (MKM) has been introduced. The models have been integrated into the treatment planning systems and successfully used in patient treatments. In this study we tried to integrate the repair kinetics into the MKM.

In the MKM, the surviving fraction of cells can be predicted from the dose absorbed by a subcellular structure referred to as a "domain" for any kind of radiation. When a population of cells is exposed to ionizing radiation of a macroscopically measured dose D , the dose absorbed by any individual domain, the specific energy z , is a random variable that varies from domain to domain throughout the population of cells. The average of z over the entire population of cells equals D . Ionizing radiation is assumed to cause two types of primary lesion, type I and II lesions, in the domain. Each type of lesion is created with a probability proportional to the specific energy z . A type I lesion is always lethal to the cell containing the domain, assuming that it corresponds to a clustered DNA damage that is difficult to repair and induces chromosome aberrations. A type II lesion may undergo one of four transformations: (1) spontaneous conversion to a lethal unreparable lesion; (2) pairwise combination with another type II lesion in the same domain to form a lethal unreparable lesion; (3) spontaneous repair; or (4) persistence for a certain length of time, before becoming lethal. In order to derive the rate constant of each pathway, we performed split-dose experiments at HIMAC. Human salivary gland (HSG) tumor cells were used for the experiments. This is a reference cell line in our RBE definition showing a typical tumor response among a variety of biological species. The flasks containing the HSG cells were irradiated with the 290 MeV/n mono-energetic carbon beam at the scanning port. The flasks were exposed to two equal doses of the carbon beam of 2.5 Gy separated by adjusting the time interval from 0 to 9 h.

With the parameters derived through the experiment, we made treatment plans for a patient with prostate cancer, with a single field from the right side of the patient. The biological doses of 2.65, 4.35 and 6.86 Gy (RBE) were prescribed to the target. In our standard prescription for prostate cancer, the fractional dose of 2.65 Gy (RBE) is delivered for 16 fractions. The prescribed dose of 4.35 Gy (RBE) for 8 fractions and 6.86 Gy (RBE) for 4 fractions were chosen to give the same biologically equivalent dose of 2.65 Gy (RBE) for 16 fractions. The structure of the patient was numerically modeled with voxels of size $D_x=D_y=D_z=2.0$ mm. The Bragg peak positions of the pencil beam were arranged on regular grids of 2 mm spacing in the x and y directions on the layers of equal depths of 2 mm water-equivalent length (mmWEL), which covers the target volume with adequate margins for lateral and distal dose falloffs. The number of carbon ions required for each position was determined by the optimization algorithm of the treatment planning system. It should be noted here that the aim of this study

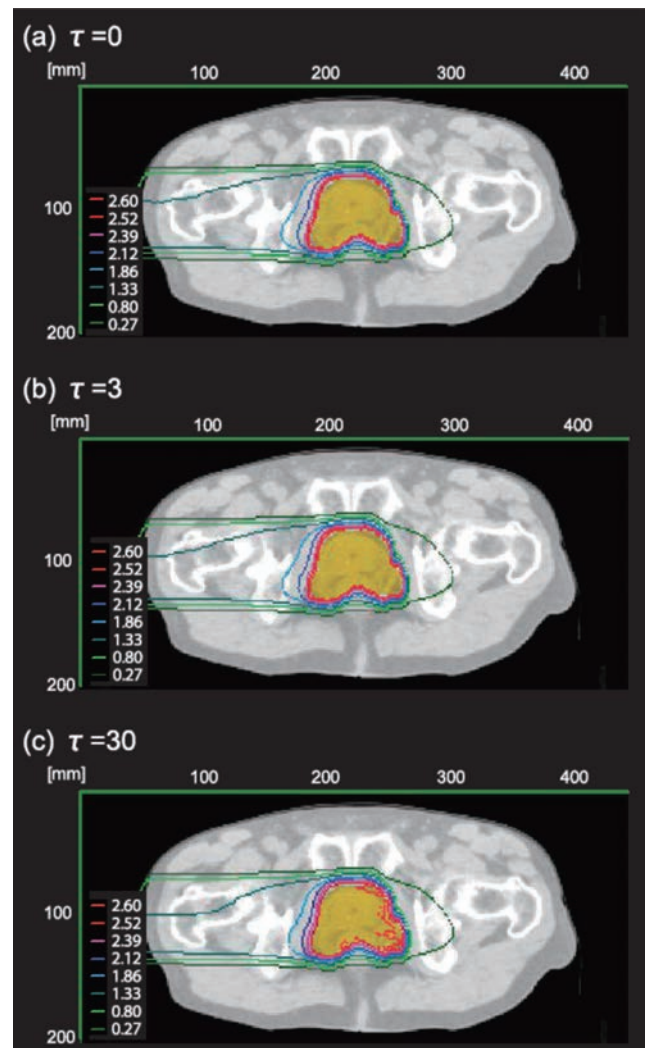


Fig.1 The equivalent acute dose distribution in a prostate-cancer patient with the interruption times of: (a) 0 min, i.e. the planned distribution; (b) 3 min; and (c) 30 min. The prescribed dose of the plan was 2.65 Gy (RBE).

was not to show the general conclusions specific for a prostate-cancer case, but to investigate the effects of dose-delivery time structure on biological effectiveness against the planning condition for typical tumors using the response of our standard HSG cells.

An example of the planned and recalculated equivalent acute dose distributions, with the interruption times of 0, 3 and 30 min, is shown as Fig.1. When the dose delivery was interrupted, the biological effectiveness can be reduced compared to the plan. The reduction will be less than 2.0% for τ shorter than 5 min. However, if the interruption is prolonged to 20 min or more, the biological effectiveness can be influenced significantly.

These outcomes will contribute to realize further optimized ion RT in the future.

References

- [1] Wada M, Suzuki M, Liu C, *et al.*: Modeling the biological response of normal human cells, including repair processes, to fractionated carbon beam irradiation, *J Radiat Res* 54, 798-807, 2013.
- [2] Inaniwa T, Suzuki M, Furukawa T, *et al.*: Effects of dose-delivery time structure on biological effectiveness for therapeutic carbon-ion beams evaluated with Microdosimetric Kinetic Model, *Rad Res* 180, 44-59, 2013.

Highlight

Oxygen enhancement ratio (OER) and LET to heavy ion beams at different pO_2 concentrations

Yoshiya Furusawa, Marco Durante

E-mail: furusawa@nirs.go.jp, M.Durante@gsi.de

Introduction

Clinical ion-beam therapy has started with carbon ions in 1996 at HIMAC-NIRS. Prior to clinical therapy, we had performed radiobiological studies, especially focused on relative biological effectiveness (RBE) and oxygen enhancement ratio (OER) to estimate suitable dose distribution in the SOBPs that will be applied for patients. The OER is believed to have a three-fold effect on the dose, and it depends both on the partial oxygen concentration (pO_2) and linear energy transfer (LET) (Fig. 1). However it was neglected and not taken into account in the dose design of the treatment beam, because it was not realistic to know the distribution of the actual pO_2 in a patient's tumor at that time. The hypoxic fractions in a tumor consist of both chronic- and acute- areas, and they change dynamically resulting from an imbalance between oxygen supply and consumption. As a tumor grows, it rapidly outgrows its blood supply, leaving portions of the tumor with regions where the oxygen concentration is lower than in normal tissues.

Recently, functional-imaging-techniques have been making rapid advances in NIRS and worldwide, and it will be possible to know the distribution of pO_2 in a tumor in the near future.

OER is still the most important factor even in heavy ion radiotherapy, however there are no biological data concerning how OER values change with the pO_2 in a tumor with respect to high-LET radiations.

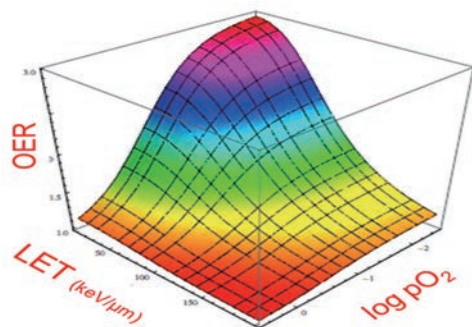


Fig.1 Expected Oxygen Enhancement Ratio (OER) and partial oxygen concentration (pO_2) to ion beams at different Linear Energy Transfer (LET).



The Particle Beam Quality Research Unit (Fig.2) has established in the International Open Laboratory in 2011 following establishment of the other 3 units in 2008, in collaboration with Dr. Marco Durante (Director of the Biophysics Department of the GSI Helmholtz Center, Darmstadt, Germany, and President of the International Association of Radiation Research (IARR)). GSI is acting as a pioneer in Europe for ion-beam radiotherapy just as NIRS acts in Japan. A kick-off meeting was held in Darmstadt in September 2011 to discuss details of a new research project with the unit in NIRS. We decided to focus on OER and LET at different pO_2 conditions in cells. We invited Dr. Walter Tinganelli to perform biological experiments at HIMAC, NIRS and to start research with other staff members in NIRS and GSI.



Fig.2 Kick off meeting of the unit at Darmstadt University of Technology, Darmstadt, Germany in September 2011. Dr. Y. Matsumoto, Dr. R. Hirayama, Dr. S. Fukuda (from the left to right of the 1st row), Dr. M. Durante (wearing a hat in the center), Dr. W. Tinganelli (on the far left in the 2nd row), and other staffs in GSI.

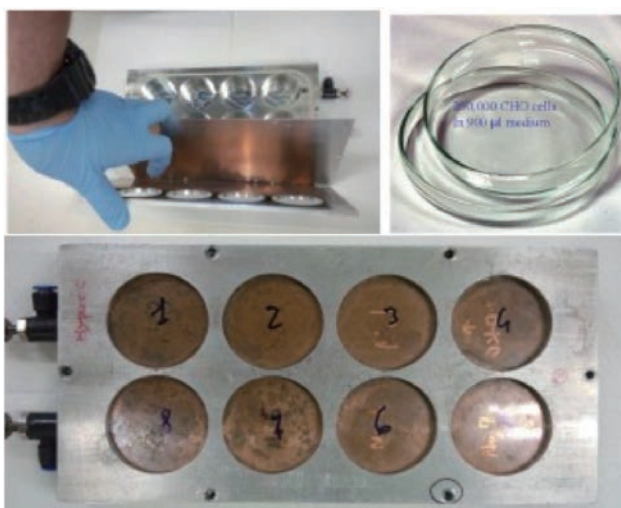


Fig.3 Irradiation chamber made by metals with thin window. CHO cells grown on the grass dishes were set in the chamber and 92-95% N₂, 5% CO₂ and 0, 0.15, 0.5, or 2.0 % O₂ mixed-gas was flow prior to 0.5-1.0 hour irradiation. Heavy ion beams were exposed to the cells at different LET and different dose through the window [2].

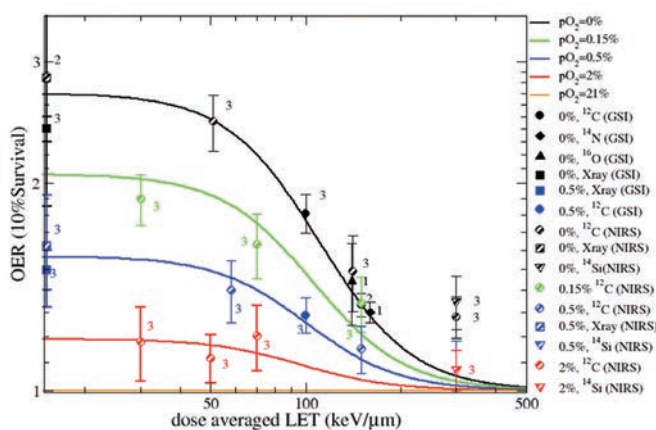


Fig.4 Oxygen enhancement ratio (OER) at 10% survival level versus linear energy transfer (LET) of heavy ion beams at different partial oxygen concentrations pO₂ (values in percent) in CHO cells [2,3].

Experimental

Glass petri dishes with 200,000 CHO cells (Chinese hamster ovary) were kept in different hypoxic gas conditions and irradiated through a thin copper and aluminum window (Fig.3). Several oxygen concentrations have been adopted for the present project. Mixing three different gases: carbon dioxide, nitrogen and air (as oxygen), we can obtain the required oxygen concentrations: 1) anoxic condition (~0% oxygen), 2) hypoxic condition (0.5%, 0.15, and 2% oxygen), and 3) oxenic condition (95 % air). The samples were irradiated with different ions and LETs (13, 30, 50, 60, 70, 100, ~150, and 300 keV/µm) at HIMAC-NIRS and SIS-GSI accelerator facilities or X-ray generators. After irradiations, colony formation assays were performed in ambient air.

It is believed that relative sensitivity of one at the anoxic condition (0% pO₂) increases with increase of pO₂ quickly to become two at the 0.5% pO₂ hypoxic condition, and reaches a saturated level of 3 at several tens of percent [1] for low-LET photons. This might be the same for high-LET radiations such as particle beams, but we do not have actual biological experimental data, so we performed OER experiments with cultured cells at different hypoxic conditions to high-LET radiations. The results showed a reasonable agreement with the prediction model and with the previous data from GSI, especially in the slope region as shown in

Fig.4. The higher OER value found for the very high LET is due to fragmentation of the large ions, since we used the HIMAC-NIRS passive beam experimental room.

The results will be used for the implementation of adaptive treatment planning [4,5] in TRiP98. This experimental OER distribution with LET and pO₂ may also be applicable for dose/LET-painting in a patient's tumor as well as RBE when an improved functional molecular image gives a distribution of oxygen concentration in the tumor.

References

- [1] Horsman MR and Overgaard J.: The oxygen effect and tumor microenvironment. In: Steel GG Ed. *Basic Clinical Radiobiology*, 3rd Ed. 158-68, Hodder Arnold, London, 2002.
- [2] Tinganelli W, Furusawa Y, Durante M, *et al.*: Oxygen enhancement ratio of heavy ions in partial hypoxic conditions, *An. Rep. NIRS-HIMAC*, 2013.
- [3] Ma NY, Tinganelli W, Maier A, *et al.*: Influence of chronic hypoxia and radiation quality on cell survival, *J Radiat Res*, 54s1, i13-22, 2013.
- [4] Scifoni E, Tinganelli W, Weyrather WK, *et al.*: Including oxygen enhancement ratio in ion beam treatment planning: model implementation and experimental verification. *Phys Med Biol*. 11, 3871-95, 2013.
- [5] Kråmer M, Durante M, Furusawa Y, *et al.*: New challenges for biologically adapted ion beam treatment planning: single and multi-ion approaches. *Radiother Oncol*, 109, 110, 2014.

Topic

Research on the standardization and clarification of charged particle therapy

Hiroshi Tsuji

E-mail: h_tsuji@nirs.go.jp

Objectives

- To perform clinical research for clarifying usefulness of carbon ion therapy in order to establish new treatments for radioresistant tumors and to standardize the treatments for common cancers.
- To perform clinical research on utilization of the advanced technique of high-speed spot scanning irradiation of carbon ion beam in the routine treatment for head & neck or pelvic tumors.
- To investigate the benefits of improving accuracy of imaging modalities, such as PET, MRI, and CT scan for carbon ion therapy.
- To investigate the possibility of prediction or evaluation of effectiveness of carbon ion therapy using novel information from imaging modalities.
- To develop and regulate a comprehensive database on radiotherapy, mainly carbon ion therapy in consideration of achieving evidence-based medicine. Additionally, to propose a national database available for multi-institutional research on particle therapy carried out at domestic and foreign institutions.

Progress of Research

The Program of Research on the Standardization and Clarification of Charged Particle Therapy consists of the Clinical Trial Research Team, Applied PET Research Team, Applied MRI Research Team, and Clinical Database Research Team. All the teams are performing research and development on charged particle therapy. Progress of research in each team is summarized below.

1) Clinical Trial Research Team

As of March 2014, a total of 8,227 patients have been treated with carbon ion beams at our institute (Fig.1). Carbon ion radiotherapy of these patients was carried out as more than 60 different phase I/II or phase II clinical trials or advanced medicine.

Eight hundred and eighty-eight patients were treated as new patients from April 2013 to March 2014. This number is a new record for NIRS and about a 10% increase compared to the last year.

Fig.2 summarizes the numbers of patients for each tumor site.



Prostate, lung, head & neck, bone & soft tissue, and liver tumors are the leading 5 tumors in the trials and recently the number of pancreatic tumor patients has increased rapidly.

Scanning irradiation became available for the routine treatment of less mobile targets in the head & neck or pelvic region. More than 300 patients could be safely and efficiently treated with scanning irradiation at the New Treatment Research Facility.

Clinical trials for pancreas, esophagus, uterus, and kidney cancer are being conducted and patient enrollment has progressed. As an advancement of hypofractionated carbon ion therapy, the single session treatment for lung cancer and 12-fraction treatment for prostate cancer could be established and their applications as advanced medicine were started.

As a result of the clinical research done so far, it has been revealed that carbon ion radiotherapy provides a definite local control and offers a survival advantage without unacceptable morbidity in a variety of tumors that were hard to cure with other modalities. In addition, it was possible to implement hypofractionated radiotherapy using carbon ion beams, with application of larger doses per fraction and a reduction of overall treatment times as compared to conventional photon radiotherapy.

2) Applied PET Research Team

In the last year, this team completed modification of the PET respiratory gating system for detecting the respiratory signals at the end of the expiratory phase just as it is being achieved in the system of gated irradiation for heavy-ion radiotherapy. With this modification, it became possible to fuse the respiratory gating PET images with CT images for treatment planning taken in synchronization with the respiratory motion.

This year, some phantom experiments were done to confirm performance of the new respiratory gating system. Results of the

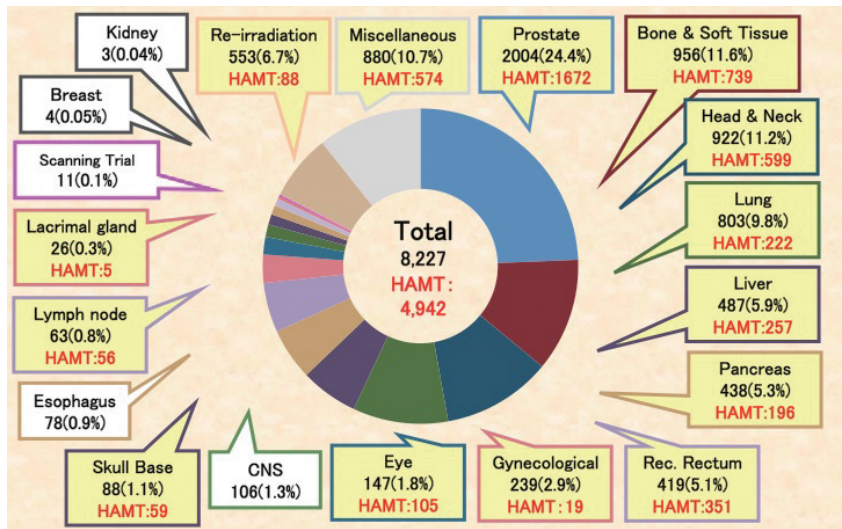


Fig.1 The yearly number of patients treated with carbon ion beams at NIRS.

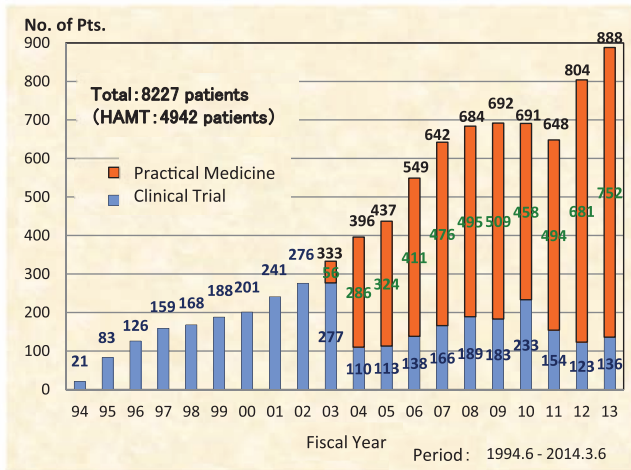


Fig.2 The number of patients for each tumor site treated with carbon ion beams.

phantom experiments confirmed that the new respiratory gating system was able to detect the end of the expiratory phase and that the PET images obtained using this new respiratory gating system were better than those obtained using the conventional system.

3) Applied MRI Research Team

To provide quantitative diagnostic information for heavy charged particle therapy, several MR methods have been applied to clinical diagnosis. Advanced water diffusion monitoring in a tumor was performed using multi-level diffusion weighted MRI. The sequences for MR elastography were refined for world-wide deliv-

ery as an NIRS-made basic program (collaborative study with Siemens). MR and ultrasonic elastography in normal subjects were performed to obtain basic information for a combined clinical trial.

4) Clinical Database Research Team

It is strongly required to conduct multi-institutional clinical trials for standardizing carbon ion therapy in various tumor entities. Four running carbon therapy facilities in Japan, NIRS, HIBMC (Hyogo), GHMC (Gunma), and HIMAT (Saga) organized a cooperative study group to collaborate for this purpose. It is essential to prepare a dedicated database system to perform multi-institutional trials and to play a leading role in future trials. Thus, a database system was developed that can store integrated information on the patients treated at all the institutions of this study group. The data includes pretreatment information, treatment data, and outcome information. In addition, a conversion tool was developed that can unify the different ways of recording the medical information of each institution. For example, institution A uses "M" and institution B uses "0" to represent "male" on their database. The tool converts such differences of descriptions to the standardized description on our database.

References

- [1] Nomiya T, Tsuji H, Toyama S, *et al.*: Management of high-risk prostate cancer: Radiation therapy and hormonal therapy, *Cancer Treatment Reviews* 39(8), 872 - 878, 2013-05.
- [2] Wakatsuki M, Kato S, Ohno T, *et al.*: Dose-escalation study of carbon ion radiotherapy for locally advanced squamous cell carcinoma of the uterine cervix (9902), *Gynecologic Oncology* 132(1), 87-92, 2014.
- [3] Matsumoto K, Imai R, Kamada T, *et al.*: Impact of carbon ion radiotherapy for primary spinal sarcoma, *Cancer* 119(19), 3496 - 3503, 2013-10.

Topic

Total-body low dose irradiation induces early transcriptional alteration without late Alzheimer's disease-like pathogenesis and memory impairment in mice

Bing Wang

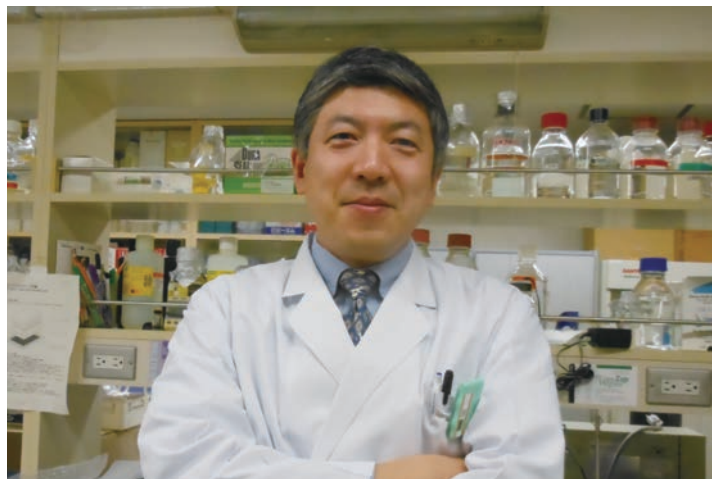
E-mail: jp2813km@nirs.go.jp

Introduction

Alzheimer's disease (AD) is characterized by formation of both senile plaques containing amyloid beta peptide (A β) derived from amyloid precursor protein (APP) and neurofibrillary tangles containing hyperphosphorylated tau protein (p-tau) in the brain that lead to progressive neuronal degeneration and death. Despite the fact that AD was identified more than 100 years ago, its cause remains elusive. There is mounting evidence, however, describing the effects of ionizing radiation (IR) on the brain, suggesting that exposure to IR is susceptible to ultimately favoring AD [1]. A recent study in mice reported early transcriptional response in the brain to low-dose (100 mGy) sparsely ionizing (low linear energy transfer (LET)) X-rays suggesting alterations of molecular networks and pathways associated with cognitive functions, advanced aging and AD. The possible cognitive and behavioral consequences induced by low-dose radiation are of great concern as humans are exposed to ionizing radiations from various sources including medical diagnosis. Although radiation therapy is an important tool in the treatment of primary and metastatic brain tumors, it is also responsible for various adverse neurological effects such as cognitive dysfunction and dementia. The present study was to investigate both the acute transcriptional alteration as well as the late pathological, cognitive and behavioral consequences induced by low-dose total body radiation (TBI).

Materials and Methods

Eight-week-old female mice of the C57BL/6J Jms strain were purchased from SLC, Inc. (Japan). The mice were maintained in a clean conventional animal facility under a 12-h light/12-h dark photoperiod. They were housed in autoclaved cages with sterilized wood chips and allowed free access to standard laboratory chow (MB-1, Funabashi Farm Co., Japan) and acidified water (pH = 3.0 ± 0.2) *ad libitum*. The mice were acclimatized to the laboratory conditions for 2 weeks as an adaptation period before use. As positive controls for detection of characteristic AD pathologies, two established AD mouse models were employed to ensure appropriateness of examination in the present study: transgenic Tg 2576 mice (Taconic Farms, Inc. USA) overexpressing human APP and PS19 mice overexpressing human tau. They were used as



positive controls for detection of amyloid-related and tau-related pathologies, respectively. All experimental protocols involving mice were reviewed and approved by The Institutional Animal Care and Use Committee of NIRS. The experiments were performed in strict accordance with the NIRS *Guidelines for the Care and Use of Laboratory Animals*.

X-rays were generated with an X-ray machine (Pantak-320S, Shimadzu, Japan) operated at 200 kVp and 20 mA, using a 0.50-mm Al + 0.50-mm Cu filter. For high-LET heavy-ion irradiations, a monoenergetic ion beam of carbon particles was generated and accelerated by a synchrotron (a cyclic particle accelerator with its guiding magnetic field synchronized to the particle beam), the HIMAC, at NIRS. The beam energy was 290 MeV/nucleon corresponding to an average LET value of about 15 keV/ μ m. Ten-week-old C57BL/6J mice were total-body irradiated with an acute dose from X-rays (100 mGy) or carbon ions (50 or 100 mGy). The hippocampus was collected 4 hours and 1 year after irradiation and the expression of 84 AD-related genes was analyzed. Morris water maze test was applied to the measurement of the learning ability and memory of the animals. Amyloid imaging with PET was performed to detect the accumulation of fibrillary A β , and characteristic pathologies of AD were examined with immunohistochemical staining of APP, A β , tau, and p-tau. Statistical evaluation of the other data was carried out with the χ^2 test and Student t-test, as appropriate. Statistical significance was assigned to a value of P of <0.05.

Results

For the transcriptional studies on 84 AD-related genes after TBI, results (Table 1) on 100 mGy X-rays showed that only 1 gene was significantly down-regulated at 4 hours and two genes were down-regulated at 1 year; results on carbon ions showed that 3 genes

Table 1 Transcriptional alteration in the expression of AD-related genes in hippocampi in mice after TBI

Radiation	Time after Irradiations	Dose	Gene	Transcriptional Alterations		
				Ratio to Control	SE	P
X-rays	4 hours	100 mGy	Apbb1	0.879	0.025	**
			Lrp1	0.845	0.032	*
	1 year	100 mGy	Il1 α	0.818	0.375	*
Carbon	4 hours	50 mGy	Abca1	1.222	0.011	*
			Casp3	1.110	0.003	*
			Chat	2.714	0.622	*
	4 hours	100 mGy	Apoe	0.929	0.006	*
			Chat	2.715	0.622	*
			Ctsd	0.908	0.024	*
			Il1 α	0.621	0.085	*
	1 year	100 mGy	Il1 α	0.932	0.024	*

Mice were exposed to TBI and the transcriptional alteration in the expression of AD-related genes in hippocampi was studied at 4 hours and 1 year after TBI. * $P < 0.05$, ** $P < 0.01$

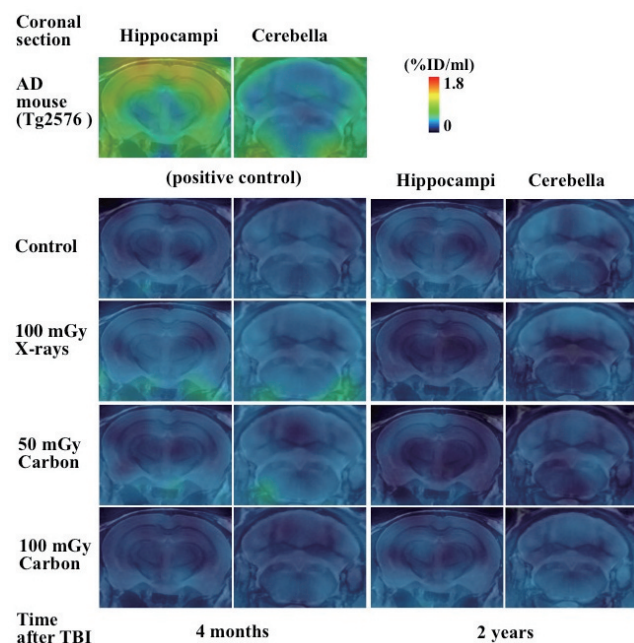


Fig.1 *In vivo* detection of A β in mice after TBI. PET images were generated by averaging dynamic scan data at 30-60 minutes after administration of ¹¹C-PIB and overlaid on the MRI template. Photos represent coronal images containing hippocampus and cerebellum regions at 2 and 6.5 mm posterior to the bregma, respectively. Images of positive control mouse (Tg2576) are shown in the upper panels.

were markedly up-regulated at 4 hours after TBI with 50 mGy, 1 gene was up-regulated and 3 genes were down-regulated at 4 hours after TBI with 100 mGy, while only 1 gene was significantly down-regulated at 1 year after TBI with 100 mGy. On the other hand, for X-rays and carbon ions, PET imaging (Fig.1) and immunohistochemical staining showed no change in the accumulation of fibrillar amyloid and the expressions of APP, A β , tau, and phosphorylated tau were detectable in the animals 4 months and 2 years after TBI; the behavioral studies showed no significant difference on learning ability (Fig.2) and memory at 1 year and 2 years after TBI [2, 3].

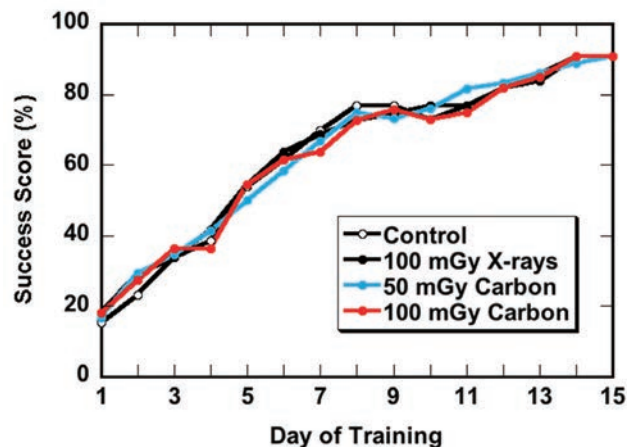


Fig.2 Test for acquisition of spatial memory of mice after TBI. Behavioral test with the Morris water maze was performed for the animals at a postnatal age of 2 years. No differences were found in irradiated animals compared with those of the unirradiated control.

Conclusion and Discussion

This study complements previously reported work examining the acute transcriptional response of mouse brain to 100 mGy X-irradiations by providing further insight into the late consequences of both X-rays and carbon ions using a battery of examinations at transcriptional, behavioral and pathological levels. These findings suggest that TBI at a dose of 100 mGy could mainly induce early acute transcriptional alterations in some AD-related genes at 4 hours, and these transcriptional alterations did not appear to cause any significant changes regarding late impairment in spatial learning and memory at 1 and 2 years after irradiations, and did not seem to have any impact on induction of AD-like pathogenesis in the brains at 4 months and 2 years after irradiations. From a clinical point of view, these findings do not explore human health concerns that are generally implied following medical diagnostic exposure to IR and that exposure to low doses such as those found in the penumbra of the field are unlikely to result in AD. These findings indicate that radiation-induced changes in the expression of genes associated with AD are not necessarily predictors of the emergence of AD. The present work suggests that it is critical to perform more thorough studies on the late effects using such as pathological and behavioral parameters rather than just assuming that a change in gene expression means that AD would develop.

References

- [1] Begum N, Wang B, Mori M, *et al.*: Does ionizing radiation influence Alzheimer's disease risk?, *J Radiat Res* 53, 815-822, 2012.
- [2] Wang B, Tanaka K, Ji B, *et al.*: Total body 100-mGy X-irradiation does not induce Alzheimer's disease-like pathogenesis or memory impairment in mice, *J Radiat Res* 55, 84-96, 2014.
- [3] Wang B, Tanaka K, Ji B, *et al.*: Low-dose total-body carbon-ion irradiations induce early transcriptional alteration without late Alzheimer's disease-like pathogenesis and memory impairment in mice, *J Neurosci Res* 92, 915-926, 2014.

Topic

Telephone consultations on radiation exposure - Tabulated results from the year following the TEPCO Fukushima Daiichi Nuclear Power Station accident -

**Reiko Kanda, Satsuki Tsuji,
Kiyomi Eguchi-Kasai, Hidenori Yonehara,
Masami Torikoshi**

E-mail: kanda_r_@nirs.go.jp

After the TEPCO Fukushima Daiichi Nuclear Power Plant accident, all of the phone lines within NIRS were overwhelmed with inquiries from the general public, local government authorities, the media, etc. On 13 March 2011, NIRS researchers opened a dedicated telephone consultation line for the public (non-experts) in order to hear their various questions and worries about radiation exposure and to provide expert knowledge and evidence-based advice. This report is a tabulation of the contents of consultation calls made to the NIRS telephone consultation for the general public from 15 March 2011 to 31 March 2012. At present, this project is ongoing; this report is a collection of consultations from the year immediately following the accident. Readers may refer to the following site for details.

http://www.nirs.go.jp/publication/irregular/pdf/nirs_m_265en.pdf

Consultants took notes during the phone consultations. Notes from 17,017 calls were amassed in the year following the accident. If data such as date/time of consultation, consultation length, attributes of the caller (gender, residence at the time of the accident and residence when calling) or details of the consultation topic were included in a note, only this information was transcribed and tabulated before the notes were disposed of.

Consultation topics were categorized as below.

- Exposure from the environment (12 topics)
(e.g., air, rain, river, ocean, dirt, yard, hotspot)
- Radiation measurements and assessments (9 topics)
(e.g., external / internal exposure, natural / accidental radiation)
- Decontamination and protection from exposure (9 topics)
(e.g., evacuation, ventilation, agents, laundry, bathing)
- Food / water (4 topics)
- Various activities (3 topics)
(e.g., hobbies / sports, agriculture, industry)
- Specific people (4 topics)
(e.g., children, evacuees, patients)
- Other consultations (3 topics)
- Not consultations (6 topics)

The results are listed below:



(1) Over 5,000 consultations were received in the 17-day period in March 2011, but the number of consultations began to decrease in April (Fig.1). Mean time length per call in the year following the accident was 14.6 min.

(2) Female callers accounted for 60%-70% of the calls, and there was not much variation in gender proportions in the year after the disaster.

(3) Fig.2 shows ratios of consultations classified by residence area at the time of the accident. The percentage of the third category (Tokyo, Kanagawa, Yamanashi, Nagano and Niigata) showed decrease decreasing tendency.

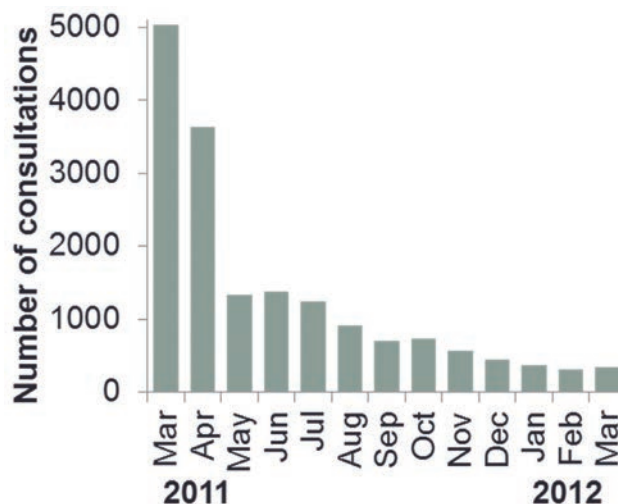


Fig.1 Changes in consultation number over one year

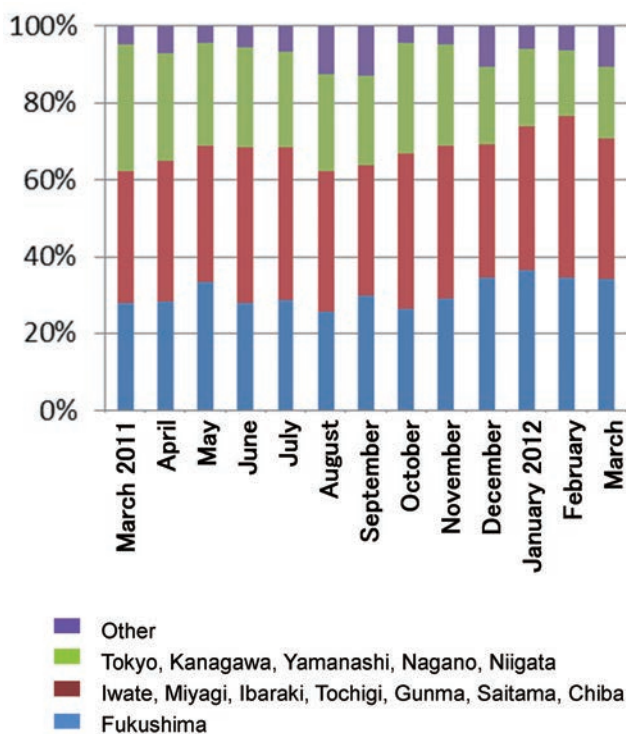


Fig.2 Consultation ratios for residences at the time of the accident

(4) In the year from March 2011 to March 2012, the following four consultation topics were most common:

- Past exposure in areas outside the Fukushima power plants vicinity
- Children (pregnancy, childcare, school, etc.)
- Overall eating habits
- Consultations related to food and drink other than fish and water

Table 1 Consultation conversation lengths for each consultation topic

Consultation topic	Mean(min)
Comparisons with atom bombs, Chernobyl	23.9
Contamination status of hotspots	20.8
Home decontamination methods	19.6
Demands/complaints for government, research institutes, etc.	19.0
Questions regarding radiation regulations and restrictions	18.3
Changes in physical condition	17.1
Mean length of all consultations	14.6
Want assessment of external exposure dose	12.2
Want an internal exposure examination	10.8
Want a different examination	9.3

(5) Time length of consultation for each consultation topic was tabulated. Those that were longer or shorter than the mean length (14.6 min) are listed in Table 1. For situations such as someone wanting to have an examination done or where answers were clear as to what was being asked, consultations tended to be shorter.

(6) Frequencies of consultations for changes in physical conditions for different residences at the time of the disaster were tabulated (Table 2). Although frequency decreased as the residence distance at the time of the accident from the Fukushima Daiichi Power Plant increased, the difference was small.

Table 2 Number of consultations about changes in physical conditions by residence at the time of the accident

(i) Fukushima	(ii) Iwate, Miyagi, Ibaraki, Tochigi, Gunma, Saitama, Chiba	(iii) Tokyo, Kanagawa, Yamanashi, Nagano, Niigata	(iv) Other areas or countries
6.0%	5.7%	5.0%	4.8%

Topic

Imaging of radioactive contaminants with a characteristic X-ray camera

**Shingo Kobayashi, Takayuki Shinomiya,
Yukio Uchihori, Yoshiyuki Shirakawa**

E-mail: shingo@nirs.go.jp

The needs for an imaging device that visualizes radioactive contamination have been considerably increased in Japan because of the Fukushima Daiichi Nuclear Power Station (FDNPS) accident in March 2011, which released large amounts of radioactive materials and contaminated the region around the FDNPS. Such an imaging device is expected to assist workers engaging in decontamination and nuclear reactor decommissioning tasks. If the distribution of radioactive contamination can be immediately and visually confirmed by an imaging device, the efficiency of decontamination work will be enhanced and the workers will be able to avoid unexpected exposure.

One of the candidates for the imaging device is a gamma camera (GC). It can visualize the distribution of radioactive contamination by detecting gamma-rays on the basis of a pinhole camera technique. Cs-137 is one of the most important radionuclides that contribute to the radiation dose rate in the region around the FDNPS and it emits gamma-rays with an energy of 662 keV (Fig.1); so the contamination by Cs-137 could be visualized by a GC.

In order to take an image of radioactive contamination by a GC, the GC has to measure each arrival direction of the gamma-rays from radiation sources to the GC, since to visualize something by gamma-rays is to know the gamma-ray flux variation dependent on arrival directions within the GC's field of view. For that purpose, a GC consists of a two-dimensional (2D) sensor array and a thick lead container with a pinhole in front of the array (Fig.2a). The container works as a shield for gamma-rays and limits the arrival direction of the gamma-rays. Only gamma-rays that enter from the pinhole are detected. In this condition, the arrival direction of a gamma-ray can be uniquely determined as the direction along the line connecting the pinhole position to the point on the 2D sensor array where the gamma-ray is detected. A GC is based on this pinhole camera technique.

The disadvantage of GCs, however, is that their weight is typically around 20 kg and therefore too heavy for a person to carry around because of the thick lead container to shield gamma-rays from environment. It would be difficult to use a heavy GC for practical decontamination and nuclear reactor decommission tasks. Therefore, we decided to develop a new imaging device that is

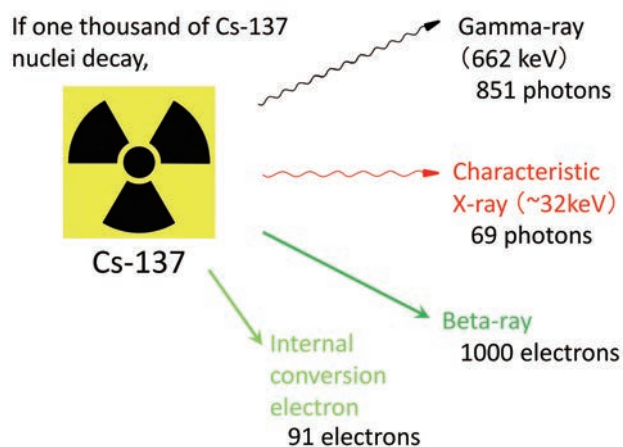


Fig.1 The kinds of radiation from Cs-137. Gamma-rays, characteristic X-rays, beta-rays and internal conversion electrons are emitted.

lightweight, low-cost and has high sensitivity.

We took note of the fact that Cs-137 emits not only gamma-rays but also characteristic X-rays with an energy of 32 keV (Fig.1) and decided to use X-ray detection instead of gamma-ray detection. The characteristic X-ray camera (CXRC) is also a kind of a pinhole camera but it is optimized to detect 32 keV X-rays from Cs-137 instead of 662 keV gamma-rays. The energy of the characteristic X-rays is about 20 times lower than that of gamma-rays and then it can be easily shielded by a thin stainless steel plate. As a result, the thickness and the weight of the CXRC container can be considerably reduced in comparison with that of a GC as illustrated in Fig.2b [1].

We have developed a proto-type CXRC (Fig.3) that is based on the pinhole camera technique [2,3]. As a 2D X-ray sensor, an ar-

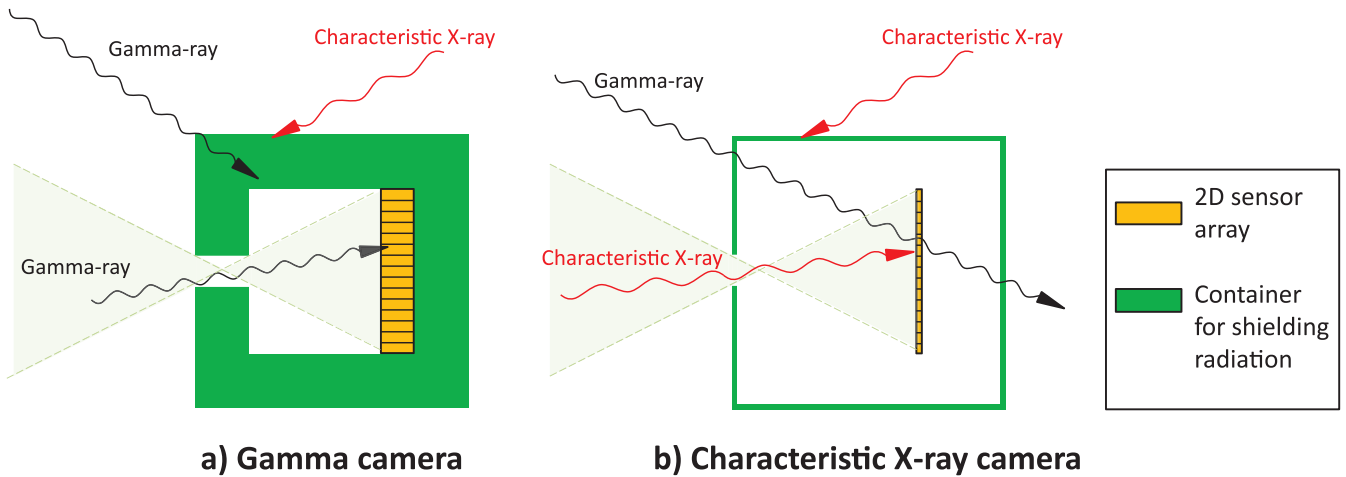


Fig.2 Schematic drawings of a gamma camera and a characteristic X-ray camera, both based on a pinhole technique. a) Gamma camera - The 2D sensor array is surrounded by a container for shielding radiation. The thickness of the container wall is typically more than 10 mm. b) Characteristic X-ray camera - The thicknesses of the 2D sensor and the container wall can be reduced in comparison with those of gamma cameras. Most of the gamma-rays penetrate the characteristic X-ray camera body.



Fig.3 The prototype characteristic X-ray camera

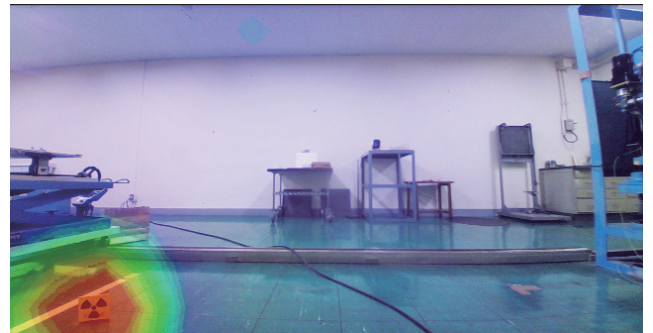


Fig.4 The standard source of Cs-137 is visualized by the characteristic X-ray camera. The source was put on the floor of a laboratory (left bottom in this photo). The X-ray image (color contour) is superimposed on the visible image. The color contour indicates probability of presence of Cs-137.

ray of modules each of which consists of a CsI(Tl) scintillator coupled to a photomultiplier is employed. The 2D X-ray sensor array is fixed in a container made of thin metal. The weight of the prototype CXRC is 6.6 kg and the size is 225 × 175 × 242 mm. The X-ray image measured by the CXRC can be superimposed on a visible image taken by a small camera installed on the front side of the CXRC.

To test the sensitivity of the CXRC, a standard source of Cs-137 with a radioactivity of 1 MBq was set on the floor of a laboratory at a distance of 1.3 m from the CXRC and it was visualized. As a reference for background level, we measured ambient dose equivalent rate with a survey meter and the dose rates with and without setting the Cs-137 source were 0.12 and 0.07 μSv/h at the CXRC position, respectively. In other words, this test was made under the condition that the signal from the Cs-137 was almost comparable to the background. An image obtained by the CXRC is shown in Fig.4 when the CXRC was exposed for 5 s. We succeeded in visualizing the source within a very short time. The camera has sufficient sensitivity to find radioactive sources in a laboratory.

In order to apply this CXRC technique to the actual decontamination and nuclear reactor decommission tasks in the region around the FDNPS, we have continued to improve the performance of the CXRC. Another result of the measurement by the prototype CXRC when it was used to visualize a real contamination spot due to the FDNPS accident can be found in [3].

In addition, we have tried to reduce the weight of the CXRC prototype further. The weight of the prototype CXRC is currently determined by that of the container that includes the bulky photomultipliers. If the volume of the 2D sensor array is reduced, the weight of the CXRC will be considerably decreased and will be 1 to 2 kg. We expect that the 2D X-ray sensor array of CsI(Tl)s and photomultipliers can be replaced by semiconductors. We have finished fabricating an CXRC prototype that employs a semiconductor sensor array. Results obtained with this prototype will be presented in the near future.

References

- [1] Kobayashi S, Uchihori Y, Shirakawa Y: Radioactive substance detection device, radiation source location visibility system, and radioactive substance detection method, Japan Patent 5400988, 2014 (in Japanese).
- [2] National Institute of Radiological Sciences: Success in developing the characteristic X-ray camera to visualize radioactive cesium, NIRS press release, Jan 23, 2014 (in Japanese).
- [3] Kobayashi S, Shinomiya T, Yoshida T, *et al.*: Development of a characteristic X-ray camera to identify contamination by radioactive cesium, Radiation Detectors and Their Uses, KEK Proceedings 2014, in press.

Designation as WHO Collaborating Centre

**Hideo Tatsuzaki, Hiroko Ino, Yumiko Suto,
Yoshiya Shimada, Keiich Akahane,
Reiko Kanda, Takeshi Murakami, Etsuko Ito,
Makoto Akashi**

E-mail: tatsuza@nirs.go.jp

NIRS was designated as a World Health Organization Collaborating Centre (hereafter referred to as "WHO-CC") on 2 September 2013. WHO-CC is a network consisting of highly regarded academic and scientific institutions worldwide designated by the WHO Director General that works together with WHO in order to implement its various programmes such as on nursing, occupational health, communicable diseases, nutrition, mental health, chronic diseases and health technologies utilizing its accumulated collective expertise. As of 2014, over 700 institutions in over 80 WHO Member States have been registered as WHO-CCs.

In accordance with the designation, NIRS cooperates with the WHO as its CC in the areas of: (1) strengthening preparedness for radiation emergencies and Radiation Emergency Medical Preparedness and Assistance Network (REMPAN) activities; (2) providing medical and technical assistance to WHO in response to and recovery after radiation emergencies; (3) carrying out biodosimetry and BioDoseNet (cytogenetics and internal contamination monitoring); (4) studying radiation protection for indoor radon; and (5) studying radioprotection in the field of medical exposure to ionizing radiation, with the focus on risks assessment and risk management.

The designation makes it possible for NIRS to further enhance contributions to national and international societies by leveraging its own large workforce, and its abundant research activities and accumulated experiences since its inception in 1957.

Radiation safety and radiation emergency medical preparedness are among the major research fields of NIRS. As the tertiary, the last bastion of, radiation emergency medical hospital in Japan, provision of medical treatment and response during accidents involving radioactive substances is also its important role. NIRS accepted three patients with high dose exposure from the JCO criticality accident in 1999. For the Tokyo Electric Power Company (TEPCO) Fukushima Daiichi Nuclear Power Station accident, NIRS immediately dispatched experts to Fukushima on the early morning of 12 March 2011, and since then has taken initiatives in providing mitigation actions and supporting residents and workers in and around Fukushima Prefecture. In addition to emergency response, international workshops and training courses have been conducted by NIRS so as to foster medical profession-



als and experts mainly in Asia who lead regional radiation emergency medicine (REM) and radiation biodosimetry programs and research. NIRS organized some of those events in cooperation with WHO and other international organizations (Fig.1). As of March 2014, more than 440 professionals from all over the world have been trained in both fields at the institute.

Describing the track record of cooperation between NIRS and WHO that led to the WHO-CC designation, NIRS had participated in WHO-REMPAN as a liaison institute since 2004. WHO-REMPAN, composed of WHO-CCs plus Liaison Institutes around the globe, provides emergency medical and public health assistance to people over-exposed to radiation and facilitates research and development of medical countermeasures against radiation/nuclear emergencies. Long-term care and follow-up of victims of radiation incidents are included in its key purpose, as well. On the basis of a request from WHO, experts on REM and biodosimetry continuously participated in the Organization's task groups and consultancy meetings for the purpose of sharing and exchanging related information as well as for contributing to WHO publications during the last decade (Fig.1). Regarding the five different cooperative areas for WHO-CC mentioned above, the former three fields are related to REM. The Radiation Emergency Medical Assistance Team called REMAT[®] (REMAT) has become a focal point of NIRS in those three domains; it was set up in January 2010 as one concrete measure for NIRS to make an international contribution in REM. In March 2013, the Institute upgraded the team to a department with 11 dedicated staff members including medical doctors, a nurse, a radiation expert and administrators. The newly formed REMAT is engaged not only in emergency medical assistance activities at radiation/nuclear emergencies in Japan and all over the world, but also in promoting establishment of the domestic medical preparedness for radiation emergencies on a regular

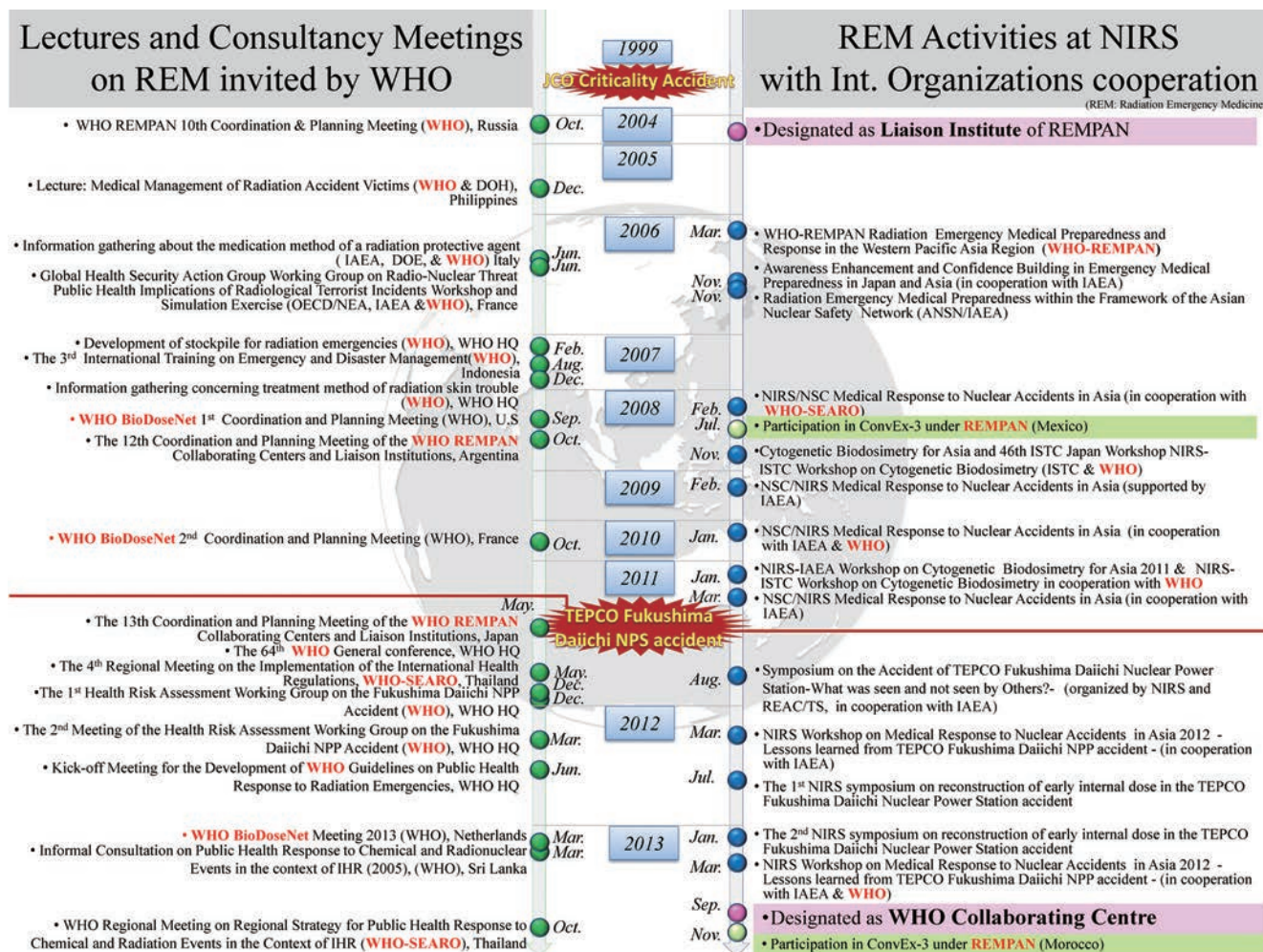
basis (i.e., conducting capacity building assistance for national and international medical professionals and first responders who are involved in the emergencies, operating a 24/7 hotline on REM for medical personnel and emergency responders, cooperating with the central and local governments in order to establish a practical domestic system of REM, operating three network councils of REM, physical dosimetry, and cytogenetic dosimetry that offer an advisory and supporting framework complementary to the NIRS's function). Furthermore, over 65 workers including medical doctors, nurses, experts on in-vivo and in-vitro dose assessment, radiation protection experts and administrators throughout the Institute are appointed as cooperative staff for REMAT. Should there be a request for REM assistance from WHO, REMAT is operated in the emergency response mode with both its original and cooperative staff members working together for WHO.

The study area of radiation protection for indoor radon is the other field included in the WHO-CC activities. Inhalation of radon gas (Rn-222 and Rn-220) and related radionuclides in the home and workplace is one of the main ionizing radiation risks causing deaths from lung cancer globally. In order to reduce this burden it is important that national authorities have methods and tools based on solid scientific evidence and sound public health policy. The NIRS is preparing to translate the *WHO Handbook on Indoor Radon* into Japanese; the handbook focuses on residential radon

exposure from a public health viewpoint and provides detailed recommendations on reducing health risks from radon and sound policy options for preventing and mitigating radon exposure.

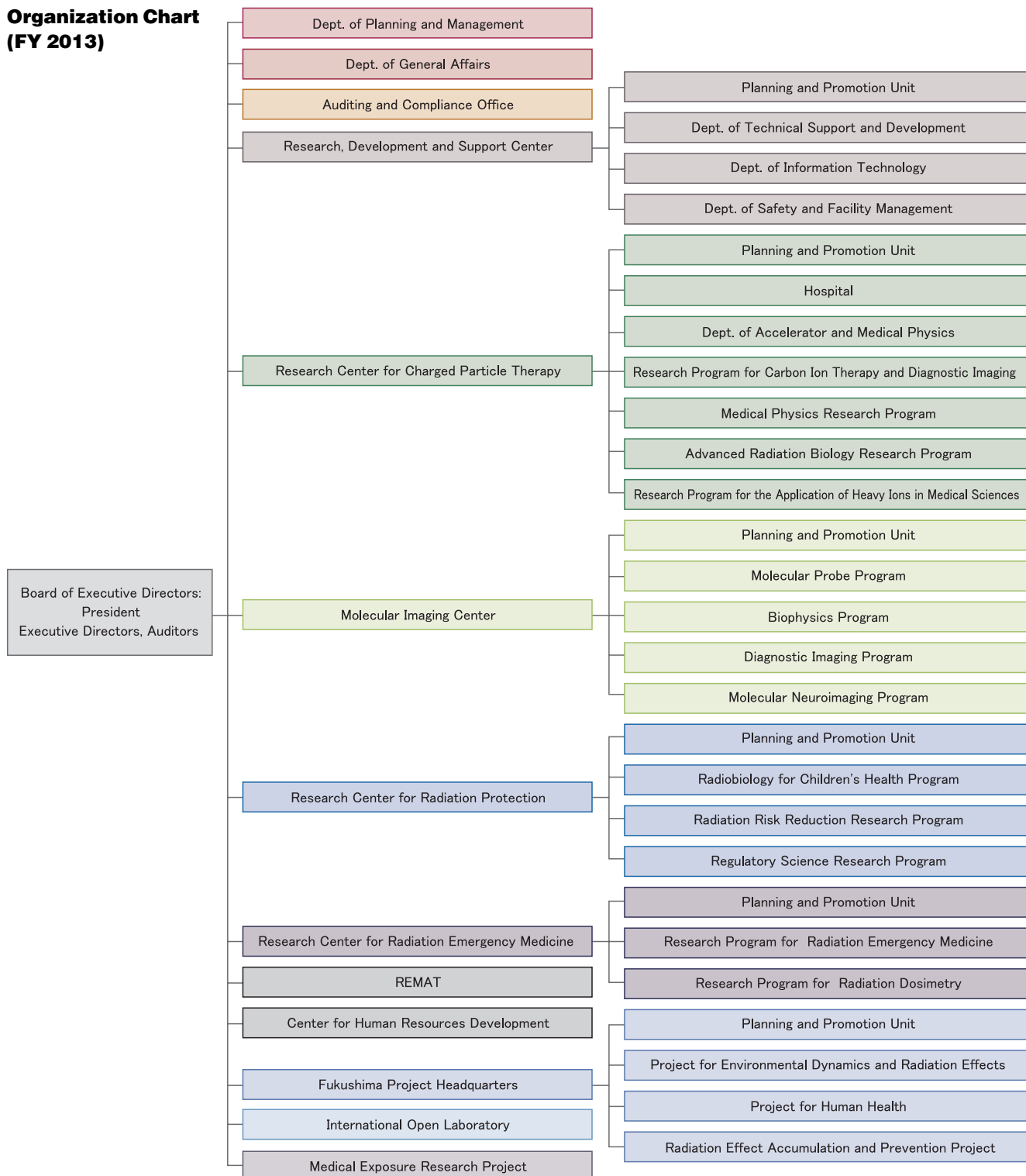
The area of radiation protection in the field of medical exposure to ionizing radiation with the focus on the risk assessment and risk management is the fifth field in the WHO-CC activities. NIRS organizes the Japanese Network for Research and Information on Medical Exposure (J-RIME), and has held meeting with experts, where a Japanese diagnostic reference level (DRL) for diagnostic modalities was discussed. NIRS also supervised translation of a booklet from the Royal College of Radiologists (RCR), *iRefer, making the best use of clinical radiology* into Japanese in order to raise awareness about medical exposure among Japanese radiologists. NIRS sent an expert to three meetings successively held in Geneva in September 2013, namely the "Radiation Risk Communication in Pediatric Imaging International Expert Meeting", the "Global Initiative on Radiation Safety in Healthcare Settings, Focused expert meeting for project scoping - Medical imaging of asymptomatic people for individual health assessment -", and the "Global Initiative on Radiation Safety in Health Care Settings, International Consultation".

NIRS will continue to fulfill its functions in the above mentioned fields in cooperation with WHO.



Organization Chart

Organization Chart (FY 2013)



Board Members

Title		Name	Tenure	Mission
President		Yoshiharu YONEKURA	April 1, 2011- March 31, 2016	Represents the Institute and is responsible for managing its operations
Executive Director		Makoto AKASHI	April 1, 2013- March 31, 2015	Assists the President in managing the operations of the Institute in accordance with the directions of the President
Executive Director		Shinichi KUROKI	April 1, 2013- March 31, 2015	Assists the President in managing the operations of the Institute in accordance with the directions of the President
Auditor		Akira NOIE	April 1, 2013- March 31, 2015	Audits the operations of the Institute
Auditor (part-time)		Masatoshi ARISAWA	April 1, 2013- March 31, 2015	Audits the operations of the Institute

International Collaboration

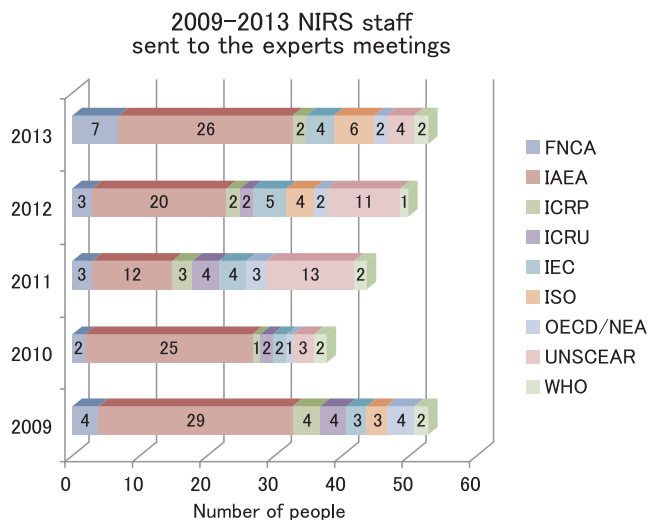
Working with international organizations

NIRS has been closely working with international organizations such as UNSCEAR, IAEA, and WHO in the field of radiological sciences, with the aims of contributing to advances in human health and creating a society that enjoys better radiation safety and peace of mind.



The meetings attended by NIRS experts from April 2013 to March 2014 included:

- 60th UNSCEAR Meeting
- Meeting of the IAEA Fukushima Comprehensive Report Working Group 4
- IAEA International Experts' Meeting on Radiation Protection after the Fukushima Daiichi Accident: Promoting Confidence and Understanding
- IAEA Research Coordination Meeting on the Production and Utilization of Emerging Positron Emitters for Medical Application with an Emphasis on ^{64}Cu and ^{124}I
- The Joint Meetings of the ICRP Main Commission and Committees and the 2nd ICRP International Symposium on the System of Radiological Protection
- WHO Regional Meeting on Regional Strategy for Public Health Response to Chemical and Radiation Events in the Context of IHR.

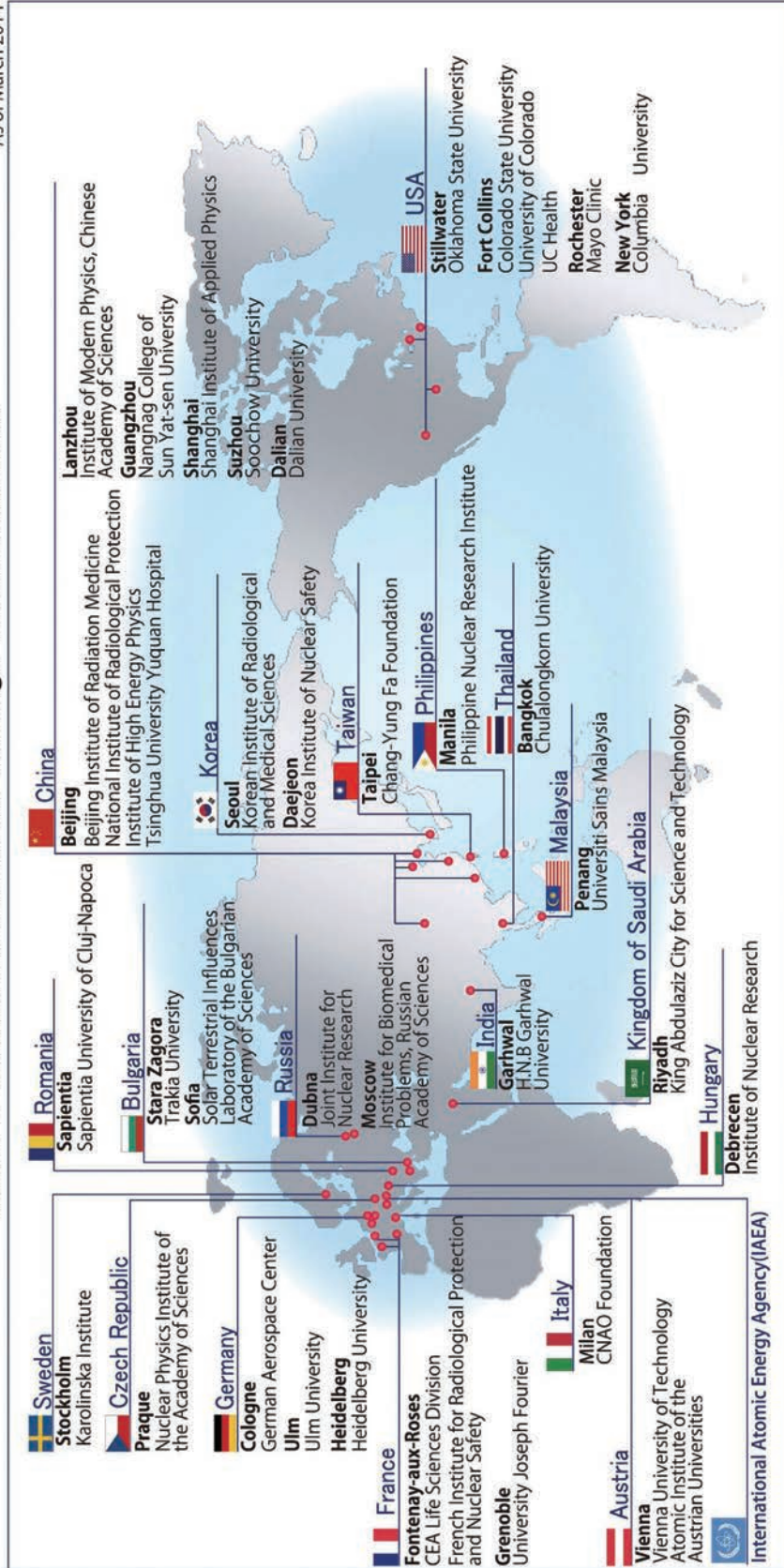


Collaborating Centres

- In September 2013, NIRS was designated as a WHO Collaborating Centre, and launched its 4-year long activities in five radiation-related areas: radiation emergency medicine and preparedness, biodosimetry, medical radiation exposure, and exposure to indoor radon.
- In January 2014, NIRS was designated again as an IAEA Collaborating Centre in radiobiology, charged particle therapy and molecular imaging for an additional 4 years.

NIRS's Overseas Partners through Memorandums

As of March 2014



International Collaboration

Year in Review – international meetings, training courses, etc.

※ The events shown in blue took place outside Japan.

NIRS-Mayo-Fermi Lab. Joint Symposium 2013 on Carbon Ion Radiotherapy: Fostering International Collaboration between Japan and the United States (Rochester, MN, USA)



The Cancer Symposium: Advanced Radiation Oncology Treatment Strategies with Photon, Proton, and Carbon Ion Radiation (Denver, CO, USA)

2013

Apr. May Jun. Jul. Aug. Sep.

2nd SNU-NIRS Workshop on Nuclear Medicine Imaging Science and Technology (Seoul, Korea)

NIRS-KIRAMS Training Course on Radiation Emergency Medicine

Heavy Ion in Therapy and Space Radiation Symposium (HITSRS 2013)

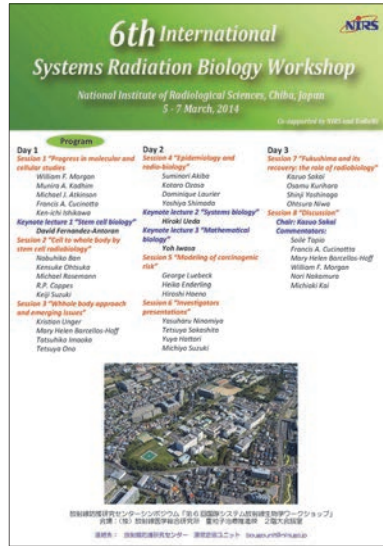
15th International Conference on Ion Sources (ICIS2013)



IAEA-ANSN Regional Workshop on Medical Response to Radiation Emergency Handling Complex Situations



IAEA Interregional Training Course for Medical Response to Radiation Emergencies



6th International Systems Radiation Biology Workshop

IAEA Collaborating Centre Commemorative Symposium "NIRS Cooperation with IAEA on Global Health Issues in the Radiology Field"

2014

Oct. Nov. Dec. Jan. Feb. Mar.

International Training Course on Carbon-ion Radiotherapy (ITCCIR2013)

Joint NIRS-BINP-FEFU Workshop on Heavy Ion Therapy (Vladivostok, Russia)

NIRS IOL Second Term Final Report Meeting

NIRS Workshop on PET Imaging Physics and Applications (PIPA2013)

NIRS-MedAustron Joint Symposium on Carbon Ion Radiotherapy & NIRS Peer Review Meeting (Wiener Neustadt, Austria)

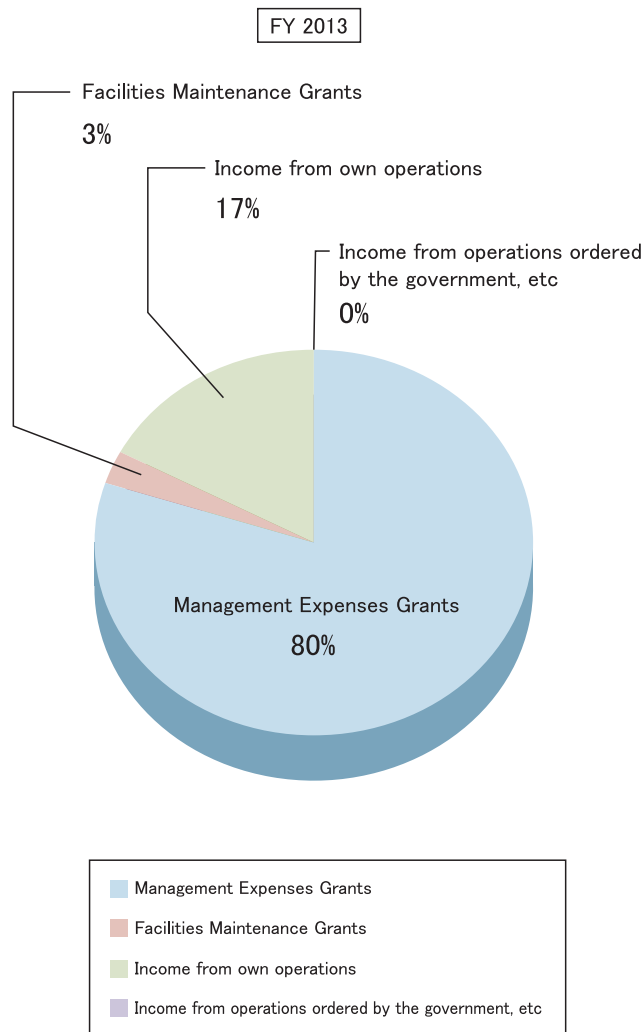


NIRS-Mafraq Hospital Joint Symposium: Carbon Ion Radiotherapy for Cancer Treatment (Abu Dhabi, UAE)



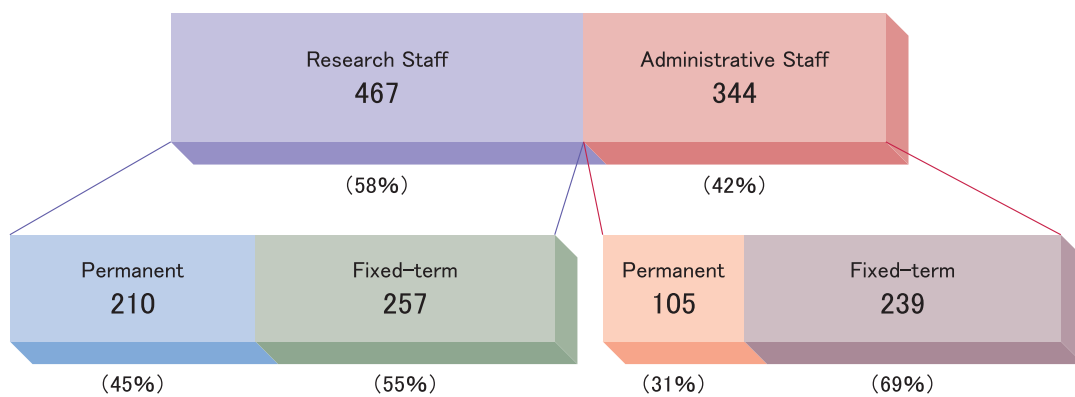
International Collaboration

Budget



Personnel

Research Staff	467
Permanent	210
Fixed-term	257
Administrative Staff	344
Permanent	105
Fixed-term	239
Total	811



(as of April 1, 2013)

Appendix

List of Original Papers

This list includes the main publications by staff members that were registered with the NIRS Institutional Repository during the period from April 1, 2013 to March 31, 2014.

■ Research on Cancer Therapy with Carbon Beams

1. Phase I/II trial of definitive carbon ion radiotherapy for prostate cancer: evaluation of shortening of treatment period to 3 weeks. T Nomiya, H Tsuji, K Maruyama, S Toyama, H Suzuki, K Akakura, J Shimazaki, K Nemoto, T Kamada, H Tsujii, *British Journal of Cancer*, 110, 2389 - 2395, 2014.
2. Effect of in vivo administration of reprogramming factors in the mouse liver. Akira Tomokuni, Hidetoshi Eguchi, Hiromitsu Hoshino, Dyah Laksmi Dewi, Shinpei Nishikawa, Yoshihiro Kano, Norikatsu Miyoshi, Arinobu Tojo, Seiichiro Kobayashi, Noriko Gotoh, Kunihiro Hinohara, Noemi Fusaki, Toshiyuki Saito, Hiroshi Suemizu, Hiroshi Wada, Shogo Kobayashi, Shigeru Marubashi, Masahiro Tanemura, Yuichiro Doki, Masaki Mori, Hideshi Ishii, *Oncology Letters*, 6(2), 323 - 328, 2013.
3. Preliminary Results from a Multi-center Prospective Study (JROSG 05-5) on Postoperative Radiotherapy for Patients with High-risk Ductal Carcinoma in situ with Involved Margins or Margin Widths 1 mm or less than. Naoto Shikama, Kenji Sekiguchi, Naoki Nakamura, Hiroshi Sekine, Yuko Nakayama, Kazufumi Imanaka, Takeshi Akiba, Masahiko Aoki, Yoshiomi Hatayama, Etsuko Ogo, Yoshikazu Kagami, Miho Kawashima, Kumiko Karasawa, *American Journal of Breast Cancer Research*, 1(1), 1 - 8, 2014.
4. Clinical trial of carbon ion radiotherapy for gynecological melanoma. Kumiko Karasawa, Masaru Wakatsuki, Shingo Kato, Hiroki Kiyohara, Tadashi Kamada, The Working Group for Gynecological Tumors *Journal of Radiation Research*, 55 (2), 343 - 350, 2014.
5. Modeling the biological response of normal human cells, including repair processes, to fractionated carbon beam irradiation. Mami Wada, Masao Suzuki, Cuihua Liu, Yumiko Kaneko, Shigekazu Fukuda, Koichi Ando, Naruhiro Matsufuji, *Journal of Radiation Research*, 54(5), 798 - 807, 2013.
6. The dosimetric impact of respiratory breast movement and daily setup error on tangential whole breast irradiation using conventional wedge, field-in-field and irregular surface compensator techniques. Tomohisa Furuya, Satoru Sugimoto, Chie Kurokawa, Shuichi Ozawa, Kumiko Karasawa, Keisuke Sasai, *Journal of Radiation Research*, 54(1), 157 - 165, 2013.
7. Preparation of Phi29 DNA Polymerase Free of Amplifiable DNA Using Ethidium Monoazide, an Ultraviolet-Free Light-Emitting Diode Lamp and Trehalose. Hirokazu Takahashi, Hiroyuki Yamazaki, Satoshi Akanuma, Hiroko Kanahara, Toshiyuki Saito, Tomoyuki Chimuro, Takayoshi Kobayashi, Toshio Ohtani, Kimiko Yamamoto, Shigeru Sugiyama, *PLOS ONE*, 9 (2), e82624, 2014.
8. Discussions on target theory: past and present. Takuma Nomiya, *Journal of Radiation Research*, 54(6), 1161 - 1163, 2013.
9. Accuracy of methionine-PET in predicting the efficacy of heavy-particle therapy on primary adenoid cystic carcinomas of the head and neck. Sachiko Toubaru, Kyosan Yoshikawa, Seiya Ohashi, Katsuyuki Tanimoto, Azusa Hasegawa, Koji Kawaguchi, Tsuneo Saga, Tadashi Kamada, *Radiation Oncology (London, England)*, 8(1), 143, 2013.
10. Carbon-ion radiotherapy for marginal lymph node recurrences of cervical cancer after definitive radiotherapy: a case report. Tomoaki Tamaki, Tatsuya Ohno, Hiroki Kiyohara, Shin-Ei Noda, Yu Ohkubo, Ken Ando, Masaru Wakatsuki, Shingo Kato, Tadashi Kamada, Takashi Nakano, *Radiation Oncology (London, England)*, 8(1), 79, 2013.
11. Interfractional change of high-risk CTV D90 during image-guided brachytherapy for uterine cervical cancer. Yu Ohkubo, Tatsuya Ohno, Shin-ei Noda, Nobuteru Kubo, Akiko Nakagawa, Masahiro Kawahara, Takanori Abe, Hiroki Kiyohara, Masaru Wakatsuki, Takashi Nakano, *Journal of Radiation Research*, 54(6), 1138 - 1145, 2013.
12. A Review of Update Clinical Results of Carbon Ion Radiotherapy for Uterine Cervical Cancer. Masaru Wakatsuki, Shingo Kato, Kumiko Karasawa, Hirohiko Tsujii, Tadashi Kamada, *iConcept Press*, 1, 2014.
13. Osteoma of the Internal Auditory Canal Mimicking Vestibular Schwannoma: Case Report and Review of 17 Recent Cases. Jun Suzuki, Yusuke Takata, Hiromitsu Miyazaki, Izumi Yahata, Yasuhiko Tachibana, Toshimitsu Kobayashi, Tetsuaki Kawase, Yukio Katori, *Tohoku Journal of Experimental Medicine*, 232 (1), 63 - 68, 2014.
14. Risk factors for brain injury after carbon ion radiotherapy for skull base tumors. Masashi Koto, Azusa Hasegawa, Ryo Takagi, Akira Fujikawa, Takamichi Morikawa, Riwa Kishimoto, Keiichi Jingu, Hirohiko Tsujii, Tadashi Kamada, *Radiotherapy and Oncology: Journal of the European Society for Therapeutic Radiology and Oncology*, 111(1), 25 - 29, 2013.
15. Usefulness of 18F-fluorodeoxyglucose Positron Emission Tomography as Predictor of Distant Metastasis in Preoperative Carbon-ion Radiotherapy for Pancreatic Cancer. Makoto Shinoto, Shigeru Yamada, Kyosan Yoshikawa, Shigeo Yasuda, Yoshiyuki Shioyama, Hiroshi Honda, Tadashi Kamada, Hirohiko Tsujii, *Anticancer Research*, 33(12), 5579 - 5584, 2013.
16. Dose-escalation study of carbon ion radiotherapy for locally advanced squamous cell carcinoma of the uterine cervix (9902). Masaru Wakatsuki, Shingo Kato, Tatsuya Ohno, Kumiko Karasawa, Ken Ando, Hiroki Kiyohara, Hirohiko Tsujii, Takashi Nakano, Tadashi Kamada, Makio Shozu, *Gynecologic Oncology*, 132(1), 87 - 92, 2014.

17. Health-related quality of life after carbon-ion radiotherapy for prostate cancer: A 3-year prospective study. Hiroyuki Katoh, Hiroshi Tsuji, Hitoshi Ishikawa, Tadashi Kamada, Masaru Wakatuki, Naoki Hirasawa, Hiroyoshi Suzuki, Koichiro Akakura, Takashi Nakano, Jun Shimazaki, Hirohiko Tsujii, *International Journal of Urology*, 21(4), 370 - 375, 2014.
18. Long-term results of carbon ion radiation therapy for locally advanced or unfavorably located choroidal melanoma: usefulness of CT-based 2-port orthogonal therapy for reducing the incidence of neovascular glaucoma. Shingo Toyama, Hiroshi Tsuji, Nobutaka Mizoguchi, Takuma Nomiya, Tadashi Kamada, Sunao Tokumaru, Atsushi Mizota, Yoshitaka Ohnishi, Hirohiko Tsujii, *International Journal of Radiation Oncology, Biology, Physics*, 86(2), 270-6, 2013.
19. Transient ischemic attack-like episodes without stroke-like lesions in MELAS. Tadahiro Mitani, Noriko Aida, Moyoko Tomiyasu, Takahito Wada, Hitoshi Osaka, *Pediatric Radiology*, 43 (10), 1400 - 1403, 2013.
20. Neonatal Brain Metabolite Concentrations: An In Vivo Magnetic Resonance Spectroscopy Study with a Clinical MR System at 3 Tesla. Moyoko Tomiyasu, Noriko Aida, Mamiko Endo, Jun Shibasaki, Kumiko Nozawa, Eiji Shimizu, Hiroshi Tsuji, Takayuki Obata, *PLOS ONE*, 8(11), e82746, 2013.
21. Magnetic displacement force and torque on dental keepers in the static magnetic field of an MR scanner. Mika Omatsu, Takayuki Obata, Kazuyuki Minowa, Koichi Yokosawa, Eri Inagaki, Kinya Ishizaka, Koichi Shibayama, Toru Yamamoto, *Journal of Magnetic Resonance Imaging*, 2013.
22. Effects of chewing on cognitive processing speed. Yoshiyuki Hirano, Takayuki Obata, Hidehiko Takahashi, Atsumichi Tachibana, Daigo Kuroiwa, Toru Takahashi, Hiroo Ikehira, Minoru Onozuka, *Brain and Cognition*, 81(3), 376 - 381, 2013.
23. The role of chemoradiotherapy in patients with unresectable T4 breast tumors. Kumiko Karasawa, Mitsue Saito, Hisako Hirowatari, Hiromi Izawa, Tomohiko Furuya, Shuichi Ozawa, Kana Ito, Takahisa Suzuki, Norio Mitsuhashi, *Breast Cancer*, 20(3), 254 - 61, 2013.
24. Impact of carbon ion radiotherapy for primary spinal sarcoma. Keiji Matsumoto, Reiko Imai, Tadashi Kamada, Tatsuya Maruyama, Hiroshi Tsuji, Hirohiko Tsujii, Yoshiyuki Shioyama, Honda Hiroshi, Kazuo Isu, *Cancer*, 119(19), 3496 - 3503, 2013.
25. Total spondylectomy following carbon ion radiotherapy to treat chordoma of the mobile spine. Tomohiro Matsumoto, Shirou Imagama, Zenya Ito, Reiko Imai, Tadashi Kamada, Naoki Ishiguro, et al., *Bone and Joint Journal*, 95-B(10), 1392 - 1395, 2013.
26. Management of high-risk prostate cancer: Radiation therapy and hormonal therapy. Takuma Nomiya, Hiroshi Tsuji, Shingo Toyama, Katsuya Maruyama, Kenji Nemoto, Hirohiko Tsujii, Tadashi Kamada, *Cancer Treatment Reviews*, 39(8), 872 - 878, 2013.
27. Position statement on ethics, equivoise and research on charged Particle radiation therapy. Mark Sheehan, Claire Timlin, Ken Peach, Tadashi Kamada, Hirohiko Tsujii, et al., *Journal of Medical Ethics*, 2013, 1 - 4, 2013.
28. Japanese structure survey of radiation oncology in 2009 with special reference to designated cancer care hospitals. Hodaka Numasaki, Masamichi Nishio, Hiroshi Ikeda, Kenji Sekiguchi, Norihiko Kamikonya, Masahiko Koizumi, Masao Tago, Yutaka Ando, et al., *International Journal of Clinical Oncology*, 18(5), 775 - 783, 2012.
29. National medical care system may impede fostering of true specialization of radiation oncologists: study based on structure survey in Japan. Hodaka Numasaki, Hitoshi Shibuya, Masamichi Nishio, Hiroshi Ikeda, Kenji Sekiguchi, Norihiko Kamikonya, Masahiko Koizumi, Masao Tago, Yutaka Ando, et al., *International Journal of Radiation Oncology Biology Physics*, 82(1), e111 - e117, 2011.
30. Japanese structure survey of radiation oncology in 2009 based on institutional stratification of the patterns of care study. Teruki Teshima, Hodaka Numasaki, Masamichi Nishio, Hiroshi Ikeda, Kenji Sekiguchi, Norihiko Kamikonya, Masahiko Koizumi, Masao Tago, Yutaka Ando, et al., *Journal of Radiation Research*, 53(5), 710 - 721, 2012.
31. Analysis of Multiple B-Value Diffusion-Weighted Imaging in Pediatric Acute Encephalopathy. Yasuhiko Tachibana, Noriko Aida, Tetsu Niwa, Kumiko Nozawa, Kouki Kusagiri, Kana Mori, Kazuo Endou, Takayuki Obata, Tomio Inoue, *PLOS ONE* (Online only:URL:http://www.plosone.org), 8(6), e63869, 2013.
32. Impact of boost irradiation on pelvic lymph node control in patients with cervical cancer. Masaru Wakatuki, Tatsuya Ohno, Shingo Kato, Ken Ando, Shinei Noda, Hiroki Kiyohara, Kei Shibuya, Kumiko Karasawa, Tadashi Kamada, Takashi Nakano, *Journal of Radiation Research*, 55(1), 139 - 145, 2013.
33. A simple algorithm for beam profile diagnostics using a thermographic camera. Ken Katagiri, Satoru Hojo, Toshihiro Honma, Kazutoshi Suzuki, Akira Noda, Koji Noda, *Review of Scientific Instruments*, 85, 033306, 2014.
34. Development of Fast Scanning Magnets and Their Power Supply for Particle Therapy. Takuji Furukawa, Toshiyuki Shirai, Taku Inaniwa, Shinji Sato, Eri Takeshita, Kota Mizushima, Yosuke Hara, Kouji Noda, et al., *IEEE Transactions on Applied Superconductivity*, 24(3), 1 - 4, 2014.
35. Patient-specific QA and delivery verification of scanned ion beam at NIRS-HIMAC. Takuji Furukawa, Taku Inaniwa, Yousuke Hara, Kota Mizushima, Toshiyuki Shirai, Kouji Noda, *Medical Physics*, 40(12), 121707-1 - 121707-7, 2013.
36. A serial 4DCT study to quantify range variations in charged particle radiotherapy of thoracic cancers. Shinichiro Mori, Lei Dong, George Starkschall, Radhe Mohan, George T.Y. Chen, *Journal of Radiation Research*, 55(2), 309 - 319, 2013.
37. A microdosimetric-kinetic model for cell killing by protracted continuous irradiation including dependence on LET I: Repair in cultured mammalian cells. Roland B Hawkins, Taku Inaniwa, *Radiation Research*, 180(6), 584 - 594, 2013.
38. Microdosimetric study on influence of low energy photons on relative biological effectiveness under therapeutic conditions using 6 MV linac. Hiroyuki Okamoto, Toshiyuki Kohno, Tatsuki Kanai, Yuuki Kase, Yoshitaka Matsumoto, Jun Itami, Yoshiya Furusawa, Yukio Fujita, et al., *Medical Physics*, 38(8), 4714 - 4722, 2011.
39. Numerical analysis of the space charge effect in a MWPC. Ken Katagiri, Takuji Furukawa, Eri Takeshita, Kouji Noda, *J. Plasma Fusion Res. Series*, 9, 614 - 619, 2010.
40. Development of a superconducting rotating-gantry for heavy-ion therapy. Yoshiyuki Iwata, Kouji Noda, Takeshi Murakami, Toshiyuki Shirai, Takuji Furukawa, Takashi Fujita, Shinichiro

- Mori, Kota Mizushima, Kouichi Shoda, et al., *Nuclear Instruments and Methods in Physics Research Section B*, 317(Part B), 793 - 797, 2013.
41. ¹¹C-CH₄-molecule production using a NaBH₄ target for ¹¹C-ion acceleration. Ken Katagiri, Koutarou Nagatsu, Katsuyuki Minegishi, Satoru Houjou, Masayuki Muramatsu, Kazutoshi Suzuki, Toshihiro Honma, Atsushi Kitagawa, Akira Noda, Kouji Noda, *Review of Scientific Instruments*, 85, 02C305-1 - 02C305-3, 2014.
 42. Development of curved combined-function superconducting-magnets for a heavy-ion rotating-gantry. Yoshiyuki Iwata, Shinji Suzuki, Kouji Noda, Toshiyuki Shirai, Takeshi Murakami, Takuji Furukawa, Takashi Fujita, Yousuke Hara, Kota Mizushima, Shinji Satou, Shinichiro Mori, Kouichi Shoda, et al., *IEEE Transactions on Applied Superconductivity*, 24(3), 2013.
 43. Measurement of Neutron Ambient Dose Equivalent in Carbon-Ion Radiotherapy with an Active Scanned Delivery System. Shunsuke Yonai, Takuji Furukawa, Taku Inaniwa, *Radiation Protection Dosimetry*, 1 - 4, 2013.
 44. Multiconductor Transmission-Line Theory with Electromagnetic Radiation. Hiroshi Toki, Kenji Satou, *Journal of the Physical Society of Japan*, 81, 014201, 2012.
 45. Plasma spectroscopy of metal ions for hyper-electron cyclotron resonance ion source. Hideshi Muto, Yukimitsu Ohshiro, Shoichi Yamaka, Shin-ichi Watanabe, Michihiro Oyaizu, Shigeru Kubono, Hidetoshi Yamaguchi, Masayuki Kase, Toshiyuki Hattori, Susumu Shimoura, *Review of Scientific Instruments*, 85, 02A905, 2013.
 46. Adaptive radiotherapy based on the daily regression of a tumor in carbon-ion beam irradiation. Ai Nagano, Shinichi Minohara, Shingo Kato, Hiroki Kiyohara, Ken Ando, *Physics in Medicine and Biology*, 57, 8343, 2012.
 47. Simulated studies on the biological effects of space radiation-Simulated studies on the biological effects of space on quiescent human fibroblasts. Nan Ding, Hailong Pei, Jinpeng He, Yoshiya Furusawa, Ryoichi Hirayama, Cuihua Liu, Yoshitaka Matsumoto, He Li, Wentao Hu, Yinghui Li, Jufang Wang, Tieshan Wang, Guangming Zhou, *Advances in Space Research*, 52, 1314 - 1319, 2013.
 48. Effects of shielding on the induction of 53BP1 foci and micronuclei after Fe ion exposures. Wentao Hu, Hailong Pei, He Li, Nan Ding, Jufang Wang, Jinpeng He, Yoshiya Furusawa, Ryoichi Hirayama, Yoshitaka Matsumoto, Cuihua Liu, Yinghui Li, Tetsuya Kawata, Guangming Zhou, *Journal of Radiation Research*, 55(1), 10 - 16, 2013.
 49. Performance of a fluorescent screen with a CCD system for quality assurance in a heavy-ion beam scanning irradiation system. Yousuke Hara, Takuji Furukawa, Eri Takeshita, Kota Mizushima, Shinji Satou, Toshiyuki Shirai, Kouji Noda, *Journal of the Korean Physical Society*, 63(7), 1446 - 1450, 2013.
 50. Misrepair of DNA double-strand breaks after exposure to heavy-ion beams causes a peak in the LET-RBE relationship with respect to cell killing in DT40 cells. Mizuho Aoki-Nakano, Yoshiya Furusawa, *Journal of Radiation Research*, 54(6), 1029 - 1035, 2013.
 51. Microdosimetric calculation of relative biological effectiveness for design of therapeutic proton beams. Yuki Kase, Wataru Yamashita, Naruhiro Matsufuji, Kenta Takada, Takeji Sakae, Yoshiya Furusawa, Haruo Yamashita, Shigeyuki Murayama, *Journal of Radiation Research*, 54(3), 485 - 493, 2013.
 52. Beam Spot Imaging System Using a Fluorescent Screen for Carbon-ion Radiotherapy. Kota Mizushima, Eri Takeshita, Takuji Furukawa, Yousuke Hara, Toshiyuki Shirai, Ken Katagiri, Kouji Noda, *Journal of the Korean Physical Society*, 63(7), 1437 - 1440, 2013.
 53. OH Radicals from the Indirect Actions of X-Rays Induce Cell Lethality and Mediate the Majority of the Oxygen Enhancement Effect. Ryoichi Hirayama, Atsushi Ito, Miho Noguchi, Yoshitaka Matsumoto, Akiko Uzawa, Gen Kobashi, Ryuichi Okayasu, Yoshiya Furusawa, *Radiation Research*, 180(5), 514 - 523, 2013.
 54. Response of a Plate-type Thermoluminescence Dosimeter to a Therapeutic Carbon Beam. Yusuke Koba, Shigekazu Fukuda, Kiyomitsu Shinsho, Genichiro Wakabayashi, Satoshi Tamatsu, *Journal of the Korean Physical Society*, 63(7), 1432 - 1436, 2013.
 55. Modeling the biological response of normal human cells, including repair processes, to fractionated carbon beam irradiation. Mami Wada, Masao Suzuki, Cui Hua Liu, Yumiko Kaneko, Shigekazu Fukuda, Koichi Ando, Naruhiro Matsufuji, *Journal of Radiation Research*, 54(5), 798 - 807, 2013.
 56. Evaluation of SCCVII tumor cell survival in clamped and non-clamped solid tumors exposed to carbon-ion beams in comparison to X-rays. Ryoichi Hirayama, Akiko Uzawa, Nobuhiro Takase, Yoshitaka Matsumoto, Miho Noguchi, Kana Koda, Masakuni Ozaki, Kei Yamashita, Huizi Li, Yuki Kase, Naruhiro Matsufuji, Sachiko Koike, Shinichiro Masunaga, Koichi Ando, Ryuichi Okayasu, Yoshiya Furusawa, *Mutation Research/Genetic Toxicology and Environmental Mutagenesis*, 756(1-2), 146 - 151, 2013.
 57. Adequate margin definition for scanned particle therapy in the incidence of intrafractional motion. Knopf Christin Antje, Shinichiro Mori, et al., *Physics in Medicine and Biology*, 58 (17), 6079 - 6094, 2013.
 58. Effects of dose-delivery time structure on biological effectiveness for therapeutic carbon-ion beams evaluated with microdosimetric kinetic model. Taku Inaniwa, Masao Suzuki, Takuji Furukawa, Yuki Kase, Nobuyuki Kanematsu, Toshiyuki Shirai, et al., *Radiation Research*, 180(1), 44 - 59, 2013.
 59. Quantitative proteomic analysis for radiation-induced cell cycle suspension in 92-1 melanoma cell line. Fengling Wang, Zhitong Bing, Yanan Zhang, Bin Ao, Sheng Zhang, Caiyong Ye, Jinpeng He, Nan Ding, Wenling Ye, Jie Xiong, Jintu Sun, Yoshiya Furusawa, Guangming Zhou, Lei Yang, *Journal of Radiation Research*, 54, 649 - 662, 2013.
 60. Effects of a difference in respiratory cycle between treatment planning and irradiation for phase controlled rescanning and carbon pencil beam scanning. Shinichiro Mori, Silvan Marius Zenklusen, Taku Inaniwa, Takuji Furukawa, Toshiyuki Shirai, Kouji Noda, *British Journal of Radiology*, 86, 20130163-1 - 20130163-9, 2013.
 61. High LET Radiation Amplifies Centrosome Overduplication through a Pathway of Gamma-Tubulin Monoubiquitination. Mikio Shimada, Ryoichi Hirayama, Kenshi Komatsu, *International Journal of Radiation Oncology Biology Physics*, 86(2), 358 - 365, 2013.
 62. Systematic evaluation of four-dimensional hybrid depth scanning for carbon-ion lung therapy. Shinichiro Mori, Takuji Furukawa, Taku Inaniwa, Silvan Marius Zenklusen, Minoru

- Nakao, Toshiyuki Shirai, Kouji Noda, *Medical Physics*, 40(3), 031720-1 - 031720-18, 2013.
63. Evaluation of plastic materials for range shifting, range compensation, and solid-phantom dosimetry in carbon-ion radiotherapy. Nobuyuki Kanematsu, Yusuke Koba, Risa Ogata, *Medical Physics*, 40(4), 041724-1 - 041724-6, 2013.
 64. Effective and organ doses in helical 4DCT for thoracic and abdominal therapies. Yuka Matsuzaki, Keisuke Fujii, Motoki Kumagai, Ichirou Tsuruoka, Shinichiro Mori, *Journal of Radiation Research*, 54, 962 - 970, 2013.
 65. Positional Dependence of the CT number use of a Cone-beam CT Scanner for an Electron Density Phantom in Particle Beam Therapy. Yohsuke Kusano, Saki Uesaka, Kaori Yajima, Motoki Kumagai, Hideyuki Mizuno, Shinichiro Mori, *Radiological Physics and Technology*, 6, 241 - 247, 2013.
 66. Current status and future prospects of multi-dimensional image guided particle therapy. Shinichiro Mori, Silvan Marius Zenklusen, Knopf Christin Antje, *Radiological Physics and Technology*, 6(2), 249 - 272, 2013.
 67. Radiosensitivity of pimonidazole-unlabeled intratumor quiescent cell population to gamma-rays, accelerated carbon ion beams and boron neutron capture reaction. Shinichiro Masunaga, Yoshinori Sakurai, Hiroki Tanaka, Ryoichi Hirayama, Yoshitaka Matsumoto, Akiko Uzawa, Minoru Suzuki, Natsuko Kondo, Akira Maruhashi, Koji Ono, *British Journal of Radiology*, 86(1021), 20120302, 2013.
 68. Radiobiological description of the LET dependence of the cell survival of oxic and anoxic cells irradiated by carbon ions. L. Antonovic, Anders Brahme, Yoshiya Furusawa, Juliana Toma-Dasu, *Journal of Radiation Research*, 54, 18 - 26, 2013.
 69. Synthesis and Radical-Scavenging Activity of a Dimethylcatechin Analogue. Kohei Imai, Ikuo Nakanishi, Akiko Ohno, Masaaki Kurihara, Naoki Miyata, Ken-ichiro Matsumoto, Asao Nakamura, Kiyoshi Fukuhara, *Bioorganic and Medicinal Chemistry Letters*, 24(11), 2582 - 2584, 2014.
 70. Scavenging of reactive oxygen species induced by hyperthermia in biological fluid. Megumi Ueno, Minako Nyui, Ikuo Nakanishi, Kazunori Anzai, Toshihiko Ozawa, Ken-ichiro Matsumoto, Yoshihiro Uto, *Journal of Clinical Biochemistry and Nutrition*, 54(2), 75 - 80, 2014.
 71. Disproportionation of a 2,2-Diphenyl-1-Picrylhydrazyl Radical as a Model of Reactive Oxygen Species Catalysed by Lewis and/or Brønsted Acids. Ikuo Nakanishi, Tomonori Kawashima, Kei Ohkubo, Tsukasa Waki, Yoshihiro Uto, Tadashi Kamada, Toshihiko Ozawa, Ken-ichiro Matsumoto, Shunichi Fukuzumi, *Chemical Communications*, 50(7), 814 - 816, 2014.
 72. Cellular Internalization of Fibroblast Growth Factor-12 Exerts Radioprotective Effects on Intestinal Radiation Damage Independently of FGFR Signaling. Fumiaki Nakayama, Sachiko Umeda, Takeshi Yasuda, Mayumi Fujita, Masahiro Asada, Viktor Meineke, Toru Imamura, Takashi Imai, *International Journal of Radiation Oncology Biology Physics*, 88(2), 377 - 384, 2014.
 73. Chromatin Compaction Protects Genomic DNA from Radiation Damage. Hideaki Takata, Tomo Hanafusa, Toshiaki Mori, Mari Shimura, Yutaka Iida, Kenichi Ishikawa, Kenichi Yoshikawa, Yuko Yoshikawa, Kazuhiro Maeshima, *PLOS ONE* (Online only:URL:<http://www.plosone.org>), 8(10), e75622, 2013.
 74. Upregulated expression of FGF13/FHF2 mediates resistance to platinum drugs in cervical cancer cells. Tomoko Okada, Kazuhiro Murata, Ryoma Hirose, Chie Matsuda, Tsunehiko Komatsu, Masahiko Ikekita, Miyako Nakawatari, Fumiaki Nakayama, Masaru Wakatsuki, Tatsuya Ohno, Shingo Kato, Takashi Imai, Toru Imamura, *Scientific Reports (Online Only URL:<http://www.nature.com/srep/index.html>)*, 3(2899), 2013.
 75. Effects of Ionic Radius of Redox-Inactive Bio-Related Metal Ions on the Radical-Scavenging Activity of Flavonoids Evaluated Using Photometric Titration. Tsukasa Waki, Shigeki Kobayashi, Kenichiro Matsumoto, Toshihiko Ozawa, Tadashi Kamada, Ikuo Nakanishi, *Chemical Communications*, 49(84), 9842 - 9844, 2013.
 76. *Medical Physics*. Shigekazu Fukuda, *Journal of Radiation Research*, 55(S1), i30 - i31, 2014.
 77. High linear-energy-transfer radiation can overcome radioresistance of glioma stem-like cells to low linear-energy-transfer radiation. Yuki Hirota, Shin-ichiro Masunaga, Natsuko Kondo, Shinji Kawabata, Hirokazu Hirakawa, Hirohiko Yajima, Akira Fujimori, Koji Ono, Toshihiko Kuroiwa, Shin-ichi Miyatake, *Journal of Radiation Research*, 55(1), 75 - 83, 2014.
 78. Induction of DNA damage, including abasic sites, in plasmid DNA by carbon ion and X-ray irradiation. Takuya Shiina, Ritsuko Watanabe, Iyo Shiraiishi, Masao Suzuki, Yuki Sugaya, Kentaro Fujii, Akinari Yokoya, *Radiation and Environmental Biophysics*, 52(1), 99 - 112, 2013.
 79. Neutron-Production Yields from 400 MeV/Nucleon Iron Stopping in Carbon, Aluminum, Copper, and Lead Targets. L. H. Heilbronn, C. J. Zeitlin, Y. Iwata, T. Murakami, T. Nakamura, S. Yonai, R. M. Ronningen, *Nucl. Sci. and Eng.*, 169, 279 - 289, 2011.
 80. Measurements of galactic cosmic ray shielding with the CRATER instrument. C. Zeitlin, A. W. Case, H. E. Spence, N. A. Schwadron, M. Golightly, J. K. Wilson, J. C. Kasper, J. B. Blake, M. D. Looper, J. E. Mazur, L. W. Townsend, Y. Iwata, *Space Weather*, 11(5), 284 - 296, 2014.
 81. The Deep-space Galactic Cosmic Ray Lineal Energy Spectrum at Solar Minimum. A. W. Case, J. C. Kasper, H. E. Spence, C. J. Zeitlin, M. D. Looper, M. J. Golightly, N. A. Schwadron, L. W. Townsend, J. E. Mazur, J. B. Blake, Y. Iwata, *Space Weather*, 11(6), 361 - 368, 2013.
 82. Experimental investigation of bubble occurrence and locality distribution of bubble detectors bombarded with high-energy helium ions. S. L. Guo, T. Doke, D.H. Zhang, L. Li, B.L. Chen, J. Kikuchi, N. Hasebe, K. Terasawa, K. Hara, T. Fuse, N. Yasuda, T. Murakami, *Radiation Measurements*, 50, 31 - 37, 2013.
 83. Activation-induced cytidine deaminase expression in CD4+ T cells is associated with a unique IL-10-producing subset that increases with age. Nakako Nakajima, Qin Hongyan, et al., *PLOS ONE* (Online only:URL:<http://www.plosone.org>), 2011.
 84. Gap junction communication and the propagation of bystander effects induced by microbeam irradiation in human fibroblast cultures: the impact of radiation quality. Narongchai Autsavapromporn, Masao Suzuki, Tomoo Funayama, Noriko Usami, Ianik Plante, Yuichiro Yokota, Yasuko Mutou, Hiroko Ikeda, Katsumi Kobayashi, Yasuhiko Kobayashi, Yukio Uchihori, Tom K Hei, Edouard I Azzam, Takeshi Murakami, *Radiation Research*, 180(4), 367 - 375, 2013.
 85. Chromosome aberrations in normal human fibroblasts ana-

- lyzed in G0/G1 and G2/M phases after exposure in G0 to radiation with different linear energy transfer (LET). Cui hua Liu, Tetsuya Kawata, Yoshiya Furusawa, Guangming Zhou, Kohei Inoue, Junichi Fukada, Ryuichi Kota, Kerry George, Francis Cucinotta, Ryuichi Okayasu, *Mutation Research*, 756(1-2), 101 - 107, 2013.
86. Experimental verification of dose calculation using the simplified Monte Carlo method with an improved initial beam model for a beam-wobbling system. Ryohei Tansho, Yoshihisa Takada, Ryosuke Kohno, Kenji Hotta, Yousuke Hara, et al., *Physics in Medical and Biology*, 58(17), 6047 - 6064, 2013.
87. Comparison of the repair of potentially lethal damage after low- and high-LET radiation exposure, assessed from the kinetics and fidelity of chromosome rejoining in normal human fibroblasts. Cui hua Liu, Guangming Zhou, Tetsuya Kawata, Yoshiya Furusawa, Ryuichi Kota, Atsuhiko Kumabe, Shinya Sutani, Junichi Fukada, Masayo Mishima, Naoyuki Shigematsu, Kerry George, Francis Cucinotta, *Journal of Radiation Research*, 54(6), 989 - 997, 2013.
88. The complexity of DNA double strand breaks is a critical factor enhancing end-resection. Hirohiko Yajima, Hiroshi Fujisawa, Nakako Nakajima, Hirokazu Hirakawa, Penny Jeggo, Ryuichi Okayasu, Akira Fujimori, *DNA Repair*, 12(11), 936 - 946, 2013.
89. Participation of Gap Junction Communication in Potentially Lethal Damage Repair and DNA Damage in Human Fibroblasts Exposed to Low- or High-LET Radiation. Narongchai Autsavapornporn, Masao Suzuki, Ianik Plante, Cui Hua Liu, Yukio Uchihori, Tom K Hei, Edouard Azzam, Takeshi Murakami, *Mutation Research/Genetic Toxicology and Environmental Mutagenesis*, 756(1-2), 78 - 85, 2013.
90. Visualisation of gH2AX Foci Caused by Heavy Ion Particle Traversal; Distinction between Core Track versus Non-Track Damage. Nakako Nakajima, Brunton Holly, Ritsuko Watanabe, Ryoichi Hirayama, Naruhiro Matsufuji, Akira Fujimori, Takeshi Murakami, Ryuichi Okayasu, Penny Jeggo, Atsushi Shibata, et al., *PLOS ONE* (Online only:URL:<http://www.plosone.org>), 2013.
91. High-Throughput Screening of Radioprotectors Using Rat Thymocytes. Emiko Sekine, Ikuo Nakanishi, Takashi Shimokawa, Megumi Ueno, Kenichiro Matsumoto, Takeshi Murakami, *Analytical Chemistry*, 85(16), 7650 - 7653, 2013.
92. Selective Enhancing Effect of Early Mitotic Inhibitor 1 (Emi1) Depletion on the Sensitivity of Doxorubicin or X-ray Treatment in Human Cancer Cells. Natsumi Shimizu, Nakako Nakajima, Ryoichi Hirayama, Akira Fujimori, Ryuichi Okayasu, Yasusei Kudo, et al., *The Journal of Biological Chemistry*, 288(24), 17238 - 17252, 2013.
93. Comparison of the bromodeoxyuridine-mediated sensitization effects between low-LET and high-LET ionizing radiation on DNA double-strand breaks. Yoshihiro Fujii, Matthew Genet, Erica Roybal, Nobuo Kubota, Ryuichi Okayasu, Miyagawa Kiyoshi, Akira Fujimori, Takamitsu Kato, *Oncology Reports*, 29(6), 2133 - 2139, 2013.
94. Long-term follow-up results of a multi-institutional phase 2 study of concurrent chemoradiation therapy for locally advanced cervical cancer in East and Southeast Asia. Shingo Kato, Tatsuya Ohno, Kullathorn Thephamongkhon, Yaowalak Chansilpa, Jianping Cao, Xiaoting Xu, C R Beena Devi, Tang Tieng Swee, Miriam J C Calaguas, Rey H de Los Reyes, Chul-Koo Cho, To Anh Dung, Nana Supriana, Dyah Erawati, Hideyuki Mizuno, Takashi Nakano, Hirohiko Tsujii, *International Journal of Radiation Oncology, Biology, Physics*, 87(1), 100 - 105, 2013.
95. On the mechanism of the sensitization of PADC (poly(allyl diglycolcarbonate)) track detectors by carbon dioxide treatment. Nabil M. Hassan, Yuri Matai, Tamon Kusumoto, Yutaka Mori, Masato Kanasaki, Keiji Oda, Hisashi Kitamura, Teruaki Konishi, Satoshi Kodaira, Nakahiro Yasuda, Tomoya Yamauchi, *Radiation Measurements*, 59, 23 - 29, 2013.
96. Applicability of the polyimide films as an SSNTD material. Tomoya Yamauchi, Shunsuke Kaifu, Yutaka Mori, Masato Kanasaki, Keiji Oda, Satoshi Kodaira, Teruaki Konishi, Nakahiro Yasuda, Rémi Barillon, *Radiation Measurements*, 50, 16 - 21, 2013.
97. Applicability of Polyimide Films as Etched-Track Detectors for Ultra-Heavy Cosmic Ray Components. Tomoya Yamauchi, Kenya Matsukawa, Yutaka Mori, Masato Kanasaki, Atsuto Hattori, Yuri Matai, Tamon Kusumoto, Akira Tao, Keiji Oda, Satoshi Kodaira, Teruaki Konishi, Hisashi Kitamura, Nakahiro Yasuda, Rémi Barillon, *Applied Physics Express*, 6, 046401-1 - 046401-4, 2013.

■ **Molecular Imaging Research for Functional Diagnosis**

- OAT3-mediated extrusion of the ^{99m}Tc-ECD metabolite in the mouse brain. Tatsuya Kikuchi, Toshimitsu Okamura, Hidekatsu Wakizaka, Maki Okada, Kenichi Odaka, Joji Yui, Atsushi Tsuji, Toshimitsu Fukumura, Ming-Rong Zhang, *Journal of Cerebral Blood Flow and Metabolism*, 34(4), 585 - 588, 2014.
- Noninvasive quantification of metabotropic glutamate receptor type 1 with [¹¹C]ITDM: a small-animal PET study. Tomoteru Yamasaki, Masayuki Fujinaga, Joji Yui, Youko Ikoma, Akiko Hatori, Lin Xie, Hidekatsu Wakizaka, Katsushi Kumata, Nobuki Nengaki, Kazunori Kawamura, Ming-Rong Zhang, *Journal of Cerebral Blood Flow and Metabolism*, 34(1), 1 - 7, 2014.
- Visualization of Acute Liver Damage Induced by Cycloheximide in Rats Using PET with [¹⁸F]FEDAC, a Radiotracer for Translocator Protein (18 kDa). Akiko Hatori, Joji Yui, Lin Xie, Tomoteru Yamasaki, Katsushi Kumata, Masayuki Fujinaga, Hidekatsu Wakizaka, Masanao Ogawa, Nobuki Nengaki, Kazunori Kawamura, Ming-Rong Zhang, *PLOS ONE* (Online only:URL:<http://www.plosone.org>), 9(1), e86625, 2014.
- Expression and Functional Analysis of the CorA-MRS2-ALR-Type Magnesium Transporter Family in Rice. Takayuki Saito, Natsuko Kobayashi, Keitaro Tanoi, Naoko Iwata, Hisashi Suzuki, Ren Iwata, Tomoko Nakanishi, *Plant Cell Physiology*, 54(10), 1673 - 1683, 2013.
- The use of tetrabutylammonium fluoride to promote N- and O-¹¹C-methylation reactions with iodo[¹¹C]methane in dimethyl sulfoxide. Tatsuya Kikuchi, Katsuyuki Minegishi, Hiroki Hashimoto, Ming-Rong Zhang, Koichi Kato, *Journal of Labelled Compounds and Radiopharmaceuticals*, 56(13), 672 - 678, 2013.
- Binding potential of (E)-[¹¹C]ABP688 to metabotropic glutamate receptor subtype 5 is decreased by the inclusion of its ¹¹C-labelled Z-isomer. Kazunori Kawamura, Tomoteru Yamasaki, Katsushi Kumata, Kenji Furutsuka, Makoto Takei, Hidekatsu Wakizaka, Masayuki Fujinaga, Kaori Kariya, Joji

- Yui, Akiko Hatori, Lin Xie, Yoko Shimoda, Hiroki Hashimoto, Kazutaka Hayashi, Ming-Rong Zhang, *Nuclear Medicine and Biology*, 41(1), 17 - 23, 2014.
7. Imaging of Activity of Multidrug Resistance-Associated Protein 1 in the Lungs. Toshimitsu Okamura, Tatsuya Kikuchi, Maki Okada, Hidekatsu Wakizaka, Ming-Rong Zhang, *American Journal of Respiratory Cell and Molecular Biology*, 49(3), 335 - 340, 2013.
 8. Synthesis and evaluation of [¹¹C]MMPiP as a potential radioligand for imaging of metabotropic glutamate 7 receptor in the brain. Tomoteru Yamasaki, Katsushi Kumata, Joji Yui, Masayuki Fujinaga, Kenji Furutsuka, Akiko Hatori, Lin Xie, Masanao Ogawa, Nobuki Nengaki, Kazunori Kawamura, Ming-Rong Zhang, *EJNMMI Research (Online Only URL: <http://link.springer.com/journal/13550>)*, 3(54), 2013.
 9. Monitoring Neuroprotective Effects Using Positron Emission Tomography With [¹¹C]ITMM, a Radiotracer for Metabotropic Glutamate 1 Receptor. Joji Yui, Lin Xie, Masayuki Fujinaga, Tomoteru Yamasaki, Akiko Hatori, Katsushi Kumata, Nobuki Nengaki, Ming-Rong Zhang, *Stroke*, 44(9), 2567 - 2572, 2013.
 10. Synthesis and Evaluation of 1-[2-(4-[¹¹C]Methoxyphenyl)phenyl] piperazine for Imaging of the Serotonin 5-HT₇ Receptor in the Rat Brain. Yoko Shimoda, Joji Yui, Lin Xie, Masayuki Fujinaga, Tomoteru Yamasaki, Masanao Ogawa, Nobuki Nengaki, Katsushi Kumata, Akiko Hatori, Kazunori Kawamura, Ming-Rong Zhang, *Bioorganic and Medicinal Chemistry*, 21(17), 5316 - 5322, 2013.
 11. Non-input analysis for incomplete trapping irreversible tracer with PET. Tomoyuki Ohya, Tatsuya Kikuchi, Toshimitsu Fukumura, Ming-Rong Zhang, Toshiaki Irie, *Nuclear Medicine and Biology*, 40(5), 664 - 669, 2013.
 12. Initial Human PET Studies of Metabotropic Glutamate Receptor Type 1 Ligand ¹¹C-ITMM. Jun Toyohara, Muneyuki Sakata, Keiichi Oda, Kenji Ishii, Kimitaru Ito, Mikio Hiura, Masayuki Fujinaga, Tomoteru Yamasaki, Ming-Rong Zhang, Kiichi Ishiwata, *Journal of Nuclear Medicine*, 54(8), 1302 - 1307, 2013.
 13. PET probes for imaging brain acetylcholinesterase. Tatsuya Kikuchi, Toshimitsu Okamura, Ming-Rong Zhang, Toshiaki Irie, *Journal of Labelled Compounds and Radiopharmaceuticals*, 56(3-4), 172 - 179, 2013.
 14. Improvement of brain uptake for in vivo PET imaging of astrocytic oxidative metabolism using benzyl [¹¹C]acetate. Maki Okada, Ryuji Nakao, Sotaro Momosaki, Kazuhiko Yanamoto, Tatsuya Kikuchi, Toshimitsu Okamura, Hidekatsu Wakizaka, Rie Hosoi, Ming-Rong Zhang, Osamu Inoue, *Applied Radiation and Isotopes*, 78, 102 - 107, 2013.
 15. Synthesis, metabolite analysis, and in vivo evaluation of [¹¹C]irinotecan as a novel positron emission tomography (PET) probe. Kazunori Kawamura, Hiroki Hashimoto, Masanao Ogawa, Joji Yui, Hidekatsu Wakizaka, Tomoteru Yamasaki, Akiko Hatori, Lin Xie, Katsushi Kumata, Masayuki Fujinaga, Ming-Rong Zhang, *Nuclear Medicine and Biology*, 40(5), 651 - 657, 2013.
 16. Different magnesium uptake and transport activity along the rice root axis revealed by a ²⁶Mg tracer experiments. Natsuko Kobayashi, Naoko Iwata, Takayuki Saito, Hisashi Suzuki, Ren Iwata, Keitaro Tanoi, Tomoko Nakanishi, *Soil Science and Plant Nutrition*, 59(2), 149 - 155, 2013.
 17. Application of ²⁶Mg for Characterization of Mg Uptake in Rice Seedling under Different pH Conditions. Natsuko Kobayashi, Naoko Iwata, Takayuki Saito, Hisashi Suzuki, Ren Iwata, Keitaro Tanoi, Tomoko Nakanishi, *Journal of Radioanalytical and Nuclear Chemistry*, 296(1), 531 - 534, 2013.
 18. GPU-based optical propagation simulator of a laser-processed crystal block for the X'tal cube PET detector. Yuma Ogata, Takashi Ohnishi, Takahiro Moriya, Naoko Inadama, Fumihiko Nishikido, Eiji Yoshida, Hideo Murayama, Taiga Yamaya, Hideaki Haneishi, *Radiological physics and technology*, 7(1), 35-42, 2014.
 19. Simulation study optimizing the number of photodetection faces for the X'tal cube PET detector with separated crystal segments. Takahiro Matsumoto, Taiga Yamaya, Eiji Yoshida, Fumihiko Nishikido, Naoko Inadama, Hideo Murayama, Mikio Suga, *Radiological Physics and Technology*, 7(1), 43 - 50, 2014.
 20. Relation between Dopamine Synthesis Capacity and Cell-Level Structure in Human Striatum: A Multi-Modal Study with Positron Emission Tomography and Diffusion Tensor Imaging. Hiroshi Kawaguchi, Takayuki Obata, Harumasa Takano, Tsuyoshi Nogami, Tetsuya Suhara, Hiroshi Ito, *PLOS ONE*, 9(1), e87886, 2014.
 21. Four-layer DOI PET detectors using a multi-pixel photon counter array and light sharing method. Fumihiko Nishikido, Naoko Inadama, Eiji Yoshida, Hideo Murayama, Taiga Yamaya, *Nuclear Instruments and Methods in Physics Research Section A*, 729, 755 - 761, 2013.
 22. Compartmental analysis of washout effect in rat brain: in-beam OpenPET measurement using a ¹¹C beam. Yoshiyuki Hirano, Shoko Kinouchi, Yoko Ikoma, Eiji Yoshida, Hidekazu Wakizaka, Hiroshi Ito, Taiga Yamaya, *Physics in Medicine and Biology*, 58(23), 8281 - 8294, 2013.
 23. Performance evaluation of a depth-of-interaction detector by use of position-sensitive PMT with a super-bialkali photocathode. Yoshiyuki Hirano, Munetaka Nitta, Naoko Inadama, Fumihiko Nishikido, Eiji Yoshida, Hideo Murayama, Taiga Yamaya, *Radiological Physics and Technology*, 7(1), 57 - 66, 2014.
 24. Reproducibility of measuring cerebral blood flow by laser-Doppler flowmetry in mice. Yosuke Tajima, Hiroyuki Takuwa, Hiroshi Kawaguchi, Kazuto Masamoto, Yoko Ikoma, Chie Seki, Junko Taniguchi, Iwao Kanno, Naokatsu Saeki, Hiroshi Ito, *Frontiers in Bioscience Elite Edition*, 6E(1), 62 - 68, 2014.
 25. Noninvasive k₃ estimation method for slow dissociation PET ligands: application to [¹¹C]Pittsburgh compound B. Koichi Sato, Kiyoshi Fukushi, Hitoshi Shinotoh, Hitoshi Shimada, Shigeki Hirano, Noriko Tanaka, Tetsuya Suhara, Toshiaki Irie, Hiroshi Ito, *EJNMMI research*, 3(1), 76, 2013.
 26. Evaluation of Rho-Kinase Activity in Mice Brain Using N-[¹¹C]Methyl-hydroxyfasudil with Positron Emission Tomography. Junko Taniguchi, Chie Seki, Hiroyuki Takuwa, Hiroshi Kawaguchi, Yoko Ikoma, Masayuki Fujinaga, Iwao Kanno, Ming-Rong Zhang, Satoshi Kuwabara, Hiroshi Ito, *Molecular Imaging and Biology*, 16(3), 395 - 402, 2014.
 27. Microvascular sprouting, extension, and creation of new capillary connections with adaptation of the neighboring astrocytes in adult mouse cortex under chronic hypoxia. Kazuto Masamoto, Hiroyuki Takuwa, Chie Seki, Junko Taniguchi, Yoshiaki Itoh, Yutaka Tomita, Haruki Toriumi, Miyuki Unekawa, Hiroshi Kawaguchi, Hiroshi Ito, Norihiro Suzuki, Iwao Kanno,

- Journal of Cerebral Blood Flow and Metabolism, 34(2), 325 - 331, 2013.
28. Imaging of amyloid deposition in human brain using positron emission tomography and [¹⁸F]FACT: comparison with [¹¹C] PIB. Hiroshi Ito, Hitoshi Shinotoh, Hitoshi Shimada, Michie Miyoshi, Kazuhiko Yanai, Nobuyuki Okamura, Harumasa Takano, Hidehiko Takahashi, Ryosuke Arakawa, Fumitoshi Kodaka, Maiko Ono, Yoko Eguchi, Makoto Higuchi, Toshimitsu Fukumura, Tetsuya Suhara, European Journal of Nuclear Medicine and Molecular Imaging, 41(4), 745 - 754, 2014.
 29. Influence of O-methylated metabolite penetrating the blood-brain barrier to estimation of dopamine synthesis capacity in human L-[β -¹¹C]DOPA PET. Keisuke Matsubara, Yoko Ikoma, Maki Okada, Masanobu Ibaraki, Tetsuya Suhara, Toshiyumi Kinoshita, Hiroshi Ito, Journal of Cerebral Blood Flow and Metabolism, 34(2), 268 - 274, 2014.
 30. Impact of Laser-Processed X'tal Cube Detectors on PET Imaging in a One-Pair Prototype System. Eiji Yoshida, Yoshiyuki Hirano, Hideaki Tashima, Naoko Inadama, Fumihiko Nishikido, Takahiro Moriya, Tomohide Omura, Mitsuo Watanabe, Hideo Murayama, Taiga Yamaya, IEEE Transactions on Nuclear Science, 60(5), 3172 - 3180, 2013.
 31. Feasibility Study of an Axially Extendable Multiplex Cylinder PET. Eiji Yoshida, Yoshiyuki Hirano, Hideaki Tashima, Naoko Inadama, Fumihiko Nishikido, Hideo Murayama, Hiroshi Ito, Taiga Yamaya, IEEE Transactions on Nuclear Science, 60(5), 3227 - 3234, 2013.
 32. Novel system using microliter order sample volume for measuring arterial radioactivity concentrations in whole blood and plasma for mouse PET dynamic study. Yuichi Kimura, Chie Seki, Nobuya Hashizume, Takashi Yamada, Hidekatsu Wakizaka, Takahiro Nishimoto, Kentaro Hatano, Keishi Kitamura, Hiroshi Toyama, Iwao Kanno, Physics in Medicine and Biology, 58(22), 7889 - 7903, 2013.
 33. Hemodynamic changes during neural deactivation in awake mice: A measurement by laser-Doppler flowmetry in crossed cerebellar diaschisis. Hiroyuki Takuwa, Yousuke Tajima, Daisuke Kokuryo, Tetsuya Matsuura, Hiroshi Kawaguchi, Kazuto Masamoto, Jyunko Taniguchi, Youko Ikoma, Chie Seki, Ichio Aoki, Yutaka Tomita, Norihiro Suzuki, Iwao Kanno, Hiroshi Ito, Brain Research, 1537(6), 350 - 355, 2013.
 34. Development of a single-ring OpenPET prototype. Eiji Yoshida, Hideaki Tashima, Hidekatsu Wakizaka, Fumihiko Nishikido, Yoshiyuki Hirano, Naoko Inadama, Hideo Murayama, Hiroshi Ito, Taiga Yamaya, Nuclear Instruments and Methods in Physics Research Section A, 729, 800 - 808, 2013.
 35. Measuring the vascular diameter of brain surface and parenchymal arteries in awake mouse. Yuta Sekiguchi, Kazuto Masamoto, Hiroyuki Takuwa, Hiroshi Kawaguchi, Iwao Kanno, Hiroshi Ito, Yutaka Tomita, Yoshiaki Itoh, Norihiro Suzuki, Ryo Sudo, Kazuo Tanishita, Oxygen Transport to Tissue XXXV (Advances in Experimental Medicine and Biology; v.789), 789, 419 - 425, 2013.
 36. Layer-specific dilation of penetrating arteries induced by stimulation of the nucleus basalis of Meynert in the mouse frontal cortex. Harumi Hotta, Kazuto Masamoto, Sae Uchida, Yuta Sekiguchi, Hiroyuki Takuwa, Hiroshi Kawaguchi, Ryo Sudo, Kazuo Tanishita, Hiroshi Ito, Iwao Kanno, et al., Journal of Cerebral Blood Flow and Metabolism, 33(9), 1440 - 1447, 2013.
 37. A proposal for PET/MRI attenuation correction with mu-values measured using a fixed-position radiation source and MRI segmentation. Hiroshi Kawaguchi, Yoshiyuki Hirano, Eiji Yoshida, Jeffrey Kershaw, Takahiro Shiraishi, Mikio Suga, Youko Ikoma, Takayuki Obata, Hiroshi Ito, Taiga Yamaya, Nuclear Instruments and Methods in Physics Research Section A, 734(Part B), 156 - 161, 2014.
 38. Hypoxia-Induced Cerebral Angiogenesis in Mouse Cortex with Two-Photon Microscopy. Kazuto Masamoto, Hiroyuki Takuwa, Yutaka Tomita, Haruki Toriumi, Miyuki Unekawa, Jyunko Taniguchi, Hiroshi Kawaguchi, Yoshiaki Itoh, Norihiro Suzuki, Hiroshi Ito, Iwao Kanno, Oxygen Transport to Tissue XXXV (Advances in Experimental Medicine and Biology; v.789), 789, 15 - 20, 2013.
 39. Reference region automatic extraction in dynamic [¹¹C]PIB. Yoko Ikoma, Paul Edison, Anil Ramlackhansingh, Federico E. Turkheimer, et al., Journal of Cerebral Blood Flow and Metabolism, 33(11), 1725 - 1731, 2013.
 40. Spatial resolution limits for the isotropic-3D PET detector X'tal cube. Eiji Yoshida, Hideaki Tashima, Yoshiyuki Hirano, Naoko Inadama, Fumihiko Nishikido, Hideo Murayama, Taiga Yamaya, Nuclear Instruments and Methods in Physics Research Section A, 728, 107 - 111, 2013.
 41. The X'tal cube PET detector with a monolithic crystal processed by the 3D sub-surface laser engraving technique: Performance comparison with glued crystal elements. Eiji Yoshida, Yoshiyuki Hirano, Hideaki Tashima, Naoko Inadama, Fumihiko Nishikido, Takahiro Moriya, Tomohide Omura, Mitsuo Watanabe, Hideo Murayama, Taiga Yamaya, Nuclear Instruments and Methods in Physics Research Section A, 723, 83 - 88, 2013.
 42. Potential for reducing the numbers of SiPM readout surfaces of laser-processed X'tal cube PET detectors. Yoshiyuki Hirano, Naoko Inadama, Eiji Yoshida, Fumihiko Nishikido, Hideo Murayama, Mitsuo Watanabe, Taiga Yamaya, Physics in Medicine and Biology, 58(5), 1361 - 1374, 2013.
 43. Design Study of the DOI-PET Scanners with the X'tal Cubes toward Sub-Millimeter Spatial Resolution. Eiji Yoshida, Hiroki Yamasita, Hideaki Tashima, Shoko Kinouchi, Hideo Murayama, Mikio Suga, Taiga Yamaya, Journal of Medical Imaging and Health Informatics, 3(1), 131 - 134, 2013.
 44. Retinol palmitate prevents ischemia-induced cell changes in hippocampal neurons through the Notch1 signaling pathway in mice. Jun-Ichiro Shimada, Jyunko Taniguchi, Masahiro Mori, Yasunori Sato, Hiroyuki Takuwa, Hiroshi Ito, Satoshi Kuwabara, Experimental Neurology, 247, 182 - 187, 2013.
 45. Carbon-11-acetate positron emission tomography (PET), versus fluorine-18 fluorodeoxyglucose PET and CT for the diagnosis of recurrent prostate cancer after radical prostatectomy in cases of prostate specific antigen of >1 to 3ng/mL. Yasuhisa Fujibayashi, et al., Hellenic Journal of Nuclear Medicine, 16(2), 146 - 147, 2013.
 46. Diagnosis of complex renal cystic masses and solid renal lesions using PET imaging: comparison of ¹¹C-acetate and ¹⁸F-FDG PET imaging. Nobuyuki Oyama, Hideaki Ito, Noriko Takahara, Yoshiji Miwa, Hironobu Akino, Takashi Kudo, Hidehiko Okazawa, Yasuhisa Fujibayashi, et al., Clinical Nuclear Medicine, 39(3), e208 - 214, 2014.
 47. Novel contribution of cell surface and intracellular M1-muscarinic acetylcholine receptors to synaptic plasticity in

- hippocampus. Abu Syed Md Anisuzzaman, Junsuke Uwada, Takayoshi Masuoka, Hatsumi Yoshiki, Matomo Nishio, Yuji Ikegaya, Naoya Takahashi, Norio Matsuki, Yasuhisa Fujibayashi, Yoshiharu Yonekura, et al., *Journal of Neurochemistry*, 126(3), 360 - 371, 2013.
48. Controlled Administration of Penicillamine Reduces Radiation Exposure in Critical Organs during ^{64}Cu -ATSM Internal Radiotherapy: A Novel Strategy for Liver Protection. Yukie Yoshii, Hiroki Matsumoto, Mitsuyoshi Yoshimoto, Takako Furukawa, Yukie Morokoshi, Chizuru Sogawa, Ming-Rong Zhang, Hidekatsu Wakizaka, Hiroshi Yoshii, Yasuhisa Fujibayashi, Tsuneo Saga, *PLOS ONE*, 9(1), e86996, 2014.
49. PET imaging and biodistribution analysis of the effects of succinylated gelatin combined with L-lysine on renal uptake and retention of ^{64}Cu -cyclam-RAFT-c(-RGDFK-), in vivo. Zhao-Hui Jin, Takako Furukawa, Chizuru Sogawa, Michael Claron, Winn Aung, Atsushi B Tsuji, Hidekatsu Wakizaka, Ming-Rong Zhang, Didier Boturyn, Pascal Dumy, Yasuhisa Fujibayashi, Tsuneo Saga, *European Journal of Pharmaceutics and Biopharmaceutics*, 86(3), 478 - 486, 2014.
50. Synthesis of a Dextran-Based Bone Tracer for in vivo Magnetic Resonance and Optical Imagings by Two Orthogonal Coupling Reactions. Hiroshi Tanaka, Sho Yamaguchi, Jun-ichiro Jo, Ichio Aoki, Yasuhiko Tabata, Takashi Takahashi, *RSC Advances*, 4, 7561 - 7565, 2013.
51. AHNAK is highly expressed and plays a key role in cell migration and invasion in mesothelioma. Hitomi Sudo, Atsushi B Tsuji, Aya Sugyo, Masaaki Abe, Okio Hino, Tsuneo Saga, *International Journal of Oncology*, 44(2), 530 - 538, 2014.
52. Imaging of superoxide generation in the dopaminergic area of the brain in Parkinson's disease, using mito-TEMPO. Zhivko Zhelev, Rumiana Bakalova-Zheleva, Ichio Aoki, Desislava Lazarova, Tsuneo Saga, *ACS Chemical Neuroscience*, 4 (11), 1439 - 1445, 2013.
53. Discovery of an uncovered region in fibrin clots and its clinical significance. Yohei Hisada, Masahiro Yasunaga, Shingo Hanaoka, Shinji Saijo, Takashi Sugino, Atsushi Tsuji, Tsuneo Saga, Kouhei Tsumoto, Shino Manabe, Jun-ichiro Kuroda, Jun-ichi Kuratsu, Yasuhiro Matsumura, *Scientific Reports* (Online Only URL: <http://www.nature.com/srep/index.html>), 2013.
54. Micro-Positron Emission Tomography/Contrast-Enhanced Computed Tomography Imaging of Orthotopic Pancreatic Tumor-Bearing Mice Using the $\alpha\text{v}\beta_3$ Integrin Tracer ^{64}Cu -Labeled Cyclam-RAFT-c(-RGDFK-). Aung U Winn, Zhao-Hui Jin, Takako Furukawa, Michael Claron, Didier Boturyn, Chizuru Sogawa, Atsushi Tsuji, Hidekatsu Wakizaka, Toshimitsu Fukumura, Yasuhisa Fujibayashi, Pascal Dumy, Tsuneo Saga, *Molecular Imaging*, 12(6), 376 - 387, 2013.
55. Molecular Imaging of Aquaglycero-Aquaporins: Its Potential for Cancer Characterization. Yuriko Saito, Takako Furukawa, Takayuki Obata, Tsuneo Saga, *Biological and Pharmaceutical Bulletin*, 36(8), 1292 - 1298, 2013.
56. Synthesis and in vitro cellular uptake of ^{11}C -labeled 5-aminolevulinic acid derivative to estimate the induced cellular accumulation of protoporphyrin IX. Chie Suzuki, Koichi Kato, Atsushi Tsuji, Tatsuya Kikuchi, Ming-Rong Zhang, Yasushi Arano, Tsuneo Saga, *Bioorganic and Medicinal Chemistry Letters*, 23(16), 4567 - 4570, 2013.
57. Quantitative ^{17}O imaging towards oxygen consumption study in tumor bearing mice at 7 T. Michiko Narazaki, Yoko Kanazawa, Sachiko Koike, Koichi Ando, Hiroo Ikehira, *Magnetic Resonance Imaging*, 31(5), 643 - 650, 2013.
58. Drugs interacting with organic anion transporter-1 affect uptake of Tc-99m-mercaptoacetyl-triglycine (MAG3) in the human kidney: Therapeutic drug interaction in Tc-99m-MAG3 diagnosis of renal function and possible application of Tc-99m-MAG3 for drug development. Noriko Takahara, Tsuneo Saga, Masayuki Inubushi, Hiroyuki Kusuhara, Sumito Ito, Yuichi Sugiyama, Yasuhisa Fujibayashi, Chie Seki, et al., *Nuclear Medicine and Biology*, 40(5), 643 - 650, 2013.
59. Manganese-Enhanced MRI Reveals Early-Phase Radiation-Induced Cell Alterations in Vivo. Shigeyoshi Saito, Sumitaka Hasegawa, Aiko Sekita, Rumiana Bakalova-Zheleva, Takako Furukawa, Kenya Murase, Tsuneo Saga, Ichio Aoki, *Cancer Research*, 73(11), 3216 - 3224, 2013.
60. Evaluation of ^{89}Zr -Labeled Human Anti-CD147 Monoclonal Antibody as a Positron Emission Tomography Probe in a Mouse Model of Pancreatic Cancer. Aya Sugyou, Atsushi Tsuji, Hitomi Sudou, Koutarou Nagatsu, Mitsuru Koizumi, Ming-Rong Zhang, Tsuneo Saga, et al., *PLOS ONE* (Online only: URL: <http://www.plosone.org>), 8(4), e61230 - e61230, 2013.
61. In Vivo Identification of Sentinel Lymph Nodes Using MRI and Size-Controlled and Monodispersed Magnetite Nanoparticles. Shuji Iida, Kensuke Imai, Sachiko Matsuda, Daisuke Kokuryo, Ichio Aoki, et al., *Journal of Magnetic Resonance Imaging: JMIR*, 38(6), 1346 - 1355, 2013.
62. Neural signal for counteracting pre-action bias in the centromedian thalamic nucleus. Takafumi Minamimoto, Yukiko Hori, Ko Yamanaka, Minoru Kimura, *Frontiers in Systems Neuroscience*, 8(8), 2014.
63. Reproducibility of PET measurement for presynaptic dopaminergic functions using L- $[\beta\text{-}^{11}\text{C}]\text{DOPA}$ and $[\text{F}^{18}]\text{FE-PE2 I}$ in humans. Masayuki Suzuki, Hiroshi Ito, Fumitoshi Kodaka, Harumasa Takano, Yasuyuki Kimura, Hironobu Fujiwara, Takeshi Sasaki, Keisuke Takahata, Tsuyoshi Nogami, Tomohisa Nagashima, Nobuki Nengaki, Kazunori Kawamura, Ming-Rong Zhang, Andrea Varrone, Christer Halldin, Yoshiro Okubo, Tetsuya Suhara, *Nuclear Medicine Communications*, 35(3), 231 - 237, 2014.
64. Emergence of realism: Enhanced visual artistry and high accuracy of visual numerosity representation after left prefrontal damage. Keisuke Takahata, Motoichiro Kato, Fumie Saito, Taro Muramatsu, Makiko Yamada, Joichiro Shirahase, Hajime Tabuchi, Tetsuya Suhara, Masaru Mimura, *Neuropsychologia*, 57, 38 - 49, 2014.
65. Extrastriatal dopamine D2 receptor density and affinity in the human brain measured by 3D PET. Tetsuya Suhara, Yasuhiko Sudo, Takashi Okauchi, Jun Maeda, Koichi Kawabe, Kazutoshi Suzuki, Yoshiro Okubo, Yoshifumi Nakashima, Hiroshi Ito, Shuji Tanada, Christer Halldin, Lars Farde, *International Journal of Neuropsychopharmacology*, 2(2), 73 - 82, 2014.
66. Central nervous system drug evaluation using positron emission tomography. Mizuho Sekine, Jun Maeda, Hitoshi Shimada, Tsuyoshi Nogami, Ryosuke Arakawa, Harumasa Takano, Makoto Higuchi, Hiroshi Ito, Yoshiro Okubo, Tetsuya Suhara, *Clinical Psychopharmacology and Neuroscience*, 9 (1), 9 - 16, 2011.

67. Design, synthesis, radiolabeling, and in vivo evaluation of carbon-11 labeled N-[2-[4-(3-cyanopyridin-2-yl)piperazin-1-yl]ethyl]-3-methoxybenzamide, a potential positron emission tomography tracer for the dopamine D(4) receptors. Enza Lacivita, Paola De Giorgio, Irene T Lee, Sean I Rodeheaver, Bryan A Weiss, Claudia Fracasso, Silvio Caccia, Francesco Berardi, Roberto Perrone, Ming-Rong Zhang, Jun Maeda, Makoto Higuchi, Tetsuya Suhara, John A Schetz, Marcello Leopoldo, *Journal of Medicinal Chemistry*, 53(20), 7344 - 7355, 2010.
68. Glial cell-mediated deterioration and repair of the nervous system after traumatic brain injury in a rat model as assessed by positron emission tomography. Iwae Yu, Motoki Inaji, Jun Maeda, Takashi Okauchi, Tadashi Nariai, Kikuo Ohno, Makoto Higuchi, Tetsuya Suhara, *Journal of Neurotrauma*, 27(8), 1463 - 1475, 2010.
69. Assessment of radioligands for PET imaging of cyclooxygenase-2 in an ischemic neuronal injury model. Bin Ji, Katsushi Kumata, Hirotaka Onoe, Hiroyuki Kaneko, Ming-Rong Zhang, Chie Seki, Maiko Ono, Miho Shukuri, Masaki Tokunaga, Takeharu Minamihisamatsu, Tetsuya Suhara, Makoto Higuchi, *Brain Research*, 1533, 152 - 162, 2013.
70. Detailed Expression Pattern of Aldolase C (Aldoc) in the Cerebellum, Retina and Other Areas of the CNS Studied in Aldoc-Venus Knock-In Mice. Hirofumi Fujita, Hanako Aoki, Itsuki Ajioka, Maya Yamazaki, Manabu Abe, Arata Oh-Nishi, Kenji Sakimura, Izumi Sugihara, *PLOS ONE* (Online only:URL: <http://www.plosone.org>), 9(1), e86679, 2014.
71. Reduced sense of agency in chronic schizophrenia with predominant negative symptoms. Maeda Takaki, Keisuke Takahata, Taro Muramatsu, Tsukasa Okimura, Akihiro Koreki, Satoru Iwashita, Masaru Mimura, *Psychiatry Research*, 209(30), 386 - 392, 2013.
72. Norepinephrine transporter occupancy by nortriptyline in patients with depression: a positron emission tomography study with (S,S)-[¹⁸F]FMeNER-D₂. Harumasa Takano, Ryosuke Arakawa, Tsuyoshi Nogami, Masayuki Suzuki, Tomohisa Nagashima, Hironobu Fujiwara, Yasuyuki Kimura, Fumitoshi Kodaka, Keisuke Takahata, Hitoshi Shimada, Yoshitaka Murakami, Amane Tateno, Makiko Yamada, Hiroshi Ito, Kazunori Kawamura, Ming-Rong Zhang, Hidehiko Takahashi, Motoichiro Kato, Yoshiro Okubo, Tetsuya Suhara, *International Journal of Neuropsychopharmacology*, 17(4), 553 - 560, 2013.
73. Norepinephrine in the brain is associated with aversion to financial loss. H Takahashi, S Fujie, C Camerer, R Arakawa, H Takano, F Kodaka, H Matsui, T Ideno, S Okubo, K Takemura, M Yamada, Y Eguchi, T Murai, Y Okubo, M Kato, H Ito, T Suhara, *Molecular Psychiatry*, 18(1), 3 - 4, 2013.
74. Endogenous Tau Aggregates in Oligodendrocytes of rTg 4510 Mice Induced by Human P301L Tau. Yan Ren, Wen-Lang Lin, Laura Sanchez, Carolina Ceballos, Manuela Polydoro, Tara L Spires-Jones, Bradley T Hyman, Dennis W Dickson, Naruhiko Sahara, *Journal of Alzheimer's disease*, 38(3), 589 - 600, 2014.
75. A Small-Animal Pharmacokinetic/Pharmacodynamic PET Study of Central Serotonin 1A Receptor Occupancy by a Potential Therapeutic Agent for Overactive Bladder. Yosuke Nakatani, Michiyuki Suzuki, Masaki Tokunaga, Jun Maeda, Miyuki Sakai, Hiroki Ishihara, Takashi Yoshinaga, Osamu Takenaka, Ming-Rong Zhang, Tetsuya Suhara, *PLOS ONE*, 8(9), e75040, 2013.
76. Synthesis and evaluation of novel radioligands for positron emission tomography imaging of the orexin-2 receptor. Norihito Oi, Michiyuki Suzuki, Taro Terauchi, Masaki Tokunaga, Yosuke Nakatani, Noboru Yamamoto, Toshimitsu Fukumura, Ming-Rong Zhang, Tetsuya Suhara, Makoto Higuchi, *Journal of Medicinal Chemistry*, 56(16), 6371 - 6385, 2013.
77. Apathy correlates with prefrontal amyloid β deposition in Alzheimer's disease. Takaaki Mori, Hitoshi Shimada, Hitoshi Shinoto, Sigeki Hirano, Yoko Eguchi, Makiko Yamada, Ming-Rong Zhang, Tetsuya Suhara, *Journal of Neurology, Neurosurgery, and Psychiatry*, 85(4), 449 - 455, 2013.
78. Total body 100-mGy X-irradiation does not induce Alzheimer's disease-like pathogenesis or memory impairment in mice. Bing Wang, Kaoru Tanaka, Bin Ji, Maiko Ono, Yaqun Fang, Yasuharu Ninomiya, Kouichi Maruyama, Nakako Izumi-Nakajima, Nasrin Begum, Makoto Higuchi, Akira Fujimori, Yoshihiko Uehara, Tetsuo Nakajima, Tetsuya Suhara, Tetsuya Ono, Mitsuru Neno, *Journal of Radiation Research*, 55(1), 84 - 96, 2014.
79. Nitric oxide signaling exerts bidirectional effects on plasticity inductions in amygdala. Ryong-Moon Shin, Makoto Higuchi, Tetsuya Suhara, *PLOS ONE*, 8(9), e74668, 2013.
80. Global brain delivery of neprilysin gene by intravascular administration of AAV vector in mice. Nobuhisa Iwata, Misaki Sekiguchi, Yoshino Hattori, Akane Takahashi, Masashi Asai, Bin Ji, Makoto Higuchi, Matthias Staufenbiel, Shin-ichi Muramatsu, Takaomi C. Saïdo, *Scientific Reports*, 3, 1472, 2013.
81. Changing the mind? Not really--activity and connectivity in the caudate correlates with changes of choice. Takehito Ito, et al., *Social Cognitive and Affective Neurosci.*, 2013.
82. Sex-specific effects of a high fat diet on indices of metabolic syndrome in 3xTgAD mice: Implications for Alzheimer's disease. Anna Barron, et al., *PLOS ONE* (Online only:URL:<http://www.plosone.org>), 8(10), e78554, 2013.
83. Ligand for translocator protein reverses pathology in a mouse model of Alzheimer's disease. Anna Barron, et al., *Journal of Neuroscience*, 33(20), 8891 - 8897, 2013.
84. In vivo evaluation of cellular activity in α CaMKII heterozygous knockout mice using manganese-enhanced magnetic resonance imaging (MEMRI). Satoko Hattori, Hideo Hagihara, Koji Ohira, Ichio Aoki, Tsuneo Saga, Tetsuya Suhara, Makoto Higuchi, Tsuyoshi Miyakawa, *Frontiers in Integrative Neuroscience*, 7, 76, 2013.
85. Imaging of tau pathology in a tauopathy mouse model and in Alzheimer patients compared to normal controls. Masahiro Maruyama, Hitoshi Shimada, Tetsuya Suhara, Hitoshi Shinoto, Bin Ji, Jun Maeda, Ming-Rong Zhang, John Q Trojanowski, Virginia M-Y Lee, Maiko Ono, Kazuto Masamoto, Harumasa Takano, Naruhiko Sahara, Nobuhisa Iwata, Nobuyuki Okamura, Shozo Furumoto, Yukitsuka Kudo, Qing Chang, Takaomi C Saïdo, Akihiko Takashima, Jada Lewis, Ming-Kuei Jang, Ichio Aoki, Hiroshi Ito, Makoto Higuchi, *Neuron*, 79(6), 1094 - 1108, 2013.
86. Effects of menopause on brain structural changes in schizophrenia. Hajime Fukuta, Itsuo Ito, Amane Tateno, Tsuyoshi Nogami, Yasutomo Taiji, Ryosuke Arakawa, Tetsuya Suhara, Kunihiko Asai, Yoshiro Okubo, *Psychiatry and Clinical Neurosciences*, 67(1), 3 - 11, 2013.

87. Deficiency of schnurri-2, an MHC enhancer binding protein, induces mild chronic inflammation in the brain and confers molecular, neuronal, and behavioral phenotypes related to schizophrenia. Keizo Takao, Katsunori Kobayashi, Hideo Hagihara, Koji Ohira, Hirotaka Shoji, Satoko Hattori, Hisatsugu Koshimizu, Juzoh Umemori, Keiko Toyama, Hironori K Nakamura, Mahomi Kuroiwa, Jun Maeda, Kimie Atsuzawa, Kayoko Esaki, Shun Yamaguchi, Shigeki Furuya, Tsuyoshi Takagi, Noah M Walton, Nobuhiro Hayashi, Hidenori Suzuki, Makoto Higuchi, Nobuteru Usuda, Tetsuya Suhara, Akinori Nishi, Mitsuyuki Matsumoto, Shunsuke Ishii, Tsuyoshi Miyakawa, *Neuropsychopharmacology*, 38(8), 1409 - 1425, 2013.
 88. Biodistribution and radiation dosimetry in humans of [¹¹C]FLB 457, a positron emission tomography ligand for the extrastriatal dopamine D₂ receptor. Yasuyuki Kimura, Hiroshi Ito, Takahiro Shiraishi, Hironobu Fujiwara, Fumitoshi Kodaka, Harumasa Takano, Hitoshi Shimada, Iwao Kanno, Tetsuya Suhara, *Nuclear Medicine and Biology*, 41(1), 102 - 105, 2014.
 89. Loss of branched O-mannosyl glycans in astrocytes accelerates remyelination. Kenji Kanekiyo, Kei-ichiro Inamori, Shinobu Kitazume, Keiko Sato, Jun Maeda, Makoto Higuchi, Yasuhiko Kizuka, Hiroaki Korekane, Ichiro Matsuo, Koichi Honke, Naoyuki Taniguchi, *The Journal of Neuroscience*, 33(24), 10037 - 10047, 2013.
 90. Superiority illusion arises from resting-state brain networks modulated by dopamine. Makiko Yamada, Hidehiko Takahashi, Makoto Higuchi, Tetsuya Suhara, Harumasa Takano, Ririko Kousa, Yasuyuki Kimura, Youko Ikoma, Yoko Eguchi, Keisuke Takahata, Hiroshi Ito, et al., *Proceedings of the National Academy of Sciences of the United States of America*, 110(11), 4363 - 4367, 2013.
- Research on Radiation Protection**
1. Evaluation of Zinc (II) chelators for inhibiting p53-mediated apoptosis. Akinori Morita, Shinya Ariyasu, Soichiro Ohya, Ippei Takahashi, Bing Wang, Kaoru Tanaka, Takatoshi Uchida, Haruna Okazaki, Kengo Hanaya, Atsushi, Enomoto, Mitsuru Neno, Masahiko Ikekita, Shin Aoki, *Oncotarget*, 4(12), 2439 - 2450, 2013.
 2. Fetal irradiation of rats induces persistent translocations in mammary epithelial cells similar to the level after adult irradiation, but not in hematopoietic cells. Minako Nakako, Mayumi Nishimura, Kenya Hamasaki, Shuji Mishima, Mitsuki Yoshida, Akifumi Nakata, Yoshiya Shimada, Asao Noda, Nori Nakamura, Yoshiaki Kodama, *Radiation Research*, 181, 172 - 176, 2014.
 3. World's first telepathology experiments employing WINDS ultra-high-speed internet satellite, nicknamed "KIZUNA". Takashi Sawai, Miwa Uzuki, Yasuhiro Miura, Akihisa Kamataki, Tsubasa Matsumura, Kenji Saito, Akira Kurose, Yoshiyuki R Osamura, Naoki Yoshimi, Hiroyuki Kanno, Takuya Moriya, Yoji Ishida, Yohichi Satoh, Masahiro Nakao, Emiko Ogawa, Satoshi Matsuo, Hiroyuki Kasai, Kazuhiro Kumagai, Toshihiro Motoda, Nathan Hopson, *Journal of Pathology Informatics*, 4, 24, 2013.
 4. Old but new methods in radiation oncology: hyperbaric oxygen therapy. Kazuhiko Ogawa, Kiyotaka Kohshi, Syogo Ishiuchi, Masayuki Matsushita, Naoki Yoshimi, Sadayuki Murayama, *International Journal of Clinical Oncology*, 18(3), 364 - 370, 2013.
 5. Age dependence of hematopoietic progenitor survival and chemokine family gene induction after gamma-irradiation in bone marrow tissue in C3H/He mice. Kentaro Ariyoshi, Takashi Takabatake, Mayumi Shinagawa, Kyoko Kadono, Kazuhiro Daino, Tatsuhiko Imaoka, Shizuko Kakinuma, Mayumi Nishimura, Yoshiya Shimada, *Radiation Research*, 181(3), 302 - 313, 2014.
 6. Molecular characterization of cancer reveals interactions between ionizing radiation and chemicals on rat mammary carcinogenesis. Tatsuhiko Imaoka, Mayumi Nishimura, Kazutaka Doi, Shusuke Tani, Ken-ichi Ishikawa, Satoshi Yamashita, Toshikazu Ushijima, Takashi Imai, Yoshiya Shimada, *International Journal of Cancer*, 134(7), 1529 - 1538, 2014.
 7. Loss of the BRCA1-interacting helicase BRIP1 results in abnormal mammary acinar morphogenesis. Kazuhiro Daino, Tatsuhiko Imaoka, Takamitsu Morioka, Shusuke Tani, Daisuke Iizuka, Mayumi Nishimura, Yoshiya Shimada, *PLOS ONE* (Online only:URL:http://www.plosone.org), 8(9), e74013, 2013.
 8. Childhood exposure to ionizing radiation and brain tumors. Tsuruoka Chizuru, Kakinuma Shizuko, Shimada Yoshiya, Hoshase Seibutsu Kenkyu, 48(2), 123 - 136, 2013.
 9. Uranium dynamics and developmental sensitivity in rat kidney Shino Homma-Takeda, Toshiaki Kokubo, Yasuko Terada, Kyoko Suzuki, Shunji Ueno, Tatsuo Hayao, Tatsuya Inoue, Keisuke Kitahara, Benjamin Blyth, Mayumi Nishimura, Yoshiya Shimada, *Journal of Applied Toxicology*, 33(7), 685 - 694, 2013.
 10. Cancer prevention by adult-onset calorie restriction after infant exposure to ionizing radiation in B6C3F1 male mice. Yi Shang, Shizuko Kakinuma, Kazumi Yamauchi, Takamitsu Morioka, Shusuke Tani, Takashi Takabatake, Yasushi Kataoka, Yoshiya Shimada, *International Journal of Cancer*, 135(5), 1038 - 1047, 2014.
 11. The C-terminal region of Rad52 is essential for Rad52 nuclear and nucleolar localization, and accumulation at DNA damage sites immediately after irradiation. Manabu Koike, Yasutomo Yutoku, Aki Koike, *Biochemical and Biophysical Research Communications*, 435(2), 260 - 266, 2013.
 12. Impact of Amino Acid Substitutions in Two Functional Domains of Ku80: DNA-Damage-Sensing Ability of Ku80 and Survival after Irradiation. Manabu Koike, Yasutomo Yutoku, Aki Koike, *Journal of Veterinary Medical Science*, 76(1), 51 - 56, 2013.
 13. Radiation-Sensitising Effects of Antennapedia Proteins (ANTP)-SmacN7 on Tumour Cells. Li Qing Du, Yan Wang, Chang Xu, Jia Cao, Qin Wang, Hui Zhao, Fei-Yue Fan, Bing Wang, Takanori Katsube, Sai Jun Fan, Qiang Liu, *International Journal of Molecular Sciences*, 14(12), 24087 - 24096, 2013.
 14. Low-dose total body carbon-ion irradiations induce early transcriptional alteration without late Alzheimer's disease-like pathogenesis and memory impairment in mice. Wang Bing, Kaoru Tanaka, Bin Ji, Maiko Ono, Yagun Hou, Yasuharu Ninomiya, Kouichi Maruyama, Nakako Izumi-Nakajima, Nasrin Begum, Makoto Higuchi, Akira Fujimori, Yoshihiko Uehara, Tetsuo Nakajima, Tetsuya Suhara, Mitsuru Neno, *Journal of Neuroscience Research*, (92), 915 - 926, 2014.
 15. ROS Stress Resets Circadian Clocks to Coordinate Pro-Survival Signals. Teruya Tamaru, Yasuharu Ninomiya, Mitsuru Hattori, Guillaume Varès, Genki Kawamura, Kousuke Honda,

- Durga Prasad Mishra, Bing Wang, Ivor Benjamin, Paolo Sassone-Corsi, Takeaki Ozawa, Ken Takamatsu, PLOS ONE, 8(12), e82006 - e82006, 2013.
16. Generation of breast cancer stem cells by steroid hormones in irradiated human mammary cell lines. Guillaume Vares, Xing Cui, Bing Wang, Tetsuo Nakajima, Mitsuru Neno, PLOS ONE, 8(10), e77124, 2013.
 17. Evaluation of the Comet Assay for Assessing the Dose-Response Relationship of DNA Damage Induced by Ionizing Radiation. Yan Wang, Chang Xu, Li Qing Du, Jia Cao, Jian Xiang Liu, Xu Su, Hui Zhao, Fei-Yue Fan, Bing Wang, Takanori Katube, Sai Jun Fan, Qiang Liu, International Journal of Molecular Sciences, 14(11), 22449 - 22461, 2013.
 18. DNA-PKcs Inhibition Sensitizes Cancer Cells to Carbon-Ion Irradiation via Telomere Capping Disruption. Xin Zhou, Xin Zhang, Yi Xie, Kaoru Tanaka, Wang Bing, Zhang Hong, PLOS ONE (Online only:URL:http://www.plosone.org), 8(8), e72641 - e72641, 2013.
 19. In situ comparison of passive radon-thoron discriminative monitors at subsurface workplaces in Hungary (Invited article). Kavasi Norbert, Tamás Vigh, Csaba Németh, Tetsuo Ishikawa, Yasutaka Omori, Mirosław Janik, Hidenori Yonehara, Review of Scientific Instruments, 85(2), 022002 - 14, 2014.
 20. Radon and thoron intercomparison experiments for integrated monitors at NIRS, Japan (Invited article). Mirosław Janik, Yasutaka Omori, Tetsuo Ishikawa, Kavasi Norbert, Review of Scientific Instruments, 85(2), 022001-01 - 22, 2014.
 21. Natural Radionuclide Analysis in Chatrapur Area of South-eastern Coastal Area of Odisha, India. Bhagwat S. Rautela, Gurupaf S Gusian, Manjulata Yadav, Sarata K Sahoo, Shinji Tokonami, Rakesh C Ramola, Acta Geophysica, 61(4), 1038 - 1045, 2013.
 22. Simultaneous sampling of indoor and outdoor airborne radioactivity after the Fukushima Daiichi Nuclear Power Plant accident. Tetsuo Ishikawa, Atsuyuki Sorimachi, Hideki Arae, Sarata Kumar Sahoo, Mirosław Janik, Masahiro Hosoda, Shinji Tokonami, Environmental Science and Technology, 48(4), 2430 - 2435, 2014.
 23. A branching process model for the analysis of abortive colony size distributions in carbon ion-irradiated normal human fibroblasts. Tetsuya Sakashita, Nobuyuki Hamada, Isao Kawaguchi, et al., Journal of Radiation Research, 55(3), 423 - 431 2014.
 24. A GIS-based evaluation of the effect of decontamination on effective doses due to long-term external exposures in Fukushima. Tetsuo Yasutaka, Yumi Iwasaki, Shizuka Hashimoto, Wataru Naito, Kyoko Ono, Atsuo Kishimoto, Kikuo Yoshida, Michio Murakami, Isao Kawaguchi, Toshihiro Oka, Chemosphere, 93(6), 1222 - 1229, 2013.
 25. A framework for analysis of abortive colony size distributions using a model of branching processes in irradiated normal human fibroblasts. Tetsuya Sakashita, Nobuyuki Hamada, Isao Kawaguchi, et al., PLOS ONE, 8(7), 1, 2013.
 26. Measurements of radon and thoron concentrations in high radiation background area using pin-hole dosimeter. R.C. Ramola, B.S. Rautela, G.S. Gusain, Ganesh Prasad, S.K. Sahoo, S. Tokonami, Sahoo Sarata Kumar, Radiation Measurements, 53-54, 71 - 73, 2013.
 27. Radon concentration of outdoor air: measured by an ionization chamber for radioisotope monitoring system at radioisotope institute. Yukari Tajika, Yumi Yasuoka, Hiroyuki Nagahama, Toshiyuki Suzuki, Yoshimi Homma, Tetsuo Ishikawa, Shinji Tokonami, Takahiro Mukai, Mirosław Janik, Atsuyuki Sorimachi, Masahiro Hosoda, et al., Journal of Radioanalytical and Nuclear Chemistry, 295(3), 1709 - 1714, 2013.
 28. Comparative analysis of radon, thoron and thoron progeny concentration measurements. Mirosław Janik, Shinji Tokonami, Chutima Kranrod, Atsuyuki Sorimachi, Tetsuo Ishikawa, Masahiro Hosoda, James McLaughlin, Byung-Uck Chang, Yong Jae Kim, Journal of Radiation Research, 54(4), 597 - 610, 2013.
 29. A simplified method for improved determination of radon concentration in environmental water samples. Risa Tanaka, Saori Araki, Yumi Yasuoka, Takahiro Mukai, Syoko Onuma, Tetsuo Ishikawa, Nobutoshi Fukuhori, Tetsuya Sanada, Radioisotopes, 62(7), 423 - 438, 2013.
 30. Determination of Radon Concentration in Air Using a Liquid Scintillation Counter and an Activated Charcoal Detector. Yasunori Mori, Sho Murata, Hideki Yoshimura, Akira Maeda, Yoko Sawada, Kyoko Shimura, Tetsuo Yamaguchi, Yukari Tajika, Tetsuo Ishikawa, Yumi Yasuoka, Journal of Hot Spring Sciences, 62(4), 306 - 317, 2013.
 31. Occupational exposure to Austrian rocks used as radon spa sources in Japan. Kazuki Iwaoka, Hiroyuki Tabe, Tetsuo Ishikawa, Shinji Tokonami, Hidenori Yonehara, Radiation Emergency Medicine, 2(1), 23 - 26, 2013.
 32. Activity concentration of natural radionuclides and radon and thoron exhalation rates in rocks used as decorative wall coverings in Japan. Kazuki Iwaoka, Masahiro Hosoda, Hiroyuki Tabe, Tetsuo Ishikawa, Shinji Tokonami, Hidenori Yonehara, Health Physics, 104(1), 41 - 50, 2013.
 33. Occupational exposure to natural radiation in zirconium refractory plants in Japan. Kazuki Iwaoka, Hiroyuki Tabe, Tosi-kazu Suzuki, Hidenori Yonehara, Health Physics, 104(2), 151 - 157, 2013.
 34. Biological proliferation of cesium-137 through the detrital food chain in a forest ecosystem in Japan. Masashi Murakami, Nobuhito Ohte, Takahiro Suzuki, Nobuyoshi Ishii, Yoshiaki Igarashi, Keitaro Tanoi, Scientific Reports, 4, 3599, 2014.
- **Research on Radiation Emergency Medicine**
1. Two cases of metastatic parathyroid carcinoma in male C3H mice following irradiation. Yasushi Ohmachi, Midori Yoshida, Toshiaki Ogiu, Journal of Toxicologic Pathology, 26(4), 413 - 417, 2013.
 2. Rapid estimation of inhaled particle size for internal dose during nuclear emergency medicine. Kumiko Fukutsu, Yuji Yamada, Health Physics, 105(6), 555 - 560, 2013.
 3. Histopathological Studies on Cases of Chronic Mouse Hepatitis by Natural Helicobacter. Infections Chunja Nam, Yasushi Ohmachi, Toshiaki Kokubo, et al., Journal of Veterinary Medical Science, 75(9), 1231 - 1235, 2013.
 4. Clinical Impact of Radiation-Resistant Mesenchymal Stem Cells in Bone Marrow Deduced from Preclinical Studies. Yuichi Michikawa, Masaharu Hazawa, Ai Saotome, Takeshi Yasuda, Takaya Gotoh, Katsushi Tajima, Journal of Bone Marrow Research (Online Only URL:http://www.esciencecentral.org/journals/bone-marrow-research.php), 1, 101, 2013.
 5. Biodosimetry of restoration workers for Tokyo Electric Power

Company (TEPCO) Fukushima Daiichi Nuclear Power Station accident. Yumiko Suto, Momoki Hirai, Miho Akiyama, Gen Kobashi, Masanari Itokawa, Makoto Akashi, Nobuyuki Sugiura, Health Physics, 105(4), 366 - 373, 2013.

6. A modified protocol for accurate detection of cell fusion-mediated premature chromosome condensation in human peripheral blood lymphocytes. Yumiko Suto, Miho Akiyama, Takaya Gotoh, Momoki Hirai, Cytologia: International Journal of Cytology, 78(1), 97 - 103, 2013.

■ Development of Fundamental Technologies in Radiological Science

1. Two-step differentiation of mast cells from induced pluripotent stem cells. Tomoko Yamaguchi, Katsuhisa Tashiro, Satoshi Tanaka, Sumie Katayama, Waka Ishida, Ken Fukuda, Atsuki Fukushima, Ryoko Araki, Masumi Abe, Hiroyuki Mizuguchi, Kenji Kawabata, Stem Cells and Development, 22(5), 726 - 734, 2013.
2. Comprehensive gene expression analyses in pluripotent stem cells of a planarian, *Dugesia japonica*. Norito Shibata, Tetsutaro Hayashi, Ryutarō Fukumura, Junsuke Fujii, Tomomi Kudome-Takamatsu, Osamu Nishimura, Syozo Sano, Fuyan Son, Nobuko Suzuki, Ryoko Araki, Masumi Abe, Kiyokazu Agata, The International Journal of Developmental Biology, 56(1-3), 93 - 102, 2012.
3. A simultaneous space sampling method for DNA fraction collection using a comb structure in microfluidic devices. Zheyu Li, Kai Sun, Misato Sunayama, Ryoko Araki, Kosei Ueno, Masumi Abe, Hiroaki Misawa, Electrophoresis, 32(23), 3392 - 3398, 2011.
4. Induced Pluripotent Stem Cell Generation-Associated Point Mutations Arise during the Initial Stages of the Conversion of These Cells. Mayumi Sugiura, Yasuji Kasama, Ryoko Araki, Yuko Hoki, Misato Sunayama, Miki Nakamura, Shunsuke Ando, Masumi Abe, Stem Cell Reports, 2(1), 52 - 63, 2014.
5. The promoter of the oocyte-specific gene, *oog1*, functions in both male and female meiotic germ cells in transgenic mice. Miya Ishida, Eriko Okazaki, Satoshi Tsukamoto, Koji Kimura, Akira Aizawa, Seiji Kito, Hiroshi Imai, Naojiro Minami, PLOS ONE, 8: (7), e68686, 2013.
6. Correlations of the Arrival Directions of Ultra-high Energy Cosmic Rays with Extragalactic Objects as Observed by the Telescope Array Experiment. T. Abu-Zayyad, R. Aida, M. Allen, Y. Uchihori, et al., Astrophysical Journal, 777(2), 88, 2013.
7. The Cosmic-Ray Energy Spectrum Observed with the Surface Detector of the Telescope Array Experiment. T. Abu-Zayyad, R. Aida, M. Allen, Y. Uchihori, et al., Astrophysical Journal Letters, 768(1), 1, 2013.
8. The energy spectrum of ultra-high-energy cosmic rays measured by the Telescope Array FADC fluorescence detectors in monocular mode. T. Abu-Zayyad, R. Aida, M. Allen, Y. Uchihori, et al., Astroparticle Physics, 48, 16 - 24, 2013.
9. An evaluation of the exposure in nadir observation of the JEM-EUSO mission. J.H. Adams Jr., S. Ahmad, J. Albert, Y. Uchihori, et al., Astroparticle Physics, 44, 76 - 90, 2013.
10. New air fluorescence detectors employed in the Telescope Array experiment. H. Tokuno, Y. Tameda, Y. Uchihori, et al., Nuclear Instruments and Methods in Physics Research Section A, 676, 54 - 65, 2012.
11. The surface detector array of the Telescope Array experiment. T. Abu-Zayyad, T. Nonaka, Y. Uchihori, et al., Nuclear Instruments and Methods in Physics Research Section A, 689, 87 - 97, 2013.
12. Output characteristics of piezoelectric lead zirconate titanate detector using high-energy heavy-ion beam. Seiji Takechi, Masahiro Sekiguchi, Takashi Miyachi, Masanori Kobayashi, Maki Hattori, Osamu Okudaira, Hiromi Shibata, Masayuki Fujii, Nagaya Okada, Takeshi Murakami, Yukio Uchihori, Nuclear Instruments and Methods in Physics Research Section A, 737, 52 - 55, 2014.
13. Basic performance of a position-sensitive tissue-equivalent proportional chamber (PS-TEPC). Yuji Kishimoto, Shinichi Sasaki, Kiwamu Saito, Kazutoshi Takahashi, Tadayoshi Doke, Kentaro Miuchi, Tetsuhito Fuse, Aiko Nagamatsu, Yukio Uchihori, Hisashi Kitamura, Kazuhiro Terasawa, Nuclear Instruments and Methods in Physics Research Section A, 732, 591 - 594, 2013.
14. Radiation counting characteristics on surface-modified polyethylene naphthalate scintillators. Yoshiyuki Shirakawa, Hidehito Nakamura, Takashi Kamata, Katsunori Watai, et al., Radioisotopes, 62(12), 879 - 884, 2013.
15. Measurement of dose equivalent distribution on-board commercial jet aircraft. J. Kubančák, I. Ambrožová, O. Ploc, K. Pachnerová Brabcová, V. Štěpán, Y. Uchihori, Radiation Protection Dosimetry, 157(4), 1 - 5, 2013.
16. Blended polyethylene terephthalate and polyethylene naphthalate polymers for scintillation base substrates. Hidehito Nakamura, Yoshiyuki Shirakawa, Hisashi Kitamura, Tatsuya Yamada, Zenichiro Shidara, Takayuki Yokozuka, Philip Nguyen, Tomoyuki Takahashi, Sentaro Takahashi, Radiation Measurements, 59, 172 - 175, 2013.
17. Light propagation characteristics of high-purity polystyrene. Hidehito Nakamura, Yoshiyuki Shirakawa, Hisashi Kitamura, Nobuhiro Sato, Osamu Shinji, Katashi Saito, Sentaro Takahashi, Applied Physics Letters, 103(16), 16111-1 - 16111-4, 2013.
18. Radiation effects on the silicon semiconductor detectors for the ASTRO-H mission. Katsuhiro Hayashi, In-Chun Park, Kyohei Dotsu, Issei Ueno, Sho Nishino, Masayuki Matsuoka, Hajimu Yasuda, Yasushi Fukazawa, Takashi Ohsugi, Tsunefumi Mizuno, Hiromitsu Takahashi, Masanori Ohno, Satoru Endo, Takaaki Tanaka, Hiroyasu Tajima, Motohide Kokubun, Shin Watanabe, Tadayuki Takahashi, Kazuhiro Nakazawa, Yukio Uchihori, Hisashi Kitamura, Nuclear Instruments and Methods in Physics Research Section A, 699, 225 - 229, 2013.
19. Single event effect characterization of the mixed-signal ASIC developed for CCD camera in space use. Hiroshi Nakajima, Mari Fujikawa, Hideki Mori, Hiroaki Kan, Shutaro Ueda, Hiroko Kosugi, Naohisa Anabuki, Kiyoshi Hayashida, Hiroshi Tsunemi, John P. Doty, Hirokazu Ikeda, Hisashi Kitamura, Yukio Uchihori, Nuclear Instruments and Methods in Physics Research Section A, 731, 166 - 171, 2013.
20. Enhancement of critical current density and vortex activation energy in proton-irradiated Co-doped BaFe₂As₂. Toshihiro Taen, Yasuyuki Nakajima, Tsuyoshi Tamegai, Hisashi Kitamura, Physical Review B, 86(9), 094527-1 - 094527-5, 2013.
21. Fragmentation ⁵⁶Fe on C, Al and CH₂ targets at 471 A MeV. Dong-Hai Zhang, Li-Chun Wang, Yan-Jing Li, Jun-Sheng Li, S. Kodaira, N. Yasuda, Nuclear Instruments and Methods in

- Physics Research Section B, 315, 99 - 104, 2013.
22. Detection of Radiation Tracks Recorded on Silver-Salt Photographic Materials by Fluorescence-Labeling Method. Ken'ichi Kuge, Ryouhei Inoue, Yasushi Oishi, Nakahiro Yasuda, Satoshi Kodaira, Osamu Sato, Japanese Journal of Applied Physics, 52, 106402, 2013.
 23. Vacuum effects on the radiation chemical yields in PADC films exposed to gamma rays and heavy ions. Yutaka Mori, Tomoya Yamauchi, Masato Kanasaki, Atsuto Hattori, Keiji Oda, Satoshi Kodaira, Teruaki Konishi, Nakahiro Yasuda, Sachiko Tojo, Yoshihide Honda, Rémi Barillon, Radiation Measurements, 50, 97 - 102, 2013.
 24. Projectile fragmentation of 471 A MeV ⁵⁶Fe in polyethylene, carbon and aluminum targets. Dong-Hai Zhang, Li-Chun Wang, Yan-Jing Li, S. Kodaira, N. Yasuda, Radiation Measurements, 50, 56 - 60, 2013.
 25. Projectile fragment emission angles in fragmentation reactions of light heavy ions in the energy region < 200 MeV/nucleon: Experimental study. L. Sihver, M. Giacomelli, S. Ota, J. Skvarc, N. Yasuda, R. Illic, S. Kodaira, Radiation Measurements, 48, 73 - 81, 2013.
 26. Projectile fragmentation of 388 A MeV ²⁰Ne in polyethylene, carbon and aluminum targets. Dong-Hai Zhang, Jin-Xia Cheng, S. Kodaira, N. Yasuda, Nuclear Instruments and Methods in Physics Research Section B, 286, 238 - 242, 2013.
 27. Fragmentation cross section of ⁵⁶Fe at 471 A MeV on Al, C and CH₂ targets. Li-Chun Wang, Dong-Hai Zhang, Shiwei Yan, Yan-Jing Li, Jin-Xia Cheng, Jun-Sheng Li, S. Kodaira, N. Yasuda, Acta Physica Polonica B, 43(8), 1769 - 1782, 2012.
 28. The role of autophagy in early mammalian embryonic development. Satoshi Tsukamoto, et al., Journal of Mammalian Ova Research, 30(3), 86 - 94, 2013.
 29. Measurement of the Deposited Energy of Tracks of High-Energy Particles. H. Kubota, K. Kuge, N. Yasuda, S. Kodaira, T. Toshito, M. Nakamura, J. Soc. Photogr. Imag. Japan, 75(4), 334 - 339, 2012.
 30. Optimized mounting of a polyethylene naphthalate scintillation material in a radiation detector. Hidehito Nakamura, Tatsuya Yamada, Yoshiyuki Shirakawa, Hisashi Kitamura, Zenichiro Shidara, Takayuki Yokozuka, Philip Nguyen, Masaya Kanayama, Sentaro Takahashi, Applied Radiation and Isotopes, 80, 84 - 87, 2013.
 31. Mechanism of wavelength conversion in polystyrene doped with benzoxanthene: emergence of a complex. Hidehito Nakamura, Yoshiyuki Shirakawa, Hisashi Kitamura, Nobuhiro Sato, Osamu Shinji, Katashi Saito, Sentaro Takahashi, Scientific Reports, 3, 2502, 2013.
 32. Effects of particle irradiations on vortex states in iron-based superconductors. Tsuyoshi Tamegai, Toshihiro Taen, Hidenori Yagyuda, Shyam Mohan, Tomotaka Taniguchi, Yasuyuki Nakajima, Satoru Okayasu, Masato Sasase, Hisashi Kitamura, Takeshi Murakami, Tadashi Kambara, Yasuyuki Kanai, Superconductor Science and Technology, 25(8), 084008, 2013.
 33. Bystander Effect between Zebrafish Embryos in Vivo Induced by High-Dose X-rays. V.W.Y. Choi, Candy Y.P. Ng, Alisa Kobayashi, Teruaki Konishi, Noriyoshi Suya, Takahiro Ishikawa, Shuk H. Cheng, K.N. Yu, Environmental Science and Technology, 47(12), 6368 - 6376, 2013.
 34. Investigation of transcriptional responses of juvenile mouse bone marrow to power frequency magnetic fields Investigation of transcriptional responses of juvenile mouse bone marrow to power frequency magnetic fields. Kabacik Sylwia, Kirschenlohr Heide, Masumi Abe, Bouffler Simon, et al., Fundamental and Molecular Mechanisms of Mutagenesis: A Section of Mutation Research, (745-746), 40 - 45, 2013.
 35. Evolutionarily Assembled cis-Regulatory Module at a Human Ciliopathy Locus. Jeong Ho Lee, Jennifer L. Silhavy, Ji Eun Lee, Lihadh Al-Gazali, Sophie Thomas, Erica E. Davis, Stephanie L. Bielas, Kiley J. Hill, Miriam Iannicelli, Francesco Brancati, Stacey B. Gabriel, Carsten Russ, Clare V. Logan, Saghira Malik Sharif, Christopher P. Bennett, Masumi Abe, et al., Science, 335, 966 - 969, 2012.
 36. SPICE-NIRS Microbeam: A Focused Vertical System for Proton Irradiation of a Single Cell for Radiobiological Research. Teruaki Konishi, Masakazu Oikawa, Noriyoshi Suya, Takahiro Ishikawa, Takeshi Maeda, Alisa Kobayashi, Naoko Shiomi, Kumiko Kodama, Tsuyoshi Hamano, Shino Takeda, Mayu Isono, Kotaro Hieda, Yukio Uchihori, Yoshiyuki Shirakawa, Journal of Radiation Research, 54, 736 - 747, 2013.

■ Fukushima Project Headquarters

1. Assessment of Fukushima-Derived Radiation Doses and Effects on Wildlife in Japan. P. Strand, T. Aono, J. E. Brown, J. Garnier-Laplace, A. Hosseini, T. Sazykina, F. Steenhuisen, Environmental Science and Technology Letters, 1(3), 198 - 203, 2014.
2. The possible interplanetary transfer of microbes: assessing the viability of Deinococcus spp. under the ISS environmental conditions for performing exposure experiments of microbes in the Tanpopo mission. Yuko Kawaguchi, Satoshi Yoshida, Kensei Kobayashi, Shin-ichi Yokobori, et al., Origins of Life and Evolution of Biospheres, 43(4-5), 411 - 428, 2013.
3. Effects of radioactive caesium on bull testes after the Fukushima nuclear plant accident. Hideaki Yamashiro, Isao Kawaguchi, Satoshi Yoshida, Manabu Fukumoto, et al., Scientific Reports (Online Only URL: <http://www.nature.com/srep/index.html>), 3(2850), 2013.
4. Rice (*Oryza sativa* L.) roots have iodate reduction activity in response to iodine. Shota Kato, Takanori Wachi, Akifumi Ishikawa, Satoshi Yoshida, Hitoshi Sekimoto, et al., Frontiers in Plant Science (Online Only URL: http://www.frontiersin.org/plant_science), 4(227), 2013.
5. Activity concentrations of environmental samples collected in Fukushima Prefecture immediately after the Fukushima nuclear accident. Masahiro Hosoda, Shinji Tokonami, Hirofumi Tazoe, Atsuyuki Sorimachi, Satoru Monzen, Minoru Osanai, Naofumi Akada, Hideki Kakiuchi, Yasutaka Omori, Tetsuo Ishikawa, Sahoo Sarata Kumar, Tibor Kovacs, Masatoshi Yamada, Akifumi Nakata, Mitsuaki A Yoshida, Hironori Yoshino, Yasushi Mariya, Ikuo Kashiwakura, Scientific Reports (Online Only URL: <http://www.nature.com/srep/index.html>), 3, 2283, 2013.
6. Prediction of the location and size of the stomach using patient characteristics for retrospective radiation dose estimation following radiotherapy. Stephanie Lamart, Rebecca Imran, Steven L Simon, Kazutaka Doi, Lindsay M Morton, Rochelle E Curtis, Choonik Lee, Vladimir Drozdovitch, Roberto Maass-Moreno, Clara C Chen, Millie Whatley, Donald L Miller, Karel Pacak, Choonsik Lee, Physics in Medicine and

Biology, 58(24), 8739-8753, 2013.

7. Colon Preneoplastic Lesions in Animal Models. Masumi Suzui, Takamitsu Morioka, Naoki Yoshimi, Journal of Toxicologic Pathology, 26(4), 335 - 341, 2013.
8. Exposure to gamma-rays at the telogen phase of the hair cycle inhibits hair follicle regeneration at the anagen phase in mice. Sugaya Kimihiko, Hirobe Tomohisa, International Journal of Radiation Biology, 90(2), 127 - 132, 2014.
9. Cancer chemoprevention by phytochemicals - Expectation for phytochemicals as preventive agents against radiation-induced carcinogenesis -. Morioka Takamitsu, Kakinuma Shizuko, Nishimura Mayumi, Sunaoshi Masaaki, Shang Yi, Tsuruoka Chizuru, Imaoka Tatsuhiko, Yamada Yutaka, Yoshimi Naoki, Shimada Yoshiya, Hoshasen Seibutsu Kenkyu, 48(2), 164 - 180, 2013.

■ International Open Laboratory

1. AFOMP Policy Statement No. 3: Recommendations for the education and training of medical physicists in AFOMP countries. W. H. Round, K. H. Ng, B. Healy, L. Rodriguez, K. Thayalan, F. Tang, S. Fukuda, et al., AFOMP Policy Statement No. 3: Recommendations for the education and training of medical physicists in AFOMP countries, 34(3), 303 - 307, 2012.
2. AFOMP Policy Statement No. 4: Recommendations for continuing professional development systems for medical physicists in AFOMP countries. W. H. Round, K. H. Ng, B. Healy, L. Rodriguez, K. Thayalan, F. Tang, S. Fukuda, et al., Australasian Physical and Engineering Sciences in Medicine, 35(4), 393 - 397, 2012.
3. Role of LET and chromatin structure on chromosomal inversion in CHO10B2 cells. Ian M Cartwright, Matthew D Genet, Akira Fujimori, Takamitsu A Kato, Genome integrity, 5(1), 1, 2014.
4. Comparative study of radioresistance between feline cells and human cells. Yoshihiro Fujii, Charles R Yurkon, Junko Maeda, Stefan C Genet, Nobuo Kubota, Akira Fujimori, Takashi Mori, Kohji Maruo, Takamitsu A Kato, Radiation Research, 180(1), 70-7, 2013.
5. Comparison of human chordoma cell-kill for 290 MeV/n carbon ions versus 70 MeV protons in vitro. Hiroshi Fujisawa, Paula C Genik, Hisashi Kitamura, Akira Fujimori, Mitsuru Uesaka, Takamitsu A Kato, Radiation Oncology, 8(1), 91, 2013.
6. Comparison of the bromodeoxyuridine-mediated sensitization effects between low-LET and high-LET ionizing radiation on DNA double-strand breaks. Yoshihiro Fujii, Matthew D Genet, Erica J Roybal, Nobuo Kubota, Ryuichi Okayasu, Kiyoshi Miyagawa, Akira Fujimori, Takamitsu A Kato, Oncology Reports, 29(6), 2133 - 2139, 2013.
7. Dose-rate effect was observed in T98G glioma cells following BNCT. Yuko Kinashi, Kakuji Okumura, Yoshihisa Kubota, Erika Kitajima, Ryuichi Okayasu, Koji Ono, Sentaro Takahashi, Applied Radiation and Isotopes, 88, 81 - 85, 2013.
8. Radiosensitization of human lung cancer cells by the novel purine-scaffold Hsp90 inhibitor, PU-H71. Tatsuya Segawa, Yoshihiro Fujii, Aya Tanaka, Shin-Ichi Bando, Ryuichi Okayasu, Ken Ohnishi, Nobuo Kubota, International Journal of Molecular Medicine, 33(3), 559-564, 2013.
9. Including oxygen enhancement ratio in ion beam treatment planning: model implementation and experimental verification. E Scifoni, W Tinganelli, W K Weyrather, M Durante, A

Maier, M Krämer, Physics in Medicine and Biology, 58(11), 3871 - 3895, 2013.

10. Influence of chronic hypoxia and radiation quality on cell survival. Ning-Yi Ma, Walter Tinganelli, Andreas Maier, Marco Durante, Wilma Kraft-Weyrather, Journal of Radiation Research, 54 Suppl 1, i13 - 22, 2013.
11. Influence of acute hypoxia and radiation quality on cell survival. Walter Tinganelli, Ning-Yi Ma, Cläre Von Neubeck, Andreas Maier, Corinna Schicker, Wilma Kraft-Weyrather, Marco Durante, Journal of Radiation Research, 54 Suppl 1, i23 - 30, 2013.
12. Resistance of Bacillus subtilis Spore DNA to Lethal Ionizing Radiation Damage Relies Primarily on Spore Core Components and DNA Repair, with Minor Effects of Oxygen Radical Detoxification. Ralf Moeller, Marina Raguse, Günther Reitz, Ryuichi Okayasu, Zuofeng Li, Stuart Klein, Peter Setlow, Wayne L Nicholson, Applied and Environmental Microbiology, 80(1), 104 - 109, 2014.
13. Interaction between DNA polymerase β and BRCA1. Aya Masaoka, Samuel Wilson, et al., PLOS ONE (Online only:URL: <http://www.plosone.org>), 8(6), e66801, 2013.
14. Parg deficiency confers radio-sensitization through enhanced cell death in mouse ES cells exposed to various forms of ionizing radiation. Hidenori Shirai, Hiroaki Fujimori, Takahisa Hirai, Keisuke Sasai, Ryuichi Okayasu, Mitsuko Masutani, et al., Biochemical and Biophysical Research Communications, 435(1), 100 - 106, 2013.
15. Influence of track directions on the biological consequences in cells irradiated with high LET heavy ions. Yoshihiro Fujii, Yurkon Chuck, Jyunko Maeda, Stefan Genet, Ryuichi Okayasu, Hisashi Kitamura, Akira Fujimori, Takamitsu Kato, International Journal of Radiation Biology, 89(6), 401 - 410, 2013.

■ Other Research Themes

1. Availability of postmortem CT for fatal bleeding attributed to common carotid artery rupture: a case report. Seiji Yamamoto, Hidefumi Ezawa, et al., Japanese Journal of Diagnostic Imaging, 31(2), 124 - 128, 2013.
2. Statistical shape model of a liver for autopsy imaging. Atsushi Saito, Akinobu Shimizu, Hidefumi Watanabe, Seiji Yamamoto, et al., International Journal of Computer Assisted Radiology and Surgery, 9(2), 269 - 281, 2013.
3. Fatty Acid synthase is a key target in multiple essential tumor functions of prostate cancer: uptake of radiolabeled acetate as a predictor of the targeted therapy outcome. Yukie Yoshii, Takako Furukawa, Nobuyuki Oyama, Yoko Hasegawa, Yashushi Kiyono, Ryuichi Nishii, Atsuo Waki, Atsushi Tsuji, Chizuru Sogawa, Hidekatsu Wakizaka, Toshimitsu Fukumura, Hiroshi Yoshii, Yasuhisa Fujibayashi, Tsuneo Saga, et al., PLOS ONE (Online only:URL:<http://www.plosone.org>), 8(5), 2013.
4. X'tal cube PET detector composed of a stack of scintillator plates segmented by laser processing. Naoko Inadama, Takahiro Moriya, Yoshiyuki Hirano, Fumihiko Nishikido, Hideo Murayama, Eiji Yoshida, Hideaki Tashima, Munetaka Nitta, Hiroshi Ito, Taiga Yamaya, IEEE Transactions on Nuclear Science, 61(1), 53 - 59, 2013.
5. Root uptake of ^{137}Cs from sedimentation sludge-amended soils by Komatsuna (*Brassica rapa* var. *perviridis*). Nobuyoshi Ishii, Keiko Tagami, Isao Kawaguchi, Shigeo Uchida, Radioisotopes, 62(7), 447 - 453, 2013.

6. Carbon-11 radiolabeling of an oligopeptide containing tryptophan hydrochloride via a Pictet-Spengler reaction using carbon-11 formaldehyde. Masayuki Hanyu, Yuuki Takada, Hiroki Hashimoto, Kazunori Kawamura, Ming-Rong Zhang, Toshimitsu Fukumura, *Journal of Peptide Science*, 19(10), 663 - 668, 2013.
7. Ultra-trace determination of plutonium in small volume seawater by sector-field inductively coupled plasma mass spectrometry with application to Fukushima seawater samples. Wenting Bu, Jian Zheng, Tatsuo Aono, Keiko Tagami, Shigeo Uchida, et al., *Journal of Chromatography A*, 1337, 171 - 178, 2014.
8. Isotopic composition and distribution of plutonium in northern South China Sea sediments revealed continuous release and transport of Pu from the Marshall Islands. Junwen Wu, Jian Zheng, Keiko Tagami, Shigeo Uchida, et al., *Environmental Science and Technology*, 48, 3136 - 3144, 2014.
9. A method of measurement of ^{239}Pu , ^{240}Pu , ^{241}Pu in high U content marine sediments by sector field ICP-MS and its application to Fukushima sediment samples. Wenting Bu, Jian Zheng, Tatsuo Aono, Keiko Tagami, Shigeo Uchida, et al., *Environmental Science and Technology*, 48(1), 534 - 541, 2014.
10. The key role of atomic spectrometry in radiation protection. Jian Zheng, Keiko Tagami, Shino Homma-Takeda, Wenting Bu, *Journal of Analytical Atomic Spectrometry*, 28(11), 1676 - 1699, 2013.
11. Vertical distributions of plutonium isotopes in marine sediment cores off the Fukushima coast after the Fukushima Daiichi Nuclear Power Plant accident. Wenting Bu, Jian Zheng, Tatsuo Aono, Keiko Tagami, Shigeo Uchida, Jing Zhang, Makio Honda, Qiuju Guo, Masatoshi Yamada, *Biogeosciences*, 10(4), 2497 - 2511, 2013.
12. Anthropogenic Plutonium in the North Jiangsu tidal flats of the Yellow Sea in China. Zhiyong Liu, Jian Zheng, Shaoming Pan, et al., *Environmental Monitoring and Assessment*, 185(8), 6539 - 6551, 2013.
13. Viral protein-coating of magnetic nanoparticles using simian virus 40 VP1. Teruya Enomoto, Yuki Yamaguchi, Mamoru Hatakeyama, Shigeo Saito, Ichio Aoki, Hiroshi Handa, et al., *Journal of Biotechnology*, 167(1), 8 - 15, 2013.
14. Relationship between Serum Reactive Oxidative Metabolite Level and Skin Reaction in an Irradiated Rat Model. Takuma Nomiyama, Takashi Kaneko, Jun Goto, Mayumi Harada, Hiroko Akamatsu, Yasuhito Hagiwara, Ibuki Ota, Kenji Nemoto, *Free Radical Research*, 48(5), 572 - 579, 2014.
15. Hydrothermally synthesized PEGylated calcium phosphate nanoparticles incorporating Gd-DTPA for contrast enhanced MRI diagnosis of solid tumors. Peng Mi, Daisuke Kokuryo, Horacio Cabral, Michiaki Kumagai, Takahiro Nomoto, Ichio Aoki, Yasuko Terada, Akihiro Kishimura, Nobuhiro Nishiyama, Kazunori Kataoka, *Journal of Controlled Release*, 174, 63 - 71, 2014.
16. Neurochemistry in shiverer mouse depicted on MR spectroscopy. Jun-Ichi Takanashi, Nobuhiro Nitta, Nobuaki Iwasaki, Shigeo Saito, Ryuta Tanaka, A James Barkovich, Ichio Aoki, *Journal of Magnetic Resonance Imaging*, 39(6), 1550 - 1557, 2014.
17. MRI-based morphometric characterizations of sexual dimorphism of the cerebrum of ferrets (*Mustela putorius*). Kazuhiko Sawada, Shigeo Saito, Ichio Aoki, et al., *NeuroImage*, 83, 294 - 306, 2013.
18. The simple preparation of polyethylene glycol-based soft nanoparticles containing dual imaging probes. Shuhei Murayama, Jun-ichiro Jo, Liang Kun, Tsuneo Saga, Ichio Aoki, Masaru Kato, et al., *Journal of Materials Chemistry B, Materials for Biology and Medicine*, 1, 4932 - 4938, 2013.
19. Estimation of internal exposure of the thyroid to ^{131}I on the basis of ^{134}Cs accumulated in the body amount evacuees of the Fukushima Daiichi Nuclear Power Station accident. Masahiro Hosoda, Shinji Tokonami, Suminori Akiba, Osamu Kurihara, Atsuyuki Sorimachi, Tetsuo Ishikawa, Takumaro Momose, Takashi Nakano, Yasushi Mariya, *Environment International*, 61, 73 - 76, 2013.
20. NIRS external dose estimation system for Fukushima residents after the Fukushima Dai-ichi NPP accident. Keiichi Akahane, Shunsuke Yonai, Shigekazu Fukuda, Nobuyuki Miyahara, Hiroshi Yasuda, Kazuki Iwaoka, Masaki Matsumoto, Akifumi Fukumura, Makoto Akashi, *Scientific Reports*, 3(1670), 1 - 6, 2014.
21. Naturally occurring radionuclides and rare earth elements in weathered Japanese soil samples. Sahoo Sarata Kumar, Masahiro Hosoda, Prasad Ganesh, Hiroyuki Takahashi, Atsuyuki Sorimachi, Tetsuo Ishikawa, Shinji Tokonami, Shigeo Uchida, *Acta Geophysica*, 61(4), 876 - 885, 2013.
22. Marine and freshwater concentration ratios (CR wo-water): Review of Japanese data. Keiko Tagami, Shigeo Uchida, *Journal of Environmental Radioactivity*, 126, 420 - 426, 2013.
23. Release of plutonium isotopes into the environment from the Fukushima Daiichi Nuclear Power plant accident: what is known and what needs to be known. Jian Zheng, Keiko Tagami, Shigeo Uchida, *Environmental Science and Technology*, 47(17), 9584 - 9595, 2013.
24. Fate of radiocesium in sewage treatment process released by the nuclear accident at Fukushima. Nao Ishikawa, Keiko Tagami, et al., *Chemosphere*, 93(4), 689 - 694, 2013.
25. Ecological half-lives of radiocesium in 16 species in marine biota after the TEPCO's Fukushima Daiichi Nuclear Power Plant accident. Kayoko Iwata, Keiko Tagami, Shigeo Uchida, *Environmental Science and Technology*, 47(14), 7696 - 7703, 2013.
26. Estimation of Te-132 distribution in Fukushima Prefecture at the early stage of the Fukushima Daiichi Nuclear Power Plant reactor failures. Keiko Tagami, Shigeo Uchida, Nobuyoshi Ishii, Jian Zheng, *Environmental Science Technology*, 47(10), 5007 - 5012, 2013.
27. Rapid and sensitive determination of tellurium in soil and plant samples by sector-field inductively coupled plasma mass spectrometry. Guosheng Yang, Jian Zheng, Keiko Tagami, Shigeo Uchida, *Talanta*, 116, 181 - 187, 2013.
28. A sensitive and simple analytical method for the determination of stable Cs in estuarine and coastal waters. Hyoe Takata, Tatsuo Aono, Jian Zheng, Keiko Tagami, Shigeo Uchida, et al., *Analytical Methods*, 5(10), 2558 - 2564, 2013.
29. Distribution coefficients (Kd) of stable iodine in estuarine and coastal regions, Japan, and their relationship to salinity and organic carbon in sediments. Hyoe Takata, Jian Zheng, Keiko Tagami, Tatsuo Aono, Kazuhiro Fujita, Shin-ichi Yamasaki, Shigeo Uchida, et al., *Environmental Monitoring and Assessment*, 185(5), 3645 - 3658, 2013.
30. Functional significance of central D1 receptors in cognition: beyond working memory. Hidehiko Takahashi, Makiko Yamada,

- Tetsuya Suhara, *Journal of Cerebral Blood Flow and Metabolism*, 32(7), 1248 - 58, 2012.
31. Disruption of *Aspm* causes microcephaly with abnormal neuronal differentiation. Akira Fujimori, Kyoko Itoh, Shoko Goto, Hirokazu Hirakawa, Bing Wang, Toshiaki Kokubo, Seiji Kito, Satoshi Tsukamoto, Shinji Fushiki, *Brain and development*, 2013.
 32. Prediction of outcomes in MCI with ¹²³I-IMP-CBF SPECT: a multicenter prospective cohort study Kengo Ito, Etsuo Mori, Hidenao Fukuyama, Kazunari Ishii, Yukihiko Washimi, Takashi Asada, Satoru Mori, Kenichi Meguro, Shin Kitamura, Haruo Hanyu, Seigo Nakano, Hiroshi Matsuda, Yasuo Kuwabara, Kazuo Hashikawa, Toshimitsu Momose, Yoshitaka Uchida, Jun Hatazawa, Satoshi Minoshima, Kenji Kosaka, Tetsuo Yamada, Yoshiharu Yonekura, *Annals of Nuclear Medicine*, (27), 898 - 906, 2013.
 33. Biochemical Distribution of Tau Protein in Synaptosomal Fraction of Transgenic Mice Expressing Human P301L Tau. Naruhiko Sahara, Miyuki Murayama, Makoto Higuchi, Tetsuya Suhara, Akihiko Takashima, *Frontiers in Neurology*, 5(26), 2014.
 34. TOC1: A valuable tool in assessing disease progression in the rTg4510 mouse model of tauopathy. Sarah M Ward, Diana S Himmelstein, Yan Ren, Yifan Fu, Xiao-Wen Yu, Kaleigh Roberts, Lester I Binder, Naruhiko Sahara, *Neurobiology of Disease*, 67, 37 - 48, 2014.
 35. "Tau oligomers," what we know and what we don't know. Naruhiko Sahara, Jesus Avila, *Frontiers in Neurology*, 5(1), 2014.
 36. Tau Oligomers as Potential Targets for Early Diagnosis of Tauopathy. Naruhiko Sahara, Yan Ren, Sarah Ward, Lester I Binder, Tetsuya Suhara, Makoto Higuchi, *Journal of Alzheimer's disease*, 40(S1), S91 - S96, 2014.
 37. Development of radon sources with a high stability and a wide range. Kumiko Fukutsu, Yuji Yamada, *Review of Scientific Instruments*, 84(12), 125110-1 - 125110-5, 2013.
 38. Clinical utility and limitations of FDG PET in detecting recurrent hepatocellular carcinoma in postoperative patients. Nobuyuki Hayakawa, Yuji Nakamoto, Koya Nakatani, Etsuo Hatano, Satoru Seo, Tatsuya Higashi, Tsuneo Saga, Shinji Uemoto, Kaori Togashi, *International Journal of Clinical Oncology*, doi: 10.1007/s10147-013-0653-3.
 39. Age-related decline in white matter integrity in a mouse model of tauopathy: an in vivo diffusion tensor magnetic resonance imaging study. Naruhiko Sahara, Pablo D Perez, Wen-Lang Lin, Dennis W Dickson, Yan Ren, Huadong Zeng, Jada Lewis, Marcelo Febo, *Neurobiology of Aging*, 35(6), 1364 - 1374, 2013.
 40. Status of radiotherapy in a multidisciplinary cancer board. Mayumi Ichikawa, Kenji Nemoto, Misako Miwa, Ibuki Ohta, Takuma Nomiya, Mayumi Yamakawa, Yuriko Itho, Tadahisa Fukui, Takashi Yoshioka, *Journal of Radiation Research*, 55 (2), 305 - 308, 2013.
 41. Primary CNS lymphoma treated with radiotherapy in Japan: a survey of patients treated in 2005-2009 and a comparison with those treated in 1985-2004. Yuta Shibamoto, Minako Sumi, Shunsuke Onodera, Haruo Matsushita, Chikao Sugie, Yukihisa Tamaki, Hiroshi Onishi, Eisuke Abe, Masahiko Koizumi, Daisuke Miyawaki, Seiji Kubota, Etsuyo Ogo, Takuma Nomiya, Mitsuhiro Takemoto, Hideyuki Harada, Ippei Takahashi, Yoshio Ohmori, Naoya Ishibashi, Sunao Tokumaru, Kazunori Suzuki, *International Journal of Clinical Oncology*, doi: 10.1007/s10147-013-0644-4.
 42. Momentum dependence of spin polarization for beta emitting nuclei produced through charge exchange reaction at intermediate energy. S. Momota, M. Mihara, D. Nishimura, M. Fukuda, Y. Kamisho, M. Wakabayashi, K. Matsuta, S. Suzuki, M. Nagashima, Shengyun Zhu, Daqing Yuan, Yongnan Zheng, Zuo Yi, Ping Fan, T. Izumikawa, A. Kitagawa, S. Sato, M. Kanazawa, M. Torikoshi, T. Minamisono, Y. Nakamura, K. Tashiro, A. Honma, N. Yoshida, H. Shirai, T. Ohtsubo, T. Nagatomo, H. Uenishi, K. Iwamoto, M. Yaguchi, T. Ogura, T. Ito, K. Yamamura, Y. Ichikawa, Y. Nojiri, J. R. Alonso, T. J. M. Symons, *Hyperfine Interactions*, 220(1-3), 53 - 58, 2013.
 43. Production of spin polarized ¹²N through heavy ion reactions. M. Mihara, K. Matsuta, D. Nishimura, M. Fukuda, M. Yaguchi, K. Iwamoto, M. Wakabayashi, Y. Kamisho, J. Ohno, Y. Morita, T. Izumikawa, T. Ohtsubo, S. Suzuki, M. Nagashima, K. Abe, T. Sakai, S. Momota, A. Ozawa, D. Nagae, Y. Ishibashi, Y. Abe, T. Niwa, T. Nagatomo, T. Minamisono, M. Kubo, A. Kitagawa, M. Torikoshi, M. Kanazawa, S. Sato, *Hyperfine Interactions*, 220(1-3), 83 - 88, 2013.
 44. Effects of the C57BL/6 strain background on tauopathy progression in the rTg4510 mouse model. Rachel M Bailey, John Howard, Joshua Knight, Naruhiko Sahara, Dennis W Dickson, Jada Lewis, *Molecular Neurodegeneration*, 9(1), 8, 2014.
 45. Lunar farside Th distribution measured by Kaguya gamma-ray spectrometer. S. Kobayashi, Y. Karouji, T. Morota, H. Takeda, N. Hasebe, M. Hareyama, M. Kobayashi, E. Shibamura, N. Yamashita, C. d'Uston, O. Gasnault, O. Forni, R.C. Reedy, K.J. Kim, *Earth and Planetary Science Letters*, 337 - 338, 10 - 16, 2012.
 46. The global distribution of calcium on the Moon: Implications for high-Ca pyroxene in the eastern mare region. N. Yamashita, O. Gasnault, O. Forni, C. d'Uston, R.C. Reedy, Y. Karouji, S. Kobayashi, M. Hareyama, H. Nagaoka, N. Hasebe, K.J. Kim, *Earth and Planetary Science Letters*, 353 - 354, 93 - 98, 2012.
 47. The South Pole-Aitken basin region, Moon: GIS-based geologic investigation using Kaguya elemental information. K.J. Kim, J. Dohm, P. Williams, J. Ruiz, T.M. Hare, N. Hasebe, Y. Karouji, S. Kobayashi, M. Hareyama, E. Shibamura, M. Kobayashi, C. d'Uston, O. Gasnault, O. Forni, S. Maurice, *Advances in Space Research*, 50(12), 1629 - 1637, 2012.
 48. Lack of High-Dose Radiation Mediated Prostate Cancer Promotion and Low-Dose Radiation Adaptive Response in the TRAMP Mouse Model. M D Lawrence, R J Ormsby, B J Blyth, E Bezak, G England, M R Newman, W D Tilley, P J Sykes, *Radiation Research*, 180(4), 376 - 388, 2013.
 49. False-positive TUNEL staining observed in SV40 based transgenic murine prostate cancer models. M D Lawrence, B J Blyth, R J Ormsby, W D Tilley, P J Sykes, *Transgenic Research*, 22(5), 1037 - 1047, 2013.
 50. Extension of lifespan and protection against oxidative stress by an antioxidant herb mixture complex (KPG-7) in *Caenorhabditis elegans*. Takahito Moriwaki, Seiji Kato, Yuichi Kato, Ayaka Hosoki, Qiu-Mei Zhang-Akiyama, *Journal of Clinical Biochemistry and Nutrition*, 53(2), 81 - 88, 2013.
 51. Efficiency Enhancement of Indirect Transverse Laser Cooling with Synchro-Betatron Resonant Coupling by Suppression of Beam Intensity. Hikaru Souda, Masao Nakao, Hiromi Okamoto,

- Akira Noda, et al., Japanese Journal of Applied Physics, 52, 030202, 2013.
52. Measurements of Individual Radiation Doses in Residents Living Around the Fukushima Nuclear Power Plant. Shigenobu Nagataki, Noboru Takamura, Kenji Kamiya, Makoto Akashi, Radiation Research , 180(5), 439 - 447, 2013.
 53. Antagonistic and stimulative role of ADAR1 in RNA silencing. Kazuko Nishikura, Masayuki Sakurai, Kentaro Ariyoshi, Hiromitsu Ota, RNA Biology, 10(8), 1240 - 1247, 2013.
 54. Forecasting the absolute and relative shortage of physicians in Japan using a system dynamics model approach. Tomoki Ishikawa, Hisateru Ohba, Yuki Yokooka, Kozo Nakamura, Katsuhiko Ogasawara, Human Resources for Health (Online Only <http://www.human-resources-health.com>), 11(41), 2013.
 55. The number of Japanese radiologic technologists will be increased in 40 years. Miwa Araseki, Yuki Yokooka, Tomoki Ishikawa, Katsuhiko Ogasawara, Radiological Physics and Technology, 6, 467 - 473, 2013.
 56. Calculation method using Clarkson integration for the physical dose at the center of the spread-out Bragg peak in carbon-ion radiotherapy. Minoru Tajiri, Takamasa Maeda, Yusuke Koba, Yosiharu Isobe, Toshitaka Kuroiwa, Shigekazu Fukuda, Katsuyuki Tanimoto, Kouichi Shibayama, Medical Physics, 40(7), 071733-1 - 071733-5, 2013.
 57. ADAR1 Forms a Complex with Dicer to Promote MicroRNA Processing and RNA-Induced Gene Silencing. Hiromitsu Ota, Masayuki Sakurai, Ravi Gupta, Louis Valente, Bjorn-Erik Wulff, Kentaro Ariyoshi, Hisashi Iizasa, Ramana V Davuluri, Kazuko Nishikura, et al., Cell, 153(3), 575 - 589, 2013.
 58. Reference levels in the context of Fukushima and related lessons learned. Kazuo Sakai, Health Physics, 105(5), 466 - 468, 2013.
 59. Regulation of gene expression in retrovirus vectors by X-ray and proton beam radiation with artificially constructed promoters. Ryohei Ogawa, Akihiro Morii, Akihiko Watanabe, Zheng-Guo Cui, Go Kagiya, Shigekazu Fukuda, et al., The Journal of Gene Medicine, 14(5), 316 - 327, 2012.
 60. Development of a therapeutically important radiation induced promoter. Ryohei Ogawa, Akihiro Morii, Akihiko Watanabe, Zheng-Guo Cui, Go Kagiya, Shigekazu Fukuda, et al., Bioengineered, 4(1), 44 - 49, 2013.
 61. Action Spectrum Analysis of UVR Genotoxicity for Skin: The Border Wavelengths between UVA and UVB Can Bring Serious Mutation Loads to Skin. Hironobu Ikehata, Shoichi Higashi, Shingo Nakamura, Yasukazu Daigaku, Yoshiya Furusawa, Yasuhiro Kamei, Masakatsu Watanabe, Kazuo Yamamoto, Kotaro Hieda, Nobuo Munakata, Tetsuya Ono, Journal of Investigative Dermatology, 133(7), 1850 - 1856, 2013.

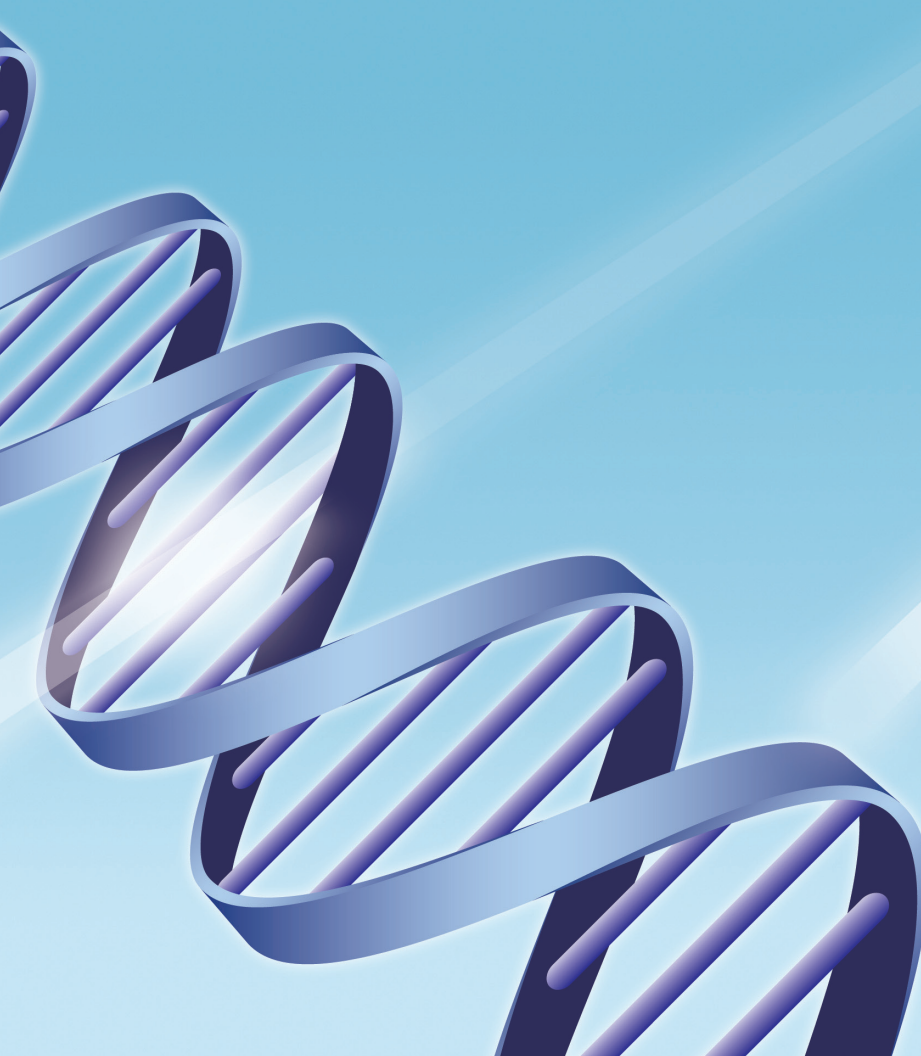
Access Map



NIRS Home Page (English)
You can access our website
by scanning the QR code.



<http://www.nirs.go.jp>



R100
本文のみ、古紙配合率100%再生紙を
使用しています